

UNIVERSITÀ DEGLI STUDI DI ROMA
“LA SAPIENZA”

Facoltà di Scienze Matematiche Fisiche e Naturali

A new polarimeter to study the curl
component of the Cosmic Microwave
Background polarization

Tesi di Laurea Specialistica in Astronomia ed Astrofisica

Anno Accademico 2005/2006

Author
Lorenzo Moncelsi

Supervisor
Prof. Paolo de Bernardis

Register: 1071681

Co-supervisor
Dott. Federico Nati

Contents

Introduzione	6
Introduction	10
1 The Hot Big Bang Model and the Inflation add-on	11
1.1 Introduction	11
1.2 The Standard Cosmological Model	11
1.3 The Unsolved Problems	17
1.3.1 The flatness problem	17
1.3.2 The horizons problem	18
1.3.3 The absence of magnetic monopoles	19
1.4 The Solution: Inflation	20
1.5 The Physics of Inflation	22
1.5.1 Scalar Fields	22
1.5.2 Slow-Roll Approximation	25
1.5.3 Exact Solutions	26
1.5.4 Hamilton-Jacobi Formulation	28
1.5.5 Reheating	29
1.5.6 Scalar Fluctuations	30
1.5.7 Tensor Fluctuations	34
2 The Cosmic Microwave Background	37
2.1 Introduction	37
2.2 Earth's Absolute Motion: The Dipole Anisotropy	39
2.3 The Last Scattering Surface	42
2.4 The Temperature Power Spectrum	44
2.4.1 Physical Effects at Recombination	44
2.4.2 Statistical Treatment	47
2.4.3 The Shape of the Spectrum	49
2.5 Polarization	54
2.5.1 Thomson Scattering at Recombination	54
2.5.2 Statistical Treatment	56
2.5.3 Quadrupole Anisotropy From Scalar Perturbations	65

2.5.4	Quadrupole Anisotropy From Tensor Perturbations	70
2.6	B-modes angular scale	73
2.7	CMB Observables	74
3	Description of the Experimental Apparatus	77
3.1	Introduction	77
3.2	Gunn Oscillator	77
3.2.1	Gunn Effect	78
3.2.2	The Resonant Cavity	82
3.3	Gaussian Optics and Beams of Radiation	84
3.3.1	Fundamental Gaussian Beam Mode	84
3.3.2	Higher Order Gaussian Beam Mode Solutions	88
3.4	Waveguides	89
3.5	Feed Horns	93
3.6	Detectors	100
3.7	Amplifiers	102
3.8	Modulation Electronics	108
3.9	Reference Signal	109
3.10	HDPE Lenses	112
3.11	Data Acquisition	114
4	Modulating the Polarization: An Innovative Approach	116
4.1	Introduction	116
4.2	Wire-Grid Polarizers: Electromagnetic Approach	116
4.2.1	Single Wire	117
4.2.2	Wire-Grid	122
4.2.3	The Reflecting Polarizer	125
4.2.4	Grids and Beams of Radiation	128
4.3	The New Polarizer	129
4.3.1	Mueller Matrix Characterization	134
4.3.2	Signal Extraction From Simulated Maps of the Polarized CMB Sky	139
4.3.3	Effect of Point Sources on CMB Polarization Measurements	142
4.4	A New Modulation Technique For Polarization: The Reflecting Polarizer	144
4.4.1	Plane Mirror and Fine Tuned Supporting System	147
4.4.2	The Rotating Support	150
4.4.3	Mueller Matrices Characterization: Expected Behaviour	150
4.4.4	Measurement Strategy	154
4.4.5	Reflecting Polarizer: Results	155

5	The Telescope	161
5.1	Introduction	161
5.2	Description of the OLIMPO Experiment	162
5.2.1	Small Scale Temperature Anisotropy of the CMB	163
5.2.2	S-Z Effect in Cluster of Galaxies	164
5.2.3	FIR Background	165
5.2.4	The Payload	166
5.3	Angular Response Measurements	169
5.3.1	Point Spread Function for a Cassegrain System	169
5.3.2	Ground Attitude Control System	170
5.3.3	Measurement Strategy	171
5.3.4	Focal Plane and Beam Coupling to the Telescope	172
5.3.5	Angular Response: Results	174
5.4	Optics Box	181
5.4.1	Optics Box Alignment: Laser Measurements	182
5.4.2	Optics Box Alignment: Focal Plane Mapping at 140 GHz	183
	Conclusions	187
	Conclusions	188
	A Stokes Parameters and Mueller Matrices	189
	B Spin-weighted Functions	199
	C Gunn Oscillators	201
	D Waveguides and Flanges	205
	E Antennas and Beams	209
	F Feed Horns	213
	List Of Figures	222
	List Of Tables	224
	Bibliography	224

Introduzione

Negli ultimi due decenni la cosmologia fisica ha subito uno sviluppo esponenziale, in particolare da un punto di vista osservativo e sperimentale. Il substrato teorico era stato già delineato negli anni 60 e 70, costruito sulle solide fondamenta della relatività generale. Gli ingredienti principali di quello che oggi viene comunemente indicato come Modello Cosmologico Standard del Big Bang caldo, erano già stati definiti a quell'epoca. Tuttavia questa prima formulazione presentava dei problemi concettuali irrisolti, che come vedremo non potevano essere ignorati. La soluzione per superare queste difficoltà concettuali fu proposta per primo dal fisico e cosmologo americano Alan Guth nel 1981 [1] e indipendentemente da Andrei Linde nel 1982 [2]: un breve periodo di espansione esponenziale dell'universo durante i suoi primi istanti, detto Inflation, è in grado di risolvere i problemi del modello cosmologico, senza modificarne gli aspetti più riusciti e di successo. L'Inflation è perciò un'aggiunta molto potente al modello cosmologico, che permette di tracciare una struttura teorica auto-consistente: il capitolo 1 è interamente dedicato alla descrizione del Modello Cosmologico Standard del Big Bang caldo e della fisica dell'Inflation.

Affinché l'Inflation possa essere considerata una teoria valida, è chiaro che essa deve fornire delle predizioni osservabili. Negli ultimi due decenni molti sforzi sono stati indirizzati da fisici e cosmologi sperimentali alla ricerca di evidenze indirette che riconducessero ad un periodo primordiale di espansione esponenziale dell'universo, raggiungendo un livello di accuratezza nelle misure tale da poter definire la cosmologia "di precisione". Un'evidenza sperimentale importantissima è data da misure molto stringenti delle piccole anisotropie di temperatura della radiazione cosmica di fondo (CMB), che è un fondo quasi perfettamente isotropo di radiazione di bassa energia che riempie in maniera omogenea il cosmo, residuo ormai freddo delle epoche primordiali dell'universo. Ad esempio l'esperimento BOOMERanG [10] ha fornito mappe ad alta risoluzione di una porzione di cielo, che evidenziano inequivocabilmente la natura puramente Euclidea della geometria del nostro universo, generica predizione di tutti i modelli inflazionari. La predizione più stringente di un generico modello di Inflation è tuttavia la creazione di un fondo stocastico di onde gravitazionali (perturbazioni tensoriali della metrica). Non c'è modo di rivelarle in maniera diretta, visto che tipicamente sono di ampiezza estremamente piccola; inoltre, dopo 14

miliardi di anni di diluizione a causa dell'espansione dell'universo, una misura diretta della loro presenza è da considerarsi impossibile. D'altra parte la teoria standard prevede che la presenza di queste onde gravitazionali primordiali debba manifestarsi nella sua interazione con la radiazione cosmica di fondo, lasciandovi un'impronta inequivocabile. Circa $3 \cdot 10^5$ anni dopo il Big Bang, quando l'universo è diventato trasparente alla radiazione (ricombinazione), i fotoni hanno subito globalmente la loro ultima interazione con gli elettroni; questo processo è stato chiaramente non istantaneo. La presenza di onde gravitazionali durante questo processo ha generato un'anisotropia di quadrupolo nell'interazione dei fotoni con gli elettroni (nel sistema di riferimento di quiete degli elettroni). A causa di ciò, è previsto che i fotoni della CMB presentino un certo grado di polarizzazione lineare. Il campo di polarizzazione lineare della CMB può essere formalmente suddiviso in due componenti: la componente gradiente (o modi E della polarizzazione), irrotazionale, e la componente rotore (modi B), rotazionale. Anisotropia di quadrupolo alla ricombinazione è anche generata dai campi di velocità, ovvero le perturbazioni scalari (di densità) della metrica. La peculiarità dei modi B della polarizzazione della CMB sta nel fatto che essi possono essere stati generati alla ricombinazione solamente dalle onde gravitazionali primordiali, mentre i modi E hanno avuto origine da perturbazioni sia scalari che tensoriali. Pertanto il rivelare in cielo il tracciato di polarizzazione tipico dei modi B significa ottenere una prova indiretta dell'esistenza delle onde gravitazionali, così come un forte vincolo sull'effettiva espansione esponenziale dell'universo primordiale. Nel capitolo 2 descriviamo in maniera dettagliata la radiazione cosmica di fondo e il suo campo di polarizzazione.

In ogni caso una misura del genere è estremamente difficoltosa, a causa delle piccolissime proporzioni dell'effetto in questione rispetto alle molteplici emissioni di luce polarizzata nello stesso intervallo di lunghezze d'onda di nostro interesse (millimetriche e sub-millimetriche), da sorgenti di natura galattica ed extragalattica, sia estese (nubi di polvere) che puntiformi (nuclei galattici attivi). Una caratterizzazione accurata dei tracciati di polarizzazione di queste sorgenti contaminanti è perciò assolutamente necessaria, se si vuole estrarre il segnale di polarizzazione di nostro interesse da un fondo dominante che deriva dalle molteplici emissioni polarizzate contaminanti. In questo lavoro non tratteremo esplicitamente i dettagli delle sorgenti polarizzate contaminanti, che sono principalmente costituite dall'emissione termica dei grani di polvere interstellare, allineati secondo una direzione preferenziale a causa dell'azione del campo magnetico galattico. I seguenti lavori sono completamente dedicati alla caratterizzazione e alla costruzione di un modello teorico di quest'emissione polarizzata contaminante, e facciamo ad essi riferimento per una descrizione dettagliata della fenomenologia: [63],[64],[65],[66],[67] e [68]. Ai fini del nostro lavoro è sufficiente riepilogare qualitativamente che, per frequenze al di sotto dei 60 GHz, il fondo cosmologico è completamente oscurato dall'emissione termica

dei grani di polvere interstellare, da emissioni di radiazione per sincrotrone e per transizioni libero-libero; a frequenze più alte, sopra i 400 GHz, l'emissione della polvere interstellare aggregata in nubi (“cirri”) domina sulla brillantezza del cielo, anche ad elevate latitudini galattiche.

La maniera canonica di progettare un esperimento per rivelare i modi B prevede la misura dei parametri di Stokes Q,U (che caratterizzano la polarizzazione lineare, vedi Appendice A) con la maggior risoluzione angolare possibile, per poi essere analizzati con metodi matematici e computazionali. Per questo tipo di approccio è necessario un array di rivelatori. In questo lavoro noi presentiamo una proposta innovativa per analizzare un campo rotazionale di polarizzazione, utilizzando un modulatore di polarizzazione di nuova concezione. Anziché un array di rivelatori (sensibili alla polarizzazione o accoppiati con polarizzatori lineari), la nostra idea è di introdurre nel piano focale di un telescopio a grande rapidità ottica un nuovo polarizzatore a griglia (wire-grid), i cui fili sono disposti in maniera da riprodurre esattamente il tracciato rotazionale tipico dei modi B. La dimensione del polarizzatore nel piano focale definisce l'area di cielo in analisi (campo di vista), che può essere di circa un grado o più, a seconda della forma dello spettro di potenza atteso per i modi B. Un unico rivelatore posto dietro al polarizzatore misura l'intensità integrata su tutta l'area efficace del polarizzatore. La caratterizzazione geometrica di questo campo rotazionale ci suggerisce fortemente l'aspetto che deve avere il tracciato di fili per modulare ottimamente la componente di nostro interesse del campo di polarizzazione della CMB. Come vedremo, alternando siffatto polarizzatore e la sua immagine speculare nella regione di cielo analizzata, la modulazione della polarizzazione è efficiente solamente per la componente rotazionale, mentre quella irrotazionale (modi E) non viene modulata. Le dimensioni ottimali e la forma di tale polarizzatore sono analizzate nel capitolo 4, eseguendo simulazioni numeriche su mappe di polarizzazione della CMB.

Questo approccio ha diversi vantaggi:

- si riduce il numero di rivelatori, non è necessario un array;
- si concentra su un unico rivelatore il segnale proveniente dall'intera area di cielo presa in considerazione per l'analisi, anziché suddividerlo tra un array di rivelatori. Viste le piccolissime proporzioni dell'effetto in questione, quest'aspetto è fondamentale, soprattutto se si considera l'accoppiamento con un telescopio con grande rapidità ottica;
- il rumore è significativamente più basso, poiché l'informazione proviene da un solo rivelatore, mentre nel caso di un array la stessa informazione proviene da N rivelatori, con un aumento complessivo del rumore di un fattore \sqrt{N} ;
- è possibile lavorare in multifrequenza, facendo uso di opportuni filtri di colore ottimizzati per la polarizzazione; infatti uno degli svantaggi prin-

cipali del nostro approccio è la possibile presenza di sorgenti puntiformi (come QSO e Blazar) nel campo di vista, che produrrebbero un forte segnale polarizzato. La separazione in canali a diversa frequenza ne consentirà invece il riconoscimento e la rimozione dal campo di vista, dato il comportamento in frequenza fortemente non termico di tali sorgenti.

In questo lavoro proponiamo quindi due differenti soluzioni per modulare campi rotazionali polarizzati, per mezzo, in entrambi i casi, di un nuovo polarizzatore a griglia, i cui fili sono disposti in maniera da riprodurre il tracciato rotazionale:

- due polarizzatori a riflessione;
- rotazione rigida di 180° dello stesso polarizzatore attorno all'asse individuato da un suo diametro.

La descrizione di queste innovative tecniche di modulazione si trova nel capitolo 4, mentre il capitolo 3 contiene i dettagli dell'intero apparato sperimentale utilizzato per effettuare le molteplici misure presentate in questo lavoro.

Naturalmente dobbiamo specificare che queste soluzioni sono pensate per un esperimento su pallone stratosferico, che in linea di principio può anche essere ottimizzato per compiere un'accurata caratterizzazione dei tracciati di polarizzazione lineare delle sorgenti contaminanti, aumentando il numero dei canali a bassa frequenza. Vale la pena ripetere che la presenza di queste sorgenti polarizzate contaminanti a lunghezze d'onda tipiche delle microonde o maggiori, deve essere assolutamente tenuta in considerazione, dal momento che le loro emissioni possono fortemente alterare le misure di polarizzazione della CMB: missioni su pallone stratosferico e osservazioni da terra sono perciò necessarie come cast di supporto a missioni su satellite interamente dedicate alla polarizzazione della CMB (come ad esempio il progetto BPOL dell'Agenzia Spaziale Europea, ESA).

Tale esperimento su pallone deve possedere un telescopio dalla grande rapidità ottica, così come dei rivelatori criogenici estremamente sensibili e di nuovo dalla grande rapidità ottica, in modo da raccogliere quanta più potenza possibile proveniente dal cielo. Nel capitolo 5 perciò ci concentriamo su OLIMPO, un telescopio per microonde ad alta risoluzione angolare, di 2.6 m in diametro, con configurazione Cassegrain (in asse): questo telescopio è il più grande che abbia mai volato su pallone stratosferico. L'accoppiamento di un esperimento di polarizzazione nelle microonde con tale telescopio (configurazione Cassegrain in asse a due specchi, primario parabolico e secondario iperbolico) è ottimale, dal momento che qualsiasi elemento ottico fuori asse può produrre polarizzazione spuria indesiderata. La configurazione Cassegrain ha diversi vantaggi: ad esempio la struttura compatta, con ripiegamento del fascio luminoso sui due specchi, che consente comunque di avere valori elevati della distanza focale; oppure la correzione delle principali aberrazioni luminose grazie alla compensazione dello

specchio secondario. Uno svantaggio importante da considerare per un esperimento su pallone, oltre alla maggiore ampiezza dei sidelobes rispetto ad una configurazione fuori asse, è la possibile diffrazione (e polarizzazione spuria) introdotta dai sostegni in acciaio dello specchio secondario di fronte al primario [76]. La loro importanza sarà valutata, insieme al profilo dei sidelobes, nel caso particolare del telescopio OLIMPO, per il quale abbiamo provveduto alla caratterizzazione della risposta angolare da terra, con ripetute misure.

Introduction

In the last two decades, physical cosmology underwent an exponential development, particularly from an observational point of view. The theoretical background had been depicted since the 60's and 70's, founded on the solid texture of general relativity. The main components of what is now commonly referred as Hot Big Bang Standard Cosmological Model had already been drawn at that epoch. However such first formulation presented some conceptual unsolved problems, which could not be disregarded, as we shall show in the following. The solution to overcome these glitches was first proposed by the American physicist and cosmologist Alan Guth in 1981 [1] and was given in its modern form independently by Andrei Linde [2] in 1982: a short period of exponential expansion of the universe occurred at very early times, named Inflation, is able to solve most of conceptual problems of the cosmological model, without modifying any of its successful features. Inflation is thus a powerful add-on to the cosmological model, which allowed to draw a self-consistent theoretical picture: chapter 1 is entirely dedicated to the description of the Hot Big Bang Cosmological Model and the physics of Inflation.

However for the Inflation to be recognized as a suitable theory, it is needed to furnish observable predictions. In the last two decades a lot of effort has been spent from experimental physicists and cosmologists to observe indirect evidences of the Inflation to have occurred, leading to the present day state of the art of what is usually referred as precision cosmology. A very important observational evidence arises from accurate measurements of temperature anisotropies in the Cosmic Microwave Background (CMB), which is an almost perfectly isotropic background of low energy radiation, filling homogeneously the universe, cooled relic of its primeval ages. For example the BOOMERanG experiment [10] provided high angular resolution maps of a patch of the sky, indicating unequivocally the pure Euclidean geometry of our universe, which is a generic prediction of inflationary models. Nevertheless the most tightening prediction arising from a generic inflationary scenario is the generation of a stochastic background of primordial gravitational waves (tensor fluctuations of the metric). There is no chance of detecting them directly, since their amplitude is usually extremely small; moreover after 14 billions years of dilution due to expansion of the universe such direct measurement turns out to be im-

possible. However these gravitational waves are predicted to have imprinted an unequivocal trace on the relic cosmic background radiation about $3 \cdot 10^5$ years after the Big Bang, when the universe became transparent to radiation (recombination). As we'll see in detail, the photons are scattered for the last time off electrons, being this process not instantaneous. The presence of such gravitational waves during this phase of the universe generated a quadrupole anisotropy in the scattering, as seen in the rest reference frame of the electrons. Because of this, some degree of linear polarization is expected in the background photons. In such linear polarization field two components can be formally distinguished: the *gradient component* (the so-called *E-modes*, irrotational field) and the *curl component* (the so-called *B-modes*, rotational field). Quadrupole anisotropy at recombination is also generated by velocity fields, i.e. scalar density fluctuations of the metric. The peculiarity of the B-modes is that they could only be generated by gravitational waves during recombination, while the E-modes were generated from both scalar and tensor perturbations to the metric. The detection of typical B-modes shear-like polarization patterns in the sky will thus provide indirect evidence of the existence of gravitational waves, as well as a strong constraint for a short period of exponential expansion to have occurred at very early times of the universe. In chapter 2 we give a detailed description of the Cosmic Microwave Background and its polarization field.

Such a measurement is however extremely difficult, because of the smallness of the effect with respect to the several polarized emissions occurring in the same range of wavelengths of our interest (millimetric and sub-millimetric), from both galactic and extragalactic sources, extended (e.g. dust clouds) or point-like (e.g. Active Galactic Nuclei). An accurate characterization of the polarization patterns of such foregrounds is thus required for just having a chance of detecting the polarized signal of interest immersed in a overwhelming polarized emission from foregrounds. We shall not give in this work the details of foregrounds polarized emission, which is mainly due to thermal emission from grains of interstellar dust, aligned because of the galactic magnetic field. The following works are completely dedicated to polarized foregrounds modelling and characterization, and we refer to them for a detailed description: [63],[64],[65],[66],[67] and [68]. For the aim of this work it is sufficient to say that at frequencies below 60 GHz interstellar emission of spinning dust grains, free-free and synchrotron emission from the interstellar medium dominate over the cosmological background, while at higher frequencies, above 400 GHz, the clumpy foreground from "cirrus clouds" of interstellar dust dominates the sky brightness even at high Galactic latitudes.

The popular way to depict experiments for B-modes detection is to measure the Stokes parameters Q,U (characterizing linear polarization, see Appendix A) with the highest possible angular resolution, and then analyze the measured data with mathematical and computational methods. An array of detectors is

needed to perform this measurement. In this work we present an innovative proposal for analyzing a curl polarization field using a new polarization modulator concept. Instead of an array detectors (polarization sensitive or coupled to common linear polarizers), we introduce in the focal plane of a big throughput telescope a wire-grid polarizer shaped to match the curl polarization pattern. The size of the polarizer on the focal plane defines the sky area under analysis (the field of view), which can be around one degree or more, depending on the shape of the theoretical power spectrum expected for the B-modes. A single detector behind the polarizer measures the intensity coming from the whole collecting area of the polarizer. The geometrical characterization of such rotational field strongly indicates that a shear-like path of the metallic wires has the required property of optimally modulating the curl component of the polarization field. Alternating such polarizer and its mirror image, we modulate the curl component, while we do not modulate the gradient (irrotational) component of the polarization field in the sky region under analysis. The optimal size and shape of such polarizers are analyzed in chapter 4, by means of numerical simulations carried out on maps of the polarized CMB sky.

This approach has several advantages:

- it reduces the number of needed detectors, and does not require an array;
- it concentrates on a single detector all the radiation power coming from the full area considered for the B-modes analysis, thus increasing the signal. Considering the smallness of the effect at issue, this aspect turns out to be fundamental, especially when taking into account the coupling with a big throughput telescope;
- the noise is lower, since the required information is obtained from a single detector, while in the array approach the same information is obtained from N detectors, with an increase in noise of a factor \sqrt{N} ;
- it allows multiband operations, by means of polarization-optimized color filters; in fact one of the main disadvantages of our approach is the possible presence of point sources (such as QSO's and Blazars) in the field of view, which would produce a strong polarized signal. Multiband channel separation will instead provide a powerful tool to recognize and remove point sources from the field of view, since they present a characteristic strongly non thermal spectrum.

We propose here two different solutions for modulating rotational polarization fields by means of shear-like polarizers:

- two reflecting polarizers;
- 180° flip of the same shear-like polarizer.

The description of these innovative modulation techniques is given in chapter 4, while chapter 3 contains the details on the whole instrumental apparatus used for the several measurements presented in this work.

Of course we must point out here that such solution is thought for a balloon-borne experiment, that in principle can also be optimized to perform an accurate characterization of linear polarization patterns from galactic foregrounds, by focusing on low frequency channels. It's worth to repeat that polarized microwave foregrounds must be absolutely taken into account since their presence can strongly affect CMB polarization measurements: ballon-borne and ground-based missions are thus required as supporting cast to satellite missions (such as the forthcoming satellite BPOL from the European Space Agency), entirely dedicated to CMB polarization. Such a ballon-borne instrument is required to possess a big throughput telescope and extremely sensitive cryogenic detectors again with very high throughput, in order to collect as much power as possible. In chapter 5 we therefore focus on OLIMPO, which is an high-resolution microwave balloon-borne 2.6 m on-axis Cassegrain telescope, the biggest one ever flown on a ballon. The coupling of such a microwave polarization experiment with a two-mirrors on-axis telescope (Cassegrain, primary parabolic mirror, secondary hyperbolic mirror) is optimal, because any off-axis optical element can produce unwanted spurious polarization. The Cassegrain configuration has several advantages, such as the compact structure providing all the same large focal length due to the two-mirrors folding of the light beam, and the correction of light aberrations thanks to the compensation by the secondary mirror. One important disadvantage to take into account (besides the increased amplitude of the sidelobes due to on-axis configuration) for balloon-borne experiments is the possible diffraction (and spurious polarization) introduced by the steel standoffs suspending the secondary mirror in front of the primary [76]. We shall evaluate their importance together with the sidelobes profile in the particular case of the OLIMPO telescope, for which intensive ground-based angular response measurements have been carried out during this work.

Chapter 1

The Hot Big Bang Model and the Inflation add-on

1.1 Introduction

The standard cosmological model (Hot Big Bang Model), widely accepted nowadays, describes the universe and its evolution; it has to be considered an unquestionable success, since nearly all of the observations and the experimental results fit with coherence in a self-consistent theoretical picture, founded on the solid texture of general relativity. Nevertheless this cosmological model, in its standard formulation, presents some unsolved conceptual problem: as I'll show later, Inflation can be treated as an add-on to the Hot Big Bang Model that solves all of its troubles without modifying any of its main successful features. The aim of this chapter is to give a general description of Inflation by means of its theoretical definition and its role of solving the conceptual problems of the standard cosmological model (par. 1.4), then introducing the basics of the physical texture upon which the inflationary scenario is build (par. 1.5). However first of all it is necessary to outline the main features of the standard cosmological model (par. 1.2) and its unsolved troubles (par. 1.3).

1.2 The Standard Cosmological Model

In the beginning it's worth to underline that any cosmological model has to be formalized by means of a set of proper parameters, the so-called cosmological parameters: the value of each parameter can be different in the various cosmological models, depending on the possibly different theoretical hypothesis on which the model is built upon. However all of them must be defined in such a way that allows them to be directly or indirectly measured, that is experimental observable. A lot of effort has been made in this sense till now, such as the

studies on gravitational lensing [3], on large-scale structures [4],[5], on galaxies and globular clusters aging [6]. But the actual turning point in this field has to be placed in the second half of the 90's, thanks to precision measurements of the anisotropies of the Cosmic Microwave Background (CMB) [9],[10],[17],[14][16] and to the improved observations of type Ia Supernovae [7],[8]: a more accurate and statistically meaningful evaluation of the cosmological parameters has been finally possible, a new era of “precision cosmology” has begun.

One of the main features shared by most of the cosmological models is the so-called Cosmological Principle: it states that the present universe is homogeneous and isotropic on large scales (of about 100 Mpc). Homogeneity means invariance of physical laws and global properties of the universe under translation, while isotropy means invariance under rotation.

The Cosmological Principle poses severe limitations on the possible basic hypothesis for a generic cosmological model, and when applied to the Einstein field equations ruling the dynamics of the universe,

$$R_{\mu\nu} - \frac{1}{2}g_{\mu\nu}R = \frac{8\pi G}{c^4} \left(T_{\mu\nu} + \frac{\Lambda c^4}{8\pi G} g_{\mu\nu} \right) \quad (1.1)$$

where $g_{\mu\nu}$ is the metric tensor, $R_{\mu\nu}$ is the Ricci tensor, R is the Ricci scalar, $T_{\mu\nu}$ is the stress-energy tensor (containing the energy and matter contribution to the universe and taken to be that of a perfect fluid, since homogeneity and isotropy imply that there is no bulk energy transport) and Λ is the so-called Cosmological Constant, while taking into account the expression of the metric for a 4-dimensional, homogeneous and isotropic space (Robertson-Walker metric),

$$ds^2 = g_{\mu\nu}dx^\mu dx^\nu = -c^2 dt^2 + a(t)^2 [dr^2 + S_k(r)^2 d\Omega^2] \quad (1.2)$$

with $d\Omega^2 = d\theta^2 + \sin^2\theta d\phi^2$, $a(t)$ dimensionless cosmic scale factor, describing the time evolution of the distances in the universe (in terms of expansion or contraction of lengths, present day is $t = t_0$, $a(t_0) = a_0 \equiv 1$) and

$$S_k(r) \text{ }^1 = \begin{cases} R_c \sin(\frac{r}{R_c}) & \text{if } k = +1, \\ r & \text{if } k = 0, \\ R_c \sinh(\frac{r}{R_c}) & \text{if } k = -1, \end{cases}$$

with R_c curvature radius of the universe (at $t = t_0$, $R_c(t_0) = R_{c,0}$), thus the field equations 1.1 reduce to the fundamental Friedmann equations for the cosmic scale factor:

¹ $k = +1$ means universe with positive curvature, hyperspheric geometry; $k = 0$ means flat universe, pure euclidean geometry; $k = -1$ means universe with negative curvature, hyperbolic geometry.

$$\frac{\ddot{a}}{a} = -\frac{4\pi G}{3c^2} \sum_i (\varepsilon_i + 3p_i) + \frac{\Lambda c^2}{3} \quad (\text{acceleration equation}) \quad (1.3)$$

$$\left(\frac{\dot{a}}{a}\right)^2 = H^2 = \frac{8\pi G}{3c^2} \sum_i \varepsilon_i - \frac{kc^2}{a^2 R_{c,0}^2} + \frac{\Lambda c^2}{3} . \quad (1.4)$$

In the equations 1.3 and 1.4 the quantities p_i and ε_i appear respectively as pressure and density of energy of the i -th component of the universe ($\varepsilon_m \rightarrow$ matter², $\varepsilon_\gamma \rightarrow$ radiation, $\varepsilon_\nu \rightarrow$ neutrinos, etc...); besides it appears Hubble's parameter $H(t)$, so defined: $H(t) = \left(\frac{\dot{a}}{a}\right)$.

Experimentally the universe is found to be in expansion, following the so-called Hubble's Law:

$$v_r(t) = \left(\frac{\dot{a}}{a}\right)d = H(t)d \quad (1.5)$$

that is two points in the universe separated by the distance d move away the one from the other with (radial) speed v_r ; $H(t)$ is therefore a proportionality factor, and its present value is $H(t_0) = H_0$ (Hubble's constant)³.

The presence of the Cosmological Constant Λ , since from eq. 1.1, represents a very important conceptual assumption: leaving out the historical reasons of its introduction (connected to Einstein's theoretical formulation of a stationary universe), the Λ -contribution (often called Dark Energy) to the physics of the universe should be interpreted as vacuum energy, a form of energy whose behaviour is opposite to gravity, i.e. a form of repulsive gravity that, in case of a Λ -dominated epoch of the universe, would lead the universe to an accelerated expansion, as we'll see later in this section.

Back to eqs. 1.3 and 1.4, a relation between p_i and ε_i is required to completely define the equations system, i.e. an equation of state $p = p(\varepsilon)$, different for each of the i components of the universe. In order to simplify the calculations in cosmology the equation of state is usually written in linear form:

$$p = w\varepsilon \quad (\text{eq. of state}), \quad (1.6)$$

where w is a dimensionless parameter in which is contained the physics of the i -th component of the universe. It's easy to find the value of w relative to

²In this context "matter" is usually used to identify not only ordinary (baryonic) matter, but also the non-baryonic component, often referred as Cold Dark Matter (CDM), believed to be about the 85% of "matter": $\varepsilon_m = \varepsilon_b + \varepsilon_{CDM}$.

³It's customary to introduce the dimensionless parameter h to write Hubble's constant: $H_0 = h \cdot 100 \frac{km}{s \cdot Mpc}$.

the main components of the universe, using the relation between $a(t)$ and the redshift $z = \frac{\lambda_{em} - \lambda_{obs}}{\lambda_{em}} = \frac{\Delta\lambda}{\lambda_{em}}$:

$$1 + z = \frac{a(t_{obs})}{a(t_{em})} = \frac{1}{a(t_{em})} \quad (\text{in fact } a(t_{obs}) = a_0 \equiv 1). \quad (1.7)$$

For non-relativistic matter we should expect the energy density to decrease as the inverse of the third power of the cosmic scale factor, $\varepsilon_{nrm} \propto a(t)^{-3}$, while for radiation energy density we should expect a decrease proportional to the inverse of the fourth power of $a(t)$, $\varepsilon_\gamma \propto a(t)^{-4}$; finally, by definition $\varepsilon_\Lambda = \text{constant}$.

Now taking the first time derivative of eq. 1.4 and substituting in it the acceleration equation (eq. 1.3), one obtains:

$$\frac{\dot{\varepsilon}_i}{\varepsilon_i} = -3(1 + w_i) \frac{\dot{a}}{a} \Rightarrow \frac{d\varepsilon_i}{\varepsilon_i} = -3(1 + w_i) \frac{da}{a} \Rightarrow \varepsilon \propto a^{-3(1+w_i)} \quad , \quad (1.8)$$

from which it easily turns out: $w_{nrm} = 0$, $w_\gamma = \frac{1}{3}$ e $w_\Lambda = -1$ (negative pressure \Rightarrow positive acceleration of the universe).

It is customary to define the following cosmological parameters: density of the i -th component of the universe Ω_i ($\Omega_m \rightarrow$ matter, $\Omega_\gamma \rightarrow$ radiation, $\Omega_\nu \rightarrow$ neutrinos, etc...), density of curvature Ω_k and density of vacuum energy (or density of Dark Energy) Ω_Λ :

$$\Omega_i = \frac{8\pi G\varepsilon_i}{3H^2c^2} \quad , \quad \Omega_k = -\frac{kc^2}{a^2H^2R_{c,0}^2} \quad , \quad \Omega_\Lambda = \frac{\Lambda c^2}{3H^2} \quad . \quad (1.9)$$

These parameters also depend on the time and when evaluated at $t = t_0$ they take the form $\Omega_{i,0}$, $\Omega_{k,0}$ e $\Omega_{\Lambda,0}$. From eq. 1.4 it turns out that:

$$\sum_i \Omega_i + \Omega_k + \Omega_\Lambda = 1 \quad . \quad (1.10)$$

It's also usual to write

$$\Omega = \sum_i \Omega_i + \Omega_\Lambda = 1 - \Omega_k = 1 + \frac{kc^2}{a^2H^2R_{c,0}^2} \quad , \quad (1.11)$$

and $\Omega(t_0) = \Omega_0$. With this notation eq. 1.4 becomes (if $\Omega_\nu \approx 0$):

$$\left(\frac{\dot{a}}{a}\right)^2 = H^2 = H_0^2 \left[\frac{\Omega_{\gamma,0}}{a(t)^4} + \frac{\Omega_{m,0}}{a(t)^3} + \Omega_{\Lambda,0} + \frac{\Omega_{k,0}}{a(t)^2} \right]. \quad (1.12)$$

Two other cosmological parameters need to be introduced to complete the scenario: σ_8 and the deceleration parameter $q = q(t)$. The first one is related to

the clustering of large scale structures in the universe and it's defined to be the root mean square (*rms*) density variation when smoothed with a sphere of uniform weight with $8h^{-1}Mpc$ radius.

The deceleration parameter q is defined as follows:

$$q \equiv -\frac{\ddot{a}a}{\dot{a}^2}, \quad (1.13)$$

and $q(t_0) = q_0$. It's easy to see from eq. 1.3 that in a matter-dominated universe ($\Omega_\Lambda, \Omega_\gamma, \Omega_\nu \approx 0, \varepsilon_m + 3p_m > 0$) the expansion is decelerated ($\ddot{a} < 0$), because of the global dominating gravitational attraction. Since matter is distributed in the universe with a very small mean density, the pressure p_m of the matter fluid is usually assumed to be negligible with respect to its energy density; under this assumption it's possible to show that q can be written as follows:

$$q = \frac{\Omega_m}{2} - \Omega_\Lambda. \quad (1.14)$$

As an example it's useful to see what happens in certain particular cases, assuming $\Omega_\gamma, \Omega_\nu = 0^4$. In the first case the contribution from the cosmological constant is negligible, ($\Omega_\Lambda \approx 0$), and the equations contain only the matter and curvature terms. There are now three alternatives: if $\Omega_m > 1$, it must be $k = +1$, that is the universe has hyperspheric geometry and it said to be closed: it reaches the maximum of expansion $a_{max} = a_0 \left[\frac{\Omega_{m,0}}{(\Omega_{m,0}-1)} \right]$, then it reverts back contracting, possibly ending with a final collapse (Big Crunch). If instead $\Omega_m < 1$, it must be $k = -1$, that is the universe has hyperbolic geometry and it said to be open: its expansion will be infinite with $a(t)$ increasing linearly in time. Finally the case $\Omega_m = 1$ requires the universe to have no curvature, it has pure Euclidean geometry and is said to be flat: its expansion will be infinite but with speed asymptotically approaching zero:

$$a(t) = a_0 \left(\frac{3}{2} H_0 t \right)^{\frac{2}{3}}, \quad \left(\frac{da}{dt} \right)_{t=\infty} = 0. \quad (1.15)$$

The precise value of ε_m corresponding to $\Omega_m = 1$ is called critical density, $\varepsilon_c = \frac{3c^2 H^2}{8\pi G}$; therefore in general $\Omega_m = \frac{\varepsilon_m}{\varepsilon_c}$.

In conclusion the De Sitter solution is briefly described: the universe is empty and flat, ($\Omega_m = \Omega_\gamma = \Omega_\nu = \Omega_k = 0$), the only energy contribution comes from

⁴This hypothesis is not restrictive, in fact it's always verified, except for a very short cosmological period, just about 10^5 yr after the Big Bang, during which radiation is dominating, $\varepsilon_\gamma \propto a(t)^{-4}$, and $a(t) \propto \sqrt{t}$ (eq. 1.12).

the vacuum, that is Λ ,

$$a(t) = a_0 e^{Ht} \quad , \quad \text{where} \quad H = \sqrt{\frac{\Lambda c^2}{3}}. \quad (1.16)$$

As said before Λ drives the universe to an accelerated expansion, therefore it will be a $\ddot{a} > 0$.

In table 1.1 the values of the cosmological parameters introduced are listed. These esteems, widely accepted by cosmologists, are the result of joining together the data from a large number of experiments, first of all the ones about CMB anisotropies and Ia Supernovae [18].

Parameter	Value
Hubble's Constant	$H_0 = 70.4 \frac{km}{s \cdot Mpc}$
Cosmological Constant	$\Omega_{\Lambda,0} = 0.732$
Matter	$\Omega_{m,0} = 0.268$
Baryonic Matter	$\Omega_{b,0} = 0.044$
Dark Matter	$\Omega_{CDM,0} = 0.223$
Curvature	$\Omega_{k,0} < 0.04$ [10]
σ_8	$\sigma_8 \simeq 0.776$
Deceleration Parameter	$q_0 = -0.77$ [20]

Table 1.1: Current values for the cosmological parameters introduced [18].

These values suggest a flat universe, dominated by two substantially unknown energy forms: the cosmological constant and the dark matter, indirectly highlighted by means of the rotation curves of galaxies and peculiar velocities in clusters of galaxies.

With the values in table 1.1 the Friedmann equations 1.3 and 1.4 can be solved, assuming $p_m = k = 0$ and $\varepsilon_\gamma, \varepsilon_\nu \approx 0$:

$$2\frac{\ddot{a}}{a} + \left(\frac{\dot{a}}{a}\right)^2 = \Lambda c^2$$

The exact solution is:

$$a(t) = A^{\frac{1}{3}} \left[\sinh \left(\frac{t}{t_\Lambda} \right) \right]^{\frac{2}{3}}, \quad A = \frac{\Omega_{m,0}}{\Omega_{\Lambda,0}} \approx 0.43, \quad t_\Lambda = \sqrt{\frac{4}{3\Lambda c^2}} \approx 3.4 \cdot 10^{17} s.$$

From a qualitative point of view the scale factor is similar to the one found for the De Sitter solution, but in this case matter initially acts as a brake against the exponential expansion. The function $a(t)$ diverges for $t \rightarrow \infty$: therefore

in this scenario the universe will forever expand. As said before the density parameters are functions of time for an expanding universe, except the case of Ω_Λ , which is supposed to remain constant: this leads to the conclusion that a period of decelerating expansion probably took place in the past, since $\frac{\Omega_m}{\Omega_\Lambda} > 1$, because of the gravitational contribution of the matter fluid. As a function of time, the deceleration parameter $q(t)$ has also changed sign, for $\frac{\Omega_m}{\Omega_\Lambda} = 1$, from initial positive values to the current negative value.

The age of the universe can be easily calculated, using the eqs. 1.7 and 1.12 to find dt :

$$dt = H_0^{-1}(1+z)^{-1} [\Omega_{m,0}(1+z)^3 + \Omega_{\Lambda,0}]^{-\frac{1}{2}} dz. \quad (1.17)$$

This expression has to be integrated between the time of the Big Bang $t = 0$ (i.e. infinite redshift, $z = \infty$) and today, $t = t_0$ ($z = 0$). The result is $t_0 = 13.1 \cdot 10^9 yr$.

1.3 The Unsolved Problems

1.3.1 The flatness problem

Taking into account the values shown in tab. 1.1, from the expression 1.11 for $\Omega(t)$ and from the Friedmann equation 1.12,

$$1 - \Omega(t) = -\frac{kc^2}{a(t)^2 H(t)^2 R_{c,0}^2} \quad (1.18)$$

evaluated at $t = t_0$,

$$1 - \Omega_0 = -\frac{kc^2}{H_0^2 R_{c,0}^2}, \quad (1.19)$$

it's clearly visible that Ω_0 is close to unity (flat universe) and also that the value of $\Omega(t)$ calculated backward in time goes more and more towards unity, since in a matter or radiation dominated epoch $a(t)H(t)$ is a decreasing function of time (see par. 1.2). Combining together eqs. 1.18 and 1.19, it results:

$$1 - \Omega(t) = \frac{H_0^2 (1 - \Omega_0)}{H(t)^2 a(t)^2}, \quad (1.20)$$

and by means of eq. 1.12 (with $\Omega_{\Lambda,0}$, $\Omega_{k,0} \approx 0$) it follows that

$$1 - \Omega(t) = \frac{a(t)^2 (1 - \Omega_0)}{\Omega_{\gamma,0} + a(t)\Omega_{m,0}}, \quad (1.21)$$

from which

$$|1 - \Omega(t)|_\gamma \propto a(t)^2 \propto t \quad (\text{radiation}), \quad |1 - \Omega(t)|_m \propto a(t) \propto t^{\frac{2}{3}} \quad (\text{matter}).$$

For example, at the time of primordial nucleosynthesis $t_{nuc} \approx 1s$, $a(t_{nuc}) \approx 3.6 \cdot 10^{-8}$, $|1 - \Omega(t_{nuc})| \lesssim 10^{-14}$; at times earlier than $1s$ $\Omega(t)$ must be even closer to unity. Assuming such a fine-tuned initial condition is quite unlikely, especially if we think that almost all of the other possible sets of initial conditions lead to a close universe rapidly collapsing on itself or to an open universe cooling below 3 K in the first second of life.

1.3.2 The horizons problem

The horizons problem comes from the assumption of large-scale isotropy and homogeneity: in fact although this is just the Cosmological Principle, on which the Big Bang scenario is build upon, there necessarily follows a paradox, that will soon be shown. In order to explain this conceptual bug an example is needed. After the first initial epoch, comprehensive of the primordial nucleosynthesis, the universe goes on expanding, cooling down⁵; as long as the kinetic thermal energy of the particles exceeds the ionization energy of atoms (13.6 eV for one hydrogen atom⁶) matter is fully ionized. After about $3 \cdot 10^5 yr = t_{rec} \rightarrow z \sim 1100$, at $T \sim 3000$ K, recombination of light nuclei with free electrons becomes possible. Until t_{rec} radiation is tightly coupled with matter, mainly via Thomson scattering off the electrons, therefore the universe is opaque to radiation. After recombination the number of free electrons drops down drastically and the electromagnetic radiation can propagate through the universe, in fact the mean free path of photons becomes much larger, of the same order of magnitude of the size of the universe. This primordial radiation still permeates the universe and appears today as a cold and isotropic background (the anisotropies in temperature are of the order of one part in 10^5 , see chapter 2 for details); the primordial high-energy photons have been redshifted to the current microwave frequencies, with a perfect blackbody behaviour at temperature $T_0 = 2.728$ K [13]. Recombination has been of course a non-instantaneous process, therefore the fossil radiation comes from a spherical shell, called Last Scattering Surface (LSS).

It's useful to calculate the proper distance between the LSS and us, by means of the expression for the metric in the case of a photon emitted at $t = t_{LSS}$

⁵Assuming adiabatic expansion $T \propto V^{-(\Gamma-1)}$, V volume of the universe, Γ adiabatic index, $\Gamma = \frac{4}{3}$ for radiation, therefore $\frac{T}{T_0} = a(t)^{-3(\Gamma-1)} = \frac{1}{a(t)} = (1+z)$ (see eq. 1.7), where T_0 is the present temperature of the universe.

⁶This quantity is actually reduced of about one order of magnitude when the baryon-to-photon numeric density ratio η is taken into account.

travelling along a null geodesic ($ds = 0$):

$$d_p(t_0) = c \int_{t_{LSS}}^{t_0} \frac{dt}{a(t)} = c \int_a^1 \frac{da}{a\dot{a}} = c \int_a^1 \frac{da}{a^2 H(a)} \quad (1.22)$$

$$d_p(t_0) = 0.98 \cdot d_{hor}(t_0) \approx 1.4 \cdot 10^4 Mpc \quad ^7$$

It follows that two points at the antipodes of the Last Scattering Surface (i.e. seen separated by 180° by an observer on Earth) are $1.96 \cdot d_{hor}(t_0)$ ⁸ far away from the other, that is they are causally disconnected: they had no way to exchange informations, neither to reach thermal equilibrium. So, how could the CMB have a perfect full-sky blackbody behaviour at $T = 2.728$ K (up to one part in 10^5)?

The problem is still more evident when an approximate calculation is made for the separation angle θ_{hor} between two regions of the sky at the time of last scattering (t_{LSS}), from the angular distance $d_A(t_{LSS})$ between the LSS and us, and from the horizon size $d_{hor}(t_{LSS})$. At that time the universe was matter-dominated, and for $w = 0$ (non-relativistic matter, see par. 1.2), it can be shown that $d_{hor}(t_{LSS}) = \frac{2c}{H(t_{LSS})}$, and that $d_A(t_{LSS}) \approx 13Mpc$, so:

$$\theta_{hor}(t_{LSS}) = \frac{d_{hor}(t_{LSS})}{d_A(t_{LSS})} \approx \frac{0.4Mpc}{13Mpc} \approx 0.03 \text{ rad} \approx 2^\circ.$$

Points separated by angles bigger than about 2° were not in causal contact at the moment of CMB release, and yet its fluctuations in temperature are not larger than one part in 10^{-5} , even on scales much bigger than 2° .

1.3.3 The absence of magnetic monopoles

The problem of magnetic monopoles (or in general of the “topological defects”) arises when the Hot Big Bang cosmological model inevitably approaches the particle physics, for $t \rightarrow 0$. In particular, as the Standard Model of particle physics, for energies higher than $E_{ew} \sim 1TeV$ ($T_{ew} \sim 10^{16}$ K), states the unification of the electromagnetic force together with the weak nuclear force to form the electroweak force, so it does the Grand Unification Theory (GUT), which states the unification of the electroweak force together with the strong nuclear force to form the Grand Unified Force, for energies of about $E_{GUT} \sim 10^{12}TeV$ ($T_{GUT} \sim 10^{28}$ K).

⁷This number is obtained using the values in tab. 1.1, and $d_{hor}(t_0) = c \int_0^{t_0} \frac{dt}{a(t)}$.

⁸Here $d_{hor}(t) = \frac{c}{H(t)} \rightarrow d_{hor}(t_0) = \frac{c}{H_0}$ stands for the particle horizon, the position of the most distant event that can presently be seen, that is, from which light has had enough time to reach us since the beginning of the universe.

In this theoretical picture, as the temperature of the universe drops down the critical value T_{GUT} (at $t = t_{GUT} \sim 10^{-36}s$) because of the expansion, the universe undergoes a phase transition, as it happens in thermodynamics, together with a spontaneous symmetry breaking leading to the separation of the electroweak force from the strong nuclear one. In general phase transitions with spontaneous symmetry breaking can produce the so-called “topological defects”, residual imperfections formed in the passage from one physical state to another: in the case of GUT phase transition they are thought to be the magnetic monopoles, that is the isolated poles (North or South) of a magnet. It’s also believed that they are very massive, $m_M c^2 \sim E_{GUT} \sim 10^{12} TeV$, from which it’s possible to esteem the associated energy density ε_M ,

$$\varepsilon_M \sim \frac{m_M c^2}{(2ct_{GUT})^3} \sim 10^{94} \frac{TeV}{m^3} \quad ,$$

so extremely high to dominate the universe immediately after the short period of radiation domination. So, why the universe is not dominated by magnetic monopoles? And why, conversely, there is no evidence at all of their actual existence?

1.4 The Solution: Inflation

As previously anticipated (see par. 1.1), a generic model of Inflation provides the solution to the listed problems (par. 1.3): it can be simply seen as an add-on to the standard Hot Big Bang cosmological model, that took place at times extremely close to $t = 0$, leaving unchanged all of the successful results. A huge number of Inflation models is currently present in the literature, but the aim of the first part of this work is to extract from a generic slow-roll (see par. 1.5.2) Inflation model a short list of observables, common to the majority of models and so as much as possible model-independent. Therefore the informations about Inflation given in these paragraphs should be read as an introductory way to approach this vast theoretical field, with only one clear intent, the isolation of a set of model-independent Inflation observables to constrain with future CMB experiments.

The definition of Inflation is simply an epoch in which the scale factor $a(t)$ has positive acceleration, $\ddot{a} > 0$. An equivalent definition takes into account the comoving Hubble’s length, $\frac{1}{aH}$, decreasing with time in an inflationary epoch, $\frac{d}{dt} \left(\frac{1}{aH} \right) < 0$. From a physical point of view the previous expression means that the observable universe, in comoving coordinates (fixed with the expansion), becomes actually smaller, because its characteristic scale goes on contracting more and more as the Inflation marches on.

As already shown in eqs. 1.14 and 1.16, an epoch with $\ddot{a} > 0$ corresponds to a

period of domination of a positive cosmological constant, in this case indicated with Λ_i , in order to distinguish it from the Λ which is supposed to dominate the universe nowadays. If the exponential growth of the scale factor (eq. 1.16) begins at $t = t_i$, during the first instants of the universe, and ends at $t = t_f$, with an instantaneous switch back to the initial radiation-dominated phase, it is possible to write:

$$a(t) = \begin{cases} a_i \sqrt{\frac{t}{t_i}} & \text{per } t < t_i, \\ a_i e^{H_i(t-t_i)} & \text{per } t_i < t < t_f, \\ a_i \sqrt{\frac{t}{t_f}} e^{H_i(t_f-t_i)} & \text{per } t > t_f, \end{cases} \quad (1.23)$$

where $a_i = a(t_i)$ and $H_i = \sqrt{\frac{\Lambda_i c^2}{3}}$. The scale factor is therefore increased of the quantity

$$\frac{a(t_f)}{a(t_i)} = e^N \quad , \quad \text{with} \quad N \equiv H_i(t_f - t_i) \quad (1.24)$$

named number of e-foldings of Inflation. To understand the effect of this primordial short exponential growth, it's useful to take into account the following typical values for a generic inflationary model: $t_i \sim t_{GUT} \sim 10^{-36} s$ ($H_i \sim t_{GUT}^{-1} \sim 10^{36} s^{-1}$) and $N \sim 100$, therefore $t_f = t_i + \frac{N}{H_i} \sim 10^{-34} s$. The scale factor is thus increased of the quantity $e^{100} \sim 10^{43}$.

The flatness problem (see par. 1.3.1) is immediately solved: from eq. 1.18

$$|1 - \Omega(t)| = \frac{c^2}{a(t)^2 H_i(t)^2 R_{c,0}^2},$$

that becomes, with $a(t) = a_i e^{H_i t}$,

$$|1 - \Omega(t)| = \frac{e^{-2H_i t} c^2}{a_i^2 H_i(t)^2 R_{c,0}^2} \propto e^{-2H_i t},$$

that is the deviation of $\Omega(t)$ from unity decreases exponentially with time. If for example the universe was strongly non-flat before t_i , $|1 - \Omega(t_i)| \sim 1$, after 100 e-foldings of Inflation it is amazingly flattened, $|1 - \Omega(t_i)| \sim e^{-2N} \sim 10^{-87}$. Let's step forward to the horizon problem: for $t = t_i$ the universe is radiation-dominated, thus the horizon size is (see par. 1.3.2):

$$d_{hor}(t_i) = a_i c \int_0^{t_i} \frac{dt}{a_i \sqrt{\frac{t}{t_i}}} = 2ct_i \approx 6 \cdot 10^{-28} m,$$

while at the end of Inflation, for $t = t_f$,

$$d_{hor}(t_f) = a_i e^N c \left(\int_0^{t_i} \frac{dt}{a_i \sqrt{\frac{t}{t_i}}} + \int_{t_i}^{t_f} \frac{dt}{a_i e^{H_i(t-t_i)}} \right) = e^N c (2t_i + H_i^{-1}) \approx 2 \cdot 10^{16} m.$$

Thus in about 10^{-34} s the horizon size is exponentially increased (of a factor $\sim e^N$), from subatomic to astronomical scales. From eq. 1.22 we find $d_p(t_i)$:

$$d_p(t_i) = e^{-N} d_p(t_f) = e^{-N} d_p(t_0) a(t_f) \approx 3 \cdot 10^{-44} m.$$

Since $\frac{d_p(t_i)}{d_{hor}(t_i)} \approx 5 \cdot 10^{-17}$, it's clear that the universe visible today could of course be completely in causal connection before the beginning of Inflation.

The problem of the absence of magnetic monopoles (par. 1.3.3) is finally considered: assuming their formation to have occurred before or during the inflationary period, their numeric density is exponentially decreased:

$$n_M(t_f) = e^{-3H_i(t_f-t_{GUT})} \frac{\varepsilon_M(t_{GUT})}{m_M c^2} \approx 15 pc^{-3},$$

where the factor 3 in the exponential takes into account that $n_M(t) \propto a(t)^{-3}$. If the value of n_M is extrapolated in time to $t = t_0$ (nowadays), also considering the further expansion from $a(t_f)$ to $a(t_0) = a_0 = 1$, it results $n_M(t_0) \approx 10^{-61} Mpc^{-3}$: the probability to find an isolate magnetic monopole is incredibly small.

1.5 The Physics of Inflation

This section is an introduction to the physics that is believed to lie beneath the Inflation scenario: there is no total agreement in the community of cosmologists about this topic, not only for the choice of a particular theoretical model (as said before, the literature offers lots of models of Inflation), but also for the set of initial conditions required to be imposed at the boundaries. Thus in the following we will refer to widely accepted generic assumptions and formalism, trying to preserve as much as possible our model-independent approach to Inflation, in order to extract the observables needed for the second part of this work.

1.5.1 Scalar Fields

Let us concentrate for a while on the physics of generic inflationary models involving symmetry breaking during a (second-order) phase transition⁹. In

⁹The first inflationary model, suggested by Guth in 1981, is usually now called "old inflation". This model was based on a scalar field theory which undergoes a first-order phase transition, oc-

general, gauge theories of elementary particle interactions involve an order parameter ϕ , determining the breaking of the symmetry, which is the expectation value of the scalar field which appears in the classical Lagrangian L_ϕ :

$$L_\phi = \frac{1}{2\hbar c^3} \dot{\phi}^2 - U(\phi) . \quad (1.25)$$

As seen before in eq. 1.8, Inflation requires a fluid with the unusual feature of having negative pressure. The scalar fields, describing scalar particles (with 0 spin) do satisfy this property; besides their potential has an extremely weak dependence on the redshift due to universe expansion, actually leading to an equation of state with negative pressure. The scalar field $\phi(\vec{r}, t)$ associated to Inflation is called Inflaton, and $U(\phi)$ is its potential energy.

If $\phi(\vec{r}, t)$ has the dimension of an energy and $U(\phi)$ of an energy density, in a region of space where ϕ is homogeneous, we have for the Inflaton energy density

$$\varepsilon_\phi = \frac{1}{2\hbar c^3} \dot{\phi}^2 + U(\phi) , \quad (1.26)$$

and for its pressure

$$p_\phi = \frac{1}{2\hbar c^3} \dot{\phi}^2 - U(\phi) . \quad (1.27)$$

Looking at eqs. 1.26 and 1.27 it's worth to notice that in general the Inflaton, although behaving as a perfect fluid, has not an equation of state relating univocally p_ϕ and ε_ϕ ; it's also clearly visible that the condition for the Inflation to occur is:

$$\dot{\phi}^2 < \hbar c^3 U(\phi) . \quad (1.28)$$

As we'll see in par. 1.5.3, even if this condition is initially not verified, if the potential $U(\phi)$ is sufficiently flat the condition immediately becomes satisfied, provided that the scalar field is far enough from the minimum of its potential $U(\phi)$.

If we want to understand when and in which circumstances this condition could have been satisfied in the primordial universe, it's necessary to find out the equations of motion for the scalar field ϕ . The first step is to write down the expression of the equation of state for an expanding or contracting universe;

curing by a process of bubble nucleation, leading to an highly chaotic universe; it was therefore abandoned. The model described here is the "new inflation", with second-order phase transition, where there is no potential barrier (see par. 1.5.3).

from the first law of thermodynamics

$$dQ = dE + pdV , \quad (1.29)$$

with dQ heat flow in or out from a given region of space, dE variation of the internal energy of the region and dV variation of its volume. If the universe is perfectly homogeneous and isotropic, it results $dQ = 0$ for every V , that means every expansion or contraction to be adiabatic. For an adiabatic expansion eq. 1.29 reduces to

$$\dot{E} + p\dot{V} = 0 . \quad (1.30)$$

We now need to find out the expression for the comoving volume of an expanding universe: let's consider a sphere of comoving radius r_s (i.e. proper radius $R_s(t) = a(t) \cdot r_s$):

$$V(t) = \frac{4}{3}\pi r_s^3 a(t)^3 \quad \Rightarrow \quad \dot{V} = \frac{4}{3}\pi r_s^3 (3a^2\dot{a}) = V \left(3\frac{\dot{a}}{a} \right) . \quad (1.31)$$

Writing the internal energy as $E(t) = V(t)\varepsilon(t)$, it turns out that

$$\dot{E} = V\dot{\varepsilon} + \dot{V}\varepsilon = V \left(\dot{\varepsilon} + 3\frac{\dot{a}}{a}\varepsilon \right) . \quad (1.32)$$

Combining eqs. 1.30, 1.31 and 1.32, we obtain the fluid equation for an expanding universe:

$$\dot{\varepsilon} + 3\frac{\dot{a}}{a}(\varepsilon + p) = 0 \quad \Rightarrow \quad \dot{\varepsilon} + 3H(t)(\varepsilon + p) = 0 . \quad (1.33)$$

If we now go back to the Inflaton, the first equation of motion is obtained substituting eqs. 1.26 and 1.27 in eq. 1.33:

$$\varepsilon_{\phi} + 3H(t)(\varepsilon_{\phi} + p_{\phi}) = 0 \quad \Rightarrow \quad \ddot{\phi} + 3H(t)\dot{\phi} = -\hbar c^3 \frac{dU}{d\phi} . \quad (1.34)$$

Instead the second equation of motion is obtained substituting eq. 1.26 in eq. 1.4:

$$H(t)^2 = \frac{8\pi}{3M_{Pl}^2} \left(\frac{\hbar}{c} U(\phi) + \frac{1}{2c^4} \dot{\phi}^2 \right) , \quad (1.35)$$

where the Planck mass is introduced, $M_{Pl} = \sqrt{\frac{\hbar c}{G}} = 2.2 \cdot 10^{-8} kg$, usually expressed in the form of Planck energy, $E_{Pl} = M_{Pl}c^2 = 1.2 \cdot 10^{19} GeV$.

1.5.2 Slow-Roll Approximation

In order to easily obtain solutions to the equations of motion 1.34 and 1.35, it's usual to work under the so-called Slow-Roll approximation: the scalar field ϕ has a weak dependence on the time, i.e.

$$\dot{\phi}^2 \ll \hbar c^3 U(\phi) , \quad (1.36)$$

in such a way that the Inflaton behaves exactly as a cosmological constant,

$$\varepsilon_\phi \approx -p_\phi \approx U(\phi) \quad \Rightarrow \quad w_\phi = -1 \quad (\text{see eq. 1.8}).$$

Under this approximation the equations of motions take the form:

$$3H(t)\dot{\phi} \approx -\hbar c^3 \frac{dU}{d\phi} \quad e \quad H(t)^2 \approx \frac{8\pi\hbar}{3cM_{Pl}^2} U(\phi) . \quad (1.37)$$

It's customary to describe the Slow-Roll condition by means of two dimensionless parameters, $\epsilon(\phi)$ and $\zeta(\phi)$, the so-called Slow-Roll parameters:

$$\epsilon(\phi) = \frac{E_{Pl}^2}{2} \left(\frac{1}{U} \frac{dU}{d\phi} \right)^2 \ll 1 , \quad (1.38)$$

$$|\zeta(\phi)| = E_{Pl}^2 \left| \frac{1}{U} \frac{d^2U}{d\phi^2} \right| \ll 1 . \quad (1.39)$$

It's possible to show that these two conditions are necessary for the Slow-Roll equation (eq. 1.36) to be satisfied, but not sufficient, since they only limit the shape of the potential $U(\phi)$: the value of $\dot{\phi}$ can thus be chosen in such a way that the Slow-Roll condition is violated. Therefore it's necessary to work under the further assumption of "attractive behaviour" for the Inflaton, that is the solution for a given potential satisfies the first one of 1.37 (see also par. 1.5.4). A generic model of Inflation therefore consists of a particular shape for the potential and of a way to cut down the inflationary period, for example violating the Slow-Roll conditions 1.38 and 1.39, in such a moment for which the field ϕ approaches a minimum of $U(\phi)$ with null (or almost null) potential energy

$(\epsilon, \zeta \rightarrow \infty)$.

In the next paragraph the exact solutions are shown for particular given shapes of the potential; in certain applications of Inflation however it's enough to know the number N of e-foldings for a given potential. This number can be easily found without solving the equations of motion for ϕ :

$$N = \ln \frac{a(t_f)}{a(t_i)} = \int_{t_i}^{t_f} H dt \approx -\frac{1}{E_{Pl}^2} \int_{\phi_i}^{\phi_f} \frac{U}{\frac{dU}{d\phi}} d\phi, \quad (1.40)$$

where $\phi_i = \phi(t_i) = \phi(t_{GUT})$ and $\phi_f = \phi(t_f)$, for which $\epsilon(\phi_f) > 1$.

1.5.3 Exact Solutions

Before the description of three exact solutions of the equations of motion (for two particular shapes of the potential), it's useful to show in a qualitative way the behaviour of the Inflaton for a generic potential in order to have an inflationary period, i.e. an exponential expansion of the universe. Let's consider the potential drawn in fig. 1.1: its absolute minimum is located at $\phi = \phi_0$ and in this case $U_{min} = U(\phi_0) = 0$. If we suppose that Inflation begins for $\phi \approx 0$, where $U(0) \approx U_0$,

$$\left(\frac{dU}{d\phi}\right)^2 \ll \frac{U_0^2}{E_{Pl}^2} \Rightarrow \epsilon(\phi) \ll 1$$

on the plateau where $U \approx U_0$, therefore the Inflaton scalar field contributes to the universe with constant energy density, $\epsilon_\phi \approx U_0$. This physical state is not stable (often referred as "metastable false vacuum state") and it lasts as long as ϕ slowly rolls towards ϕ_0 . When finally $\phi = \phi_0$ and $U(\phi_0) = 0$, the potential has reached a "stable true vacuum state", for which the Slow-Roll condition is no longer satisfied and therefore the Inflation has come to an end. The number of e-foldings of Inflation (i.e. its duration) depends on how long the scalar field takes to roll down to the minimum of its potential, that is the length of the plateau where $U \approx U_0$.

The first example of exact solution of the equations of motion 1.34 and 1.35 is often referred as "Polynomial Inflation": the potential is taken to be $U \propto \phi^\alpha$, then the scale-factor behaviour is very close to exponential. This becomes less true as α increases, but investigations are usually limited to ϕ^2 and ϕ^4 potentials. The second example is the "Power-law Inflation", the associated potential has an exponential behaviour:

$$U(\phi) = U_0 e^{-\left(\sqrt{\frac{2}{\xi}} \cdot \frac{\phi}{E_{Pl}}\right)}, \quad (1.41)$$

where U_0 and ξ are constant. The exact solutions for a flat universe are:

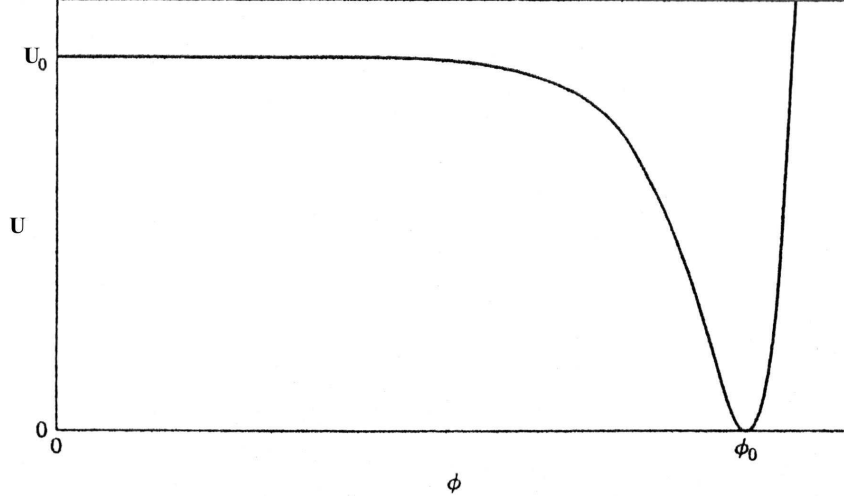


Figure 1.1: Shape of a generic potential $U(\phi)$ giving rise to a period of exponential expansion for the universe.

$$a = a_0 \cdot t^\xi \quad (1.42)$$

$$\frac{\phi}{E_{Pl}} = \sqrt{2\xi} \ln \sqrt{\frac{U_0 G}{\xi(3\xi - 1)} \cdot \frac{t}{c}} \quad (1.43)$$

The condition for Inflation to occur is satisfied provided $\xi > 1$; with this potential there is no analytic end point for Inflation, but this problem can be avoided by means of theoretical constructions in which we are not interested in this work.

Another example of exact solution is the “Intermediate Inflation”, generated by the potential

$$U(\phi) \propto \left(\frac{\phi}{E_{Pl}} \right)^{-\beta} \left(1 - \frac{\beta^2}{6} \cdot \frac{E_{Pl}^2}{\phi^2} \right), \quad (1.44)$$

with $\beta = 4(\varpi^{-1} - 1)$, $0 < \varpi < 1$, leading to an expansion

$$a \propto e^{B \cdot t^\varpi}, \quad (1.45)$$

with $B > 0$; this solution is swifter than any power-law but not than a pure

exponential expansion, because of the presence of ϖ . As in the “Power-law Inflation”, there is no analytic end point for Inflation.

1.5.4 Hamilton-Jacobi Formulation

The evolution of the scalar field at a given point of the potential must be independent of the initial conditions, otherwise the results supplied by a certain model of Inflation would depend on the unknown initial conditions. As previously mentioned (par. 1.5.2), the Slow-Roll approximation as presented above needs the further assumption of “attractive behaviour” of the Inflaton to correctly work: in fact “attractive behaviour” means that solutions obtained from different initial conditions must quickly converge to the same solution. This is the only way Inflation can be considered a reliable theory.

With regard to this fact, it’s worth to briefly introduce an analogous formulation of Inflation, based on the Hamilton-Jacobi formalism and which has the remarkable feature of working under the Slow-Roll condition without any other further assumption. This important feature will not be described here, this paragraph only deals about the main lines of the Hamilton-Jacobi formalism applied to Inflation.

Consider the scalar field $\phi(\vec{r}, t)$, monotonically variable with time, and suppose for example $\dot{\phi} > 0$ (if this condition is not verified, it’s always possible to redefine $\phi \rightarrow -\phi$). Differentiating eq. 1.35 with respect to the time and substituting it into eq. 1.34, we have:

$$2\dot{H} = -\frac{\dot{\phi}^2}{E_{Pl}^2} \Rightarrow \dot{\phi} = -2E_{Pl}^2 \frac{dH}{d\phi}, \quad (1.46)$$

where the monotonic behaviour of ϕ has been used when dividing both LHS and RHS of eq. 1.46 for $\dot{\phi}$. With this relation between $\dot{\phi}$ and $\frac{dH}{d\phi}$, we can write down the equation of motion in the Hamilton-Jacobi formalism:

$$H(\phi)^2 = \frac{8\pi\hbar}{3cM_{Pl}^2}U(\phi) + \frac{2E_{Pl}^2}{3} \left(\frac{dH}{d\phi} \right)^2. \quad (1.47)$$

In this approach $H(\phi)$ must be specified, from which the expression for the potential is immediately obtained, while from eq. 1.46 it’s possible to find $H(t)$ and so $a(t)$. For example we have:

- $H(\phi) \propto \phi^{-\frac{\beta}{2}} \Rightarrow$ “Intermediate Inflation” ,
- $H(\phi) \propto e^{-\left(\sqrt{\frac{1}{2\xi}} \cdot \frac{\phi}{E_{Pl}}\right)} \Rightarrow$ “Power-law Inflation” .

With this formalism it is possible to redefine the Slow-Roll parameters (see 1.38 and 1.39):

$$\epsilon_H = 2E_{Pl}^2 \left(\frac{1}{H} \cdot \frac{dH}{d\phi} \right)^2, \quad (1.48)$$

$$\zeta_H = 2E_{Pl}^2 \left(\frac{1}{H} \cdot \frac{d^2 H}{d\phi^2} \right). \quad (1.49)$$

It's clear that in the Slow-Roll limit $\epsilon_H \rightarrow \epsilon$ and $\zeta_H \rightarrow \zeta$. It's possible to show that $\epsilon_H \ll 1$ and $\zeta_H \ll 1$ are exactly the conditions that allow to neglect the term $\ddot{\phi}$ in eq. 1.34 and the term proportional to $\dot{\phi}^2$ in eq. 1.35, leading to eqs. 1.37. Besides the exact definition of Inflation is now

$$\ddot{a} > 0 \quad \Leftrightarrow \quad \epsilon_H < 1, \quad (1.50)$$

and the exact equation for the number of e-foldings becomes:

$$N = \ln \frac{a(t_f)}{a(t_i)} = \int_{t_i}^{t_f} H dt = -\frac{1}{E_{Pl}^2} \int_{\phi_i}^{\phi_f} \frac{H}{\frac{dH}{d\phi}} d\phi. \quad (1.51)$$

It's worth to remember finally that, with the new definition of the Slow-Roll parameters 1.48 and 1.49, the validity of the Slow-Roll approximation no longer requires further assumptions on the ‘‘attractive behaviour’’ of the Inflaton.

1.5.5 Reheating

In this paragraph a brief description of the so-called ‘‘Reheating’’ process is given, a very short period immediately following the end of Inflation, necessary to explain why Inflation does not reduce the numeric density of photons as it happens for the magnetic monopoles (see par. 1.4), in such a way that the universe can currently have the radiation density we actually measure.

Referring to fig. 1.1, we see that the Inflaton ϕ , after the slow roll along the plateau where $U(\phi) \approx U_0$, approaches the minimum by means of oscillations around it: the amplitude of these oscillations, in the first equation of motion 1.34, is only dimmed by the term $3H\dot{\phi}$ (proportional to the first time derivative of the scalar field, in an analogous way to the viscous friction). If however we suppose that ϕ is tightly coupled with other fields in the universe (as it's believed to be), the oscillations around ϕ_0 are dimmed more rapidly and part of the energy of the Inflaton is carried away by the vector bosons of the coupled fields, for example the photons. These photons are just the ones that reheat again the universe after the sudden fall in temperature caused by the exponential expansion, from $T(t_i) = T(t_{GUT}) \sim 10^{28}$ K to

$T(t_f) = e^{-N}T(t_{GUT}) \approx e^{-100} T(t_{GUT}) \sim 10^{-15}$ K, temperature to which corresponds a numeric density of photons extremely lower than the one we observe today ($n_\gamma \sim 400\text{cm}^{-3}$). Therefore the “Reheating” process is indispensable to convert the energy density of the Inflaton in energy density of photons and thus it allows the universe to get back to the temperature before Inflation, $T(t_i)$.

1.5.6 Scalar Fluctuations

Inflation does more than solving the listed problems. The power of Inflation is its ability to correlate scales that would otherwise be disconnected. The zero-order scheme outlined in the previous sections ensures that the universe will be uniform on all scales of interest today. However there are perturbations about this zero-order scheme and these perturbations (quantum fluctuations), produced early on when the scales are causally connected, persist long after Inflation has terminated. We are most interested in scalar perturbations to the metric since these couple to the density of matter and radiation and ultimately are responsible for most of the inhomogeneities and anisotropies in the universe. In this section we will study these in detail. In addition to scalar perturbations, though, inflation also generates tensor fluctuations in the gravitational metric, the so-called gravity waves. These are not coupled to the density and so are not responsible for the large-scale structure of the universe, but they do induce fluctuations in the CMB. In fact, these fluctuations turn out to be a unique signature of Inflation and offer the best window on the physics driving Inflation; their description is treated in the next section.

During Inflation, the universe consists primarily of a uniform scalar field and a uniform background metric. Against this background, the fields fluctuate quantum mechanically. At any given time, the average fluctuation is zero, because there are regions in which the field is slightly larger than its average value and regions in which it is smaller. The average of the square of the fluctuations (the variance), however, is not zero. Our goal is to compute this variance and see how it evolves as Inflation progresses.

In practice, we need a basic calculation of how the zero-point fluctuations in small-scale quantum modes freeze out as classical density fluctuations once the modes have been inflated to super-horizon scales. We can note that a natural prediction will be a spectrum of perturbations that are nearly scale invariant. This means that the metric fluctuations of space-time receive equal levels of distortion from each decade of perturbation wavelength, and may be quantified in terms of the *rms* fluctuations, σ_Φ , in Newtonian gravitational potential, Φ :¹⁰

$$(\delta\rho_H)^2 \equiv \delta_\Phi^2 = \frac{d}{d \ln k} \sigma_\Phi^2 = \text{constant} , \quad (1.52)$$

¹⁰We shall work in natural units from now till the end of the chapter.

where k is the comoving wavenumber of the perturbation $\delta\phi$, supposed to take the form of a comoving plane-wave of amplitude A :

$$\delta\phi(\vec{x}) = A e^{(i\vec{k}\cdot\vec{x} - i\frac{k}{a}t)} . \quad (1.53)$$

The first equivalence arises because the perturbation $\delta\phi$ in the Newtonian gravitational potential is of the same order as the density fluctuation $\delta\rho_H$ on the scale of the horizon at any given time (see [22], chapter 15). It is commonly argued that the prediction of scale invariance arises because of the invariance of our space under time translation. At a given time, the only length scale in the model is the horizon size $\frac{c}{H}$, so it is inevitable that the fluctuations that exist on this scale are the same at all times. After the end of Inflation, the resulting fluctuations (at constant amplitude on the scale of the horizon) give us the Zel'dovich or scale-invariant spectrum. The problem with this argument is that it ignores the issue of how the perturbations evolve while they are outside the horizon: in fact only for the last generation of perturbations, those on the horizon scale at t_f , the amplitude can be calculated. Fluctuations generated at earlier times will be inflated outside the horizon, and will re-enter it at some time after t_f . For the aim of this work, we shall rely on simply motivating the inflationary result, which is that potential perturbations re-enter the horizon with the same amplitude they had on leaving. This may be made reasonable because perturbations outside the horizon are immune to causal effects, so it is hard to see how any large-scale non-flatness in space-time could know whether it was supposed to grow or decline.

Imagine that the main effect of fluctuations is to make different parts of the universe have fields that are perturbed by an amount $\delta\phi$. In other words, we are dealing with various copies of the same rolling-behaviour, $\phi(t)$, but viewed at different times $\delta t = \frac{\delta\phi}{\dot{\phi}}$. These parts of the universe will then finish Inflation at different times, leading to a spread in energy density. The horizon-scale density amplitude is given by the different amounts that each part has expanded following the end of Inflation:

$$\delta\rho_H \simeq H \cdot \delta t = \frac{H^2}{2\pi\dot{\phi}} , \quad (1.54)$$

where the last equality follows from the quantum field theory result that the *rms* $\delta\phi$ is given by $H/2\pi$ (see [21] and [26]). In fact, if we consider the equation of motion obeyed by perturbations $\delta\phi$ of the Inflaton field ϕ

$$\left(\ddot{\delta\phi}\right) + 3H\left(\dot{\delta\phi}\right) + \left(\frac{k}{a}\right)^2(\delta\phi) = 0 , \quad (1.55)$$

which is a standard wave equation for a massless field evolving in an expanding universe, it's possible to find out the field variance $\sigma_{\delta\phi}^2(k)$, defined to be

$$\sigma_{\delta\phi}^2(k) = \left\langle \delta\phi(\vec{k}) \cdot \delta\phi^*(\vec{k}') \right\rangle , \quad (1.56)$$

where $\delta\phi(\vec{k}) = \delta\phi_k$ is the Fourier transform of the field perturbation $\delta\phi(\vec{x})$,

$$\delta\phi_k = \delta\phi(\vec{k}) = \frac{1}{(2\pi)^3} \int \delta\phi(\vec{x}) \cdot e^{i\vec{k}\cdot\vec{x}} d^3x . \quad (1.57)$$

We also define the Power Spectrum $P_{\delta\phi}(k)$ of the perturbations of the scalar field ϕ :

$$\left\langle \delta\phi(\vec{k}) \cdot \delta\phi^*(\vec{k}') \right\rangle = (2\pi)^3 P_{\delta\phi}(k) \delta^3(\vec{k} - \vec{k}') . \quad (1.58)$$

With these definitions above, it follows that $\sigma_{\delta\phi}^2(k) = (2\pi)^3 P_{\delta\phi}(k) \delta^3(\vec{k} - \vec{k}')$. To find the power spectrum of the perturbations of the scalar field it's often used an analogy with the harmonic oscillator in quantum mechanics (see for example chapter 6 of [23] or chapter 11 of [22]): eq. 1.55 is solved starting well inside the horizon ($\frac{k}{a} \gg H$) where flat-space quantum theory works, and ending outside the horizon where $\frac{k}{a} \ll H$. The result is that at $\frac{aH}{k} \gg 1$, the fluctuation amplitude becomes frozen out at the value

$$\sigma_{\delta\phi}^2(k) = \frac{(2\pi)^3 \cdot H^2}{2k^3} \implies P_{\delta\phi}(k) = \frac{H^2}{2k^3} . \quad (1.59)$$

The initial quantum zero-point fluctuations in the field have been transcribed to a constant classical fluctuation that can eventually manifest itself as large-scale structure. The fluctuations in ϕ depend on k in such a way that the fluctuations per decade are constant:

$$\frac{d(\delta\phi)^2}{d \ln k} = \frac{4\pi k^3}{(2\pi)^6} \sigma_{\delta\phi}^2(k) = \left(\frac{H}{2\pi} \right)^2 , \quad (1.60)$$

as previously anticipated. The *rms* value of the fluctuations in ϕ can be used to deduce the power spectrum of mass fluctuations well after Inflation is over. In fact, since $\delta t = \frac{\delta\phi}{\dot{\phi}}$ and $\delta\rho_H \simeq H \cdot \delta t$, it follows that:

$$\delta\rho_H \simeq H \frac{\delta\phi}{\dot{\phi}} . \quad (1.61)$$

In terms of variance per $\ln k$ in Newtonian potential perturbations, we have:

$$(\delta\rho_H)^2 \equiv \delta_\Phi^2(k) = \frac{H^4}{(2\pi\dot{\phi})^2} . \quad (1.62)$$

If H and $\dot{\phi}$ are both constant, then the predicted spectrum is exactly scale invariant, with some characteristic inhomogeneity on the scale of the horizon. The fluctuations in ϕ start as normal flat-space fluctuations, which change their nature as they go beyond the horizon and become frozen-out classical fluctuations. All that matters is that Hubble's parameter is roughly constant for the few e-foldings required for this freezing to be completed. Two other characteristics of the perturbations are more general: they will be Gaussian and adiabatic in nature. A Gaussian density field is one for which the joint probability distribution of the density at any given number of points is a multivariate Gaussian. The easiest way for this to arise in practice is for the density field to be constructed as a superposition of Fourier modes with independent random phases; it's easy to see in the case of Inflation that this requirement will be satisfied: the quantum commutation relations only apply to modes of the same k , so that modes of different wavelength behave independently and have independent zero-point fluctuations. Finally, the principal result of the inflationary fluctuations in their late-time classical guise is as a perturbation to curvature (adiabatic fluctuations, with constant matter-to-radiation ratio everywhere), and it is not easy to see how to produce the separation in behaviour between photon and matter perturbations that is needed for isocurvature modes (non constant matter-to-radiation ratio). Towards the end of inflation, the universe contains nothing but scalar field and whatever mechanisms that generate the matter-antimatter asymmetry have yet to operate. When they do act, the result will be a universal ratio of photons to baryons, but with a total density modulated by the residual inflationary fluctuations: these are exactly the adiabatic conditions.

In analogous way to eq. 1.58 we define the Power Spectrum of the scalar density perturbations $P_S(k)$:

$$\left\langle \delta\rho_H(\vec{k}) \cdot \delta\rho_H^*(\vec{k}') \right\rangle = (2\pi)^3 P_S(k) \delta^3(\vec{k} - \vec{k}') . \quad (1.63)$$

In order to find its expression we can write explicitly the relation between the scalar field perturbations $\delta\phi$ and the scalar density perturbations $\delta\rho_H$: from eq. 1.61

$$\frac{\delta\rho_H}{\rho_H} \sim \frac{\delta a}{a} \sim \frac{\delta\phi}{\dot{\phi}} , \quad (1.64)$$

and remembering the definition 1.5 of $H(t)$, we have:

$$\frac{\delta\rho_H}{\rho_H} = H \frac{\delta\phi}{\dot{\phi}} . \quad (1.65)$$

We can now write down the expression for $P_S(k)$, also considering possible deviations from scale invariance:

$$P_S(k) = \frac{4}{9} \left(\frac{H}{\dot{\phi}} \right)^2 P_{\delta\phi}(k) \left(\frac{k}{aH} \right)^{n_S-1} = \frac{2}{9k^3} \left(\frac{H^2}{\dot{\phi}} \right)^2 \left(\frac{k}{aH} \right)^{n_S-1} , \quad (1.66)$$

where the factor $(2/3)^2$ arises because the pressure of radiation is equal to a third of the energy density (see [23], chapter 6); n_S , spectral index for scalar perturbations, is the parametrization of deviations from scale invariance ($n_S = 1$ gives us the Zel'dovich or scale-invariant spectrum, the current measured value is $n_S = 0.947$ [18]), and

$$n_S - 1 = \frac{d \ln(\delta\rho_H^2)}{d \ln k} .$$

Another way to express the power spectrum of scalar perturbations is to eliminate $\dot{\phi}$ in favor of the slow-roll parameter ϵ (see eqs. 1.46 and 1.48): in fact it's easy to show that

$$\epsilon = \frac{\dot{\phi}^2}{2H^2 E_{Pl}^2} ,$$

thus $P_S(k)$ becomes:

$$P_S(k) = \frac{1}{9k^3} \left(\frac{H^2}{\epsilon E_{Pl}^2} \right) \left(\frac{k}{aH} \right)^{n_S-1} . \quad (1.67)$$

1.5.7 Tensor Fluctuations

Scalar density perturbations are not the only consequence of the primordial quantum fluctuations of the scalar field ϕ : a background of gravity waves is also predicted to be generated. In this section we briefly describe how these waves arise.

Tensor perturbations are described by the two functions h_+ and h_\times , each of

which obeys the perturbations equation (see [23], chapter 5):

$$\ddot{h} + 2\frac{\dot{a}}{a}\dot{h} + k^2h = 0 . \quad (1.68)$$

In linear theory, any quantum field is expanded into a sum of oscillators with the usual creation and annihilation operators (as previously noted in par. 1.5.6). The linearized contribution of a gravity wave $h_{+, \times}$ to the Lagrangian looks like a scalar field

$$\phi_{gw} = \frac{M_{Pl}}{4\sqrt{\pi}} h_{+, \times} , \quad (1.69)$$

so the expected gravity wave amplitude is $h_{rms} \sim \frac{H}{M_{Pl}}$ (see [22], problem 11.5). The linearization of the gravity waves contribution implies that the fluctuations in ϕ_{gw} are transmuted into density fluctuations together with the scalar field fluctuations $\delta\phi$ seen in the previous section, but the gravity waves will survive to the present day, although redshifted. This redshifting produces a break in the spectrum of waves. Prior to horizon entry, the gravity waves produce a scale-invariant spectrum of metric distortions, with amplitude h_{rms} per $\ln k$. These distortions are observable via the large-scale CMB anisotropies, where the tensor modes produce a spectrum with the same scale dependence as the Sachs-Wolfe gravitational redshift from scalar metric perturbations. In the scalar case we have $\delta T/T \sim \Phi/3c^2$ (see section 2.4), i.e. of the order of the Newtonian metric perturbation; similarly, the tensor effect is:

$$\left(\frac{\delta T}{T}\right)_{gw} = h_{rms} \lesssim \delta\rho_H , \quad (1.70)$$

because the tensor modes can constitute no more than 100% of the observed CMB anisotropy. The energy density of the waves is $\varepsilon_{gw} \sim M_{Pl}^2 h_{rms}^2 k^2$, where $k \sim H \cdot a_{he}$ is the proper wavenumber of the waves at horizon entry: we therefore expect $\varepsilon_{gw} \sim M_{Pl}^2 h_{rms}^2 H^2 a_{he}^2$. After horizon entry, the waves redshift away like radiation, as a^{-4} , and generate the present-day energy spectrum per $\ln k$ that is constant for modes that entered the horizon while the universe was radiation dominated (because $a \propto t^{\frac{1}{2}} \Rightarrow H^2 a^4 = \text{constant}$, see eq. 1.12). We can adopt the usual Ω -notation to parameterize the contribution of this gravity waves background to the energy density of the universe:

$$\Omega_i = \frac{8\pi G\varepsilon_i}{3H^2 c^2} \Rightarrow \text{in natural units } \Omega_{gw} = \frac{8\pi}{3} h_{rms}^2 , \quad (1.71)$$

at the time of horizon entry, at which epoch the universe was radiation dominated, with $\Omega_\gamma = 1$ to an excellent approximation. Thereafter, the wave density

maintains a constant ratio to the radiation density, since both redshift as a^{-4} , giving the present-day density as:

$$\Omega_{gw} = \Omega_\gamma \left(\frac{H}{M_{Pl}} \right)^2 . \quad (1.72)$$

The gravity-wave spectrum therefore displays a break between constant metric fluctuations on super-horizon scales and constant density fluctuations on small scales.

The Power Spectrum of tensor perturbations $P_h(k) = P_T(k)$ is defined in analogous way to eqs. 1.58 and 1.63. It is obtained as usual solving eq. 1.68 (see for example [23]):

$$P_h(k) = P_T(k) = \frac{8\pi H^2}{E_{Pl}^2 k^3} \left(\frac{k}{aH} \right)^{n_T-1} . \quad (1.73)$$

Since the fractional changes of the power spectra with scales are much smaller than unity, it is possible to consider the power spectra $P_S(k)$ and $P_T(k)$ as roughly constant on scales relevant for the CMB anisotropy and define a tensor-to-scalar amplitude ratio:

$$r = \frac{P_T(k)}{P_S(k)} \propto \epsilon , \quad (1.74)$$

where the factor of proportionality depends on the conventions used to define the power spectra. A generic inflationary model predicts a spectrum of gravitational waves with $n_T = n_S - 1$ and $r \propto (1 - n_S) = -n_T$ [24], [25].

Chapter 2

The Cosmic Microwave Background

2.1 Introduction

The primordial perturbations set up during inflation (see 1.5.6) manifest themselves in the radiation as well as in the matter distribution. Perturbations to the photons evolved completely differently before and after the epoch of recombination at $z \sim 1100$. In fact after about $3 \cdot 10^5 yr = t_{rec} \rightarrow z \sim 1100$, at $T \sim 3000$ K, recombination of light nuclei with free electrons becomes possible because the kinetic thermal energy of the particles no longer exceeds the ionization energy of atoms: this is for example $13.6 eV$ for one hydrogen atom, but in a cosmological environment this quantity is actually reduced of about one order of magnitude when the baryon-to-photon numeric density ratio ($\eta \sim 3 \cdot 10^{-10}$) is taken into account. Until t_{rec} , radiation is tightly coupled with matter, mainly via Thomson scattering off the electrons, therefore the universe is opaque to radiation; all together they can be described as a single baryon-photon fluid. After recombination the number of free electrons drops down drastically and the electromagnetic radiation can propagate through the universe because the mean free path of photons becomes of the same order of the size of the universe. This primordial radiation still permeates the universe and appears today as a cold and isotropic background; these primordial high-energy photons have been redshifted to the current microwave frequencies, with a perfect blackbody behaviour at temperature:

$$T_0 = (2.728 \pm 0.004)K \quad [13] . \quad (2.1)$$

There are anisotropies in temperature of the order of one part in 10^5 : they are the footprints left by quantum fluctuations during the inflative period on the fossil background of photons and represent the seeds of the structures we see

in the universe today. This topic is extremely important and we shall describe the well-known physics of anisotropies formation on large, medium and small angular scales; we will also give an overview of the related experimental efforts from which it has been possible to achieve anisotropy maps (patches and fullsky) with fundamental implications in cosmology: they allow to place constraints on the cosmological parameters. In fact through multipole expansion (see later on), the Temperature Power Spectrum of the CMB can be measured and its shape strongly depends on the cosmological parameters ($h, \Omega_k, \Omega_b, \sigma_8, n_s\dots$).

Recombination has been of course a non-instantaneous process, therefore the fossil radiation comes from a spherical shell, called Last Scattering Surface (LSS). If the local distribution of incoming radiation in the rest frame of the electrons has a quadrupole moment, the Thomson scattered radiation acquires some degree of linear polarization. One source of quadrupole anisotropy are the velocity fields at recombination (inside the LSS). Another source of quadrupole anisotropy is the gravity waves background (see 1.5.7). As we'll see later in detail (2.5), it is possible to distinguish between two components of the polarization field of the Cosmic Microwave Background, the *gradient component* (the so-called *E-modes*) and the *curl component* (the so-called *B-modes*), the former with contributions from both velocity fields at recombination and gravity waves, the latter instead only due to tensor perturbations.

In the last fifteen years a lot of effort has been made to improve our knowledge about the Cosmic Microwave Background. The COBE (Cosmic Background Explorer, [13]) satellite in 1992 was able to measure with the on-board instrument FIRAS (Far Infrared Absolute Spectrophotometer) the perfect black-body behaviour at $T = 2.728 \pm 0.004$ K. Then several new generations sub-orbital experiments has been developed to achieve more informations about the CMB spectrum, about its fluctuations in temperature (anisotropies) and also about its polarization: among them BOOMERanG [9] [11], ACBAR [14], CBI [15] and MAXIMA [16]. Moreover, after COBE, the new satellite experiment WMAP (Wilkinson Microwave Anisotropy Probe) [17] has provided the fullsky anisotropy maps with a 13 arcminute FWHM resolution.

The aim of this chapter is to give a general description of the properties of the Microwave Background, starting with the well-known dipole anisotropy due to Earth's absolute motion (par. 2.2) and the properties of the Last Scattering Surface (par. 2.3). Then we give an accurate description of the CMB Temperature power spectrum (par. 2.4), investigating the physical effects producing such temperature anisotropies at different angular scales (par. 2.4.1), presenting the appropriate statistical treatment of the anisotropies (par. 2.4.2) and finally tracing the expected shape of the spectrum, as well as the most important related measurements (par. 2.4.3). Section 2.5 is entirely dedicated to CMB polarization, again starting with the physical effects causing linear polarization patterns to be imprinted on the CMB photons (par. 2.5.1). The

statistical treatment given in 2.4.2 is redrawn in a more general theoretical picture, which includes polarization fields (par. 2.5.2) and has the remarkable property of identifying two different contributions to linear polarization (pars. 2.5.3, 2.5.4 and 2.6). The final section (2.7) represents an useful connection between the theoretical aspects exposed in this chapter and the more experimental approach that is going to follow in the next ones.

2.2 Earth's Absolute Motion: The Dipole Anisotropy

Before we start describing the intrinsic anisotropies of the Cosmic Microwave Background it is necessary to study one important special case: the effect of Earth's absolute motion. An observer on Earth is in motion with respect to the Last Scattering Surface, and this leads to a Doppler shift while receiving the photons from the LSS. Let us introduce some observational concept: probably the most important relation for observational cosmology is the one between monochromatic flux density and luminosity. If we assume isotropic emission, the photons emitted by the source flow with a uniform flux density through any sphere surrounding the source. We can now make a shift of origin, and consider the Robertson-Walker metric (1.2) as being centered on the source; however, because of homogeneity, the comoving distance between the source and the observer is the same as we would calculate if we place the origin on Earth. The photons from the source are therefore flowing through a sphere of proper surface area $4\pi(S_k R_c)^2$. But redshift still affects the flux density in four further ways: photon energies and arrival rates are redshifted, reducing the flux density by a factor $(1+z)^2$; opposing this, the bandwidth $d\nu$ is reduced by a factor $(1+z)$, so the energy flux per unit bandwidth goes down as $(1+z)$; finally, the observed photons at frequency ν_0 were emitted at frequency $\nu_{em} = \nu_0(1+z)$, so the flux density is the luminosity at this frequency, divided by the total area, divided by $(1+z)$:

$$F_\nu(\nu_0) = \frac{L_\nu(\nu_{em})}{4\pi(S_k R_c)^2(1+z)}, \quad (2.2)$$

where $L_\nu(\nu_{em})$ is the specific luminosity of the source in WHz^{-1} and $F_\nu(\nu_0)$ is the specific flux density in $WHz^{-1} m^{-2}$. The specific flux density received by an observer can be expressed as the product of the Specific Intensity I_ν (the flux density received from unit solid angle of sky per unit frequency) and the solid angle subtended by the source, $F_\nu = I_\nu d\Omega$. With the usual definition of Angular-Diameter Distance, $D_a = S_k R_c(1+z)^{-1}$, and Surface Brightness B_ν (luminosity emitted into unit solid angle per unit area of source per unit frequency), eq. 2.2 yields the Surface Brightness conservation:

$$I_\nu(\nu_0) = \frac{B_\nu(\nu_{em})}{(1+z)^3} . \quad (2.3)$$

We can now go back to the CMB and see how the effect of the observer's motion on the specific intensity of the CMB can be calculated by using $I_\nu/\nu^3 = \textit{invariant}$. It applies because the invariant is proportional to the phase-space density of the CMB photons: $\nu^2 d\nu$ is proportional to the volume element in momentum space, so that the number of photons is given by:

$$N_\gamma = \frac{c^2}{(2\pi\hbar)^4} \frac{I_\nu}{\nu^3} d^3x d^3p , \quad (2.4)$$

which justifies the statement that I_ν/ν^3 is proportional to the phase-space density. Now, it is easy to see through direct application of the Lorentz transformation that the phase-space volume element is a relativistic invariant, just because dx gets length-contracted, but dp_x gets boosted: the phase-space density must then also be invariant. Assuming for the microwave background a perfect blackbody behaviour, the surface brightness B_ν (energy per unit area, solid angle, time and frequency) is simply given by the Planck formula:

$$B_\nu(\nu, T) = \frac{4\pi\hbar\nu^3}{c^2} \left(e^{(2\pi\hbar\nu)/(k_B T)} - 1 \right)^{-1} , \quad (2.5)$$

where k_B is Boltzmann's constant¹. From eq. 2.3 we find that the invariant is proportional to the occupation number:

$$\frac{I_\nu}{\nu^3} \propto \left(e^{(2\pi\hbar\nu)/(k_B T)} - 1 \right)^{-1} = \left(e^{(2\pi\hbar\nu)/(\Gamma_D k_B T_{em})} - 1 \right)^{-1} , \quad (2.6)$$

where ν is the observation frequency $\nu = \nu_{em}\Gamma_D$ (Γ_D is the Doppler factor)

¹To the current epoch, after 14 *Gyr* of dilution due to the expansion of the universe, the number of CMB photons results to be: $N_\gamma \sim 411 \text{ cm}^{-3}$. In fact it's easy to find the expression for the energy density from the brightness 2.5: since all of the photons contained in a cylinder of length cdt and volume $cdtdA$ aligned within the unit solid angle $d\Omega$ (energy in the cylinder: $dE = c dAdtd\nu d\Omega \varepsilon_{bb}$) will flow through dA during dt , it turns out that:

$$B_\nu(\nu, T) = \frac{dE}{dAdtd\Omega d\nu} = c \varepsilon_{bb}(\nu, T)$$

Thus the mean number of photons per unit volume is:

$$N_\gamma(\nu, T) = \frac{4\pi\varepsilon_{bb}}{2\pi\hbar\nu} \Rightarrow N_\gamma(T) = 8\pi \left(\frac{k_B T}{2\pi\hbar c} \right)^3 \int_0^\infty \frac{x^2}{e^x - 1} dx \simeq 20.3 T^3 \text{ cm}^{-3} ,$$

integrating over all frequencies, with $x = \frac{2\pi\hbar\nu}{k_B T}$.

and T_{em} the actual temperature of the emitting source, the only quantities affected by the Doppler shift. Therefore the Doppler boosted thermal radiation appears exactly thermal, with a new temperature boosted by the same Doppler factor, $T = \Gamma_D T_{em}$. The Doppler factor is easily evaluated by writing the time and x -axis components of the comoving wavenumber 4-vector k^μ for photons travelling towards the observer at an angle θ to the x -axis:

$$k^\mu = \frac{2\pi\nu}{c}(1, -\cos\theta) .$$

Transforming out of the moving frame with the usual Lorentz formalism, $\gamma = (1 - \beta^2)^{-1/2}$, $\beta = v/c$ (v is the radial velocity with respect to the observer) and $c dt' = \gamma (c dt + \frac{v}{c} dx)$, it turns out:

$$T(\theta) = \frac{T_{em}}{\gamma (1 - \frac{v}{c} \cos\theta)} , \quad (2.7)$$

which can be expanded as a series of multipoles:

$$T(\theta) = T_{em} \left[1 + \frac{v}{c} \cos\theta + \frac{1}{2} \left(\frac{v}{c} \right)^2 \cos 2\theta + O(v^3) \right] . \quad (2.8)$$

This fluctuations in temperature with respect to $T_0 = T_{CMB}$ (2.1) correspond to CMB brightness fluctuations, which can be found deriving the Planck formula 2.5 with respect to the temperature:

$$\Delta B_\nu(\nu, T) = \frac{d}{dT} B_\nu(\nu, T) \Delta T = \frac{x e^x}{e^x - 1} B_\nu(\nu, T) \frac{\Delta T}{T} \quad \text{with } x = \frac{2\pi\hbar\nu}{k_B T} . \quad (2.9)$$

This conversion from temperature to brightness fluctuations is the same for the large-scale dipole anisotropy and for any smaller scale temperature or polarization anisotropy (in fact, as we'll see in par. 2.7, also polarization anisotropies are observable by means of temperature fluctuations). Only the dipole term in eq. 2.8 has been detected, but its effect is very significative for every kind of CMB anisotropy measure: in fact, as clearly visible from fig. 2.1, the dipole-induced fluctuations are at least one order of magnitude bigger than the intrinsic CMB anisotropies:

$$\Delta T_{dip} = (3.346 \pm 0.017) mK \quad [17]. \quad (2.10)$$

The measure of the dipole term ($\propto \cos\theta$) allows the absolute space velocity of the Earth to be evaluated. The WMAP [17] measurement of this motion is:

$$v_\oplus = (371 \pm 1) \frac{km}{s} \quad \text{towards } l = (263.9 \pm 0.1)^\circ, \quad b = (48.25 \pm 0.04)^\circ , \quad (2.11)$$

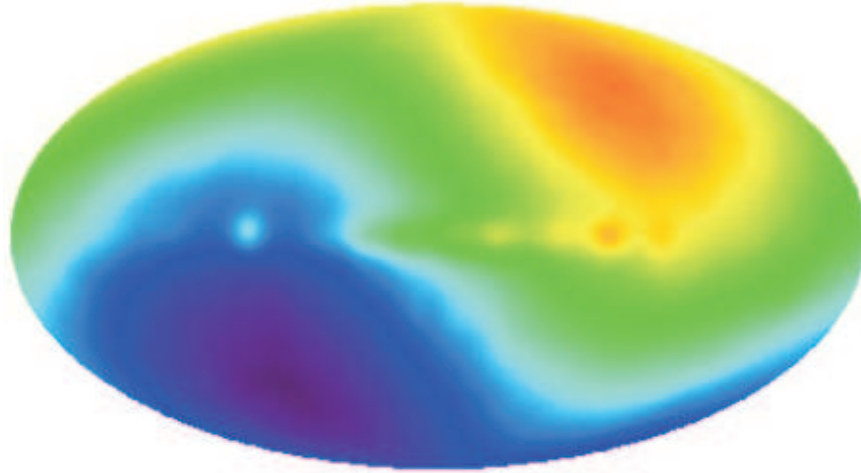


Figure 2.1: Fullsky map provided by the COBE satellite [13] clearly showing the dipole anisotropy due to Earth’s proper motion with respect to the Last Scattering Surface from which we see the incoming Doppler shifted CMB photons. The colors follows the usual convention: once T_0 (eq. 2.1) is subtracted, green regions are those with $\Delta T \approx 0$, red regions are the hottest ones, with $\Delta T \rightarrow +\Delta T_{max}$, while blue regions are the coldest ones, with $\Delta T \rightarrow -\Delta T_{max}$.

where l, b are respectively the galactic longitude and latitude. Because of the huge amplitude of this kind of anisotropies, this effect is often used as a very powerful calibration source, for several reasons: first, its amplitude is well-known, also from astrometric data, second, its spectrum is exactly the same as the intrinsic anisotropies one, third, it is not polarized, and finally detectors non-linearities are avoided, because this signal is one order of magnitude larger than CMB anisotropies.

2.3 The Last Scattering Surface

Let’s briefly discuss an important consideration in the post-recombination epoch about the optical depth τ of the Universe due to Thomson scattering in the Last Scattering spherical Shell. This is a dimensionless quantity such that $e^{-\tau}$ describes the attenuation of the photon flux as it traverses a certain length, as usual. Suppose for simplicity that the plasma in the LSS is made only of protons (p), electrons (e) or hydrogen atoms (H) and photons (γ). The probability dP that a photon has suffered a scattering event from an electron while

travelling a distance $c dt$ is given by:

$$dP = -\frac{dI_\nu}{I_\nu} = n_e \sigma_T c dt = -\frac{x \rho_m}{m_p} \sigma_T c \frac{dt}{dz} dz = -d\tau . \quad (2.12)$$

We have introduced the following quantities:

- $\sigma_T = \frac{8\pi}{3} \left(\frac{e^2}{m_e c^2} \right)^2$, is the Thomson cross-section (units: m^2), i.e. the low-energy cross-section for electron-photon scattering, with no exchange in energy between them;
- m_e is the electron mass;
- m_p is the proton mass;
- n_e is the number density of electrons (units: m^{-3});
- $x = \frac{n_e}{n_p + n_H} \approx \frac{n_e}{n_{tot}}$ is the ionization fraction;
- ρ_m is the matter density of the plasma (units: $kg \cdot m^{-3}$).

I_ν is as usual the specific intensity, and

$$I_\nu(t_0, z) = I_\nu(t) e^{-\int \frac{x \rho_m}{m_p} \sigma_T c \frac{dt}{dz} dz} = I_\nu(t) e^{-\tau(z)} . \quad (2.13)$$

$I_\nu(t_0, z)$ is the specific intensity of the background radiation reaching the observer at time t_0 with a redshift z : $\tau(z)$ is called the optical depth of such a region. The probability that a photon, which arrives at the observer at the present epoch, suffered its last scattering event between z and $z - dz$ is:

$$-\frac{d}{dz} (1 - e^{-\tau(z)}) dz = e^{-\tau(z)} d\tau = g(z) dz . \quad (2.14)$$

The quantity $g(z)$ is the so-called *effective width* of the Surface of Last Scattering; typically $g(z)$ is well approximated by a Gaussian with peak at $z_{LSS} \sim 1100$ and width $\Delta_{z_{LSS}} \sim 80$, which represents the thickness of the Shell. The integral of $g(z)$ over the range $0 \leq z \leq \infty$ is clearly unity. At redshift z_{LSS} we also have $\tau(z) = 1$. Assuming $x \sim 1$, from eqs. 2.12, 1.17 and 1.11, recalling the critical density $\varepsilon_c = \frac{3c^2 H^2}{8\pi G}$, we obtain:

$$\tau(z) = \frac{\varepsilon_c \Omega_0 \sigma_T c}{m_p H_0} \int_0^z \frac{(1+z)}{(1+\Omega_0 z)^{1/2}} dz . \quad (2.15)$$

Since $\Omega_0 z \gg 1$, recalling the dimensionless parameter h for Hubble's constant, $H_0 = h \cdot 100 \frac{km}{s \cdot Mpc}$, we get the approximate result:

$$\tau(z) \approx 10^{-2} \sqrt{\Omega_0} h^2 z^{3/2} \simeq 0.073 [18] . \quad (2.16)$$

2.4 The Temperature Power Spectrum

2.4.1 Physical Effects at Recombination

It is worth to distinguish the primary anisotropies, those that arose at the time of recombination, from the secondary anisotropies, which are imprinted on the CMB photons by scattering along the line of sight, such as the Sunyaev-Zel'dovic (SZ) effect. In this work we shall only refer to primary anisotropies, even if the Olimpo experiment (see chapter 5) has as first scientific objective the detection of about 40 cluster of galaxies by measuring the SZ effect induced by intracluster hot gas electrons via Compton scattering off CMB photons. This choice will appear clearer at the end of chapters 4 and 5.

There are three basic primary effects at recombination, which are important on respectively large, intermediate and small angular scales²:

- Gravitational (Sachs-Wolfe [27]) perturbations: this is the dominant large-scale effect, and arises from gravitational potential perturbations $\delta\Phi$ at last scattering: it is a relativistic effect, the photons travelling to an observer from the Last Scattering Surface encounter metric perturbations which cause them to change frequency. There are however two opposing contributions: first, potential perturbations $\delta\Phi$ redshift the photons we see, so that an overdensity region cools the background as the photons climb out of the potential well, $\delta T/T = \delta\Phi/c^2$ (*gravitational redshift*); second, they cause time dilation at the Last Scattering Surface, so that it seems we are looking at a younger (and hence hotter) universe where there is an overdensity. The time dilation is $\delta t/t = \delta\Phi/c^2$; since the time dependence of the scale factor is $a \propto t^{2/3}$ in a matter-dominated epoch (see 1.15) and $T \propto a^{-1}$ (see footnote in section 1.3.2), this yields:

$$\frac{\delta T}{T} = -\frac{\delta a}{a} = -\frac{2}{3} \frac{\delta t}{t} = -\frac{2}{3} \frac{\delta\Phi}{c^2} . \quad (2.17)$$

The net effect is thus one-third of the gravitational redshift:

$$\frac{\delta T}{T} = \frac{\delta\Phi}{3c^2} . \quad (2.18)$$

By means of Poisson's equation we can relate the gravitational perturbations $\delta\Phi$ to the density perturbations $\delta\rho_H$ (see 1.5.6) at the LSS. The expression assumed for the gravitational perturbation $\delta\Phi$ is analogous to the one used in par. 1.5.6 for the scalar field perturbation (eq. 1.53).

²The parametrization of the angular scale will result clear after the multipole expansion of the distribution of $\frac{\Delta T}{T}$ on the sky. For the time being we mean the large angular scales to be of the same angular size of the universe or just a little smaller; small angular scales are instead the ones of sub-degree (arcmin) size.

Since k represents the comoving wavenumber, Poisson's equation

$$\nabla^2 \delta\Phi_k = 4\pi G \rho \delta\rho_H^k, \quad (2.19)$$

writing ρ in terms of Ω_0 (1.11) and z_{LSS} , gives:

$$\delta T_k = -\frac{\Omega_0(1+z_{LSS})}{2} \left(\frac{H_0}{c}\right)^2 \frac{\delta\rho_H^k(z_{LSS})}{k^2}, \quad (2.20)$$

because the application of ∇^2 on $\delta\Phi$ only produces a multiplicative term $-\frac{k^2}{a^2}$. Here δT_k indicates the Fourier transform of $\delta T/T$, after the integration over the Last Scattering Spherical Surface:

$$\frac{\delta T}{T} = \frac{1}{(2\pi)^3} \int \int \delta T_k e^{-i\vec{k}\cdot\vec{r}} d^3k e^{-\tau} d\tau, \quad (2.21)$$

where $e^{-\tau} d\tau$ is usually approximated by a Gaussian in comoving radius centered in $r(z_{LSS})$ with thickness $\sigma_r(\Delta_{z_{LSS}}) = 7(\Omega_0 h^2)^{-1/2} Mpc$ (see par. 2.3 and [22], chapter 9):

$$e^{-\tau} d\tau \propto e^{-\frac{[r-r(z_{LSS})]^2}{2\sigma_r^2(\Delta_{z_{LSS}})}} dr. \quad (2.22)$$

- Velocity (Doppler) perturbations: the plasma has a non-zero velocity at recombination, leading to Doppler shifts in frequency and hence in brightness temperature. If \vec{v} is the velocity of the moving plasma as seen by the scattered photons, we have:

$$\frac{\delta T}{T} = -\frac{\delta(\vec{v}\cdot\hat{r})}{c}, \quad (2.23)$$

which gives ([22], chapter 16):

$$\delta T_k = -i\sqrt{\Omega_0(1+z_{LSS})} \left(\frac{H_0}{c}\right) \frac{\delta\rho_H^k(z_{LSS})}{k} \hat{k}\cdot\hat{r}. \quad (2.24)$$

- Intrinsic (adiabatic) perturbations: in high-density regions, the coupling of matter and radiation can compress the radiation also, giving a higher temperature. This happens because in a denser spot the recombination takes place a little bit later, therefore its outgoing photons are observed

less redshifted and so the spot appears slightly hotter. The perturbations in the matter-radiation plasma are said to be adiabatic (as predicted by all generic Inflation models, see 1.5.6) if matter and radiation densities fluctuate together, in such a way that the entropy of the plasma remains constant. The entropy of the plasma is $S_{m\gamma} = k_B \frac{n_m}{n_\gamma}$, where n_m and n_γ are respectively the numeric density of matter particles and photons. From par. 1.2 we have $n_m \propto \varepsilon_m$, energy density of matter, and $n_\gamma \propto \varepsilon_\gamma^{3/4} \propto T^3$, where ε_γ is the energy density of photons. Adiabatic perturbations imply $\delta S_{m\gamma}/S_{m\gamma} = 0$, therefore the observed temperature perturbation is:

$$\frac{\delta T}{T} = -\frac{\delta z}{1+z} = \frac{1}{4} \frac{\delta \varepsilon_\gamma}{\varepsilon_\gamma} = \frac{1}{3} \frac{\delta n_\gamma}{n_\gamma} = \frac{1}{3} \frac{\delta \varepsilon_m}{\varepsilon_m}. \quad (2.25)$$

The corresponding k -space result for density perturbations at the LSS is:

$$\delta T_k = \frac{\delta \rho_H^k(z_{LSS})}{3}. \quad (2.26)$$

The above expressions apply to perturbations for which only Newtonian gravitational potential has been important up till last scattering, i.e. those larger than the horizon at z_{eq} ³. For smaller wavelengths, a variety of additional physical processes act on the radiation perturbations, generally reducing the predicted anisotropies. The thickness of the Last Scattering Shell, $\sigma_r(\Delta_{z_{LSS}})$ has clearly to be of the same order of magnitude as the photon mean free path at this time; on any smaller scales, a fluid approximation for the radiation is inadequate and only some qualitative insight into the small scale processes is possible. The radiation fluctuations will be damped via photon diffusion in the baryon fluid: this process is called Silk damping [29]. The mean free path of photons due to scattering by the plasma is non-zero, and so radiation can diffuse out of a perturbation, convecting the plasma with it. The typical damping length is $\lambda_S \simeq \sqrt{d_{hor}(n\sigma_T)^{-1}}$ [30], where d_{hor} is the size of the horizon just before recombination, while the product of the Thomson cross-section σ_T and the numeric density of particles n is the photon mean free path. There is also another important effect to consider: before recombination the density perturbations oscillate as a result of the opposite effects of gravity ($\delta\rho/\rho$ increases and so does the local temperature) and photon pressure (the increasing temperature makes the radiation pressure higher, $p_\gamma \propto \sigma_{SB}T^4$, the perturbations

³ z_{eq} is the redshift of *matter-radiation equality*, at which the universe switches from radiation domination to matter domination and its value is just slightly smaller than z_{LSS} . The time of this change in the global equation of state is one of the key epochs in determining the appearance of the present-day universe. Prior to matter-radiation equality, the speed of expansion is so high that fluctuations in matter density cannot collapse under their own gravity; only at later times cosmological structures can start to form.

bounce back until T is reduced enough that gravity wins again). After recombination, photons are no longer tightly coupled to matter and their radiation pressure is no longer effective: density perturbations can grow and create the structures we see in the Universe. The important effect is that photons/baryons density perturbations start to oscillate only when the sound horizon ($\sim c_s t_{rec}$, with c_s defined just below) becomes larger than their linear size: when these photons/baryons perturbations get inside the horizon, they oscillate as sound waves:

$$\delta_{bar} \propto \sqrt[4]{3c_s} e^{\pm i \int k c_s dt}, \quad \text{with} \quad c_s = \sqrt{\frac{\partial p}{\partial \rho}}. \quad (2.27)$$

These ‘‘acoustic’’ oscillations in the photons/baryons fluid cause a set of *acoustic peaks* in the power spectrum of CMB fluctuations (see also below), specially at small angular scales, since small wavelength perturbations oscillate faster than large ones.

2.4.2 Statistical Treatment

After this overview of the physics of CMB temperature anisotropies, we can step forward to their statistical characterization of fluctuations from point to point on the celestial sphere. The usual procedure is to expand the distribution of T on the sky as a sum over *spherical harmonics*:

$$\frac{\delta T}{T}(\hat{n}) = \sum_{l=0}^{\infty} \sum_{m=-l}^{m=l} a_{lm} Y_{lm}(\hat{n}), \quad (2.28)$$

where \hat{n} is the versor representing the direction on the sky. In fact for any given direction on the sphere specified by the usual spherical coordinates (θ, ϕ) , one can define three orthogonal unit vectors (versors), one radial and two tangential to the sphere. Let us denote the radial direction versor with \hat{n} and the tangential with (\hat{e}_1, \hat{e}_2) . The latter two are only defined up to a rotation around \hat{n} . The $l = 0$ term is a monopole correction which essentially just alters the mean temperature on a particular observer’s sky with respect to the global mean over an ensemble of all possible such skies. We shall ignore this term from now on because it is not measurable. The $l = 1$ term is the dipole term due to Earth’s absolute motion on the celestial sphere (see 2.2). The remaining modes, from the quadrupole ($l = 2$) upwards, represent the intrinsic anisotropies and so the sum in eq. 2.28 is taken over $l \geq 2$. Higher l modes correspond to fluctuations on smaller angular scales, according to the approximate relation $\theta \sim \pi/l$. The spherical harmonics satisfy the orthonormality relation

$$\int_0^{2\pi} d\phi \int_{-1}^1 d\cos\theta Y_{lm} Y_{l'm'}^* = \delta_{ll'} \delta_{mm'} , \quad (2.29)$$

where $\delta_{ii'}$ is the Kronecker symbol. The a_{lm} are generally complex, and satisfy the conditions

$$\langle a_{lm} a_{l'm'}^* \rangle = C_l \delta_{ll'} \delta_{mm'} . \quad (2.30)$$

The quantity C_l is the *angular power spectrum* or *ensemble average power*:

$$C_l \equiv \langle |a_{lm}|^2 \rangle . \quad (2.31)$$

It is also useful to define an *autocovariance* function for the temperature fluctuations:

$$C(\theta) = \left\langle \frac{\delta T}{T}(\hat{n}_1) \frac{\delta T}{T}(\hat{n}_2) \right\rangle , \quad (2.32)$$

where $\hat{n}_1 \cdot \hat{n}_2 = \cos\theta$. The expectation values in 2.30 and 2.32 are taken over an ensemble of all possible skies. One can try to estimate C_l or $C(\theta)$ from an individual sky using the hypothesis that an average over the probability ensemble is the same as an average over all spatial positions within a given realization. This only works on small angular scales when it is possible to average over many different pairs of directions with the same θ , or many different modes with the same l . On larger scales, however, it is extremely difficult to estimate the true $C(\theta)$, because there are so few independent directions at large θ or, equivalently, so few independent l modes at small l . Large-angle statistics are therefore dominated by the effect of *cosmic variance*: we inhabit one realization and there is no reason why this should possess exactly the ensemble average values of the relevant statistics.

The analogues of the Fourier relations for the correlation functions and the power spectrum are:

$$C(\theta) = \frac{1}{4\pi} \sum_{l=2}^{\infty} \sum_{m=-l}^{m=l} |a_{lm}|^2 P_l(\cos\theta) , \quad (2.33)$$

$$|a_{lm}|^2 = 2\pi \int_{-1}^1 C(\theta) P_l(\cos\theta) d\cos\theta , \quad (2.34)$$

where P_l is the l -th Legendre polynomial. These are exact relations, governing

the actual correlation structure of the observed sky. However, the sky we see is only one of infinite possible realizations, so we have to use the *ensemble average power*. There is a simple relationship between the angular power spectrum and covariance function, from eqs. 2.31 and 2.33:

$$C(\theta) = \frac{1}{4\pi} \sum_{l=2}^{\infty} (2l+1) C_l P_l(\cos \theta) , \quad (2.35)$$

where now $C(\theta)$ is the ensemble-averaged autocorrelation function.

2.4.3 The Shape of the Spectrum

The δT are recovered at individual directions on the sky (in order to draw a map, fullsky or patches) by means of telescopes, capable of observing the microwave sky with finite beamwidth: the temperature therefore is not observed point by point, but would instead be a discrete picture of the sky, convolved with some smoothing function (*window function*) $W(\theta)$; when the telescope beam is sufficiently narrow in angular terms, the Fourier limit can be used to find the corresponding l -dependent filter function, W_l . For example for a Gaussian beam of $\text{FWHM} = 2\sqrt{2 \ln 2} \sigma_{\text{beam}}$:

$$W(\theta) = \frac{1}{2\pi\sigma_{\text{beam}}^2} e^{-\frac{1}{2}\frac{\theta^2}{\sigma_{\text{beam}}^2}} \implies W_l = e^{-l(l+1)\sigma_{\text{beam}}^2} [31] . \quad (2.36)$$

In general the effect of a finite beam width is to provide a high- l cutoff at scales of the beam size $l \sim \sigma_{\text{beam}}^{-1}$ (see fig. 2.2). With the definitions above, we can finally write the expression for the *rms* temperature signal from an instrument with window function W_l :

$$\left\langle \left(\frac{\delta T}{T} \right)^2 \right\rangle_{\text{meas}} = \frac{1}{4\pi} \sum_{l=2}^{\infty} (2l+1) W_l C_l , \quad (2.37)$$

which implies $C_l = C_l^{\text{meas}}/W_l$. We shall now describe from a qualitative point of view the expected shape of Temperature Power Spectrum shown in fig. 2.3, taking into account the physical processes listed above. The Power Spectrum can in fact be thought as the angular distribution of the different sized bumps of anisotropy, in other words it counts at each different multipole how many anisotropy structures have exactly the corresponding angular scale ($\theta \sim \pi/l$). Before we continue it's necessary to explain that the expected power spectra (also the ones including CMB polarization, see 2.6) are found by means of numeric codes such as CMBFAST [33][34] and CAMB [35], which are based on integration over the sources along the photon past light cone: in this approach the temperature anisotropy is written as a time integral over the product of

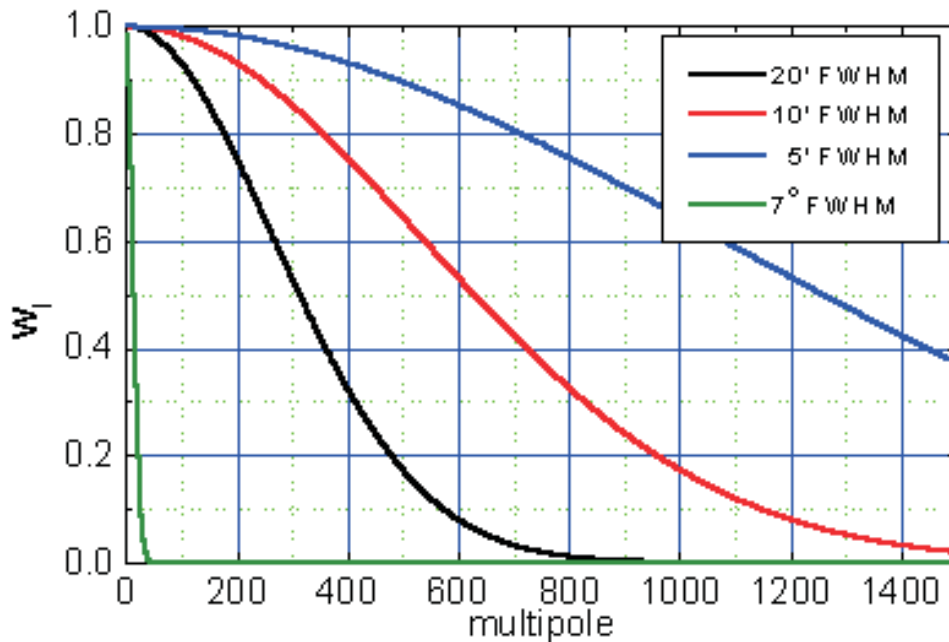


Figure 2.2: The window function W_l is displayed against the multipole number l , for different values of $\text{FWHM} = 2\sqrt{2\ln 2} \sigma_{beam}$. The effect of a finite beam width (angular resolution) of the instrument is clear: the smaller is σ_{beam} , the larger is the sensitivity to the highest multipoles, i.e. to the smallest angular scales.

a geometrical term and a source term. The importance of these codes is that they make amazingly easier to compute the C_l directly from the values of the cosmological parameters. Thus now the cosmologists have an extremely powerful tool to relate quantitatively the cosmological parameters with the Power Spectra: the comparison with the measured Power Spectra is therefore immediate and straightforward.

The behaviour at small l is due to the Sachs–Wolfe effect and the Temperature PS should appear almost flat, because for an initial Power Spectrum of the Scalar Perturbations of the form $P_S(k) \propto k$ (scale-invariant), from eq. 2.20 it’s quite straightforward to show that for low l the quantity $l(l+1)C_l$ is independent of the mode order l (see [23], chapter 8): the shape of C_l at large angular scales is determined purely by the shape of $P_S(k)$. The physical reason is that fluctuations on angular scales larger than the scale of the horizon at t_{rec} will retain their primordial character since they should not have been modified by any causal process inside the horizon before t_{rec} . One must therefore find the primordial unprocessed scale-invariant spectrum. After this Sachs-Wolfe “plateau” a steep increase in the angular power spectrum is expected for $l \sim 200$. This angular scale corresponds to a $1deg$ horizon scale at

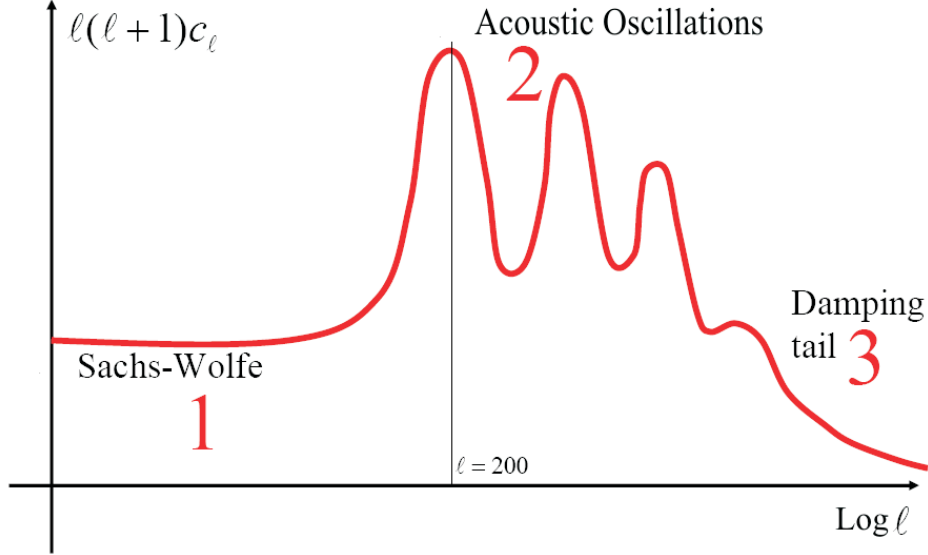
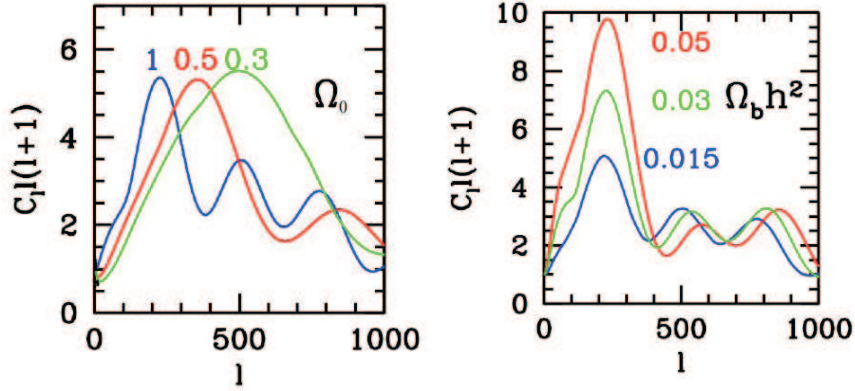


Figure 2.3: Drawing of the qualitative expected behaviour of the Temperature Power Spectrum of the Cosmic Microwave Background. The three main physical effects acting on different angular scales are indicated.

t_{rec} in a flat-geometry universe ($\Omega_k = -0.037_{-0.039}^{+0.033}$ [10]): this first and most powerful peak around the horizon scale is usually interpreted as being due to velocity perturbations on the last scattering surface (see eqs. 2.23 and 2.24) and is consequently sometimes called the “Doppler peak”.

Its height above the SW “plateau” is sensitive to Ω_b and its angular location depends on Ω_0 and Ω_Λ (see fig. 2.4a). The shape of the spectrum beyond this peak is complicated and depends on the relative contribution of baryons and dark matter. For example, the smaller peaks at larger l change amplitude and position in dependence of the value of Ω_b (see fig. 2.4b). The features at higher l are connected with the acoustic oscillations. Basically what happens is that perturbations inside the horizon on these angular scales oscillate as acoustic standing waves with a particular phase relation between density and velocity perturbations. After recombination when the pressure of radiation become negligible, these waves are left with phases which depend on their wavenumber (eq. 2.27). Both the photon temperature fluctuations (eq. 2.25) and the velocity perturbations (eq. 2.23) are therefore functions of wavenumber of these sound waves because both contribute to $\delta T/T$ in this regime and this results in an almost periodic behaviour of C_l . The “Doppler peak” is actually the first maximum of these oscillations and although velocities are undoubtedly important in



(a) Dependence on Ω_0 .

(b) Dependence on Ω_b .

Figure 2.4: Drawings of the dependence of the Temperature Power Spectrum on the cosmological parameters Ω_0 and Ω_b .

the generation of this particular feature, it is wrong to think that the physical origin of the first peak in the angular power spectrum is qualitatively different from the other ones: this is the reason why the “Doppler peak” is often called the “acoustic peak”. As said before, the shape of the spectrum at very small angular scales ($l \gtrsim 1000$) should reflect the diffusion damping process underwent by density fluctuations inside $\delta\rho_H$ the LSS ($\delta\rho_H^k$ is the usual Fourier transform with modes of wavevector \vec{k}). These spatial perturbation modes have a contribution that is in general damped by averaging over the shell of last scattering because of photon diffusion (Silk damping, typical damping length: λ_S [29], see par. 2.4.1). Short-wavelength modes ($|\vec{k}| = 2\pi/\lambda$) are more heavily affected because more of them fit inside the scattering shell and because their wavevectors \vec{k} point more nearly radially for a given projected wavelength. This part of the spectrum is thus often referred as the “diffusion damping tail”.

In fig. 2.5 [32] the latest experimental results at different angular scales are joined together: the evaluations of the cosmological parameters are obtained from the best fit of these observational data.

The CBI measurements show that the spectrum has begun to damp significantly by $l_S \sim 1000$, as expected from photon diffusion during recombination [29]. A finer binning in l would be required to verify that the damping is (close to) exponential and to constrain the damping scale, λ_S more precisely from the shape of the decline in power. The new observational limit here is

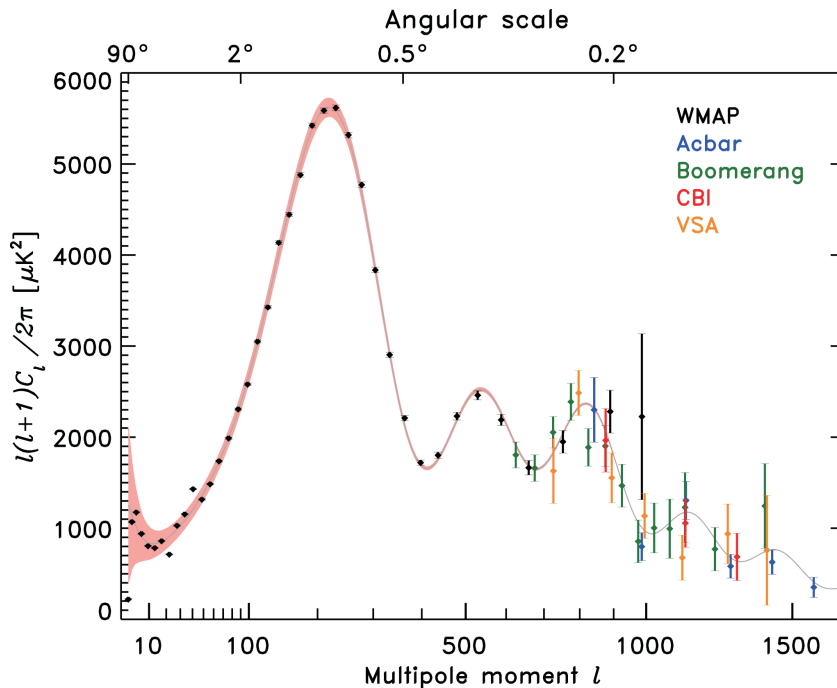


Figure 2.5: The measured Temperature Power Spectrum of the Cosmic Microwave Background [32]. The data shown come from the WMAP (2006 [17]), Acbar (2004 [14]) Boomerang (2005 [11]), CBI (2003 [15]) and VSA (2004 [40]) instruments.

on the damping scale, which has the nice property that it depends primarily on the background cosmology and not on the assumed model of structure formation. As seen in par. 2.4.1, to a first approximation the damping scale is the geometric mean of the horizon and the photon mean free path just before recombination: thus, an increase in the matter density, which decreases the size of the horizon at last scattering (see 1.3.2), will shift the damping to smaller angular scales. For baryon densities consistent with Big Bang nucleosynthesis the damping scale is also shifted to smaller angular scales by a decrease in the mean free path (an increase in the baryon density). The ratio l_S/l_A thus measures the delay in recombination: under the instantaneous recombination assumption it corresponds to the number of observable peaks. The actual observable value for any given model will be lowered in a manner dependent on the details of recombination. Even if recombination never occurred, the Thomson mean free path will eventually reach the horizon size due to dilution in the electron number density from the expansion. At this point the universe is effectively transparent and the photons free stream to the present. Since by definition the diffusion length roughly corresponds to the horizon scale at this epoch, $l_S/l_A \sim 1$ and no acoustic oscillations are apparent. Thus, recombination is a necessary condition for the acoustic signature to be observable. Since

the first acoustic peak appears to lie at $l_A \sim 200$, a first rough measurement yields $l_S/l_A \sim 5$, which is in accord with the theoretical expectations by [37]. A ratio in the range 4-6 is a strong indication that the fluctuations are adiabatic, such as are produced uniquely by inflation [38],[39]. Unfortunately, within the current uncertainties on l_S , the constraints are not very tight, although disfavoring a shift in l_S/l_A by a factor of 1.5 as predicted by isocurvature models (see par. 1.5.6), [36].

2.5 Polarization

2.5.1 Thomson Scattering at Recombination

As previously mentioned, Thomson scattering of the background photons with free electrons on the Last Scattering Surface generated a linear polarization pattern on the sky: in fact if the local distribution of incoming radiation in the rest frame of the electron has a *quadrupole moment*, the Thomson scattered radiation acquires some degree of linear polarization. In turn these inhomogeneities in the distribution of radiation have direct reference to the scalar modes (par. 1.5.6) of cosmological perturbations. As we'll shown, also tensor perturbation (gravitational waves, par 1.5.7) produce quadrupole anisotropy in the distribution of incoming radiation. Scalar and Tensor inhomogeneities produce in the background radiation two different patterns of linear polarization: in this section we explain the origin and phenomenology of the geometric distinction between these two patterns in terms of the so-called electric and magnetic parity modes, as well as their correlation with the temperature pattern.

The Thomson scattering differential cross-section depends on polarization as:

$$\frac{d\sigma_T}{d\Omega} \propto |\hat{\epsilon} \cdot \hat{\epsilon}'|^2, \quad [41] \quad (2.38)$$

where Ω is the solid angle and $\hat{\epsilon}, \hat{\epsilon}'$ are respectively the directions of the incident and of the scattered polarization (see fig. 2.6). Qualitatively speaking, only an anisotropic radiation field can lead to non-zero outgoing polarization, because by symmetry if the radiation incident on an electron is isotropic there is no preferred direction for polarization of the scattered light. The incident light sets up oscillations of the target electron in the direction of the electric field vector \vec{E} , i.e. the polarization. The scattered radiation intensity thus peaks in the direction normal to, with polarization parallel to, the incident polarization. If the incoming radiation field is isotropic, orthogonal polarization states from incident directions separated by 90° would balance so that the outgoing radiation would remain unpolarized. Conversely, if the incident radiation field possesses a quadrupolar variation in intensity or temperature

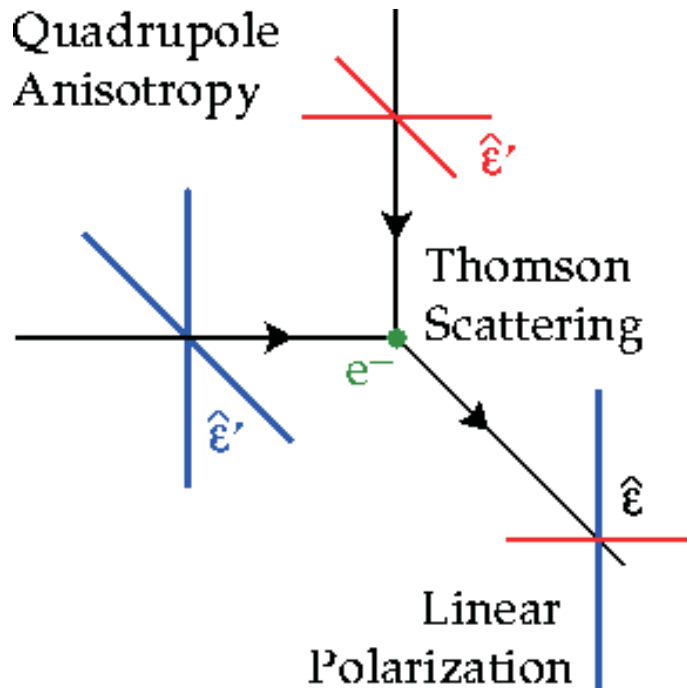


Figure 2.6: Thomson scattering of radiation with quadrupole anisotropy generates linear polarization. In the rest frame of the electron, blue lines represent hotter radiation, while red lines represent colder radiation. In par. 2.5.3 this color convention will be better understood in terms of redshift and blueshift with respect to the rest frame of the electron.

(which possess intensity peaks at $90^\circ \rightarrow \pi/2$ separations), the result is a linear polarization of the scattered radiation. A reversal in sign of the temperature fluctuation corresponds to a 90° rotation of the polarization, that is the physical reason lying beneath the spin-2 nature of CMB polarization (see par. 2.5.2). If Thomson scattering is rapid, then the randomization of photon directions that results destroys any quadrupole anisotropy and polarization. The problem of understanding the polarization pattern of the CMB thus reduces to understanding the quadrupolar temperature fluctuations at last scattering. Temperature perturbations have two geometrically distinct sources, the scalar (compressional) and tensor (gravitational waves) perturbations: this leads to two different patterns of polarization. Before we describe the details of the quadrupole anisotropies generated in the radiation field by scalar and tensor perturbations we need to introduce the appropriate formalism developed by Matias Zaldarriaga and Uroš Seljak (in [42], for example). The decomposition in electric and magnetic modes (*E-modes* and *B-modes*) together with the formalism of the spin-2 spherical harmonics is here introduced merely as an extremely powerful mathematical instrument to better understand the properties of CMB polarization. We shall turn back to the polarization patterns after

this next, more formal, section.

2.5.2 Statistical Treatment

This $E - B$ statistical treatment of the polarization rests upon the classical Stokes treatment, to which Appendix A is fully dedicated. The theoretical framework we are going to introduce starts from the general point of view of a 2×2 intensity tensor which includes also the temperature anisotropy described above (par. 2.4.2). The CMB anisotropy field is described by a 2×2 intensity tensor I_{ij}

$$I_{ij}(\hat{n}) = \begin{pmatrix} I_{11} & I_{12} \\ I_{21} & I_{22} \end{pmatrix}, \quad (2.39)$$

that is normalized and dimensionless, i.e. it represents the fluctuations in units of the mean intensity I_0 : $I_{ij} = \delta I / I_0$. As explicitly indicated in eq. 2.39, it is a function of the direction on the sky \hat{n}^4 . The Stokes parameters Q and U (see Appendix A) are defined as $Q = (I_{11} - I_{22})/4$ and $U = I_{12}/2$, while the temperature anisotropy is given by $T = (I_{11} + I_{22})/4^5$. The fourth Stokes parameter V , describing circular polarization, is ignored in this approach, since it cannot be generated through Thomson scattering. While the temperature is invariant under a right-handed rotation by an angle α in the plane perpendicular to \hat{n} , which is described by the rotation matrix

$$\mathcal{R}(\alpha) = \begin{pmatrix} 1 & 0 & 0 \\ 0 & \cos(2\alpha) & \sin(2\alpha) \\ 0 & -\sin(2\alpha) & \cos(2\alpha) \end{pmatrix}, \quad (2.40)$$

Q and U transform under rotations as:

$$\begin{aligned} Q' &= Q \cos(2\alpha) + U \sin(2\alpha), \\ U' &= -Q \sin(2\alpha) + U \cos(2\alpha), \end{aligned} \quad (2.41)$$

where $\hat{e}'_1 = \hat{e}_1 \cos \alpha + \hat{e}_2 \sin \alpha$ and $\hat{e}'_2 = -\hat{e}_1 \sin \alpha + \hat{e}_2 \cos \alpha$. Referring to Appendix B for an introduction to the spin-weighted functions, it is possible to construct two quantities from the Stokes parameters Q and U :

$$(Q \pm iU)'(\hat{n}) = e^{\mp 2i\alpha} (Q \pm iU)(\hat{n}). \quad (2.42)$$

⁴For any given direction on the sphere specified by the usual spherical coordinates (θ, ϕ) , one can define three orthogonal versors, one radial and two tangential to the sphere. Let us denote the radial direction versor with \hat{n} and the tangential with (\hat{e}_1, \hat{e}_2) . The latter two are only defined up to a rotation around \hat{n} .

⁵The factor 4 comes from the intensity-temperature relation $I \propto T^4$.

We may therefore expand the \hat{n} -dependence of each of these quantities in the appropriate spin-weighted basis, obtaining the Angular Spectra:

$$\begin{aligned}
T(\hat{n}) &= \sum_{l=0}^{\infty} \sum_{m=-l}^{m=l} a_{T,lm} Y_{lm}(\hat{n}) , & (2.43) \\
(Q + iU)(\hat{n}) &= \sum_{l=0}^{\infty} \sum_{m=-l}^{m=l} a_{2,lm} {}_2Y_{lm}(\hat{n}) , \\
(Q - iU)(\hat{n}) &= \sum_{l=0}^{\infty} \sum_{m=-l}^{m=l} a_{-2,lm} {}_{-2}Y_{lm}(\hat{n}) .
\end{aligned}$$

Using the first among eqs. B.6, it is possible to show that the expansion coefficients for the polarization satisfy $a_{-2,lm}^* = a_{2,l-m}$, while for the temperature the relation is $a_{T,lm}^* = a_{T,l-m}$. Now the trick is to use the spin raising and lowering operators $\bar{\partial}$ and $\bar{\partial}$ defined in Appendix B to obtain spin zero quantities, which have the great advantage of being rotationally invariant like the temperature field. Acting twice with $\bar{\partial}$ and $\bar{\partial}$ on $(Q \pm iU)$ in eq. 2.43 leads to:

$$\begin{aligned}
\bar{\partial}^2(Q + iU)(\hat{n}) &= \sum_{l=0}^{\infty} \sum_{m=-l}^{m=l} \sqrt{\frac{(l+2)!}{(l-2)!}} a_{2,lm} Y_{lm}(\hat{n}) , & (2.44) \\
\bar{\partial}^2(Q - iU)(\hat{n}) &= \sum_{l=0}^{\infty} \sum_{m=-l}^{m=l} \sqrt{\frac{(l+2)!}{(l-2)!}} a_{-2,lm} Y_{lm}(\hat{n}) ,
\end{aligned}$$

where the expressions for the expansion coefficients are:

$$\begin{aligned}
a_{T,lm} &= \int Y_{lm}^*(\hat{n}) T(\hat{n}) d\Omega , & (2.45) \\
a_{2,lm} &= \int {}_2Y_{lm}^*(\hat{n}) (Q + iU)(\hat{n}) d\Omega \\
&= \left[\frac{(l+2)!}{(l-2)!} \right]^{-1/2} \int {}_2Y_{lm}^*(\hat{n}) \bar{\partial}^2(Q + iU)(\hat{n}) d\Omega , \\
a_{-2,lm} &= \int {}_{-2}Y_{lm}^*(\hat{n}) (Q - iU)(\hat{n}) d\Omega \\
&= \left[\frac{(l+2)!}{(l-2)!} \right]^{-1/2} \int {}_{-2}Y_{lm}^*(\hat{n}) \bar{\partial}^2(Q - iU)(\hat{n}) d\Omega .
\end{aligned}$$

Instead of $a_{\pm 2,lm}$ it is convenient to introduce their linear combinations:

$$\begin{aligned} a_{E,lm} &= -(a_{2,lm} + a_{-2,lm})/2 , \\ a_{B,lm} &= i(a_{2,lm} - a_{-2,lm})/2 . \end{aligned} \quad (2.46)$$

We can thus define in real space the two quantities, E (scalar) and B (pseudoscalar⁶):

$$\begin{aligned} E(\hat{n}) &= \sum_{l=0}^{\infty} \sum_{m=-l}^{m=l} a_{E,lm} Y_{lm}(\hat{n}) , \\ B(\hat{n}) &= \sum_{l=0}^{\infty} \sum_{m=-l}^{m=l} a_{B,lm} Y_{lm}(\hat{n}) . \end{aligned} \quad (2.47)$$

We can combine the last two equations in 2.43 with eqs. 2.46 and B.5 to obtain:

$$\begin{aligned} (Q + iU)(\hat{n}) &= \bar{\partial}^2 [{}_E(\hat{n}) + i {}_B(\hat{n})] , \\ (Q - iU)(\hat{n}) &= \bar{\partial}^2 [{}_E(\hat{n}) - i {}_B(\hat{n})] , \end{aligned} \quad (2.48)$$

where we have defined, respectively, the scalar and pseudoscalar “potentials”:

$$\begin{aligned} {}_E(\hat{n}) &= - \sum_{l=0}^{\infty} \sum_{m=-l}^{m=l} \sqrt{\frac{(l-2)!}{(l+2)!}} a_{E,lm} Y_{lm}(\hat{n}) , \\ {}_B(\hat{n}) &= - \sum_{l=0}^{\infty} \sum_{m=-l}^{m=l} \sqrt{\frac{(l-2)!}{(l+2)!}} a_{B,lm} Y_{lm}(\hat{n}) . \end{aligned} \quad (2.49)$$

Thus Q and U can be written in terms of second derivatives of the scalar ${}_E$ and pseudoscalar ${}_B$ “potentials”, which are directly related to E and B . Eqs. 2.48 is analogous to the fact that a vector field can be written as a sum of a gradient (E , irrotational) and a curl component (B , rotational). The difference for spin-2 fields is that one has to write them as second derivatives of the scalar and pseudoscalar “potentials” (see also [46]). This is the first analogy

⁶A pseudoscalar denotes a physical quantity analogous to a scalar. Both are physical quantities which assume a single value which is invariant under proper rotations. However, under the parity transformation, pseudoscalars flip their signs while scalars do not.

with electric and magnetic fields, from which the $E - B$ notation arises. The temperature is a scalar quantity and under a rotation of the coordinate systems behaves as: $T'(\hat{n}' = \mathcal{R}\hat{n}) = T(\hat{n})$, where \mathcal{R} is the rotation matrix 2.40. As usual the quantities with a prime are in the transformed coordinate system. Equation 2.45 shows that up to an l -dependent factor $a_{\pm 2, lm}$ are the expansion coefficients of two spin zero quantities $\bar{\delta}^2(Q + iU)(\hat{n})$ and $\bar{\delta}^2(Q - iU)(\hat{n})$. As a result $E(\hat{n})$ and $B(\hat{n})$ are also invariant under rotations. Their behaviour is instead different under a parity transformation: we can thus reverse the sign of the x cartesian coordinate, leaving the others unchanged. It is convenient for us to work in spherical coordinates, in such a way that $(\hat{e}_1, \hat{e}_2) = (\hat{e}_\theta, \hat{e}_\phi)$. The effect of the parity transformation is then simply to reverse the sign of the versor relative to the ϕ coordinate, $\hat{e}'_\phi = -\hat{e}_\phi$, while $\hat{e}'_\theta = \hat{e}_\theta$. In terms of the Stokes parameters this means that $Q'(\hat{n}') = Q(\hat{n})$, while $U'(\hat{n}') = -U(\hat{n})$. Using eqs. B.2 it's possible to show that:

$$\begin{aligned}\bar{\delta}^2(Q + iU)'(\hat{n}') &= \bar{\delta}^2(Q - iU)(\hat{n}) , \\ \bar{\delta}^2(Q - iU)'(\hat{n}') &= \bar{\delta}^2(Q + iU)(\hat{n}) ,\end{aligned}\tag{2.50}$$

from which follows, also considering eqs. 2.45, 2.46 and 2.47:

$$\begin{aligned}E'(\hat{n}') &= E(\hat{n}) , \\ B'(\hat{n}') &= -B(\hat{n}) ,\end{aligned}\tag{2.51}$$

that is these two new variables behave differently under parity: while E remains unchanged, B changes sign, in analogy with electric and magnetic fields (the $E - B$ notation also arises from this analogy). To characterize the statistics of the CMB perturbations only four power spectra are needed, those for T (TT), E (EE), B (BB) and the cross correlation between T and E (TE). The cross correlation between B and E or B and T vanishes because B has the opposite parity to T or E . The power spectra are defined as the rotationally invariant quantities:

$$\begin{aligned}
C_{TT,l} &= \frac{1}{2l+1} \sum_{m=-l}^{m=l} \langle a_{T,lm}^* a_{T,lm} \rangle , \\
C_{EE,l} &= \frac{1}{2l+1} \sum_{m=-l}^{m=l} \langle a_{E,lm}^* a_{E,lm} \rangle , \\
C_{BB,l} &= \frac{1}{2l+1} \sum_{m=-l}^{m=l} \langle a_{B,lm}^* a_{B,lm} \rangle , \\
C_{TE,l} &= \frac{1}{2l+1} \sum_{m=-l}^{m=l} \langle a_{T,lm}^* a_{E,lm} \rangle ,
\end{aligned} \tag{2.52}$$

in terms of which,

$$\begin{aligned}
\langle a_{T,l'm'}^* a_{T,lm} \rangle &= C_{TT,l} \delta_{ll'} \delta_{mm'} , \\
\langle a_{E,l'm'}^* a_{E,lm} \rangle &= C_{EE,l} \delta_{ll'} \delta_{mm'} , \\
\langle a_{B,l'm'}^* a_{B,lm} \rangle &= C_{BB,l} \delta_{ll'} \delta_{mm'} , \\
\langle a_{T,l'm'}^* a_{E,lm} \rangle &= C_{TE,l} \delta_{ll'} \delta_{mm'} , \\
\langle a_{B,l'm'}^* a_{E,lm} \rangle &= \langle a_{B,l'm'}^* a_{T,lm} \rangle = 0 .
\end{aligned} \tag{2.53}$$

Being defined in the Fourier space, the E and B fields are *non-local*, thus in principle to know them at a given point requires measurements all over the sky. In order to fit the data with models, it is necessary to invert these relations in order to obtain signal correlations from the Angular Spectra in eqs. 2.52 and 2.53, in terms of the real quantities $T - Q - U$. The full calculation can be found in [43]; for our aim it is sufficient to define the following quantities:⁷

⁷For a spin- ± 2 system we need two functions, $F_{1,lm}(\theta)$ and $F_{2,lm}(\theta)$, that can be expressed in terms of the Legendre polynomials.

$$\begin{aligned}
F_{1,lm}(\theta) &= 2\sqrt{\frac{(l-2)!(l-m)!}{(l+2)!(l+m)!}} \left[\frac{m^2-l}{\sin^2\theta} - \frac{l(l+1)}{2} \right] P_l^m(\cos\theta) \quad (2.54) \\
&+ 2\sqrt{\frac{(l-2)!(l-m)!}{(l+2)!(l+m)!}} (l+m) \frac{\cos\theta}{\sin^2\theta} P_{l-1}^m(\cos\theta) , \\
F_{2,lm}(\theta) &= 2\sqrt{\frac{(l-2)!(l-m)!}{(l+2)!(l+m)!}} \frac{m}{\sin^2\theta} [-l(l-1)\cos\theta] P_l^m(\cos\theta) \\
&+ 2\sqrt{\frac{(l-2)!(l-m)!}{(l+2)!(l+m)!}} \frac{m}{\sin^2\theta} [(l+m)P_{l-1}^m(\cos\theta)] ,
\end{aligned}$$

These two functions allow to write the expressions relating fluctuations to spectra for the Stokes parameters (and their correlations), in analogous way to the expression found for temperature only (eq. 2.35), here rewritten in the unified formalism:

$$\langle T(\hat{n}_1) T(\hat{n}_2) \rangle = \frac{1}{4\pi} \sum_{l=0}^{\infty} (2l+1) C_{TT,l} P_l(\cos\theta) , \quad (2.55)$$

where $\hat{n}_1 \cdot \hat{n}_2 = \cos\theta$. The relations for the Stokes parameters assume a very simple form in the coordinate system where the basis versor \hat{e}_1 , for both \hat{n}_1 and \hat{n}_2 , is aligned with the great circle connecting the two directions \hat{n}_1 , \hat{n}_2 (and the \hat{e}_2 versor perpendicular to \hat{e}_1 , by definition):

$$\begin{aligned}
\langle Q_r(\hat{n}_1) Q_r(\hat{n}_2) \rangle &= \frac{1}{4\pi} \sum_{l=0}^{\infty} (2l+1) [C_{EE,l} F_{1,l2}(\theta) - C_{BB,l} F_{2,l2}(\theta)] , \\
\langle U_r(\hat{n}_1) U_r(\hat{n}_2) \rangle &= \frac{1}{4\pi} \sum_{l=0}^{\infty} (2l+1) [C_{BB,l} F_{1,l2}(\theta) - C_{EE,l} F_{2,l2}(\theta)] , \\
\langle T(\hat{n}_1) Q_r(\hat{n}_2) \rangle &= -\frac{1}{4\pi} \sum_{l=0}^{\infty} (2l+1) C_{TE,l} F_{1,l0}(\theta) , \\
\langle T(\hat{n}_1) U_r(\hat{n}_2) \rangle &= 0 . \quad (2.56)
\end{aligned}$$

The subscript r indicates that the Stokes parameters are measured in this particular coordinate system: we can use the transformation laws in equation 2.40 to find (Q, U) in terms of (Q_r, U_r) . More generally, recalling eqs. 2.40 and 2.41, it's worth to define the vector:

$$\vec{D} \equiv (T, Q, U) \quad \text{which transforms as} \quad \vec{D}' = \mathcal{R}(\alpha) \times D. \quad (2.57)$$

Therefore, the correlations in eq. 2.56, can be written as components of a 3×3 matrix $\langle \vec{D}(\hat{n}_1) \vec{D}(\hat{n}_2) \rangle$, which transforms as follows:

$$\langle \vec{D}'(\hat{n}_1) \vec{D}'(\hat{n}_2) \rangle = \mathcal{R}(\alpha_1) \times \langle \vec{D}(\hat{n}_1) \vec{D}(\hat{n}_2) \rangle \times \mathcal{R}(\alpha_2), \quad (2.58)$$

where α_1, α_2 are the rotation angles, along the line of sight, that can be different in the positions \hat{n}_1 and \hat{n}_2 on the celestial sphere.

In case of measuring the temperature or polarization anisotropies in small patches of the sky, it's possible to work under the approximation of flat sky and spherical harmonics can be replaced by Fourier modes. This is extremely relevant for computational reasons, because it becomes possible to make use of Fast Fourier Transforms. In the small-scale limit we consider only directions in the sky \hat{n} which are close to \hat{z} ⁸, in which case instead of spherical decomposition one may use a plane wave expansion. For temperature anisotropies we replace:

$$\sum_{l=0}^{\infty} \sum_{m=-l}^{m=l} a_{TT,lm} Y_{lm}(\hat{n}) \rightarrow \int d^2\vec{k} T(\vec{k}) e^{i\vec{k}\cdot\vec{r}} \Rightarrow T(\hat{n}) = \frac{1}{4\pi^2} \int d^2\vec{k} T(\vec{k}) e^{i\vec{k}\cdot\vec{r}}, \quad (2.59)$$

where the Fourier coefficients must satisfy:

$$\langle T(\vec{k}) T(\vec{k}') \rangle = 4\pi^2 C_{TT,l} \delta^2(\vec{k} - \vec{k}'). \quad (2.60)$$

The expansion of spin-2 weighted functions takes the form:

$$\begin{aligned} {}_2Y_{lm} &= \sqrt{\frac{(l-2)!}{(l+2)!}} \partial^2 Y_{lm} \rightarrow \frac{1}{4\pi^2} \frac{1}{\vec{k}^2} \partial^2 e^{i\vec{k}\cdot\vec{r}}, \\ {}_{-2}Y_{lm} &= \sqrt{\frac{(l-2)!}{(l+2)!}} \bar{\partial}^2 Y_{lm} \rightarrow \frac{1}{4\pi^2} \frac{1}{\vec{k}^2} \bar{\partial}^2 e^{i\vec{k}\cdot\vec{r}}, \end{aligned} \quad (2.61)$$

which lead to the following expressions:

⁸Here \hat{z} denotes the versor perpendicular to a given (flat) patch of the sky.

$$\begin{aligned}
(Q + iU)(\hat{n}) &= -4\pi^2 \int d^2\vec{k} \left[E(\vec{k}) + iB(\vec{k}) \right] \frac{1}{k^2} \bar{\partial}^2 e^{i\vec{k}\cdot\vec{r}} , \\
(Q - iU)(\hat{n}) &= -4\pi^2 \int d^2\vec{k} \left[E(\vec{k}) - iB(\vec{k}) \right] \frac{1}{k^2} \bar{\partial}^2 e^{i\vec{k}\cdot\vec{r}} .
\end{aligned} \tag{2.62}$$

From eq. B.2, in the small scale limit, we obtain:

$$\begin{aligned}
\frac{1}{k^2} \bar{\partial}^2 e^{i\vec{k}\cdot\vec{r}} &= -e^{-2i(\phi-\phi_k)} e^{i\vec{k}\cdot\vec{r}} , \\
\frac{1}{k^2} \bar{\partial}^2 e^{i\vec{k}\cdot\vec{r}} &= -e^{2i(\phi-\phi_k)} e^{i\vec{k}\cdot\vec{r}} ,
\end{aligned} \tag{2.63}$$

where ϕ is the generic rotation angle, while ϕ_k is the angle between \vec{k} and \vec{r} , $\vec{k} \cdot \vec{r} = \cos \phi_k$. The above expressions have been derived in the spherical basis where $\hat{e}_1 = \hat{e}_\theta$ and $\hat{e}_2 = \hat{e}_\phi$, but in the small scale limit one can define a fixed basis in the sky perpendicular to \hat{z} , $\hat{e}'_1 = \hat{e}_x$ and $\hat{e}'_2 = \hat{e}_y$, thus $(k_x + ik_y) = k e^{i\phi_k}$ and $r = \sqrt{x^2 + y^2}$. The Stokes parameters in the two coordinate systems are related by:

$$\begin{aligned}
(Q + iU)' &= e^{-2i\phi} (Q + iU) , \\
(Q - iU)' &= e^{2i\phi} (Q - iU) .
\end{aligned} \tag{2.64}$$

Combining eqs. 2.62 and 2.64 we find:

$$\begin{aligned}
Q(\vec{r}) &= \frac{1}{4\pi^2} \int d^2\vec{k} \left[E(\vec{k}) \cos(2\phi_k) - B(\vec{k}) \sin(2\phi_k) \right] e^{i\vec{k}\cdot\vec{r}} , \\
U(\vec{r}) &= \frac{1}{4\pi^2} \int d^2\vec{k} \left[E(\vec{k}) \sin(2\phi_k) + B(\vec{k}) \cos(2\phi_k) \right] e^{i\vec{k}\cdot\vec{r}} .
\end{aligned} \tag{2.65}$$

We can finally write the correlation functions in the small scale limit (in their natural coordinate system denoted with a subscript r in eq. 2.56):

$$\begin{aligned}
C_{TT}(r) &= \frac{1}{4\pi^2} \int d^2\vec{k} e^{ikr \cos \phi_k} C_{TT,l} , \\
C_{EE}(r) &= \frac{1}{4\pi^2} \int d^2\vec{k} e^{ikr \cos \phi_k} [C_{EE,l} \cos^2(2\phi_k) + C_{BB,l} \sin^2(2\phi_k)] , \\
C_{BB}(r) &= \frac{1}{4\pi^2} \int d^2\vec{k} e^{ikr \cos \phi_k} [C_{EE,l} \sin^2(2\phi_k) + C_{BB,l} \cos^2(2\phi_k)] , \\
C_{TE}(r) &= \frac{1}{4\pi^2} \int d^2\vec{k} e^{ikr \cos \phi_k} C_{TE,l} \cos(2\phi_k) .
\end{aligned} \tag{2.66}$$

We can summarize the above results using a vector notation: the polarization field is written in the form of a vector, $\vec{P} = \begin{pmatrix} Q \\ U \end{pmatrix}$, while the spin raising and lowering operators are combined to defined the two second-order differential operators:

$$\begin{aligned}\vec{D}_E &= \frac{1}{2} \begin{pmatrix} \partial^2 + \bar{\partial}^2 \\ -i(\partial^2 - \bar{\partial}^2) \end{pmatrix}, \\ \vec{D}_B &= \frac{1}{2} \begin{pmatrix} i(\partial^2 - \bar{\partial}^2) \\ \partial^2 + \bar{\partial}^2 \end{pmatrix}.\end{aligned}\tag{2.67}$$

Now eq. 2.48 takes the simple form:

$$\vec{P} = \vec{D}_E \quad E + \vec{D}_B \quad B ,\tag{2.68}$$

where we have again highlighted the analogy with the gradient-curl decomposition. In the flat-sky approximation $\partial \rightarrow -(\partial_x + i\partial_y)$, $\bar{\partial} \rightarrow -(\partial_x - i\partial_y)$, and the differential operators reduce to:

$$\begin{aligned}\vec{D}_E &= \frac{1}{2} \begin{pmatrix} \partial_x^2 - \partial_y^2 \\ 2\partial_x\partial_y \end{pmatrix}, \\ \vec{D}_B &= \frac{1}{2} \begin{pmatrix} -2\partial_x\partial_y \\ \partial_x^2 - \partial_y^2 \end{pmatrix}.\end{aligned}\tag{2.69}$$

\vec{D}_E and \vec{D}_B are the spin-2 analogues of the familiar gradient and curl operators. Applying \vec{D}_E or \vec{D}_B to a scalar field gives E and B fields that have vanishing curl (rotational) and gradient (irrotational), respectively. Eq. 2.69 shows that $\vec{D}_B = \mathcal{R} \times \vec{D}_E$, where the 2×2 matrix

$$\mathcal{R} = \begin{pmatrix} 0 & -1 \\ 1 & 0 \end{pmatrix},\tag{2.70}$$

simply performs a rotation taking $Q \rightarrow -U$ and $U \rightarrow Q$. When drawing polarization fields as two-headed arrows with length $\sqrt{Q^2 + U^2}$ and angle $\frac{1}{2} \arctan(U/Q)$, this corresponds to rotating the polarization direction by 45° at each point. In other words, rotating the polarization directions of an E -field by 45° gives a B -field. The analogue of eqs. 2.65 is now:

$$\vec{P}(\vec{r}) = \frac{1}{4\pi^2} \int d^2\vec{k} \left[E(\vec{k}) \begin{pmatrix} \cos(2\phi_k) \\ \sin(2\phi_k) \end{pmatrix} + B(\vec{k}) \begin{pmatrix} -\sin(2\phi_k) \\ \cos(2\phi_k) \end{pmatrix} \right] e^{i\vec{k}\cdot\vec{r}}, \quad (2.71)$$

$$\vec{r} = \begin{pmatrix} x \\ y \end{pmatrix} \quad \text{and} \quad \vec{k} = k \begin{pmatrix} \cos\phi_k \\ \sin\phi_k \end{pmatrix}.$$

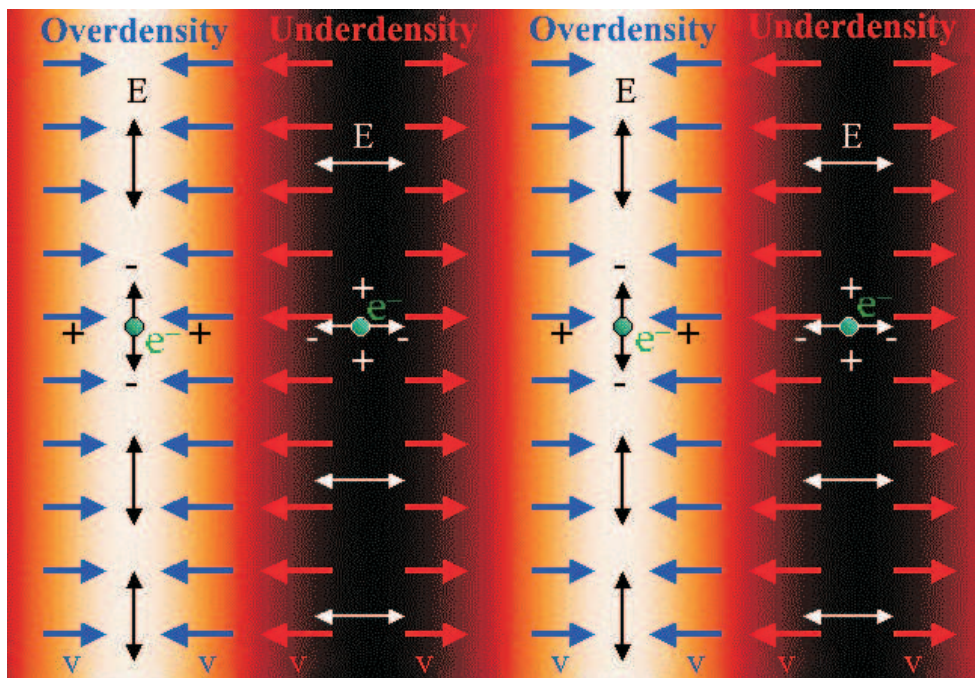
In other words, the $E - B$ decomposition becomes local in Fourier space: the polarization direction of the E -component is parallel or perpendicular to \vec{k} , whereas that of the B -component makes a 45° angle with \vec{k} .

2.5.3 Quadrupole Anisotropy From Scalar Perturbations

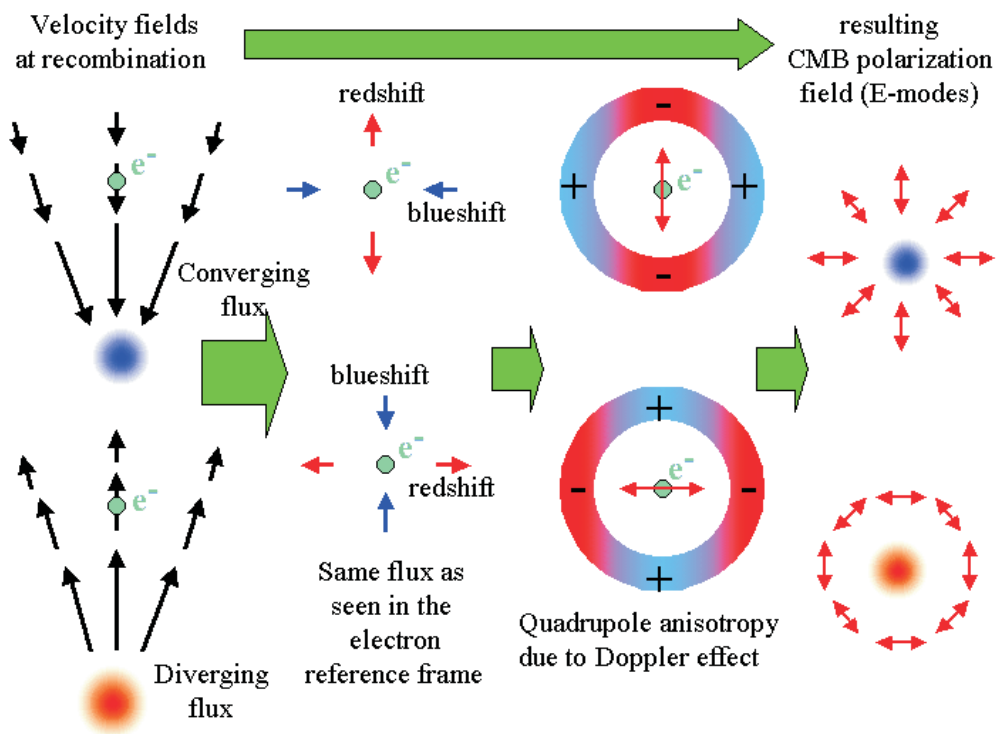
After the introduction to the $E - B$ formalism, we can now go back to CMB polarization and its cause, the quadrupole anisotropies at recombination. First we investigate the case of scalar adiabatic fluctuations, where initial perturbations to the density imply potential fluctuations that dominate at large scales (Sachs-Wolfe effect, see par. 1.5.6 and 2.4.1): let us consider a single large-scale Fourier component of the fluctuation, for the photons this is a single plane wave in the temperature perturbation (with wavevector \vec{k}) and gradients in the temperature always create flows from hot to cold. As shown in fig. 2.7, gravity overwhelms pressure in overdense regions causing matter to flow towards density peaks initially (with velocity \vec{v}). However overdense regions are effectively cold initially because photons must climb out of the potential wells they create and hence lose energy in the process (see par. 2.4.1). The color convention reflects redshift or blueshift with respect to the rest frame of the electron. Though flows are established from cold to hot temperature regions on large scales, they still go from hot to cold effective temperature regions. Let us consider the quadrupole component of the temperature pattern seen by an observer located in a trough of a plane wave. Lobes are in the directions of the hot and cold photons. Notice that the hot and cold lobes are separated by 90° due to their quadrupole nature. Planes represent the fluctuation in intensity of the underlying plane wave fluctuation. The azimuthal symmetry (symmetry to rotations about the plane wave axis) in the problem requires that $\vec{v} \parallel \vec{k}$ and hence the flow is irrotational, $\nabla \times \vec{v} = 0$ ⁹. Because hotter photons from the crests flow into the trough from the directions $\pm\hat{k}$, while cold photons surround the observer in the plane, the quadrupole pattern seen in a trough has an $m = 0$ structure with angle $\hat{n} \cdot \hat{k} = \cos\theta$:

$$Y_{20}(\hat{n}) = \frac{1}{4} \sqrt{\frac{5}{\pi}} (3 \cos^2\theta - 1), \quad (2.72)$$

⁹Here the \times operator means vector cross product, $\nabla \times \vec{a}$ takes the curl of the vector \vec{a} .



(a) Overdensities and underdensities at recombination



(b) Generation of E -modes by velocity fields at recombination

Figure 2.7: Scalar perturbations at recombination only generate E polarization modes. The color convention reflects redshift or blueshift with respect to the rest frame of the electron.

where \hat{n} here represents the scattering direction. The opposite effect occurs at the crests, reversing the sign of the quadrupole but preserving the $m = 0$ nature in its local angular dependence. The full effect is thus described by a local quadrupole modulated by a plane wave in space, $-Y_{20}(\hat{n})e^{i\vec{k}\cdot\vec{x}}$, where the sign denotes the fact that photons flowing into cold regions are hot.

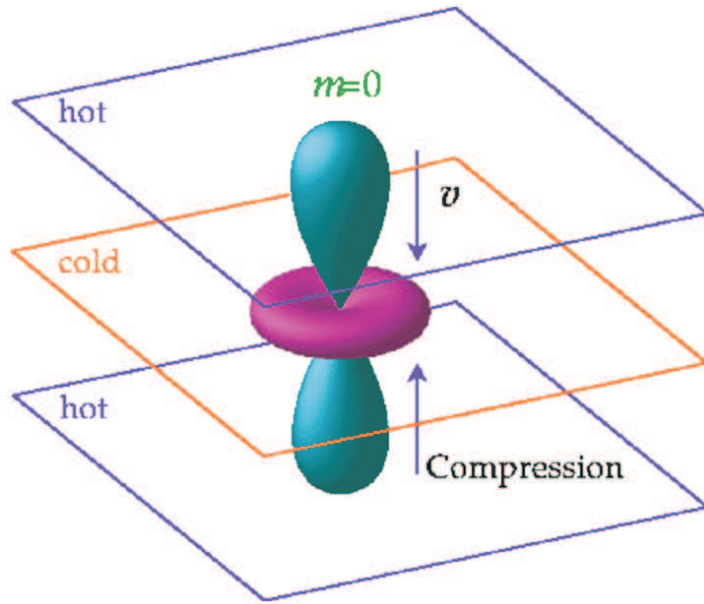


Figure 2.8: The scalar quadrupole moment ($l = 2$, $m = 0$). Flows from hot (blue) regions into cold (red) ones, produce the azimuth symmetric pattern Y_{20} shown ($\vec{v} \parallel \vec{k}$).

The sense of the quadrupole moment determines the polarization pattern through Thomson scattering. Recall that polarized Thomson cross-section peaks when the temperature varies in the direction orthogonal to \hat{n} (eq. 2.38). Consider then the plane perpendicular to \hat{n} , described by the usual two basis versors ($\hat{e}_\theta, \hat{e}_\phi$), in spherical coordinates ($\hat{n} \cdot \hat{k} = \cos \theta$). This may be visualized in an angular lobe diagram such as fig. 2.8, as a plane which passes through the origin of the quadrupole pattern, perpendicular to the line of sight. The polarization is maximal when the hot and cold lobes of the quadrupole are in this tangent plane, and is aligned with the component of the colder lobe which lies in the plane. As θ varies from 0 (pole) to $\pi/2$ (equator), the temperature differences in this plane increase from zero (see fig. 2.9a). The local polarization of the temperature perturbation is thus purely in the North-South (N-S) direction, decreasing in amplitude towards the poles (see fig. 2.9b). This pattern represents a pure Q -field on the sky whose amplitude varies in angle as an

$l = 2, m = 0$ spin-2 spherical harmonic: $Q = \sin^2 \theta$ and $U = 0$.

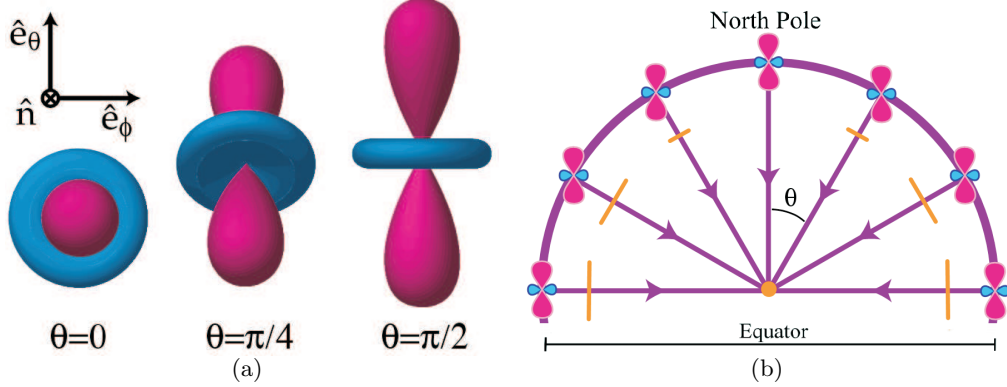


Figure 2.9: 3-D sketch describing the transformation of $m = 0$ quadrupole anisotropies into linear E -mode polarization. (a) The orientation of the $m = 0$ quadrupole moment with respect to the scattering direction \hat{n} determines sense and magnitude of the linear E polarization, which is aligned with the cold long lobe in the plane identified by $(\hat{e}_\theta, \hat{e}_\phi)$. (b) $\hat{n} \cdot \hat{k} = \cos \theta$. The polarization points North-South (Q), with magnitude varying as $\sin^2 \theta$ (yellow lines).

In different regions of space, the plane wave modulation of the quadrupole can change the sign of the polarization, but not its sense. In fact, we should remind that we have considered a single Fourier component of the fluctuation, (a single plane wave for the photons), but the polarization pattern on the sky is not simply this local signature from scattering but is modulated over the Last Scattering Surface by the plane wave spatial dependence of the perturbation, i.e. $e^{i\vec{k}\cdot\vec{x}}$. The modulation changes amplitude, sign, and angular structure of the polarization but not its nature: it does not mix Q and U , a pure Q -polarization remains Q . Nevertheless modulation can mix E and B if U -polarization is also present (see next section).

More formally, we can now recall the formalism introduced in par. 2.5.2 to obtain the expression for the polarization power spectrum, making use of the integral solution of the Boltzmann equation (see [45] for details). In the case of scalar perturbations we have just seen that for any given Fourier mode \vec{k} of the perturbations, in the frame where $\vec{v} \parallel \vec{k}$ (azimuthal symmetry), only Q is generated:

$$Q(\hat{n}, \vec{k}) = \frac{3}{4} \sin^2 \theta \int d\tau e^{i|\vec{k}|(\tau_0 - \tau) \cos \theta} g(\tau) \Pi(|\vec{k}|, \tau), \quad (2.73)$$

where τ is the conformal time¹⁰ with τ_0 its present value. We have also in-

¹⁰In a FRW universe the conformal time τ at time t this given by: $\tau = \int_0^t \frac{dt'}{a(t')}$, see also par. 1.2.

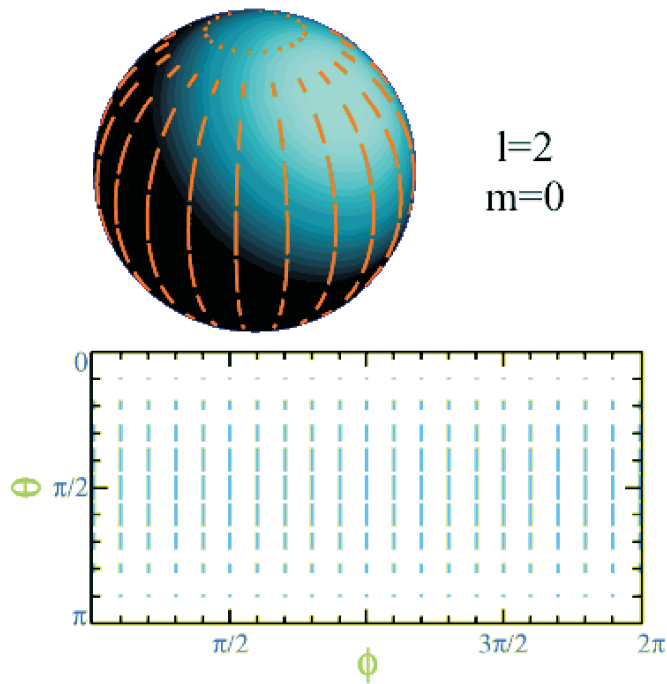


Figure 2.10: Pure E -polarization pattern for $l = 2, m = 0$.

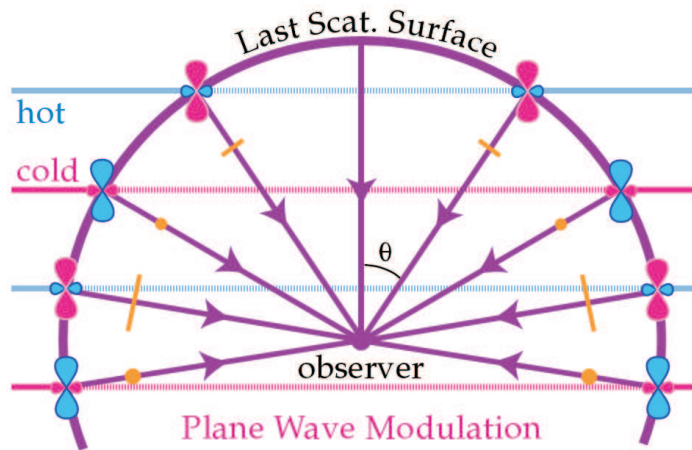


Figure 2.11: Modulation of the local polarization pattern due to plane wave perturbations inside the Last Scattering Surface. Yellow points represent polarization out of the plane with magnitude proportional to their size. The plane wave modulation changes amplitude and sign of the polarization but does not mix Q and U . Modulation can however mix E and B U is also present (see par. 2.5.4).

produced the so-called visibility function $g(\tau) = \kappa e^{-\kappa\tau}$, which expresses the probability that a photon is last scattered between τ and $\tau + d\tau$, in terms of

$\dot{\kappa}(\tau)$, differential cross-section for Thomson scattering, $\dot{\kappa}(\tau) = a(\tau)n_e(\tau)x(\tau)\sigma_T$ and $\kappa = \int_{\tau}^{\tau_0} d\tau' \dot{\kappa}(\tau')$ ¹¹. The term $\Pi(|\vec{k}|, \tau)$ represents the source term, and can be expressed as a sum of contributions from the temperature quadrupole $\Delta_{l=2}^T$, the polarization monopole $\Delta_{l=0}^P$ and the polarization quadrupole $\Delta_{l=2}^P$: $\Pi(|\vec{k}|, \tau) = \Delta_{l=2}^T + \Delta_{l=0}^P + \Delta_{l=2}^P$. Now using eqs. 2.43 and 2.50, since $U = 0$ and Q is only function of θ , for the expansion coefficients we get, $a_{2,lm} = a_{-2,lm}$; therefore, recalling eq. 2.45, the result is that, for scalar perturbations, $a_{B,lm} = 0$ and only the $a_{E,lm}$ are different from zero. The polarization power spectra are defined in eqs. 2.52: for E the ensemble average can be obtained by acting twice with the spin raising (or lowering) operator (eq. B.2) on eq. 2.73, leading to (see [42] for details):

$$C_{EE,l} = 9\pi^2 \frac{(l+2)!}{(l-2)!} \int k^2 dk P_S(k) \left(\int d\tau g(\tau) \Pi(k, \tau) \frac{j_l(x)}{x^2} \right)^2, \quad (2.74)$$

where $j_l(x)$ is the spherical Bessel function of order l , $P_S(k)$ is the primordial power spectrum of scalar perturbations of eq. 1.66 and $k = |\vec{k}|$.

2.5.4 Quadrupole Anisotropy From Tensor Perturbations

Tensor fluctuations (see par. 1.5.7) are transverse-traceless perturbations to the metric, i.e. gravitational waves. A plane gravitational wave perturbation represents a quadrupolar stretching of space in the plane of the perturbation. As the wave passes (or its amplitude changes), a circle of test particles in the plane is distorted into an ellipse whose semi-major axis \rightarrow semi-minor axis as the spatial phase changes from crest \rightarrow trough (see fig. 2.12, yellow ellipses). The accompanying stretching of the wavelength of photons produces a quadrupolar temperature variation with an $m = \pm 2$ pattern:

$$Y_{2\pm 2}(\hat{n}) = \frac{1}{4} \sqrt{\frac{15}{2\pi}} \sin^2 \theta e^{\pm 2i\phi}. \quad (2.75)$$

Thomson scattering again produces a polarization pattern from the quadrupole anisotropy, but in the tensor case it is not symmetric like the density quadrupole: this asymmetry causes a ‘‘handedness’’ to the pattern of polarization¹². At the equator, the quadrupole pattern intersects the tangent plane identified by $(\hat{e}_\theta, \hat{e}_\phi)$, with hot and cold lobes rotating in and out of the \hat{e}_ϕ direction with the azimuthal angle ϕ . The polarization pattern is therefore purely Q with a $\cos(2\phi)$ dependence (see next eq. 2.76).

¹¹ $a(\tau)$ is the expansion factor, while $n_e(\tau)$ and $x(\tau)$ (defined in par. 2.4.1) are the electron numeric density and the ionization fraction.

¹²This handedness of the tensor polarization pattern is clearly related to the non-invariance under parity transformation of the B field, see par. 2.5.2.

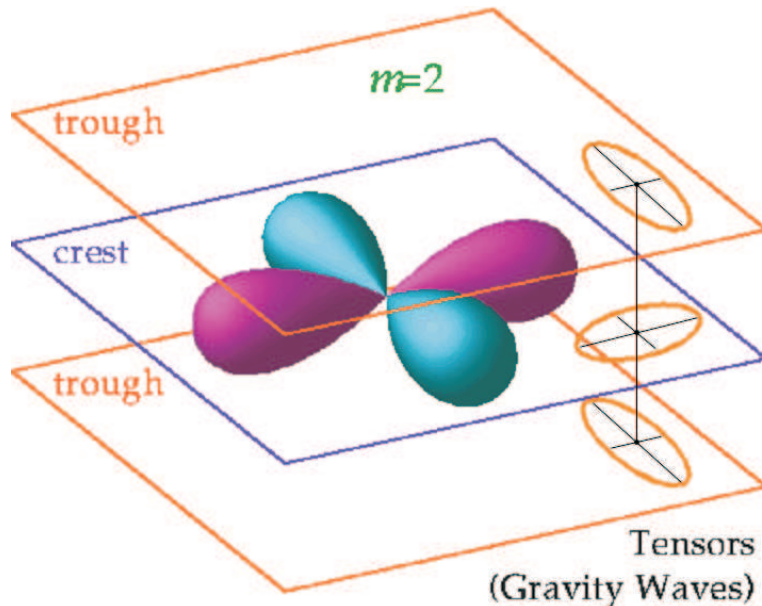


Figure 2.12: Tensor quadrupole moment ($l = 2, m = 2$) due to gravity waves.

At the pole, the quadrupole lobes lie completely in the polarization plane and produces the maximal polarization unlike the scalar case. The full polarization pattern is shown in fig. 2.14:

$$Q = (1 + \cos^2 \theta)e^{2i\phi} \quad , \quad U = -2i \cos \theta e^{2i\phi} \quad , \quad (2.76)$$

Note that Q and U are present in nearly equal amounts for the tensors. In particular, notice that the pattern is no longer all North-South (N-S) or even East-West (E-W) but also have NorthEast-SouthWest (NE-SW) and NorthWest-SouthEast (NW-SE) components. Recalling fig. 2.11, let us consider the modulation over the Last Scattering Surface by the plane wave spatial dependence in the case of tensor perturbations. If the U -component is also present in the polarization pattern, modulation can mix E and B modes, the reason why this occurs is best seen from the local distinction between E and B -modes: E -modes have polarization amplitudes that change parallel or perpendicular to the polarization direction, and B -modes in directions 45° away from it, resulting in a characteristic shear-like footprint. B -modes retain their special nature as manifest in the fact that they can possess a handedness that distinguishes left from right (see fig. 2.13). On the other hand, plane wave modulation always changes the polarization amplitude in the direction \hat{k} or N-S on the sphere. Whether the resultant pattern possesses E or B -contributions depends on whether the local polarization has Q or U -contributions. For scalars, the

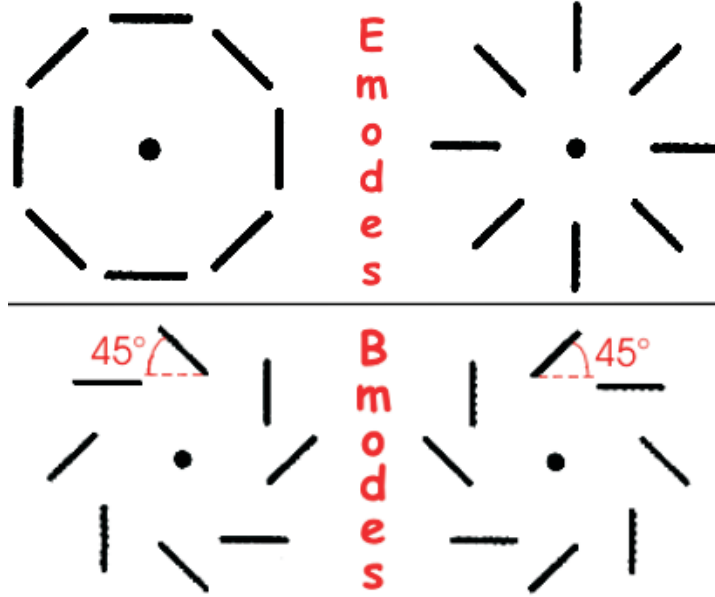


Figure 2.13: Shear-like polarization pattern of the B -modes as compared to the radial-tangential pattern of the E -modes. Only tensor perturbations (gravity waves) causing quadrupole anisotropy at recombination can produce such shear-like pattern of linear polarization.

modulation is of a pure Q -field and thus its E -mode nature is preserved. For the tensors, the comparable Q and U components of the local pattern imply a more comparable distribution of E and B modes at short wavelengths. The full polarization pattern is a random superposition of these plane-wave-modulated patterns, as shown in fig. 2.14. In a way similar to scalar perturbations we want to find expression for the polarization power spectrum in the case of tensor perturbations, again making use of the integral solution of the Boltzmann equation (see [45] for details). The form of Q and U is:

$$\begin{aligned}
 Q(\hat{n}, k) &= -(1 + \cos^2 \theta) e^{2i\phi} \int d\tau e^{ik(\tau_0 - \tau) \cos \theta} g(\tau) \Psi(k, \tau), \quad (2.77) \\
 U(\hat{n}, k) &= -\sin^2 \theta e^{2i\phi} \int d\tau e^{ik(\tau_0 - \tau) \cos \theta} g(\tau) \Psi(k, \tau).
 \end{aligned}$$

The source term $\Psi(k, \tau)$ is a complex sum over the two independent tensor polarization states, $\Psi = (\Psi_+ - i\Psi_\times)/2$ (see par. 1.5.7), and can also be expressed in terms of temperature and polarization multipoles. This time $\bar{\partial}^2(Q + iU)(\hat{n})$ and $\bar{\partial}^2(Q - iU)(\hat{n})$ are no more equal, so both $a_{E,lm}$ and $a_{B,lm}$ will be different from zero. Following a similar procedure as for scalar perturbation, it is possible to find out:

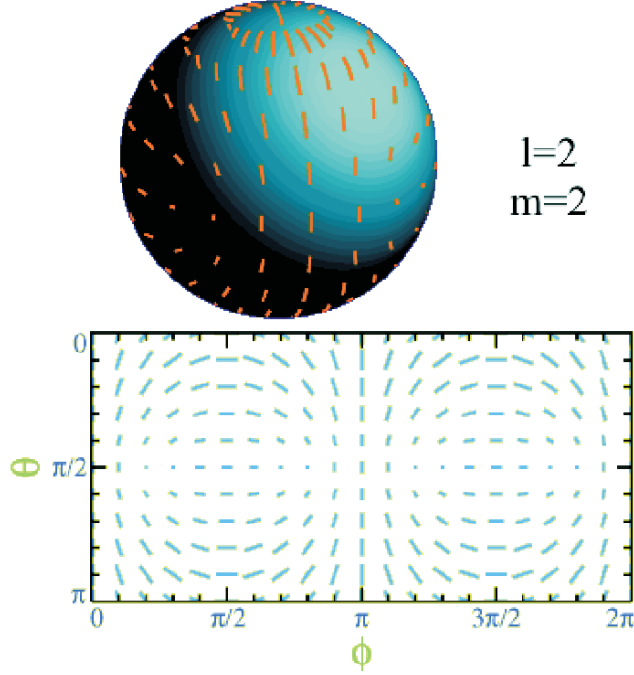


Figure 2.14: Full polarization pattern for $l = 2, m = 2$, combination of both Q and U (eq. 2.76).

$$\begin{aligned}
 C_{EE,l} &= 16\pi^2 \int k^2 dk P_T(k) \left| \int d\tau g(\tau) \Psi(k, \tau) \left[-j_l(x) + j_l''(x) + \frac{2j_l(x)}{x^2} + \frac{4j_l'(x)}{x} \right] \right|^2, \\
 C_{BB,l} &= 16\pi^2 \int k^2 dk P_T(k) \left| \int d\tau g(\tau) \Psi(k, \tau) \left[2j_l'(x) + \frac{4j_l(x)}{x} \right] \right|^2, \quad (2.78)
 \end{aligned}$$

where $P_T(k)$ is the primordial power spectrum of tensor perturbations of eq. 1.73. A generic inflationary model predicts a spectrum of gravitational waves with $n_T = n_S - 1$ and $r \propto (1 - n_S) = -n_T$ [24], [25] (see par. 1.5.7). It follows that the detectability of such primeval tensor fluctuations strongly depends on the deviation from a scale-invariant scalar spectrum and on the tensor-to-scalar ratio r .

2.6 B-modes angular scale

Let us now focus on the B-modes of polarization. First of all we must briefly introduce the gravitational lensing, which is related to the cosmic shear, and its impact on CMB polarization. Without giving the details of this effect (see for example [3]) and its physical meaning, we must take it into account, since

it causes the conversion of E-modes into B-modes, even if primeval gravitational waves were absent. This mechanism however is effective only above a suitable multipole l value, i.e. at suitable small angular scales, since it is related to the presence of massive structures along the line of sight. Fig. 2.15a shows the relative amplitude and angular scale of temperature and polarization power spectra, while fig. 2.15b focuses on the B-modes spectrum, also showing possible lensing contamination (black dashed line). This plot is very significative because it clearly shows that the best observational window for B-modes goes up to $l \sim 100 \Rightarrow \theta \sim 3^\circ$, while at smaller scales lensing effects would hide the traces left by primordial gravitational waves. We see that also in the pessimistic case of very low τ (see par. 2.3), inspecting the B-modes on the angular scale of a few degrees will eventually allow to appreciate an essential and unique footprint of an inflationary generic scenario.

2.7 CMB Observables

In this section we finally describe the CMB observables, as a useful connection between the theoretical aspects exposed in the preceding and the more experimental approach that is going to follow in the next chapters. First of all let us repeat that the Cosmic Microwave Background follows extremely well the spectral behaviour of a blackbody at $T_{CMB} = 2.728$ K [12], with specific brightness:

$$B(\nu, T) = \frac{4\pi\hbar\nu^3}{c^2} \left(e^{(2\pi\hbar\nu)/(k_B T)} - 1 \right)^{-1} . \quad (2.79)$$

The maximum specific brightness is at $\nu_{max} = 159$ GHz, so that the interesting spectral range for CMB studies is across the microwave and far infrared regions of the electromagnetic spectrum. The total power in the CMB brightness is obtained integrating $B(\nu, T)$ over all frequencies:

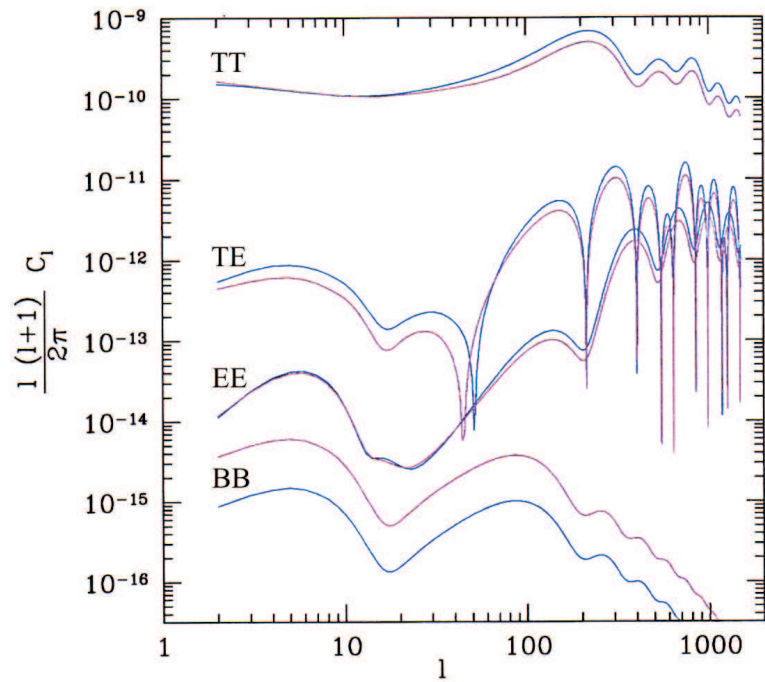
$$\int_0^\infty B(\nu, T) d\nu = 1.01 \cdot 10^{-10} \frac{W}{m^2 \cdot srad} . \quad (2.80)$$

As previously calculated in par. 2.2, the number of CMB photons per unit volume of the universe is $N_\gamma \simeq 411 \text{ cm}^{-3}$, each with average energy of about $0.7 \cdot 10^{-3} eV$. This huge number of microwave photons contributes today to the total density of the universe with $\Omega_{CMB,0} \sim 5.06 \cdot 10^{-5}$.

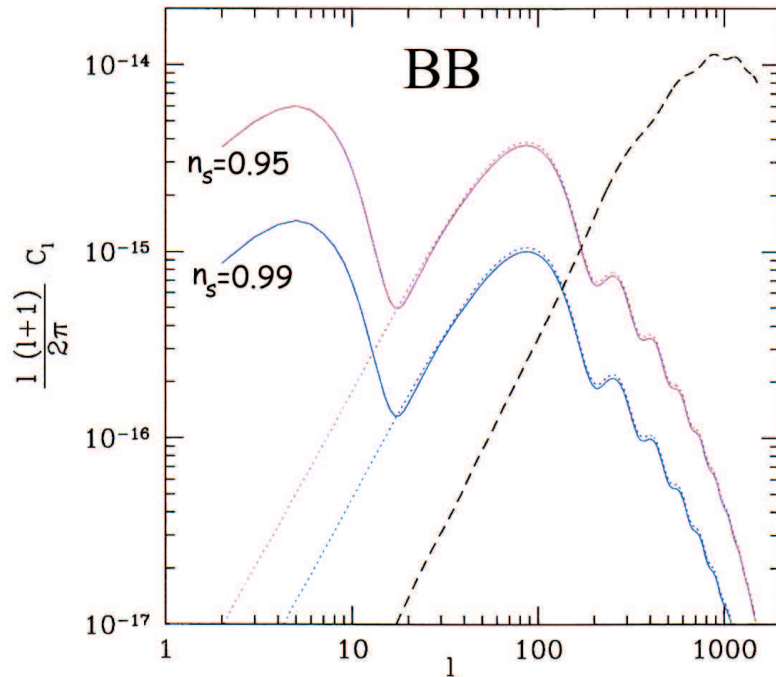
The brightness fluctuation generated by an anisotropy field with $\Delta T/T_{CMB} \sim 10^{-5} \ll 1$ is:

$$\Delta B(\nu, T) = B(\nu, T) \frac{x e^x}{e^x - 1} \frac{\Delta T}{T} , \quad (2.81)$$

with $x = \frac{2\pi\hbar\nu}{k_B T}$. This function has its maximum for $\nu_{max} = 217$ GHz. The small



(a) $C_{TT,l}$, $C_{TE,l}$, $C_{EE,l}$, $C_{BB,l}$ spectra, from top to bottom.



(b) B-modes power spectra. Solid lines are for $\tau = 0.17$, while dotted ones are for $\tau = 0$. The black dashed line shows B-modes generated by gravitational lensing of E-modes (see text).

Figure 2.15: Temperature and polarization power spectra. For all curves $\Omega_{m,0} = 0.3$, $\Omega_{b,0} = 0.05$, $h = 0.7$ and $\tau = 0.17$ (see pars. 1.2 and 2.3). Blue (pink) curves refer to scalar spectral index $n_s = 0.99$ (0.95).

degree of linear polarization has exactly the same spectrum as the anisotropies, but the level of the polarized signal in temperature is much smaller than the level of the anisotropies:

$$\Delta B_{pol}(\nu, T) = B(\nu, T) \frac{x e^x}{e^x - 1} \frac{\Delta T_{pol}}{T}, \quad (2.82)$$

Photon noise of the CMB itself is the natural, unavoidable limit for ultra-sensitive observations of the CMB observables. Photon noise for blackbody radiation can be computed from basic statistical physics, using the Bose-Einstein statistics for bosons. Let us now define the throughput of an optical system as the product of the actual collecting area A and the solid angle projected perpendicularly to the system optical axis, Ω . In the far-field limit of a source we know that the *aperture-beam area relation* holds, $\lambda^2 = A\Omega$ (see Appendix E). When working with big throughput telescopes at microwave wavelengths, we can safely work under the assumption $A\Omega \gg \lambda^2$. The power spectrum of blackbody power fluctuations is:

$$\frac{1}{\sqrt{A\Omega}} \sqrt{\frac{d\langle(\Delta W)^2\rangle}{d\nu}} = \sqrt{\frac{k_B^5}{2\pi^3 c^2 \hbar^3} T^5 \int_{x_1}^{x_2} \frac{x^4 e^x dx}{(e^x - 1)^2}}. \quad (2.83)$$

In the case of CMB, integrating over all frequencies, we get:

$$\frac{1}{\sqrt{A\Omega}} \sqrt{\frac{d\langle(\Delta W)^2\rangle}{d\nu}} = 1.74 \cdot 10^{-16} \frac{W}{\sqrt{cm^2 \cdot srad \cdot Hz}}, \quad (2.84)$$

which can be converted in temperature fluctuations by means of eq. 2.82:

$$\frac{\Delta T_{CMB}^{noise}}{\sqrt{\frac{\Delta\nu}{A\Omega}}} \sqrt{\frac{8\pi^3 \hbar^3}{k_B^3 T} \frac{1}{\int_{x_1}^{x_2} \frac{x^4 e^x dx}{(e^x - 1)^2}}}. \quad (2.85)$$

For example, for observations of the CMB in a 20% band around 150 GHz, with $A\Omega \sim 1 \text{ cm}^2/\text{srad}$, CMB photon noise produces temperature fluctuations of $\sim 4.1 \mu\text{K}/\sqrt{\text{Hz}}$, which increases up to $\sim 21 \mu\text{K}/\sqrt{\text{Hz}}$ if $A\Omega \gg \lambda^2$ is no longer satisfied and $A\Omega \sim \lambda^2$. These numbers represent the natural sensitivity limit for CMB observations (BLIP). Cryogenic bolometers working at 150 GHz are foreseen to reach CMB noise limited performance in the near future.

Chapter 3

Description of the Experimental Apparatus

3.1 Introduction

In this chapter we give a detailed description of the experimental apparatus we have dealt with for the measurements described in this work. In fact either for the polarimetry laboratory measurements (chapter 4) or for the beam measurements of OLIMPO telescope (chapter 5) we used microwave coherent sources (Gunn oscillators, par. 3.2), whose beams of radiation are directed out by means of waveguides (par. 3.4) and feed horns (par. 3.5). The signals were collected by broadband diodes (par. 3.6), coupled as well to the respective waveguides and feed horns. Synchronous modulation-demodulation technique was used to extract our microwave signals from the dominant background, by means of modulation electronics (pars. 3.8 and 3.9). In order to detect the far sidelobes of the OLIMPO telescope beam, we needed to amplify the signal by means of amplifiers coupled to the diodes or amplifying circuits (par. 3.7), which instead had to be removed for laboratory measurements, otherwise the signal would saturate the detectors. We finally describe the HDPE lenses used as focusing elements (par. 3.10) and spend some words about data acquisition (par. 3.11). We only leave out of this chapter the description of the wire-grid and its rotating support, that is given in detail in chapter 4.

3.2 Gunn Oscillator

Gunn oscillators are electronic devices used as coherent¹ sources of radiation in the microwave, mm-wave and Terahertz frequency range. These oscillators are usually made of a negative resistance diode (Gunn diode), exploiting the

¹A source of radiation is said to be coherent if the emitted waves have the same frequency and are phase-linked, i.e. they have zero or constant phase difference.

Gunn effect (briefly described in the following), and of a resonant cavity which allows fine tuning of the frequency by means of micrometric screws changing the size of the cavity. The output power from such a coherent source is directed out into free space using a waveguide (par. 3.4) and an antenna (feed horn, par. 3.5). Various sorts of semiconductor do possess the property of having negative resistance, among them GaAs and InP are mostly used for commercial purposes. The specifications of the two Gunn oscillators used in this work are described in Appendix C. Fig. 3.1 illustrates the I/V curve of a piece of such semiconductor material, showing how the current through the material varies with the voltage applied across it.

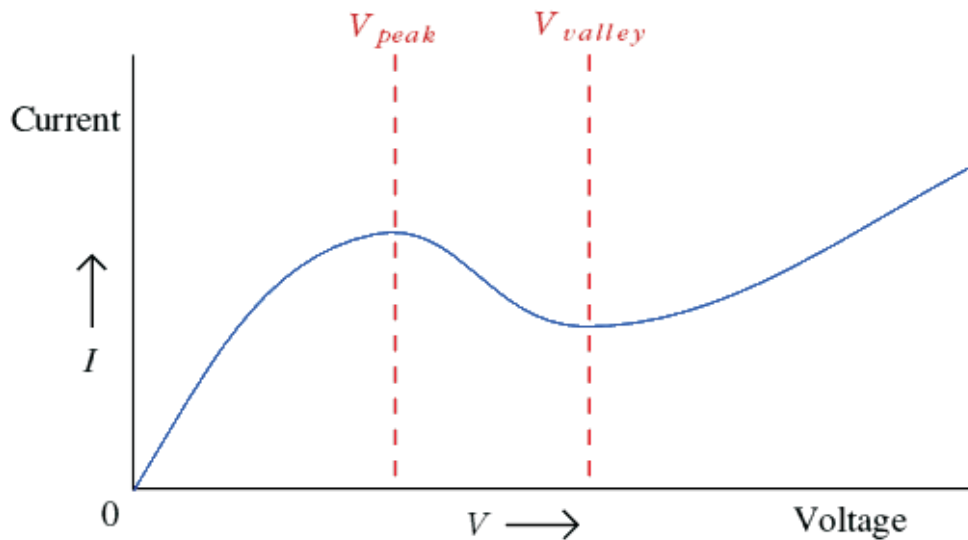


Figure 3.1: Characteristic I/V curve of a Gunn diode.

3.2.1 Gunn Effect

A Gunn diode (in its simplest form) is essentially just a piece of doped semiconductor with two electrical contacts on opposite ends. It's called a "diode" because it has just two wires and has a non-linear I/V behaviour like normal diodes. However, unlike "real" diodes its I/V behaviour is symmetric, that is if an applied voltage V gives a current I , then a voltage $-V$ will give a current $-I$. For most materials the current is simply proportional to the applied voltage, so the *static resistance*, $R \equiv V/I$, coincides with the differential definition

of resistance or *dynamic resistance*, $r \equiv \frac{dV}{dI}$, and they are said to obey *Ohm's Law*, while the Gunn diode do not. In general, its current increases with increasing voltage, but there is a region (*Negative Resistance Region*) between the peak voltage, V_{peak} , and valley voltage, V_{valley} , where the current falls as the voltage is increased ($r < 0$). The peak voltage is often called “threshold voltage” since it represents a threshold we have get over to reach the negative resistance region. The role of negative resistance can be well understood by considering the circuits shown in fig. 3.2. Fig. 3.2a shows a standard resonant RLC configuration, for which the total voltage around the RLC loop will be²:

$$\frac{di(t)}{dt}L + i(t)R + \int dt \frac{i(t)}{C} = 0 , \quad (3.1)$$

whose solution is simply:

$$i(t) = i(0)e^{At} , \quad \text{where} \quad A = \frac{-R \pm \sqrt{R^2 - 4L/C}}{2L} , \quad (3.2)$$

Now if $R^2 < 4L/C$ then A is a complex number and the current read as:

$$i(t) = i(0)e^{(\alpha+i\omega)t} , \quad \text{where} \quad \alpha = -\frac{R}{2L} , \quad \omega = \left| \frac{\sqrt{R^2 - 4L/C}}{2L} \right| . \quad (3.3)$$

If we suppose $i(0)$ to be different from zero, from eq. 3.3 it's easy to see that in each case the current oscillates sinusoidally with the angular frequency ω , while the amplitude of the oscillation varies exponentially with time in a way which depends upon the resistance. In the case of usual positive resistances, $\alpha < 0$ and the amplitude of the oscillation declines exponentially with time, because the energy stored in the inductance by the starting current $i(0)$ is progressively dissipated by the resistor via Joule effect (the resistor warms up). If the resistance is zero ($\alpha = 0$) the amplitude remains unchanged in time, no energy is dissipated. If instead the resistance has negative value, $\alpha > 0$, then the oscillation amplitude and energy grow exponentially with time. In practice, of course we can't ever obtain an oscillation whose energy grows larger without limit.

We can now look at fig. 3.2b, where the resistor R is replaced by a load resistance R_L and a Gunn diode, which has a negative dynamic resistance $r(V) < 0$. Fig. 3.3 shows how the total dynamic resistance of this combination depends on the voltage across the diode.

² L, C are, respectively, the inductance and the capacity of the circuit in fig. 3.2, while $i(t)$ is the time-dependent current flowing in it.

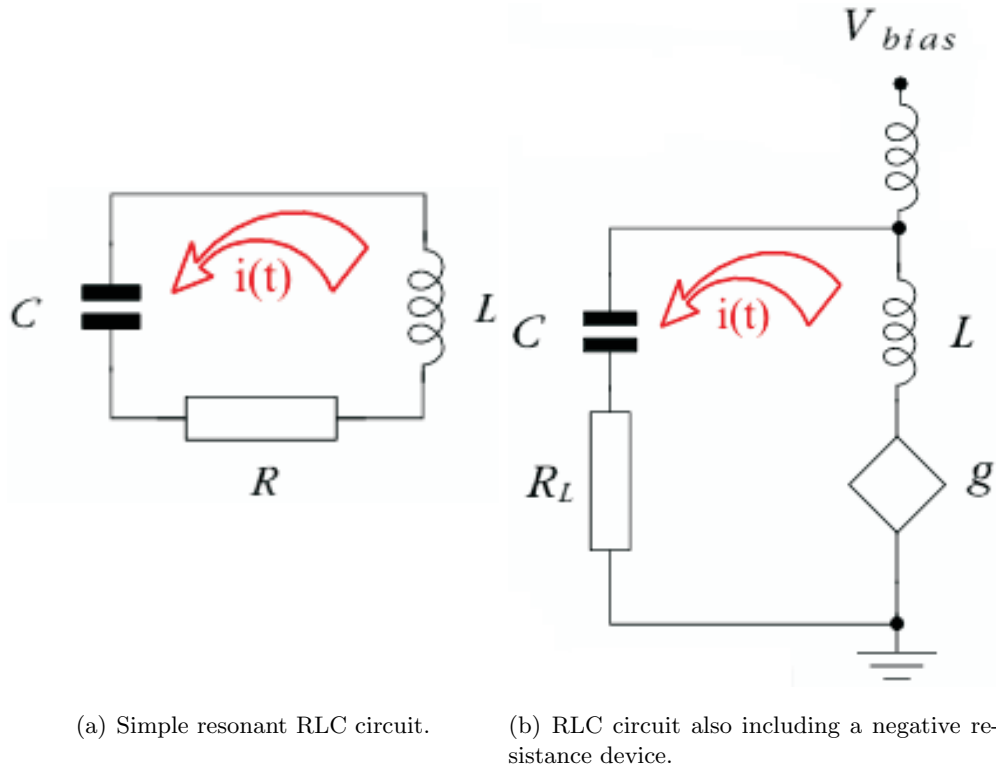


Figure 3.2: AC circuit analysis of a simple RLC resonant circuit and of one including also a negative resistance device.

The energy source for such an increase in the oscillation amplitude is provided by the extra DC voltage V_{bias} applied to the diode via a second inductance (whose value is normally very large): thus, as shown in fig. 3.3, the average voltage on the Gunn diode is V_{bias} and the diode is said to be biased into the negative resistance region. Any small fluctuations at the oscillation frequency will tend to grow because, for voltages $\sim V_{bias}$, the total circuit dynamic resistance is negative, $r = R_L + r(V) < 0$. The oscillation causes the diode voltage to go back and forth about V_{bias} , eventually driving r into the regions where its value becomes positive (damping of the oscillations because of resistive dissipation). As a result the size of the oscillation tends to reach a value for which the amount of energy per cycle generated while in the $r < 0$ region equals that dissipated per cycle while in the $r > 0$ region. The net effect is best described in terms of an averaged device negative resistance value, $g(i_{rms})$, which depends on i_{rms} , the *rms* size of the oscillation current: i.e. $g(i_{rms})$ is the value of $r(V)$ averaged over one oscillation cycle. When the oscillation is small $g(i_{rms}) \rightarrow r(V_{bias})$. If one instead allows the device voltage to oscillate over a wider range (larger oscillation) then the diode spends more time at less negative resistance values. This qualitative behavior is displayed in fig. 3.4.

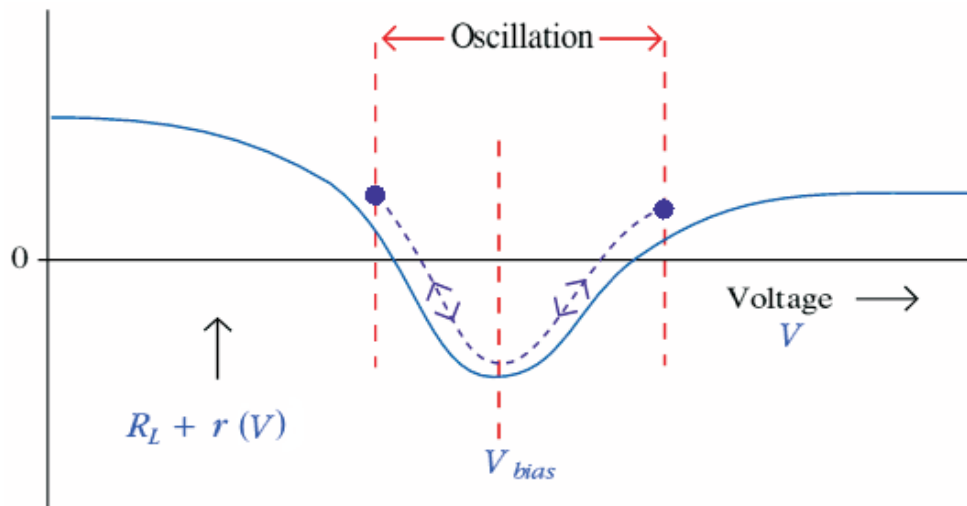


Figure 3.3: Dynamic resistance behaviour of the load resistance plus a Gunn diode.

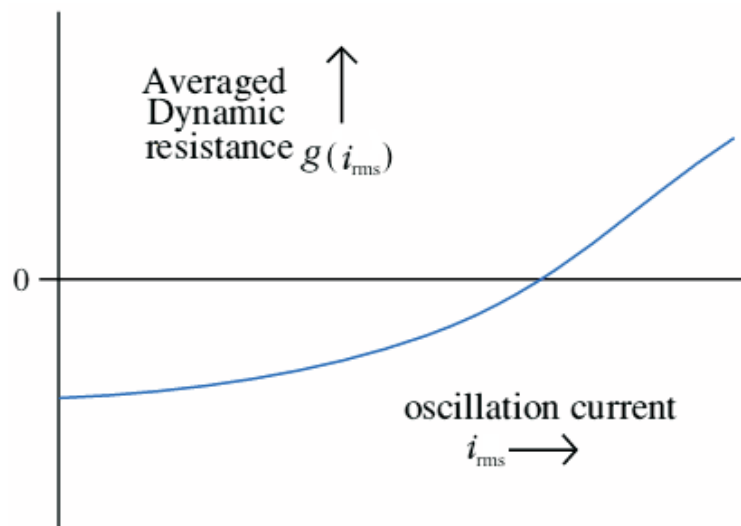


Figure 3.4: Average device resistance vs *rms* oscillation current.

The steady oscillation amplitude will be determined by the particular size of the current/voltage oscillation for which the condition $R_L + g(i_{rms}) = 0$ is satisfied (no energy dissipation, amplitude unchanged): hence the system becomes

simply an LC circuit oscillating with angular frequency $\omega = (LC)^{-1/2}$.

As said before, the oscillatory power P_0 generated by the negative resistance oscillator comes from the DC bias power, $P_{in} = i_{rms}V_{bias} \geq P_0 \geq 0$, where the last inequality ensures that we are always providing bias power into the system: this means that the mean current and voltage must always have the same sign, so that the static resistance is always be positive. In practice the amount of power we can get from the oscillator will depend on how large a range of voltages and currents the negative resistance region covers. Referring to fig. 3.1, we expect that:

$$P_0 < [V_{valley} - V_{peak}] [i(V_{peak}) - i(V_{valley})] . \quad (3.4)$$

3.2.2 The Resonant Cavity

The oscillation cavity is usually a metallic coaxial cavity, typically a short piece of coaxial cable, which provides the resonant effect. A typical oscillator is shown in fig. 3.5. The size of this cavity determines the time/phase delay which sets the resonant frequency.

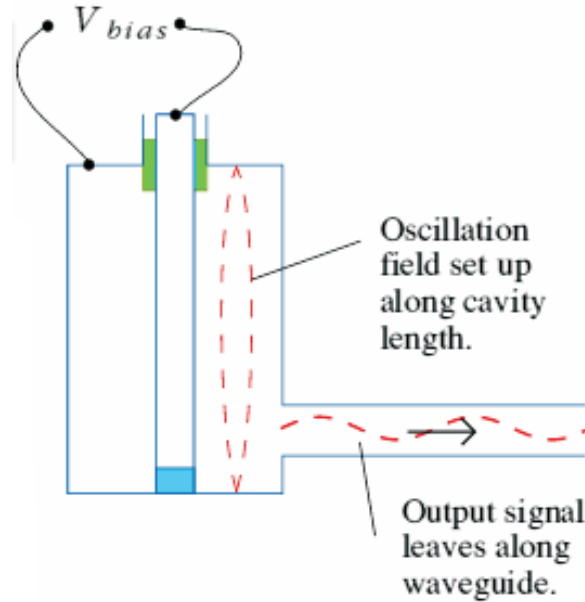


Figure 3.5: Typical mm-wave coaxial cavity of a Gunn oscillator.

In this case, each diode-induced fluctuation travels up the cavity and reflected from the far end, returning to the diode after a time $\Delta t = 2l/c$, where l is

the length of the cavity. Therefore an oscillation can only take place at those frequency such that $\nu_n = nc/2l$, where n is the number of half-waves fitting into the cavity at a given frequency. In practice, the diode has a finite response time Δt_d to react to any change in the voltage across it. Since the diode needs Δt_d for a voltage increase and Δt_d for a decrease, we can't expect it to oscillate at a frequency greater than about $\nu_{max} = (2\Delta t_d)^{-1}$. This means that the oscillator can only operate at frequencies such that:

$$\frac{c}{2l} \leq \nu_n \leq \nu_{max} = \frac{1}{2\Delta t_d} \quad \longrightarrow \quad 1 \leq n \leq \frac{l}{c\Delta t_d}, \quad (3.5)$$

that is the maximum possible oscillation frequency is determined by the response time of the diode. Using the shortest possible cavity length, $l \sim c\Delta t_d$, we force the system to oscillate at the only possible mode $n = 1$ (see eq. 3.5): it cannot neither oscillate at a lower frequencies, because the cavity is too short to permit it, nor at a higher frequencies, because the diode is too slow, hence we are ensuring a narrow bandwidth in the oscillation frequency. Real Gunn devices have a response time which varies with the applied voltage, hence we can electronically tune the oscillation frequency by slightly adjusting the bias voltage, changing Δt_d and hence altering ν_n . Alternatively it's possible to adjust the size of the resonant cavity, by means of micrometric screws (typically two, called "Tuning Mic" and "Backshort"), again providing the fine frequency tuning (see eq. 3.5).

The arguments presented above tell us the fundamental oscillation frequency. However, the system will also generate power at harmonics of this frequency³. This property of harmonics production is useful. Conventional GaAs Gunn devices can't oscillate above about 65 GHz, and yet they are commonly used as 90-140 GHz sources. These mm-wave oscillators extract the first harmonic from an oscillator which is actually oscillating at half the observed output frequency. Appendix C is entirely concerned about the specifications of the two 78-114 GHz and 120-147 GHz Gunn oscillators used in this work.

We can now understand the definition of a Gunn oscillator as a coherent microwave and mm-wave source (par. 3.2): the oscillations are generated with the same frequency and phase. However we should of course consider that propagation out of the oscillator can produce some loss of coherence: for electromagnetic waves, the coherence time is usually defined as the time over which a propagating wave may be considered coherent or, in other words, it is the time within which its phase is, on average, predictable. More formally, it is defined as the time over which the field correlation (or coherence) function $g(\tau)$

³The harmonic of a wave is a component frequency of the signal that is an integer multiple of the fundamental frequency, i.e. 2ν , 3ν , 4ν , etc. The harmonics are all periodic at the main signal frequency, and due to the properties of Fourier series, the sum of the signal and its harmonics is also periodic at that frequency.

decays. We have:

$$g(\tau) = \frac{\langle E^*(t)E(t+\tau) \rangle}{\langle E^*(t)E(t) \rangle}, \quad (3.6)$$

where $E(t)$ is the complex electric field at a certain location. This function is 1 for $\tau = 0$ and usually decays monotonically for larger time delays τ . For an arbitrary shape of this function, the coherence time can be defined by:

$$\tau_{coh} = \int_{-\infty}^{+\infty} d\tau |g(\tau)|^2. \quad (3.7)$$

In case of an exponential coherence decay, this is the same as the exponential decay time, i.e. $\propto e^{-t/\tau_{coh}}$, and the spectrum has a Lorentzian shape $(1 + \nu^2)^{-1}$, with a FWHM frequency bandwidth of the source given by $\Delta\nu = (\pi\tau_{coh})^{-1} \rightarrow \tau_{coh} = (\pi\Delta\nu)^{-1}$. Instead of the coherence time, the coherence length L_{coh} is often used, which is simply the coherence time times the velocity of light in the medium $L_{coh} = c(n\tau_{coh})^{-1}$ (n is the refractive index of the medium), and thus also quantifies temporal (rather than spatial) coherence.

3.3 Gaussian Optics and Beams of Radiation

In this section we briefly introduce some elements of Gaussian optics, focusing on the characterization of Gaussian beams of radiation in free space (see [74] for a complete treatment). This will be useful to better understand the transition of the signal from the resonant cavity to the waveguide and then to the feed horn, but also in the analysis of beam coupling when we'll discuss about the telescope (chapter 5). Here we are dealing with the free space propagation of beams of electromagnetic radiation, approximately collimated, with transverse size of the order of some wavelengths, that's why this approach is the best one in the far-infrared, microwave and mm-wave regions of the electromagnetic spectrum: it lies between geometric optics ($\lambda \rightarrow 0$) with optical components much bigger in size than λ , and physical optics, dealing with sources smaller in size with respect to λ .

3.3.1 Fundamental Gaussian Beam Mode

Let us consider a beam propagating along the z -axis. In Gaussian optics the electric field has a Gaussian distribution in the plane orthogonal to z . At each point on the axis of propagation a Gaussian beam can be described by the width of the beam w (*beam radius*), defined as the distance from the z -axis at which the electric field becomes $1/e \simeq 0.3679$ of its maximum value. Moreover

it's possible to define the *radius of curvature* R of a beam, defining the surfaces of equal phase, that coincides with the actual propagation distance only in the far field approximation ($R \rightarrow \infty$, plane wave). Finally a Gaussian beam cannot be focused in a point (or cannot have a point origin), instead it only can have a region of minimal dispersion, called *beam waist*, of size depending on the wavelength, where R is assumed to be infinite. Each single component (x, y, z) of the vector fields \vec{E} (electric field) and \vec{H} (magnetic field) composing an electromagnetic wave propagating in a uniform medium, has to satisfy the Helmholtz equation⁴:

$$(\nabla^2 + k^2) (x, y, z) = 0 , \quad (3.8)$$

where $k = 2\pi/\lambda$ is the absolute value of the wavevector \vec{k} , as usual. For a plane wave, the amplitudes of the electric and magnetic fields are constant and their directions are mutually perpendicular and also perpendicular to the propagation vector. For a beam of radiation that is similar to a plane wave but which is allowed to have some variation perpendicular to the axis of propagation, we can still assume that the electric and magnetic fields are mutually perpendicular and also perpendicular to the direction of propagation. Writing the distribution for any component of the electric field as $E(x, y, z) = u(x, y, z)e^{-ikz}$ (u is a complex scalar function containing the non-plane part of the beam) and substituting it in eq. 3.8, we get:

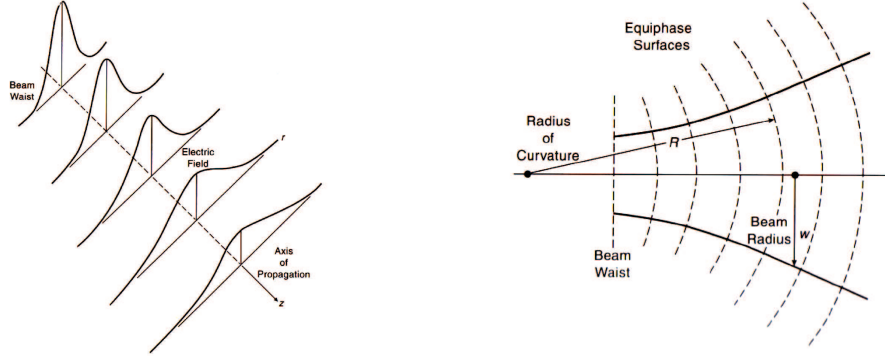
$$\frac{\partial^2 E}{\partial x^2} + \frac{\partial^2 E}{\partial y^2} + \frac{\partial^2 E}{\partial z^2} + k^2 E = 0 \quad \Rightarrow \quad \frac{\partial^2 u}{\partial x^2} + \frac{\partial^2 u}{\partial y^2} + \frac{\partial^2 u}{\partial z^2} - 2ik \frac{\partial u}{\partial z} = 0 . \quad (3.9)$$

Now if the variation of u along z can be considered negligible with respect to the variations along x and y , the third term in eqs. 3.9 disappears and the problem is thus best described in cylindrical coordinates (r, φ, z) . The axial symmetry requires $u(r, \varphi, z) = u(r, z)$ and so we get:

$$\frac{\partial^2 u}{\partial r^2} + \frac{1}{r} \frac{\partial u}{\partial r} - 2ik \frac{\partial u}{\partial z} = 0 \quad \Rightarrow \quad u(r, z) = A(z)e^{-\frac{ikr^2}{2q(z)}} , \quad (3.10)$$

where A and q are complex functions of z , while $u(r, z)$ looks like the well-known Gaussian profile. The one in eq. 3.10 is the simplest possible solution, called *fundamental Gaussian beam mode*, but there are higher order Gaussian beam mode solutions that will be briefly discussed in the next section, for their importance in waveguides and feed horns also. It's now possible to get the

⁴The Helmholtz equation is the time-independent form of the original wave equation, $(\nabla^2 - \frac{1}{c^2} \frac{\partial^2}{\partial t^2}) (\vec{r}, t) = 0$, resulting from variables separation technique.



(a) Variation of beam radius and peak amplitude during the propagation. (b) Section of the Gaussian beam, showing equiphase surfaces, beam radius w and radius of curvature R .

Figure 3.6: Schematic diagrams of Gaussian beam propagation along the z -axis.

expressions for A and q by inserting eq. 3.10 in eq. 3.9:

$$-2ik \left(\frac{\partial A}{\partial z} + \frac{A}{q} \right) + \frac{k^2 r^2 A}{q^2} \left(\frac{\partial q}{\partial z} - 1 \right) = 0 \quad \Rightarrow \quad \frac{\partial q}{\partial z} = 1, \quad \frac{\partial A}{\partial z} = -\frac{A}{q}. \quad (3.11)$$

We first analyze the complex function $q(z)$: from eq. 3.11 it's easy to see that its solution is $q(z) = q(0) + z$. Since in eq. 3.10 it appears as q^{-1} , we can make the decomposition $q^{-1} = \Re e(q^{-1}) - i \Im m(q^{-1})$, so that from eq. 3.10 the exponential argument now reads as:

$$\left(-\frac{ikr^2}{2q} \right) = \left[\left(\frac{-ikr^2}{2} \right) \Re e \left(\frac{1}{q} \right) - \left(\frac{kr^2}{2} \right) \Im m \left(\frac{1}{q} \right) \right]. \quad (3.12)$$

The imaginary part of the argument has the form of a phase variation, relative to a reference plane of a plane wave for a fixed value of z , produced by the spherical wave front tangent to that reference plane: in the limit $R \gg r$, the phase delay can be evaluated as:

$$\phi(r) \simeq \frac{\pi r^2}{\lambda R} = \frac{kr^2}{2R} \quad \Rightarrow \quad \Re e \left(\frac{1}{q(z)} \right) = \frac{1}{R(z)}. \quad (3.13)$$

Now the second term in eq. 3.12 is real and Gaussian in shape: having defined the beam radius $w = w(z)$ as the distance from the z -axis at which the electric field becomes $1/e$ of its maximum, it turns out that:

$$\frac{1}{q(z)} = \frac{1}{R(z)} - \frac{ikr^2}{2} = \frac{1}{R(z)} - \frac{i\lambda}{\pi w^2(z)} \quad \Rightarrow \quad \Im m \left(\frac{1}{q(z)} \right) = \frac{\lambda}{\pi w^2(z)}. \quad (3.14)$$

The beam waist at $z = 0$ is $w_0 = \sqrt{-i\lambda q(0)/\pi}$. Then from eq. 3.10 we get:

$$u(r, 0) = u(0, 0) e^{-\frac{r^2}{w_0^2}} \Rightarrow q(z) = \frac{i\pi w_0^2}{\lambda} + z, \quad (3.15)$$

where w_0 is thus the *beam waist radius*. From eqs. 3.14 and 3.15 we have:

$$R(z) = z + \frac{z_R^2}{z} \quad \text{and} \quad w(z) = w_0 \sqrt{1 + \left(\frac{z}{z_R}\right)^2}, \quad \text{where} \quad z_R = \frac{\pi w_0^2}{\lambda} \quad (3.16)$$

is called *Rayleigh range*. The beam waist radius w_0 is the minimum possible value for the beam radius w , for $R \rightarrow \infty$ (plane wave). We can now find from eq. 3.11 the expression for $A(z)$: since $dq = dz$, it turns out that $dA/A = -dq/q$, and from eq. 3.15 we obtain:

$$\frac{A(z)}{A(0)} = \frac{1 + iz/z_R}{1 + (z/z_R)^2} \Rightarrow \frac{A(z)}{A(0)} = \frac{w}{w_0} e^{i\phi_0}, \quad (3.17)$$

where we have defined the *Gaussian beam phase shift* $\phi_0 = \arctan(z/z_R)$. The electric field is:

$$E(r, z) = \frac{w_0}{w} e^{\Upsilon(r, z)} \quad \text{with} \quad \Upsilon(r, z) = -\frac{r^2}{w^2} - ikz - \frac{i\pi r^2}{\lambda R} + i\phi_0. \quad (3.18)$$

In order to find the total power in a propagating Gaussian beam, we assume again that the electric and magnetic field components are related to each other like those in a plane wave. The total power is thus proportional to the square of the electric field integrated over the area of the beam. Hence we require the normalization $2\pi \int_0^\infty |E(r, z)|^2 r dr = E_0^2$, and eq. 3.18 becomes $E(r, z) = E_0 \sqrt{2} (\pi w^2)^{-1/2} e^{\Upsilon(r, z)}$. The corresponding time-averaged intensity is, from eq. A.10:

$$I(r, z) = \frac{cn\epsilon_0}{2} |E(r, z)|^2 = \frac{cn\epsilon_0 E_0^2}{\pi w^2} e^{-\frac{2r^2}{w^2}}, \quad (3.19)$$

while the power P passing through a circle of radius r in the transverse plane at position z is:

$$P(r, z) = 2\pi \int_r^0 \frac{cn\epsilon_0 E_0^2}{\pi w^2} r' dr' e^{-\frac{2r'^2}{w^2}} = P_0 \left(1 - e^{-\frac{2r^2}{w^2}}\right), \quad (3.20)$$

where $P_0 = cn\epsilon_0 E_0^2/2$ is the total power transmitted by the beam.

Let us spend now some words about what are usually referred as *near field* ($z \ll z_R$) and *far field* ($z \gg z_R$). At the beam waist, the beam radius w attains

its minimum value w_0 , and the electric field distribution is most concentrated, as clearly shown in fig. 3.6. The phase shift ϕ_0 at the beam waist is zero by definition, since the phase front is planar ($R \rightarrow \infty$). Away from the beam waist, the beam radius increases monotonically, with hyperbolic behaviour in z (eq. 3.16). In the near field the beam radius is essentially unchanged from its value at the beam waist, $w \leq \sqrt{2}w_0$. We can therefore say that the Rayleigh range defines the distance over which the Gaussian beam propagates without significant growth, remaining collimated. In the far field limit $z \gg z_R$ we see from eq. 3.16 that the beam radius grows linearly with distance. The growth of the $1/e$ radius of the electric field can be defined in terms of the angle $\theta = \arctan(w/z)$, which in the far field limit becomes:

$$\theta_0 = \lim_{z \gg z_R} \left[\arctan \left(\frac{w}{z} \right) \right] = \arctan \left(\frac{\lambda}{\pi w_0} \right) \sim \frac{\lambda}{\pi w_0}, \quad (3.21)$$

called *asymptotic beam growth angle*. In the far field the electric field distribution is best described as a function of angle-away from the propagation axis, that just turns out to be Gaussian in θ :

$$\frac{E(\theta)}{E(0)} = e^{-\left(\frac{\theta}{\theta_0}\right)^2}. \quad (3.22)$$

If a source (or a detector) has a maximum overall dimension D , large as compared to the wavelength, the far field region is commonly taken to occur at distances greater than $2D^2/\lambda$ from it.

3.3.2 Higher Order Gaussian Beam Mode Solutions

As previously anticipated, in order to introduce the discussion about waveguides and horns, we need to spend some effort in writing down the *higher order Gaussian beam mode solutions*, whose beam radius and radius of curvature behave as those of the fundamental mode, while their phase shifts are different. We again work in cylindrical coordinates, but this time we no longer assume axial symmetry, i.e. a general solution must allow variations of the electric field as a function of the polar angle φ . Moreover there will be terms with additional radial variation as well as the pure Gaussian profile. A possible solution is:

$$u(r, \varphi, z) = A(z)S(r) e^{i\left(n\varphi - \frac{kr^2}{2q(z)}\right)}, \quad (3.23)$$

where the complex amplitude $A(z)$ and the complex beam parameter $q(z)$ depend only on distance along the propagation axis, $S(r)$ is an unknown radial function and n is an integer. Assuming the same form for $q(z)$ as for the fundamental mode, it's possible to solve eq. 3.10 (which now must also include

the term $\frac{1}{r} \frac{\partial^2 u}{\partial \varphi^2}$, and find (normalizing at $E_0 = 1$):

$$\begin{aligned}
E_{m,n}(r, \varphi, z) &= \sqrt{\frac{2m!}{\pi(m+n)!}} \frac{1}{w(z)} \left(\frac{\sqrt{2}r}{w(z)} \right)^n L_{m,n} \left(\frac{2r^2}{w^2(z)} \right) e^{\Upsilon_{m,n}} e^{in\varphi}, \\
\Upsilon_{m,n}(r, z) &= -\frac{r^2}{w^2(z)} - ikz - \frac{i\pi r^2}{\lambda R(z)} - i\phi_0(z)(2m+n+1), \quad (3.24)
\end{aligned}$$

where $E_{m,n}$ is the mn *Gaussian beam mode*. In the Gaussian beam context n is the angular index, while m (also an integer) is the radial index: the generalized Laguerre polynomials $L_{m,n}(x)$ are also defined in terms of these two indices:

$$L_{m,n}(x) = \frac{e^x x^{-n}}{m!} \frac{d^m}{dx^m} (e^{-x} x^{m+n}) \quad \text{or} \quad L_{m,n}(x) = \sum_{l=0}^m \frac{(m+n)! (-x)^l}{(m+l)! (m-l)! l!}.$$

We can now step back and select only axially symmetric φ -independent modes by setting $n = 0$, obtaining:

$$E_{m,0}(r, z) = \sqrt{\frac{2}{\pi w^2(z)}} L_{m,0} \left(\frac{2r^2}{w^2(z)} \right) e^{\Upsilon_{m,0}}. \quad (3.25)$$

3.4 Waveguides

At low frequencies (up to about 1 GHz) electromagnetic signals are carried over short distances using metal wires. The energy is carried by the electromagnetic fields which link and surround the wires. Normal metal wiring only works well in guiding electromagnetic waves when the dimensions of the wires and the distances between them are much smaller than the free space wavelength of the signals. As we progress to higher frequencies there is a tendency for wires to act as antennas and allow the signals to radiate away instead of guiding them from place to place. At microwave and millimetric wavelengths the solution to this problem are metallic waveguides. A normal wire consists of a strip of conductor surrounded by free space or dielectric: fields radiating away from the wire are lost. A standard microwave guide consists instead of a strip of space or dielectric surrounded by a metal pipe: the electromagnetic fields propagate inside the pipe by subsequent reflections. The field pattern which exists in the pipe must obey Maxwell's Equations and the appropriate boundary conditions: the electric field component in the plane of the metal surface must always be zero. In the case of a rectangular pipe of the type illustrated in fig. 3.7 it is

possible to find a series of solutions for the electric field components in terms of the m, n indices defined in par. 3.3.2. From eq. 3.24, imposing the boundary conditions, it's possible to show that the unity-normalized electric and magnetic field components, in cartesian coordinates, are:

$$E_{m,n}^x = \frac{Z_0 k_0}{\beta_{m,n}} H_{m,n}^y = -\frac{i Z_0 k_0 n \pi}{k_{m,n}^2 b} \cos\left(\frac{m\pi x}{a}\right) \sin\left(\frac{n\pi y}{b}\right) e^{-i\beta_{m,n} z}, \quad (3.26)$$

$$E_{m,n}^y = -\frac{Z_0 k_0}{\beta_{m,n}} H_{m,n}^x = \frac{i Z_0 k_0 m \pi}{k_{m,n}^2 a} \sin\left(\frac{m\pi x}{a}\right) \cos\left(\frac{n\pi y}{b}\right) e^{-i\beta_{m,n} z}, \quad (3.27)$$

$$E_{m,n}^z = H_{m,n}^z = 0, \quad (3.28)$$

$$k_{m,n}^2 = \left(\frac{m\pi}{a}\right)^2 + \left(\frac{n\pi}{b}\right)^2 \quad \text{and} \quad \beta_{m,n} = \sqrt{k_0^2 - k_{m,n}^2}, \quad (3.29)$$

where a and b are the sides of the rectangular guide (fig. 3.7), $Z_0 = \sqrt{\mu_0/\epsilon_0} = 376.7 \Omega$ is the impedance of free space, z is the propagation axis and $k_0 = 2\pi/\lambda$. This set of solutions are called the TE-modes where TE here stands for Transverse Electric since the electric field vector is always transverse to the long axis of the guide. In fact there is another similar set of solutions, the TM-modes, which have transverse magnetic field vector. The values of m, n determine the shape of the field distribution across the guide: each choice of m, n represents an independent valid solution of Maxwell's equations. In general the fields in the guide are a linear superposition of these modes, i.e. $E = \sum_{m,n} a_{m,n} E_{m,n}$, where $E_{m,n}$ are defined in eqs. 3.26, 3.27, 3.28, and the $a_{m,n}$ are a set of complex coefficients which determine the relative amplitudes and phases of each modal contribution to the total field. The condition for a mn mode to propagate along the guide is that $\beta_{m,n}$ (eq. 3.29) must be real, while an imaginary value would imply exponential variation with z , i.e. no propagation. Combining the expressions of $k_{m,n}^2$ and $\beta_{m,n}$, we find that, in order for the signal to propagate, its frequency must be greater than (or equal to) the so-called *cut-off frequency*:

$$\nu_{mn}^{co} = \frac{c}{2} \sqrt{\frac{m^2}{a^2} + \frac{n^2}{b^2}} \quad \Rightarrow \quad \lambda_{mn}^{co} = 2 \left(\frac{m^2}{a^2} + \frac{n^2}{b^2} \right)^{-1/2}. \quad (3.30)$$

Standard rectangular microwave guides have a 2:1 aspect ratio ($a = 2b$): table 3.2 shows the relative cut-off wavelengths of the first few modes in a standard rectangular waveguide. From these values we argue that in a standard waveguide no TE_{mn} modes exist for wavelengths longer than $\lambda_{10}^{co} = 2a$, hence this is the wavelength of the lowest signal frequency which a given size of guide can carry: the guide behaves as a high-pass filter with cut-off frequency ν_{mn}^{co} . This means that in between the wavelengths $\lambda = 2a$ and $\lambda = a = \lambda_{20}^{co} = \lambda_{01}^{co}$ only one mode (TE_{10}) can propagate: in this region the behaviour of the guide is

said to be *single mode*.

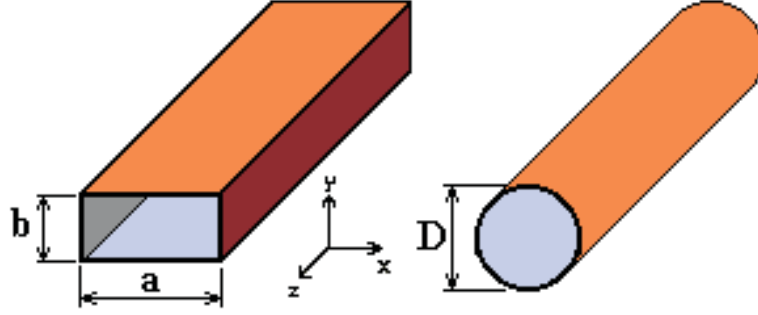


Figure 3.7: Rectangular and circular microwave guides. The fields propagate in the z direction. The rectangular waveguide has the a side along the x -axis, while b is along y .

λ_{mn}^{co}/a	$m = 0$	$m = 1$	$m = 2$	$m = 3$
$n = 0$	∞	2	1	0.6666
$n = 1$	1	0.8944	0.7071	0.5477
$n = 2$	0.5	0.4850	0.4	0.3535
$n = 3$	0.3333	0.3288	0.3162	0.2981

Table 3.1: Relative cut-off wavelengths of TE_{mn} modes in a standard waveguide.

As a result we can say that, anywhere along the guide, the TE_{10} mode field will be:

$$E_{1,0}^y = -\frac{Z_0 k_0}{\beta_{1,0}} H_{1,0}^x = \frac{i Z_0 k_0 \pi}{k_{1,0}^2 a} \sin\left(\frac{\pi x}{a}\right) e^{-i\beta_{1,0} z}, \quad (3.31)$$

$$E_{1,0}^x = H_{1,0}^y = E_{1,0}^z = H_{1,0}^z = 0, \quad (3.32)$$

$$k_{1,0}^2 = \frac{\pi^2}{a^2} \quad \text{and} \quad \beta_{1,0} = \sqrt{k_0^2 - \frac{\pi^2}{a^2}}. \quad (3.33)$$

From eqs. 3.31 and 3.32 it clearly results that, as long as the Gaussian optics treatment is valid, the signal out of such a waveguide has non-zero electric

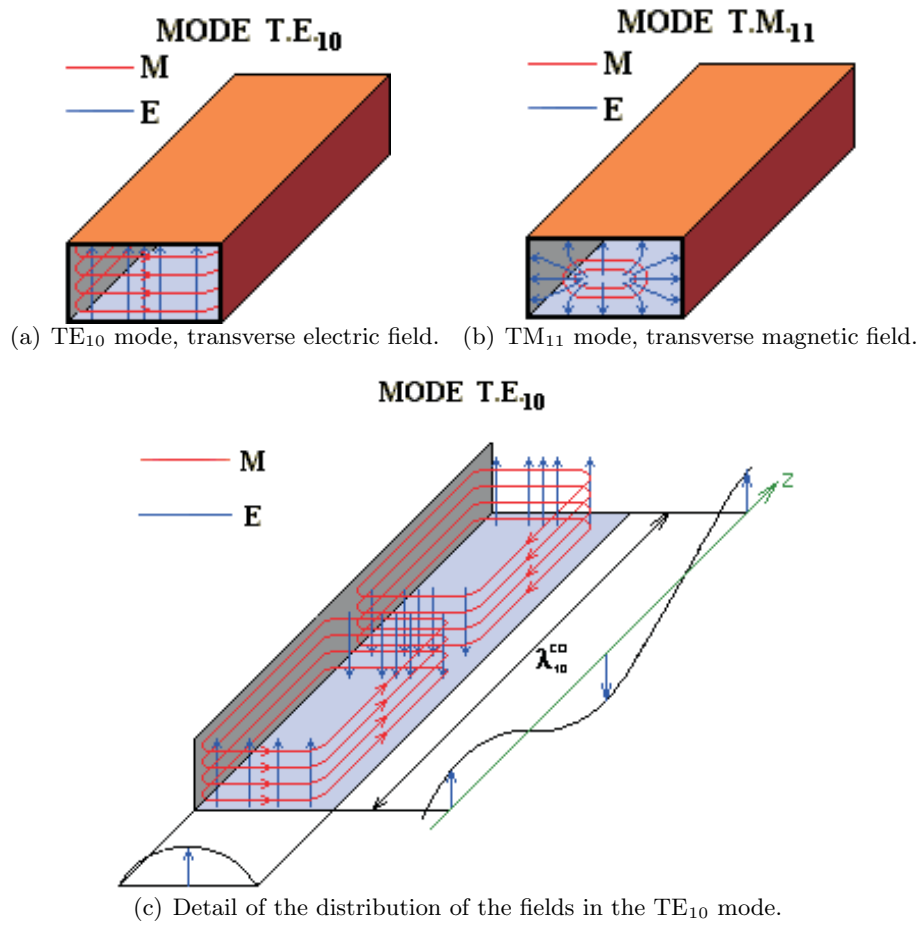


Figure 3.8: Distribution of the electric and magnetic fields inside a rectangular waveguide in the TE₁₀ and TM₁₁ modes.

field component only along the y -axis (along the b side), while non-zero magnetic field component is along the x -axis (along the a side). In other words we are dealing with a signal that is fully polarized along the shortest side of the waveguide (see Appendix A for polarization basics). This is exactly the case for the waveguides used to direct out the signal from the two Gunn oscillators described in Appendix C. In tab. 3.2 we resume the significant specifications for the standard waveguides WR-6, WR-8 and WR-10 (see Appendix D for details: note that waveguides are mounted on flanges as mechanical supports). A similar analysis of the TM-mode family reveals that the field expressions are identically zero if either m or n is zero, leading to the conclusion that TM₁₁ is the lowest possible TM mode and so none of these modes can propagate for wavelengths above $\lambda_{11}^{co} = 0.8944a$. Finally, it's worth to say that the propagation constant $\beta_{m,n}$ determines how quickly the field phase varies along the guide: for this reason it is sometimes called the *phase rate* or *phase*

velocity. Its value depends upon the mode numbers (eq. 3.29), i.e. different modes propagate along the guide with different velocities. A *multi-mode* field, composed of a linear superposition of various modes, will therefore produce a total field pattern which varies along the guide as the components move in and out of phase. Some modes will also carry power along the guide quicker than others. This tends to smear out any information-carrying modulations of the field. Multi-mode fields are therefore usually undesirable, using the guide in the single mode range allows us to avoid these problems.

Frequency Band	Standard	Frequency Limits (GHz)	Inside Dimensions (mm)
W band	WR-10	75 to 110	$a = 2.54, b = 1.27$
F band	WR-8	90 to 140	$a = 2.032, b = 1.016$
D band	WR-6	110 to 170	$a = 1.651, b = 0.826$

Table 3.2: Standard waveguides frequency bands and interior dimensions.

3.5 Feed Horns

An antenna is a device that accepts radiation propagating in a transmission line and transforms it to a beam propagating in free space, or vice versa. Almost all antennas of interest at our wavelengths are *aperture antennas*, which produce an electric field distribution over an aperture that is in size greater than or at least equal to the wavelength, that is their function is to produce a uniform phase front with a larger aperture than that of the coupled waveguide. In the following we'll make use of the reciprocity theorem [70], considering equally well a forward and a backward mode for antenna operations. Apropos of this, we anticipate that radiation detectors use at millimeter and sub-millimeter wavelengths are usually single-mode devices, in the sense described in the previous section. What is thus critical is not the actual detector itself (see par. 3.6), but its coupling to free space by means of the feed horn. The majority of feed horns couple to a beam of radiation that is reasonably well represented by a single Gaussian beam mode, thus we can represent a detector system as having an equivalent Gaussian beam waist (par. 3.3.1) at a specified location.

The horns can be substantially divided in rectangular and circular horns, the former powered by rectangular waveguides, the latter by circular waveguides. In this work we are mostly dealing with rectangular horns: in fact only one circular (corrugated) horn has been used for the beam measurements of OLIMPO telescope at 90 GHz (see chapter 5), for its optimal beam coupling with the telescope, while another circular (corrugated) horn has been tested at 137 GHz in order to understand the beam profile out of it, for providing optimal coupling

with the OLIMPO telescope as well. We will show the results at the end of this section (a picture of the circular horn at 137 GHz is shown in Appendix F), but we shall not focus here neither on circular nor on corrugated feed horns. However it's important to notice that such circular horns were both provided of adequate transitions between their circular waveguides and the two rectangular waveguide standards WR-10 (90 GHz), WR-6 (137 GHz) for coupling with the diodes (par. 3.6).

The rectangular horns are generally made with straight flares: if the flare is only in one dimension they are said to be *sectoral*. Assuming a TE₁₀ mode out of the waveguide (see par. 3.4) with electric field only along the y direction, the *sectoral H-plane* horn is flared out in a plane perpendicular to \vec{E} , i.e. in the plane of the magnetic field \vec{H} . If instead the horn is flared out in the \vec{E} plane, it is called *sectoral E-plane* horn. Finally a rectangular horn with flare in both planes is called *pyramidal horn*: with a TE₁₀ wave out of the waveguide, the magnitude of the electric field is quite uniform in the y direction across the aperture of such a horn, but tapers to zero in the x direction across the aperture. For small flare angles the field variation across the aperture of the horn is similar to the sinusoidal distribution of the TE₁₀ mode across the waveguide (eq. 3.31). We can now go back to our Gaussian approach when describing the resulting beam out of a generic feed horn, then we will focus on the pyramidal horns used in this work. It's easy to invert the expressions in eq. 3.16, to obtain the characteristic parameters of a feed horn:

$$w_0 = w \left[1 + \left(\frac{\pi w^2}{\lambda R} \right)^2 \right]^{-1/2} \quad \text{and} \quad z = R \left[1 + \left(\frac{\lambda R}{\pi w^2} \right)^2 \right]^{-1}. \quad (3.34)$$

The meaning of these two quantities becomes clearer looking at fig. 3.10: the waist offset z tells us that the Gaussian beam out of a feed horn does not generate exactly at the edge of the antenna, but somewhat inside it. It turns out to be very important to take into account this offset when working with focusing elements, such as an optics box (as we'll see in par. 5.4). The waist radius w_0 is also important when comparing the declared gain of the antenna with effective measured beamwidth (see later). We can now focus on pyramidal horns and state that for independent expansion of the fields in the two perpendicular coordinates, optimum coupling to a horn with aperture dimensions a_H, a_E (fig. 3.9) is obtained for $2w_x = 0.35 a_H$ and $2w_y = 0.5 a_E$ (see [74] for details). The resulting fundamental mode Gaussian beam is thus asymmetric, but this turns out not to be a problem, since propagation in the two orthogonal planes is independent. Moreover the beam waist will be located at different distances behind the aperture (eq. 3.34). The beam becomes symmetric when a particular ratio of E plane to H plane widths is attained, $a_H/a_E = 0.7 \Rightarrow w_x = w_y$. Finally rectangular feed horns powered by TE₁₀ mode have ideal polarization

coupling, no cross polarization is introduced. This feature has been well measured to be zero with at least 0.1% precision by paralleling the source and the detector.

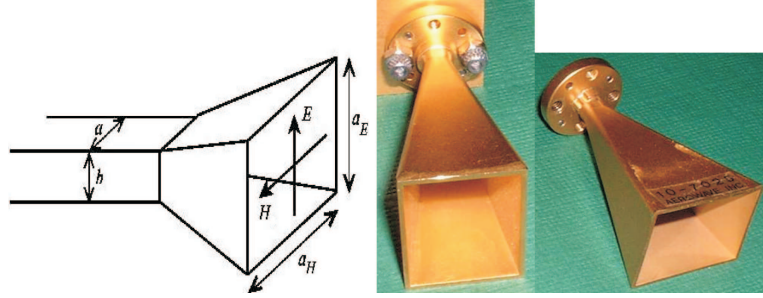


Figure 3.9: Pyramidal horn antennas.

In tab. 3.3 we show the significant parameters of the four feed horns used in this work, two with WR-10 waveguide, coupled to the 78-114 GHz Gunn oscillator and its respective WDH detector (see par. 3.6), the other two with WR-8 and WR-6 waveguides, coupled, respectively, to the 120-147 GHz Gunn oscillator and its respective DD detector. The external dimensions H , W and L of the horns refer to the drawing in Appendix F, while the gain (in dB⁵) is defined in Appendix E, together with the directivity of an antenna and its semi-angle of aperture α . Referring to fig. 3.10, we see that the beam out of the horn has radius of curvature R (eq. 3.34) which coincides with the horn slant length R_h . In order to evaluate the waist radii and offset, we need the effective aperture dimensions $a_H = 2w_x/0.35$ and $a_E = 4w_y$, which are slightly different from, respectively, W and H of tab. 3.3, because of the finite thickness of the pyramid walls, which are measured to be $(1.20 \pm 0.05)mm$ for WR-10 and WR-8 horns, while it is $(1.00 \pm 0.05)mm$ for the WR-6 horn. Moreover the evaluation of R_h requires some care because, as shown in fig. 3.10, we also need to take into account the finite dimensions of the waveguide and the thickness of the flange (since L in tab. 3.3 is comprehensive of these as well): using the drawings in Appendix D and doing some trigonometry we get the values shown in tab. 3.3.

⁵A decibel is defined in two equivalent ways: when referring to measurements of power or intensity it is $X_{dB} = 10 \log_{10} \left(\frac{X}{X_0} \right)$, while when referring to measurements of amplitude it is $X_{dB} = 20 \log_{10} \left(\frac{X}{X_0} \right)$, where X_0 is a specified reference with the same units as X .

Waveguide	Gain (dB)	2α ($^\circ$)	H (mm)	W (mm)	L (mm)
WR-10	25	12.89	(20.32 ± 0.05)	(26.16 ± 0.05)	(49.53 ± 0.05)
WR-8	25	12.89	(16.54 ± 0.05)	(21.34 ± 0.05)	(38.10 ± 0.05)
WR-6	25	12.89	(13.72 ± 0.05)	(17.53 ± 0.05)	(31.75 ± 0.05)
Waveguide	a_H, a_E (mm)		w_x, w_y (mm)		R_h (mm)
WR-10	$(23.76 \pm 0.07), (17.92 \pm 0.07)$		$(4.16 \pm 0.07), (4.48 \pm 0.07)$		(47.4 ± 0.1)
WR-8	$(18.94 \pm 0.07), (14.14 \pm 0.07)$		$(3.31 \pm 0.07), (3.54 \pm 0.07)$		(38.6 ± 0.1)
WR-6	$(15.53 \pm 0.07), (11.72 \pm 0.07)$		$(2.72 \pm 0.07), (2.93 \pm 0.07)$		(29.9 ± 0.1)
Waveguide	$w_{0,x}, w_{0,y}$ (mm) @137 GHz		z_x, z_y (mm) @137 GHz		
WR-10	$(3.68 \pm 0.07), (3.83 \pm 0.07)$		$(10.2 \pm 0.4), (12.8 \pm 0.4)$		
WR-8	$(3.07 \pm 0.07), (3.20 \pm 0.07)$		$(5.5 \pm 0.3), (6.9 \pm 0.3)$		
WR-6	$(2.56 \pm 0.07), (2.70 \pm 0.07)$		$(3.4 \pm 0.2), (4.3 \pm 0.2)$		

Table 3.3: Main parameters for the four Aerowave pyramidal feed horns used in this work (two WR-10). We refer to Appendix F for the drawing and the specifications.

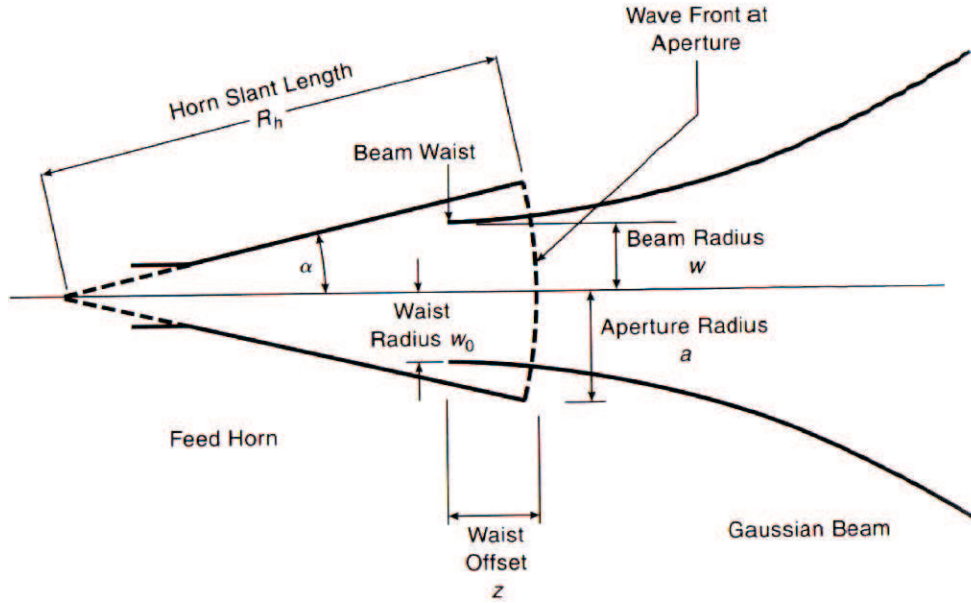


Figure 3.10: Cross-section of a feed horn and the Gaussian beam it produces.

Let us now spend a few words about uncertainties: in the case of single measurements (lengths, for example) the instrumental error is always taken as uncertainty associated to that single measure. In the case of multiple measure-

ments we take the mean value as best estimate: its associated uncertainty is the largest number between the standard deviation, divided by the square root of the number of measurements, and the instrumental error, while the uncertainty associated to the single measurement is of course simply the standard deviation. The propagation of such uncertainties through quantities which depend on several independent quantities (each with different uncertainty) is carried out by means of the usual partial derivatives formula:

$$\sigma(f[a_1, a_2, \dots, a_k, \dots, a_n]) = \sqrt{\sum_{k=1}^n \left(\frac{\partial f[a_1, a_2, \dots, a_k, \dots, a_n]}{\partial a_k} \right)^2 \sigma^2(a_k)}. \quad (3.35)$$

From now on, we'll always make use of this expression and thus it will be omitted in the following. The aperture angle 2α is defined in Appendix E as a function only of the directivity (gain): it's a first rough estimate of the cone into which the antenna is able to concentrate a beam of radiation. What really happens with pyramidal horns is that the beam is not symmetric along the two orthogonal planes, and the resulting FWHM will be slightly different for the H and E planes. We present here the results of the measurements of the beam of the two horns coupled to the detectors, i.e. the one with WR-6 and one of the two with WR-10. For the WR-6 horn, the measurements were made contextually with the OLIMPO telescope beam measures (chapter 5), while the WR-10 horn had been previously used by Cecilia Marini Bettolo and Federico Nati for laboratory polarimetry tests, so we just limit ourselves to use their result [78]. In both cases the measurements were simply made by positioning the detector in the far field of the source (Gunn oscillators plus coupled horn, without any additional focusing element), which results to be a very short distance, of the order of few meters or less (see the end of par. 3.3.1). In this situation we can simply perform the scans moving the detector (coupled to horn we want to investigate) in elevation with fixed and optimized azimuth, or in azimuth with fixed and optimized elevation, provided that the transmitting and receiving horns have the same orientation. In our case the H plane (longer side) is always kept perpendicular to the ground (elevation), while the E plane (shorter side) is parallel to the ground (azimuth). We postpone to the following sections the details about detectors, electronics, attitude control system and data acquisition, giving directly the final results of these measurements (figs. 3.11, 3.12 and tabs 3.4, 3.5). As previously anticipated we also used a circular corrugated feed horn for the beam measurements of OLIMPO telescope at 90 GHz (see chapter 5), for its optimal beam coupling with the telescope. We do not focus on the details of circular corrugated feed horns, for which of course the beam is assumed to be symmetric: we limit ourselves to shown here the results of our measurements (fig. 3.13 and tab. 3.6). We also tested a circular corrugated feed horn at 137 GHz in order to understand the beam profile out

of it for providing optimal coupling with the OLIMPO telescope (fig. 3.14 and tab. 3.7).

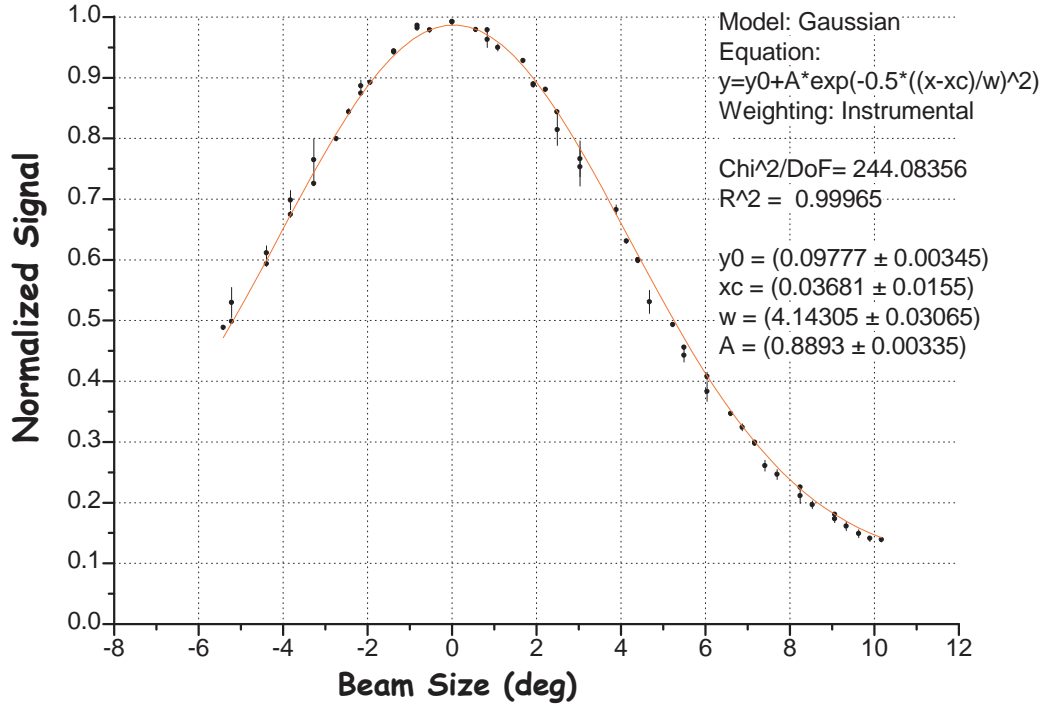


Figure 3.11: Beam measurements of the WR-6 horn along the H plane. The scan is performed varying the elevation, while the optimized azimuth is kept fixed. Each experimental point is the mean value upon 10 measures, displayed with the associated uncertainty. The red line is the Gaussian fit, whose parameters are shown.

Plane	Coordinate	Gaussian SD (°)	FWHM (°)
H	elevation	(4.14 ± 0.03)	(9.75 ± 0.07)
E	azimuth	(4.02 ± 0.01)	(9.47 ± 0.03)

Table 3.4: Measured beamwidth for the WR-6 pyramidal feed horn in both H and E planes (see figs. 3.11 and 3.12).

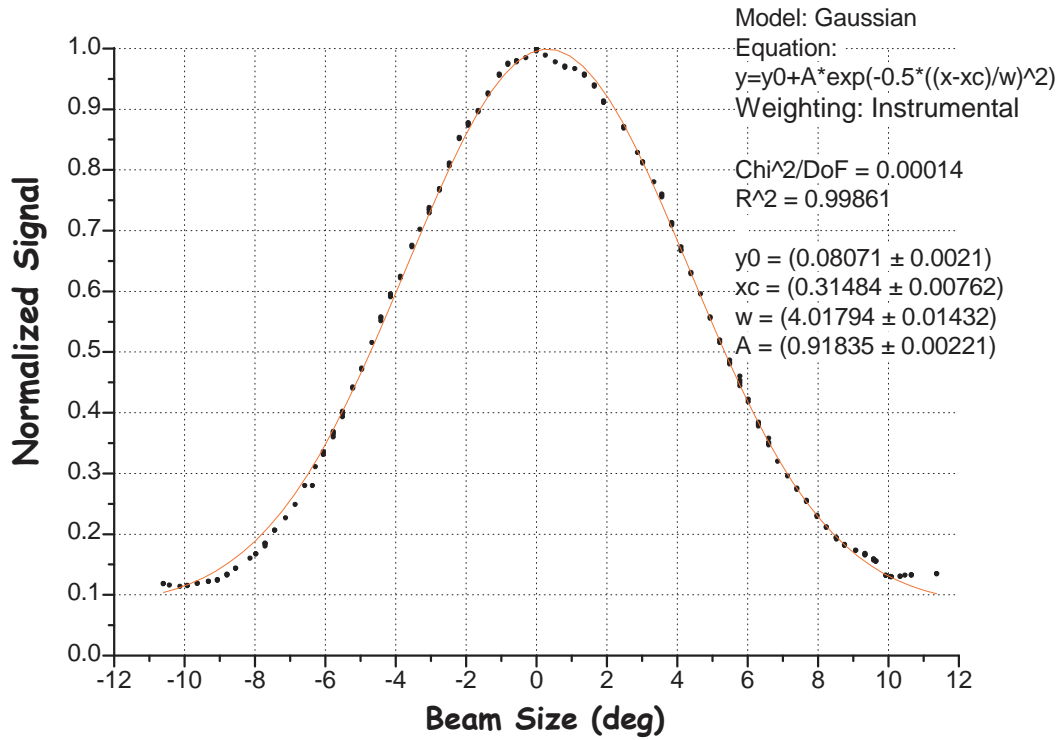


Figure 3.12: Beam measurements of the WR-6 horn along the E plane. The scan is performed varying the azimuth, while the optimized elevation is kept fixed. Each experimental point is the mean value upon 10 measures, displayed with the associated uncertainty. The red line is the Gaussian fit, whose parameters are shown.

Plane	Coordinate	Gaussian SD (°)	FWHM (°)
H	elevation	(3.29 ± 0.07)	(7.8 ± 0.2)
E	azimuth	(3.40 ± 0.06)	(8.0 ± 0.2)

Table 3.5: Measured beamwidth for the WR-10 pyramidal feed horn in both H and E planes [78].

Coordinate	Gaussian SD (°)	FWHM (°)
azimuth	(8.13 ± 0.05)	(19.14 ± 0.12)

Table 3.6: Measured beamwidth for the 90 GHz circular corrugated feed horn.

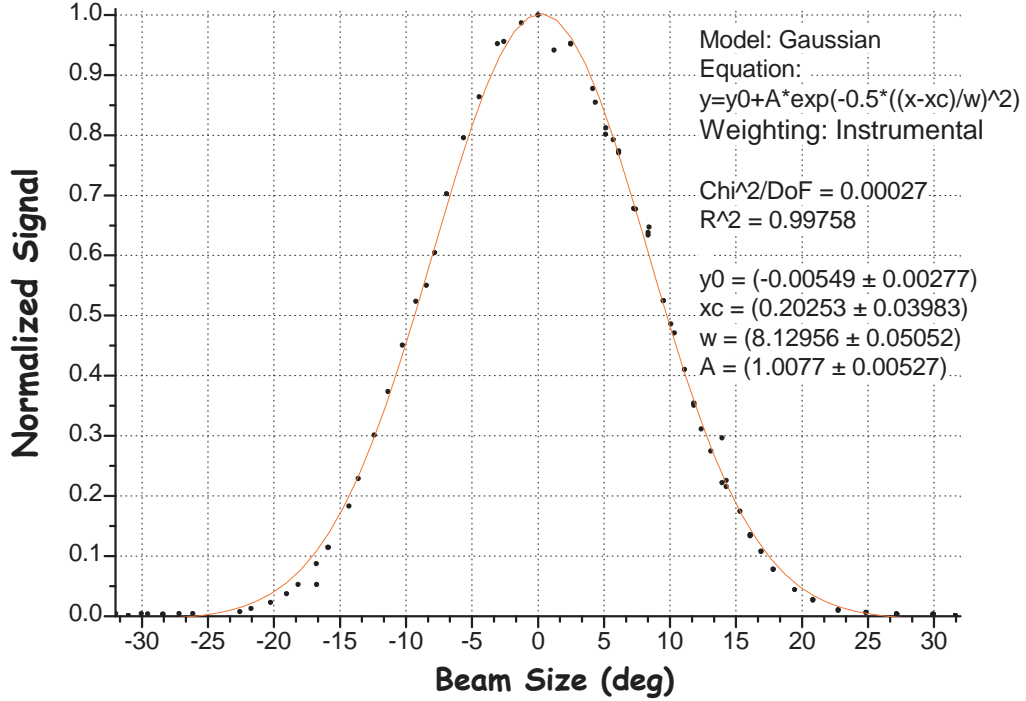


Figure 3.13: Beam measurements of the 90 GHz circular corrugated horn. The scan is performed varying the azimuth, while the optimized elevation is kept fixed. Each experimental point is the mean value upon 10 measures, displayed with the associated uncertainty. The red line is the Gaussian fit, whose parameters are shown.

Coordinate	Gaussian SD (°)	FWHM (°)
azimuth	(4.45 ± 0.01)	(10.48 ± 0.03)

Table 3.7: Measured beamwidth for the 137 GHz circular corrugated feed horn (see Appendix F for a picture).

3.6 Detectors

The detectors used in this work are two broadband diodes produced by Millimeter Pacific Products. The one coupled to waveguide WR-10 (used to detect signals out of the 78-114 GHz Gunn oscillator) is a silicon gold plated diode mounted on a planar stripline circuit to obtain an extremely rugged and compact device (model WDH). Most millimeter wave broadband detectors have very poor VSWR (voltage standing waves ratio) due to the difficulty in obtaining a good wideband impedance match between the diode and the waveguide.

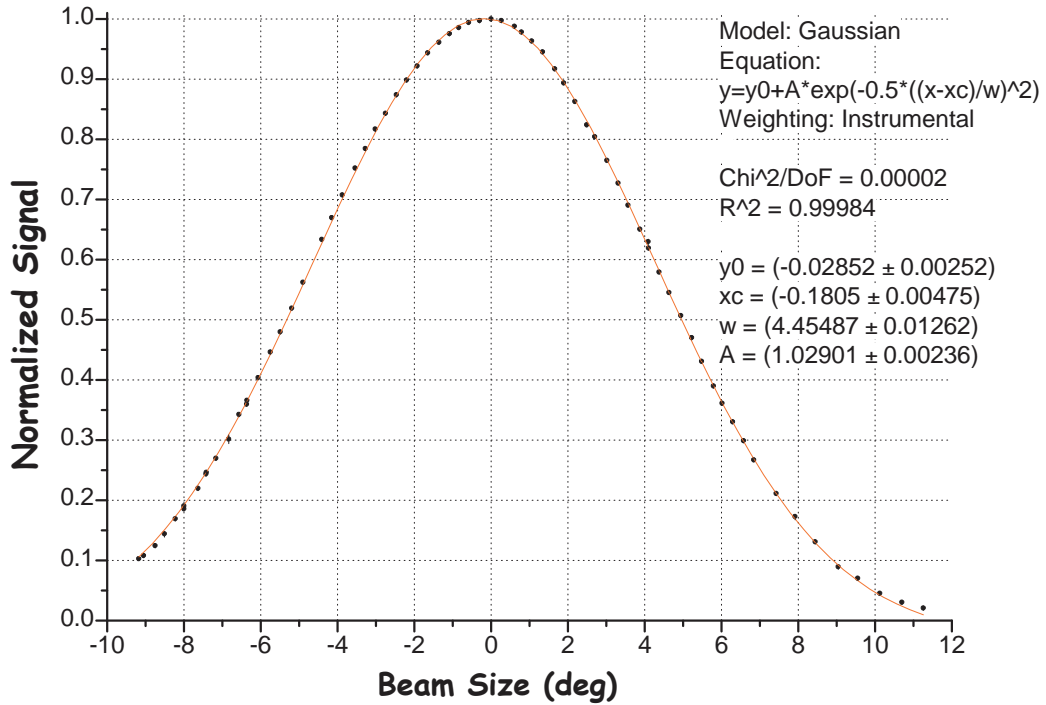


Figure 3.14: Beam measurements of the 137 GHz circular corrugated horn. The scan is performed varying the azimuth, while the optimized elevation is kept fixed. Each experimental point is the mean value upon 10 measures, displayed with the associated uncertainty. The red line is the Gaussian fit, whose parameters are shown.

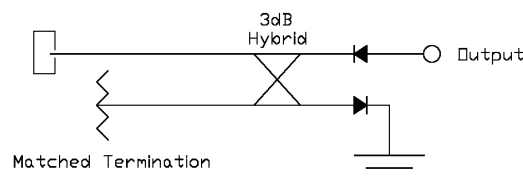


Figure 3.15: Circuit of the WDH detector composed by two diodes, an internal matched termination and a 3dB hybrid.

To overcome this problem, these detectors utilize two diodes and an internal matched termination and 3dB hybrid as shown in fig. 3.15. This circuit allows a VSWR of 2.0 or better over a full waveguide bandwidth. The detector for

waveguide WR-8 (signals out of the 120-147 GHz Gunn oscillator) use instead a single zero bias planar doped barrier GaAs diode (model DD). In tab. 3.8 we resume the specifications of the two broadband diodes.

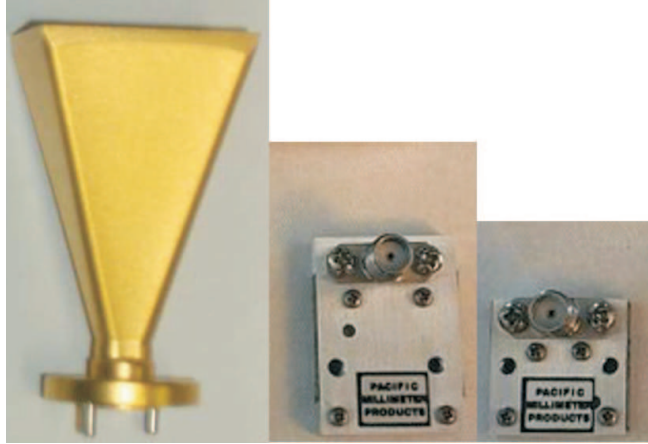


Figure 3.16: The detectors WDH (center) and DD (right) as compared in size to the standard WR-10 25dB feed horn (see Appendix F).

Model	Frequency (GHz)	Responsivity (mV/mW)	Waveguide	Dimensions (mm)
WDH	75 to 110	250	WR-10	$19.05 \times 24.89 \times 5.08$
DD	110 to 170	900	WR-6	$19.05 \times 19.05 \times 5.08$

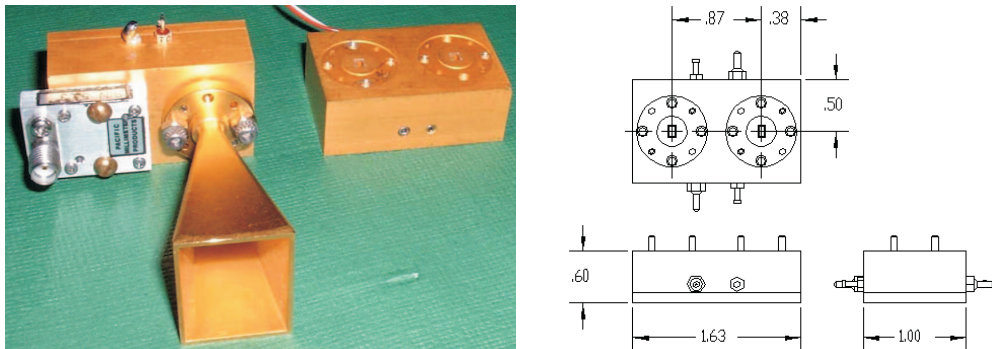
Table 3.8: Specifications of the two broadband diodes produced by Millimeter Pacific Products. Maximum input power 100 mW. Responsivity (see next section for definition) is measured into 1 M Ω load.

3.7 Amplifiers

In order to detect the far sidelobes of the OLIMPO telescope beam (see chapter 5), we needed to amplify the signal by means of amplifiers coupled to the diodes. Note that we had to remove them for laboratory measurements (chapter 4), otherwise the signal would saturate the detectors. We took different solution for the two diodes. For the WDH diode (75-110 GHz) we used HEMT low noise preamplifiers (placed before the diode, see fig. 3.17), produced by Quinstar Technology, INC. We have two of them, one with single amplifying stage, the other one with two amplifying stages, respectively 14 and 28 dB in gain (nominal). Here we show their specifications:

- Broadband Low Noise Amplifier Model QLW-92986014-P0

- Frequency band: 92-98 GHz (95 GHz center)
 - Gain (nominal): (14 ± 3) dB
 - Noise Figure: 6 dB
 - DC current @ 12V: 60 mA max
- Broadband Low Noise Amplifier Model QLW-92986028-P0
 - Frequency band: 92-98 GHz (95 GHz center)
 - Gain (nominal): (28.0 ± 3.5) dB
 - Noise Figure: 6 dB
 - DC current @ 12V: 150 mA max



(a) The HEMT is placed between the horn waveguide and the WDH diode. (b) Technical drawings. Quotes are in inches.

Figure 3.17: Low noise HEMT preamplifiers.

The HEMT window is protected by a glass window: Quinstar has waveguide windows on these amplifier WR-10 housings to make sure of the sealing. The windows is bigger than the standard WR-10 size, because the dielectric constant of the glass windows is higher than that of the air. Thus these low noise amplifiers can be coupled with standard WR-10 systems.

At this point we briefly introduce the concepts of *responsivity*, *Noise Equivalent Power* (NEP) and *Noise Equivalent Temperature* (NET), commonly used to characterize detectors and amplifiers performances. The responsivity \mathfrak{R} is just the proportionality factor between the input power and the output signal (units: V/W or often mV/mW): it turns out to be a constant only when a detector is working in the linear regime, otherwise a calibration would be needed by means of a known source. Moreover the responsivity can in general depend on the frequency. The Noise Equivalent Power is instead a parameter characterizing the noise in a way that is independent on the detector or on the physical origin of the noise itself. It is defined as the power (in W) that, in one second of integration time, produces a signal equal to the standard deviation of

the noise of a detector; in other words, it is the minimum signal that a detector can reveal. If we assume that the noise produced by a detector is Gaussian in shape, the uncertainty on the measurements scales as $N^{-1/2}$, where N is the number of independent measures. On the other hand, the number of independent measures is proportional to the integration time: the uncertainty on the measurements will thus drop down as the square root of the integration time. Expressing the NEP in $W(\text{Hz})^{-1/2}$, integration times different from one second are also taken into account: now, indicating with $\sqrt{\langle \Delta V^2 \rangle} = \sqrt{\langle \Delta V^2(\nu) \rangle}$ the *rms* value of the fluctuations in the signal (that is just the power spectrum of the signal fluctuations), we get:

$$NEP(\nu) = \frac{\sqrt{\langle \Delta V^2(\nu) \rangle}}{\mathfrak{R}(\nu)}, \quad (3.36)$$

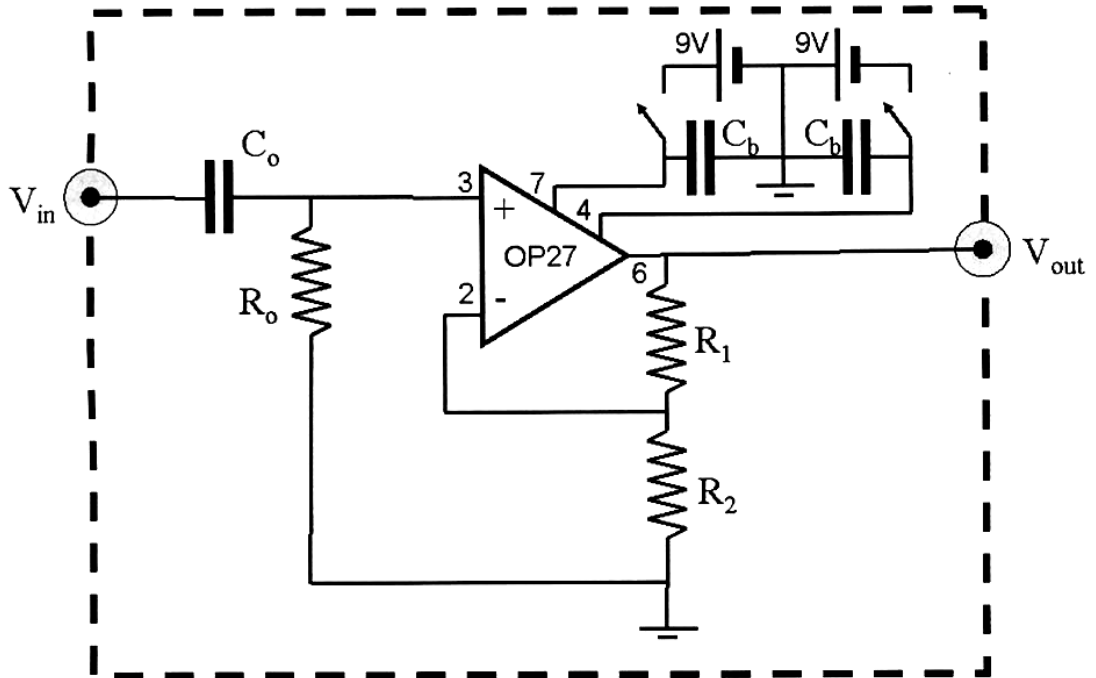
which in general would depend on the frequency ν . Finally the Noise Equivalent Temperature (NET) is defined analogously to NEP, in the case we are dealing with a temperature signal instead of a voltage signal and is measured in $K(\text{Hz})^{-1/2}$.

We can now go back to our amplifiers and recall here the estimates made by Federico Nati for the WDH diode and HEMT preamplifier NEP, in the HEMT frequency band, by means of the diode nominal responsivity [79]:

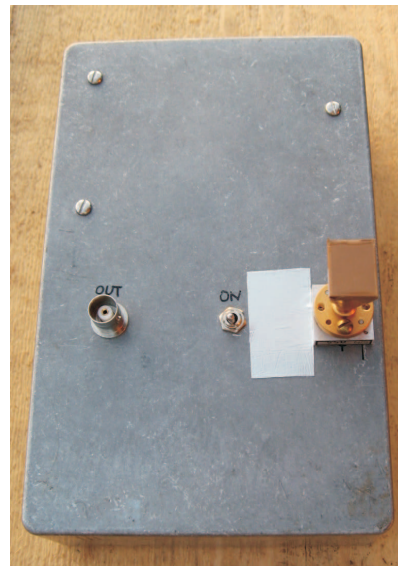
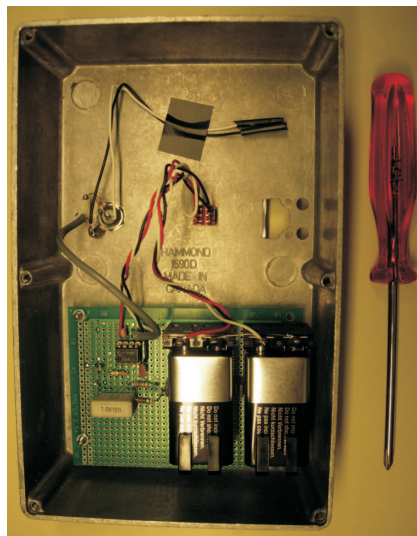
$$NEP_{WDH} = 1.90 \cdot 10^{-11} \frac{W}{\sqrt{Hz}}, \quad NEP_{HEMT} = 2.27 \cdot 10^{-9} \frac{W}{\sqrt{Hz}}. \quad (3.37)$$

In the case of the DD diode (110-170 GHz) we realized a simple circuit with a low noise non-inverting precision operational amplifier (OP27), whose power is supplied by two 9V batteries with associated switch to turn them off. The signal out of the diode is connected via BNC to V_{in} (see fig. 3.18a) and the amplified signal is directed out also via BNC (V_{out}). The capacities C_0 and C_b can be chosen to have negligible impedance (Z_C , eq. 3.38), because the work frequency is set to be $\nu_0 = 1.3$ kHz (the reason of this choice will be clarified in par. 3.9). This high work frequency also allows to neglect the resistance R_0 in the evaluation of V_{out} , which turns out to be just a function of the ratio R_1/R_2 and of the signal out of the diode, V_{in} (eq. 3.39). Thus R_0 can be adjusted to reach the maximum possible signal-to-noise ratio (S/N): qualitatively speaking, the more we decrease R_0 , the less is its Johnson noise⁶, while, on the other hand, the resulting signal out of the diode, V_{in} , will also decrease as R_0 goes down, since the actual signal out of the diode, V_d , is divided

⁶Johnson noise is the name for spontaneous voltage fluctuations at the ends of a resistor, whose physical origin are charge fluctuations in the material of which the resistor is made of: $N^2 = \langle \delta V^2 \rangle = 4k_B T R$, where T and R are, respectively, the temperature and the value of the resistance.



(a) Scheme of the circuit.



(b) The circuit placed in a metallic box: inside view. (c) The circuit placed in a metallic box: external view.

Figure 3.18: The circuit used to amplify signals out of the DD diode.

between R_0 and the internal impedance of the diode itself, Z_d . We can now go through a more quantitative analysis and set $C_0 = C_b = C = 1\mu F$, $R_1 = 100k\Omega$, $R_2 = 1k\Omega$.

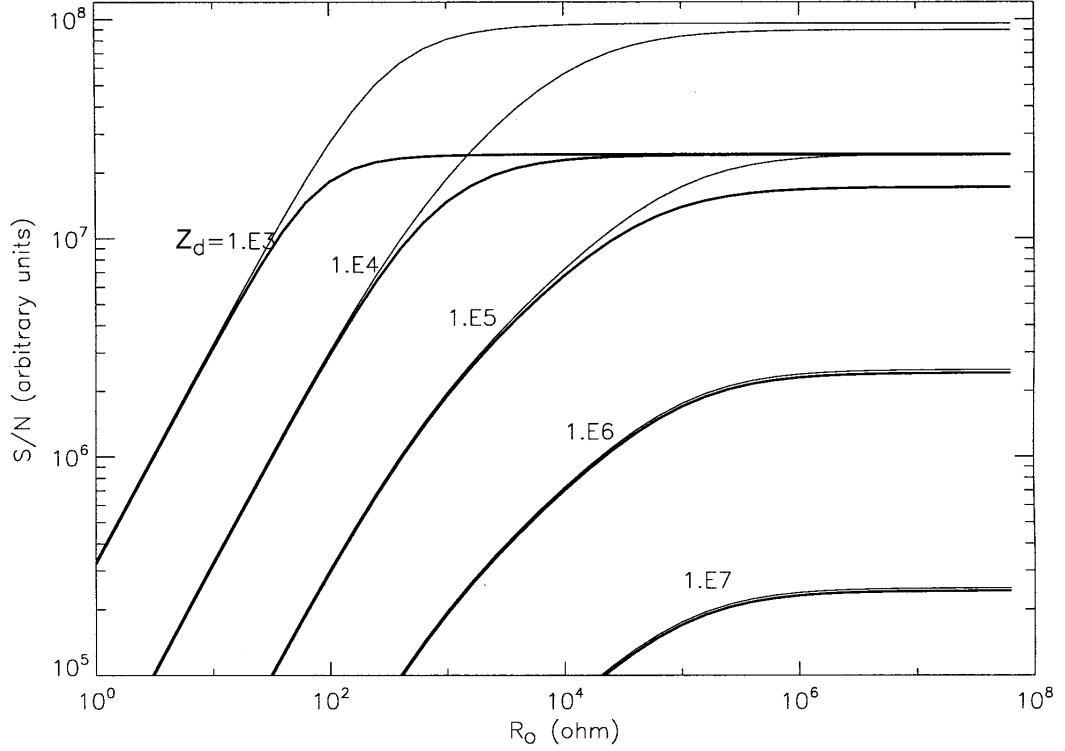


Figure 3.19: Expected behaviour of the signal-to-noise ratio (S/N) as a function of R_0 . The plot is obtained using the following typical values: $i_a^n = 0.4 \text{ pA}/\text{Hz}^{-1/2}$, $N_a^2 = 3 \text{ nV}/\text{Hz}^{-1/2}$, $N_d^2 = 10 \text{ nV}/\text{Hz}^{-1/2}$ (thin lines) and $N_d^2 = 40 \text{ nV}/\text{Hz}^{-1/2}$ (thick lines). The parameter is the internal impedance of the diode, Z_d .

$$Z_C = \frac{1}{2\pi\nu_0 C} \simeq 1.22 \cdot 10^2 \Omega, \quad (3.38)$$

$$V_{out} = \left(1 + \frac{R_1}{R_2}\right) V_{in}, \quad \text{for } \nu_0 \gg \frac{1}{2\pi R_0 C_0} \Rightarrow R_0 \gg 122\Omega, \quad (3.39)$$

$$S = V_{in} = V_d \frac{R_0}{R_0 + Z_d}, \quad (3.40)$$

$$N^2 = (4\pi k_B T R_0) \left(\frac{Z_d}{Z_d + R_0}\right)^2 + N_d^2 \left(\frac{R_0}{R_0 + Z_d}\right)^2 + N_a^2 + (i_a^n)^2 \left(\frac{R_0 Z_d}{R_0 + Z_d}\right)^2. \quad (3.41)$$

We have introduced the quantities N_d^2 , N_a^2 and i_a^n , which are, respectively, the noise fluctuations in voltage of the diode, those of the amplifier, and the

noise fluctuations in current of the amplifier. Using eqs. 3.40 and 3.41 we obtain the behaviour of the signal-to-noise ratio (S/N) as a function of R_0 (see fig. 3.19), for the typical values $i_a^n = 0.4pA/Hz^{-1/2}$, $N_a^2 = 3nV/Hz^{-1/2}$, $N_d^2 = 10nV/Hz^{-1/2}$ (thin lines) and $N_d^2 = 40nV/Hz^{-1/2}$ (thick lines). We see that in general R_0 should be increased up to $1M\Omega$, unless $Z_d \lesssim 10k\Omega$. Of course this can be done, as long as the bias current of the amplifier is very low: in fact the bias current produces a DC offset when passing through R_0 . From the datasheet we find $i_{bias} = 10nA$, that means a DC offset of about $10mV$ if $R_0 = 1M\Omega$. After the amplification factor $\sim R_1/R_2 = 100$ we get about $1V$ offset. Of course such a DC offset is unwanted, in order not to saturate the amplifier: we need to measure the actual DC offset for various values of R_0 and find a compromise between high S/N ratio and low DC offset in output.

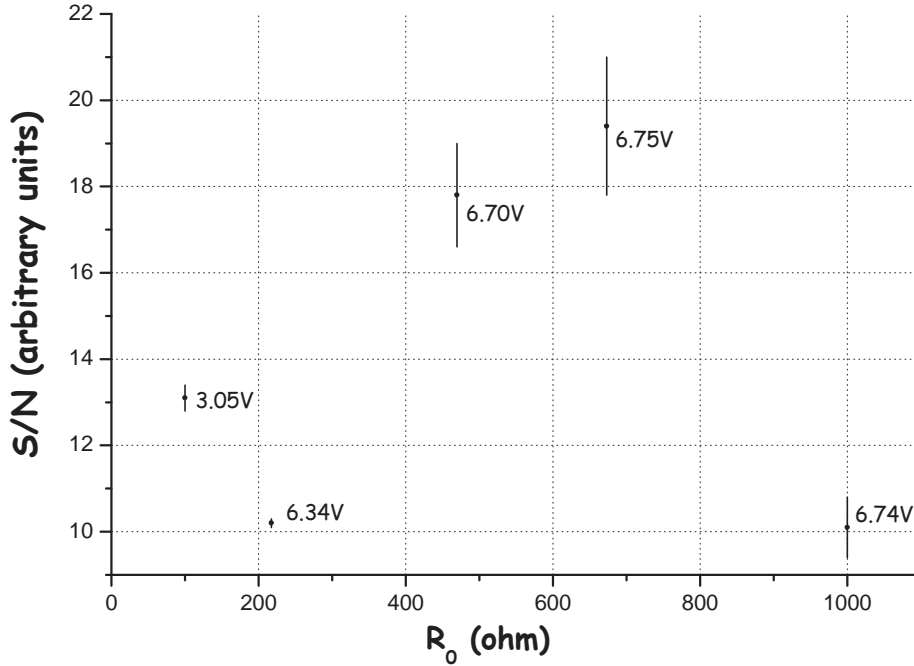


Figure 3.20: Measured behaviour of the signal-to-noise ratio (S/N) as a function of R_0 . Each point is the result of 10 measures. The number displayed close to the experimental points is the measured DC offset for each value of R_0 .

We carried out these measurements by positioning the 120-147 GHz Gunn oscillator in front of the DD detector (as shown in fig. 3.18b, the diode together with its horn are placed on the front face of the metallic box), fixing them to mechanical supports, in order for the measurements with various resistance to

be reproducible. The metallic box containing the amplifying circuit was kept open in its back and the resistor could be easily substituted. The signal out of the circuit was analyzed by means of a Dynamic Signal Analyzer (Hewlett Packard, model “35665A”). Looking at the results, shown in fig. 3.20, we see that such circuit achieves a satisfying S/N ratio, (19.4 ± 1.6) , when $R_0 = 673$ k Ω , but a DC offset of 6.75 V should be possibly avoided. We thus substituted the low-noise OP27 operational amplifier with a low offset, low drift JFET Operational Amplifier (LF411) and repeated the measurements with $R_0 = 1.27$ M Ω . Our best estimate of the S/N ratio over 20 measures is now (18.5 ± 0.9) , that is reasonably close to the OP27- $R_0=673$ k Ω case, with a very low DC offset, 0.7 V. It turns out that this last solution is the one we adopted.

3.8 Modulation Electronics

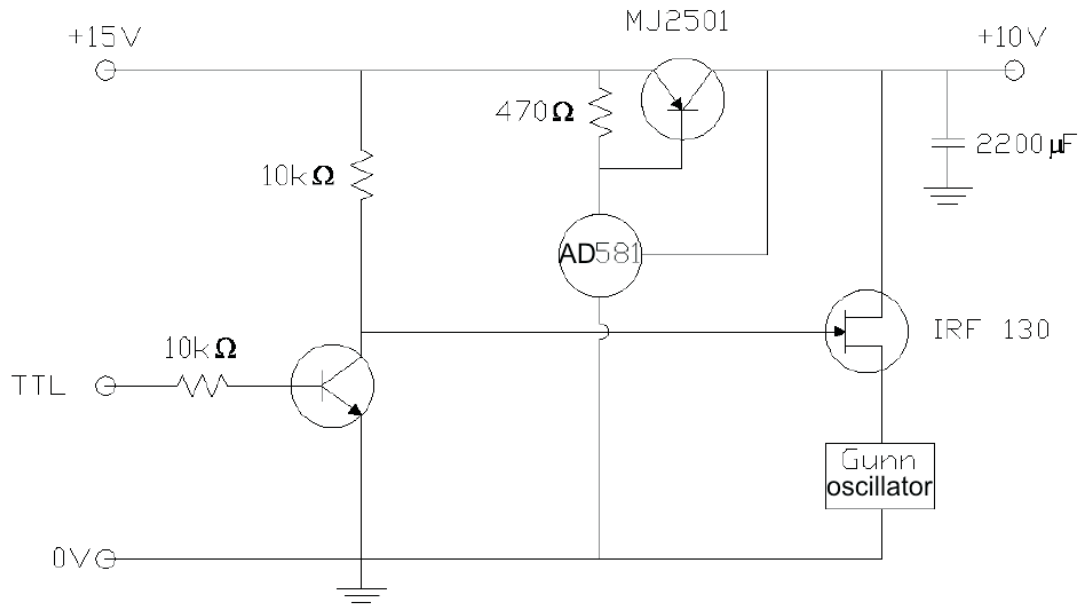
A standard procedure when dealing with small signals immersed in a dominant background is the *synchronous modulation-demodulation*. If we know a priori some properties of the signal we want to detect, we can extract it from the noise due to the dominant background. This is exactly the case for cosmological signals and also for laboratory microwave measurements. What usually happens is that the signals are modulated at a known fixed frequency and reconstructed by means of a *synchronous demodulator* or *Lock-in*. The modulation of a generic signal can be achieved by hardware mechanical devices and/or by modulation electronics (in the case of double or multiple modulation the condition to satisfy is that the modulation frequencies differs at least of three orders of magnitude, in order to avoid filtering of any information-carrying signal). A chopping modulation is not suitable at millimetric wavelengths, because chopper blades can introduce diffraction effects. Therefore for our laboratory measurements, instead of modulating the source after the emission, we can modulate the power supplying the source (the two Gunn oscillators) by means of a circuit which produces in output a $0-V_{Gunn}$ square wave at given frequency, where V_{Gunn} indicated the bias voltage of the two Gunn oscillators. This value needs to be very stable in voltage, as explicitly required in the Carlstrom datasheets (see Appendix C), and are different for the two devices: the 78-114 GHz oscillator needs a 10.0 V bias, while the 120-147 GHz one needs 9.0 V. The two circuits must therefore include a voltage stabilizer, together with a reference signal (TTL), bringing only the frequency information. The same reference signal has also to be sent to the Lock-in, together with the signal out of the detector. Lock-in amplifiers have therefore two inputs: one for the signal from the detector, made of a signal proportional to the incoming flux plus noise, $S(t) + N(t)$, the other for the reference signal $R(t)$. Our signal, i.e. only the component of $S(t)$ due to the modulated flux, must have an high correlation with $R(t)$. The basic operation of a Lock-in amplifier is to compute an averaged product over

a user-defined time constant τ : $V_{out} = \langle S(t)R(t) \rangle_\tau + \langle N(t)R(t) \rangle_\tau$. The output voltage will thus be a quasi-DC signal, produced by the averaged product $\langle S(t)R(t) \rangle_\tau$, proportional to $S(t)$. The term $\langle N(t)R(t) \rangle_\tau$ will instead fluctuate around zero, since there is no correlation at all between $N(t)$ and $R(t)$. The time constant should be of course smaller than the typical time of variation of the signal amplitude we want to detect, but high enough to average over several periods of modulation, in order to better reduce the noise. It's possible to show that the signal-to-noise ratio (S/N) out of a Lock-in amplifier increases as the square root of the time constant τ . All of the measurements described in this work are obtained via lock-in demodulation, with $\tau = 1$ s, which always represented a good compromise between the modulation frequency ($\nu_0 = 1.3$ kHz $\Rightarrow \tau_0 \sim 7.7 \cdot 10^{-4}$ s) and the variation time of the signal amplitude. The different measurements have in fact been always quasi-static, in the sense that each single measure was recorded in a static situation: after varying the experimental conditions as a function of the examined observable, the operator always waited for the signal to be stable around a given value. The fluctuations around that value are a residue of the non-optimal extraction from noise and are recorded as instrumental uncertainty associated to those measures. The Lock-in amplifiers used in this work are from Stanford Research Systems, model "SR850". Here we show the modulation circuits for both the Gunn oscillators, together with a picture of the circuit when placed in a metallic box for reliability. The TTL⁷ signal controls the interdiction current of a N-channel Power MOSFET (IRF130 in both cases), used as a switch in series to a) a power supply made extremely stable by means of a high precision voltage reference at 10.0 V (AD581) (fig. 3.21a, 78-114 GHz oscillator) or to b) a 5 A output current low dropout positive adjustable regulator (LT1084) (fig. 3.22a, 120-147 GHz oscillator).

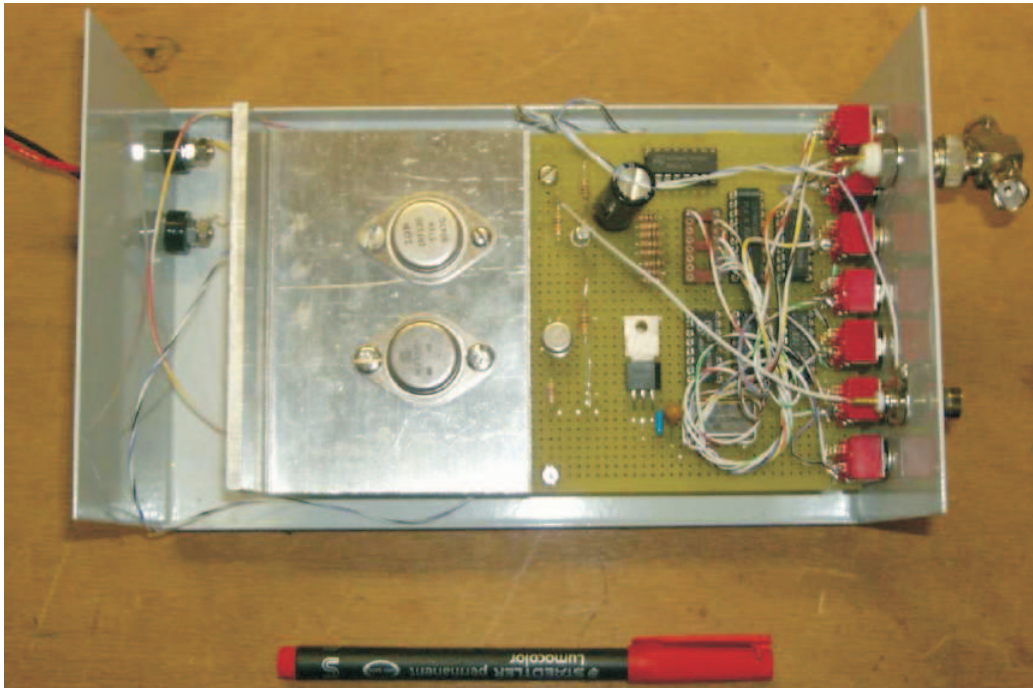
3.9 Reference Signal

Here we explain the reason of $\nu_0 = 1.3$ kHz modulation frequency: as we'll see in detail in chapter 5, beam measurements of the OLIMPO telescope needed the source to be located in the far field of the telescope. For such a 2.6 m diameter telescope, working at wavelengths of 2-3 mm, the far field is located at distances greater than about $2D^2/\lambda \sim 6.7$ km (see the end of par. 3.3.1). OLIMPO is currently hosted by the CNR research area in "Tor Vergata": from this place it's possible to point the telescope at an elevation up to about 20° and see the hills around Rome, where Villa Mondragone (now property of "Tor Vergata" University) is located, about 7 km far away from OLIMPO. The

⁷All standardized common TTL circuits operate with a 5 volt power supply. A TTL signal is defined as "low" or L or "0" when between 0 V and 0.8 V with respect to the ground terminal, and "high" or H or "1" when between 2 V and 5 V.

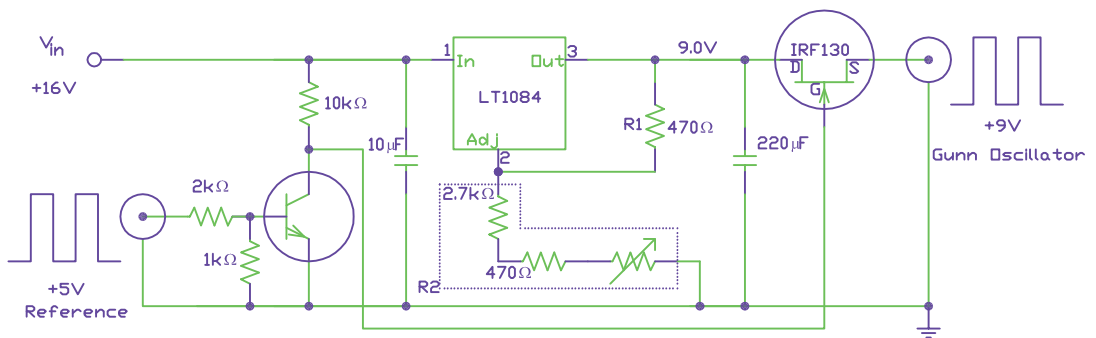


(a) Scheme of the circuit.

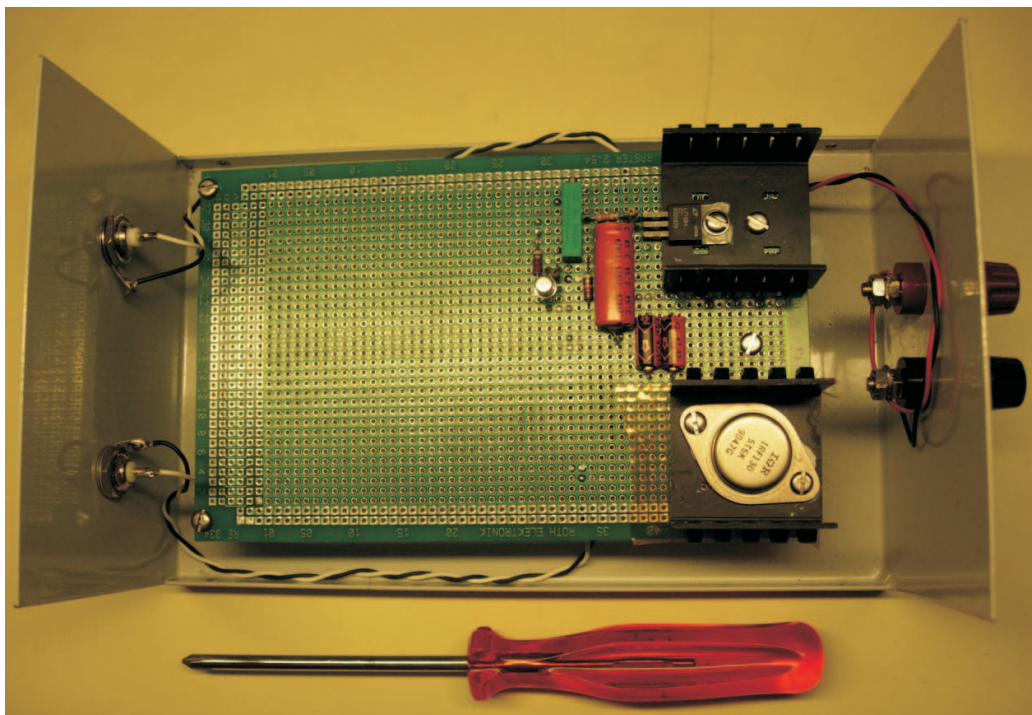


(b) The circuit placed in a metallic box: inside view.

Figure 3.21: The circuit used to modulate the 78-114 GHz Gunn oscillator.



(a) Scheme of the circuit.



(b) The circuit placed in a metallic box: inside view.

Figure 3.22: The circuit used to modulate the 120-147 GHz Gunn oscillator.

sources were placed on a balcony of Villa Mondragone, with clear and direct sight of the experiment down in the CNR area. We thus needed the reference signal modulating the Gunn oscillators in Villa Mondragone to be transmitted down to CNR area for synchronous demodulation via Lock-in amplifier (see previous section). We used a pair of dual band radio transmitter/receivers (TX/RX), produced by Intek, model “MT4000” (LPD+PMR) 2 W, with square wave frequency modulation at $\nu_0 = 1.3$ kHz. They have a nominal range of about 7 km in open space, and have been tested with very satisfying results. These devices have input and output audio jacks, with auto-sensing for input signals, so it is enough to feed the transmitter with the input signal in order to start the transmission. A voltage divider was used to adapt the TTL square wave 5 V peak⁷ to the peak of the reference square wave needed as input for the transmitter: tension is lowered by a factor 100. After it was sent through the TX/RX pair, we got the output from the receiver audio out, which was analyzed with an oscilloscope, while serving as reference signal for the Lock-in amplifier. For laboratory measurements we used exactly the same instruments for modulation-demodulation (while signal amplification was not needed), but we could easily generate a $\nu_0 = 1.3$ kHz TTL reference by means of a waveform generator (Hewlett Packard, model “33120A”).

3.10 HDPE Lenses

Except for the beam measurements of the horns (par. 3.5), we always made use of two identical lenses as focusing elements: the first one to convert the beam out of the source horn in a parallel beam of horizontally polarized light (par. 3.4), while the second one doing the reverse action, that is focusing the incoming parallel beam into the detector horn⁸. They are made of high density polyethylene (HDPE), which is almost transparent in our frequency range (at 90 GHz loss is less than 0.1 dB/cm [83]) and has refractive index $n = (1.5276 \pm 0.0066)$ at $\lambda = 3$ mm [81]. These lenses were designed by Cecilia Marini Bettolo for laboratory measurements with the 78-114 GHz Gunn oscillator and the WDH diode, and were made identical since the two horns had the same configuration (i.e. same aperture, see tab. 3.3). The focal length required was estimated with the usual expression

$$F = \frac{d}{2 \arctan\left(\frac{FWHM}{2}\right)}, \quad (3.42)$$

where d is the diameter over which the beam was required to be spread parallel and FWHM is the beamwidth. Let us point out that, since we are dealing with

⁸This second lens was used only for the laboratory measurements described in chapter 4, while of course it was not needed for the beam measurements of OLIMPO telescope, since its secondary mirror was directly coupled to the detector horn, see chapter 5.

pyramidal horns, whose beamwidth is different in the E and H planes, and since the lenses are circular, the FWHM to insert in eq. 3.42 must be a compromise between the aperture angles in the two orthogonal planes (see tab. 3.5). Since the diameter of the wire-grids (see 4.2) is $d = (127.50 \pm 0.05)$ mm, for the lenses the diameter was chosen to be $d = 110$ mm, so that the whole collecting area of the polarizer is illuminated, with a 17.5 mm guard ring to avoid border effects. The workshop of our Physics Department could not realize lenses with large curvature radii, such as the ones required for convex or biconvex lenses: the meniscus configuration was thus chosen, with two non-concentric spherical surfaces of radii a, b , whose centers are separated by c (see fig. 3.23).

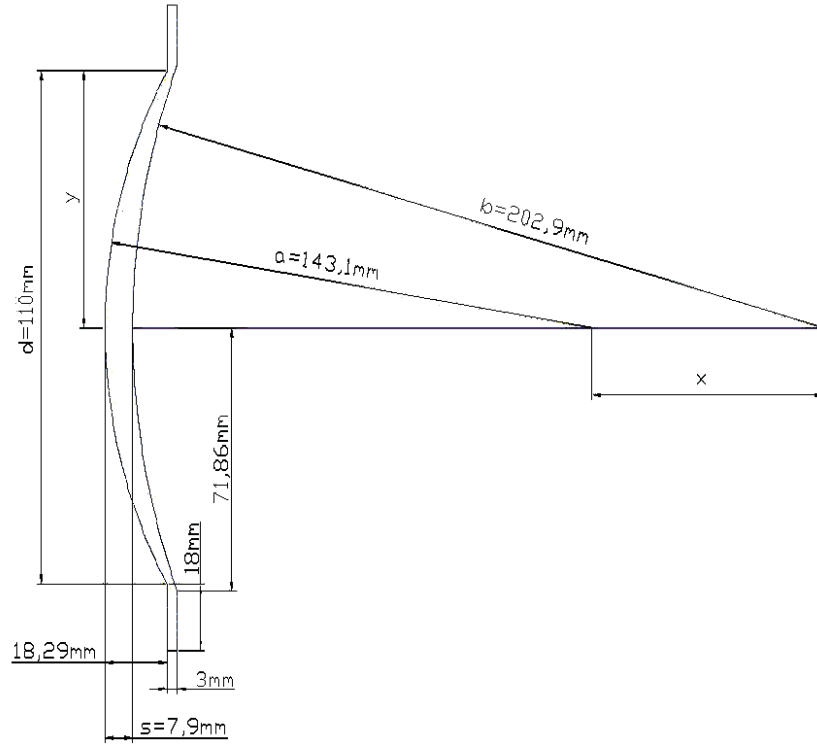


Figure 3.23: Cross-section of the meniscus lens [78].

If the lens has thickness s , we have $x^2 + y^2 = a^2$, $(x - c)^2 + y^2 = b^2$ and $b + c - a = s$, where y is imposed to be $d/2$. Finally, making use of the thick lenses relation (with $n_{air} = 1$) [82]

$$F = \frac{n}{n-1} \frac{ab}{s(n-1) + n(a-b)}, \quad (3.43)$$

the system was solved, obtaining $s = 1$ cm, $a = 14.31$ cm and $b = 20.29$ cm. The resulting focal length is $F = 81.3$ cm. After the realization, the actual focal

length has been measured with the very satisfying result $F = (81.0 \pm 0.5)$ cm [78]. We used the same lenses for laboratory measurements with the 120-147 GHz Gunn oscillator and the DD diode: in fact, as we'll now explain, the same lenses can be safely adapted. First of all the HDPE refractive index varies very slowly with wavelength in our frequency range (less than 5% in a frequency interval of 50 GHz centered at 90 GHz, see [83]). Second, even if the coupling between the focal length of the lenses (eq. 3.42) is non-optimal because WR-8 and WR-6 horns have slightly wider opening angles with respect to the WR-10 one (compare tabs. 3.4 and 3.5), this turns out not to be a problem, let's see why. The two lenses were positioned at the end of two same-sized PVC pipes, with the appropriate diameter to fit the lenses and length slightly bigger than F : this allowed us to place the Gunn oscillators at the other end of the pipes, by means of cylindrical PVC supports fitting the diameter of the pipes and guaranteeing an optimal alignment between the optical axis of the lenses and those of the horns. Moreover we could shift these supporting cylinders along the pipe to place the beam waist (slightly inside the edge of the horns, see tab. 3.3) at distance F from the lenses, with 1 mm precision. Finally the pipes were internally covered completely with eccosorb⁹, in order to avoid possible reflections on the PVC walls. Now the beam out of the source, after propagating along the distance $F = 81$ cm, in the case of the WR-8 horn will be simply illuminating a wider area than that of the WR-10 horn, in principle of diameter $d = 2F \arctan (FWHM) / 2 > 110$ mm (from eq. 3.42). But, since these exceeding tails are absorbed, this fact can only cause some reduction of the signal and no other disturbing effects. On the other hand the beam converging on the WR-6 detector horn, will undergo no alterations too, since the signal, after a distance F , is simply collected on a horn with aperture angle wider than expected.

Finally we discuss the eventuality of spurious polarization introduced by the lenses, whose optical properties could in principle depend on the direction: such anisotropic behaviour cannot be excluded a priori, particularly when the lenses are produced via lamination process. However in our case we are dealing with horizontally polarized sources and the detectors are themselves sensible only to horizontally polarized signals (see par. 3.4). This means that the only effect due to lens anisotropy could be a variation of the signal intensity as a function of the rotation angle of the lens about its optical axis. This variation has been measured to be 6% maximum [78].

3.11 Data Acquisition

Data acquisition was carried out always by interfacing the instruments with a laptop, for reliability and quickness not only during the acquisition, but also

⁹High efficiency microwave absorbing material.

for data storing and analysis. In both the measurement sessions (laboratory polarimetry, chapter 4, and OLIMPO telescope beam, chapter 5) we had to acquire the signal out of the Lock-in amplifier, after its synchronous demodulation, together with one or two angular variables: the rotation angle of the polarizer or the elevation/azimuth angles of the telescope. Stanford Research Systems “SR850” Lock-in amplifiers are equipped with a serial output port, which was interfaced with the serial port of the laptop by means of a simple receiving-transmitting serial cable, realized following the standard pin convention (transmission, reception, ground). The serial port was read by means of Linux-based bash shell scripts and Python scripts. On the other hand, the angular positions were interfaced through the parallel port: in fact in both cases the devices measuring the angular position had parallel output (the details about these two devices are described in pars. 4.4.2 and 5.3.2). We wrote an ad-hoc program in C language, controlling each single pin of the parallel port by means of the *parapin* library. We again used bash shell and Python scripts to wrap, decode and finally join this parallel input together with the serial input coming from the Lock-in amplifier. The raw data were stored in ASCII files: for each angular position at least 10 independent signal measurements were automatically recorded, but in certain cases we chose to collect more than 10 records for each single position. We also wrote programs in IDL language for data cleaning and averaging, providing as output ASCII files with signal values averaged over the same angular position, together with the associated statistical uncertainties.

Chapter 4

Modulating the Polarization: An Innovative Approach

4.1 Introduction

In this chapter we give a detailed description of our innovative approach for modulating the B-modes, i.e. the curl component of the polarization of the Cosmic Microwave Background. First of all we introduce in par. 4.2 linear polarizers from an electromagnetic point of view, first treating the case of a single wire (par. 4.2.1), then analyzing the case of the full wire-grid (par. 4.2.2). The same formalism is also applied to the reflecting polarizer (par. 4.2.3), also considering the effect of incoming beams of radiation of size only a few times smaller than the actual dimensions of the grid (par. 4.2.4). In section 4.3 we present the new-shaped polarizers, the criteria for their mechanical realization, the Mueller matrices characterization (par. 4.3.1), the modulation techniques, the effect of point sources in the field of view (par. 4.3.3). Section 4.3.2 contains the description and the results of the intensive simulations performed over maps of the polarized CMB sky, in order to optimize the size of the shear-like polarizer on the focal plane, as a function of the shape of the B-modes power spectrum. Then, section 4.4 is dedicated to the reflecting polarizer modulation technique and the preliminary laboratory test measurements: the experimental set-up is described in pars. 4.4.1 and 4.4.2, while in 4.4.3 we furnish the theoretical expected behaviour of such measurements, making use of the Stokes and Mueller formalism described in Appendix A. After a brief outline of the measuring strategy (par. 4.4.4), we give the results in par. 4.4.5.

4.2 Wire-Grid Polarizers: Electromagnetic Approach

The wire-grid is a polarizer in the microwave frequency band, in fact for large incident wavelengths with respect to the step of the grid, the component of

the incoming electric field parallel to the metallic wires generates an induced current on them, leading to an almost perfect reflection of such a parallel component; instead the component orthogonal to the wires is almost perfectly transmitted. Conversely for small wavelengths with respect to the step of the grid, the polarizer only provides a geometric opacity. In our specific case the grid is made of tungsten wires, $2a = 12\mu m$ thick and $25\mu m$ distant the one from the other, tightened inside a steel circular ring (diameter: internal 12.75 cm, external 13.6 cm). As we'll see, such a wire-grid can be treated as an ideal polarizer in our frequency range of interest, from $80 - 90GHz$ ($\lambda \sim 3.5mm$) up to $600GHz$ ($\lambda \sim 0.5mm$). In the following we will closely refer to [61] for the analysis of the behavior of polarizing grids and reflecting polarizers by solving Maxwell's equations, for arbitrary angles of incidence and grid rotation, for cases where the excitation is provided by an incident plane wave or a beam of radiation. Their treatment does not assume a priori that the wires of the grid are induced with only a longitudinal current, an azimuthal component is also present. The equations are solved for the induced current by considering the tangential components of both the electric and magnetic fields at the surface of the wires. Before describing the problem of the full grid or the reflecting polarizer, it is necessary to study the case of a single conducting wire, which is the foundation for the study of the more complicated cases of the full grid (par. 4.2.2) or the reflecting polarizer (par. 4.2.3).

4.2.1 Single Wire

Let us consider a wire of radius a oriented parallel to the x -axis at $y = y_0$, $z = z_0$ and subjected to an incident plane wave $\vec{E}_i(\vec{r})$ of arbitrary direction and polarization (see fig. 4.1):

$$\begin{aligned}\vec{E}_i(\vec{r}, t) &= E_0(\alpha'\hat{e}_x + \beta'\hat{e}_y + \gamma'\hat{e}_z) e^{-i(\vec{k}\cdot\vec{r}-\omega t)} , \\ \vec{E}_i(\vec{r}, t) &= E_0(a\hat{e}_u + b\hat{e}_v) e^{-i(\vec{k}\cdot\vec{r}-\omega t)} ,\end{aligned}\tag{4.1}$$

where $\omega = 2\pi\nu$ is the angular frequency and the wavevector \vec{k} is:

$$\vec{k} = k(\alpha\hat{e}_x + \beta\hat{e}_y + \gamma\hat{e}_z) .\tag{4.2}$$

The normalization and orthogonality conditions read as:

$$\alpha^2 + \beta^2 + \gamma^2 = (\alpha')^2 + (\beta')^2 + (\gamma')^2 = 1 \quad \text{and} \quad \alpha\alpha' + \beta\beta' + \gamma\gamma' = 0 .\tag{4.3}$$

Referring to fig. 4.1, where the angle of incidence is indicated with χ_i , while

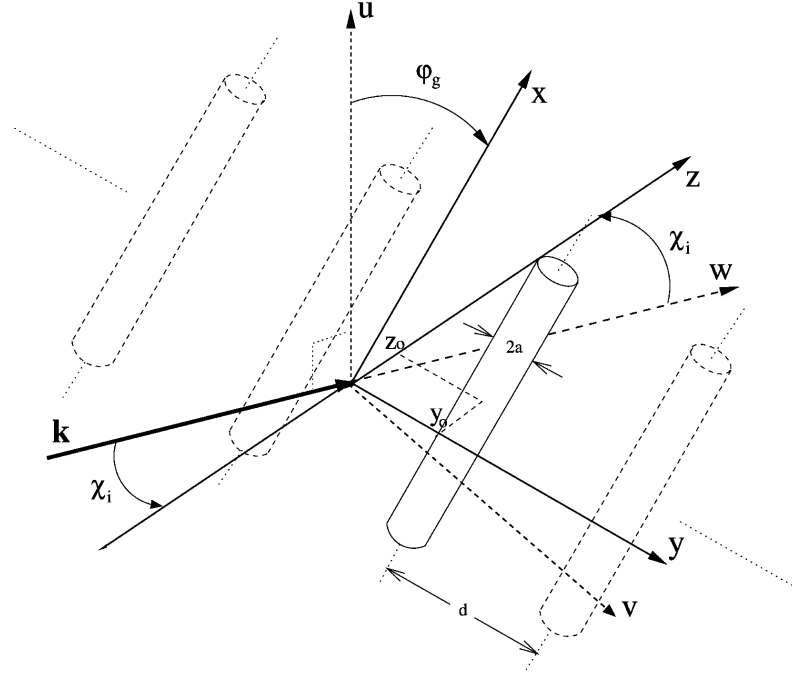


Figure 4.1: Coordinate systems for the study of a polarizing grid or a single wire. The wavevector \vec{k} of the incident radiation is aligned with the w -axis, the u , x and y -axes are in the plane of the page, the w and z -axes are in the plane perpendicular to the u -axis, and the wires are parallel to the $x - y$ plane. (u, v, w) is the laboratory system, while (x, y, z) are the grid coordinates.

φ_g is the angle of grid rotation with respect to the vertical ($\varphi_g = 0$), we get:

$$\begin{aligned}
 \alpha &= \sin \chi_i \sin \varphi_g & \alpha' &= a \cos \varphi_g + b \sin \varphi_g \cos \chi_i , \\
 \beta &= \sin \chi_i \cos \varphi_g & \beta' &= -a \sin \varphi_g + b \sin \varphi_g \cos \chi_i , \\
 \gamma &= \cos \chi_i & \gamma' &= -\sin \chi_i .
 \end{aligned} \tag{4.4}$$

In the following the time dependence $e^{i\omega t}$ will be omitted and assumed to be implicit in the equations. We shall also work under the assumptions of infinite length of the wires and high electric conductivity of their material ($\sigma = 1.77 \cdot 10^7 \Omega^{-1}m^{-1}$ for tungsten), in such a way that any current flowing through the single wire can be represented by a surface current vector \vec{K} , which is related to the current density $\vec{J}(\vec{r})$ as follows:

$$\vec{J}(\vec{r}) = \vec{K} \delta(\rho - a) e^{-i\vec{k} \cdot \vec{r}} , \tag{4.5}$$

where $y - y_0 = \rho \cos \theta$, $z - z_0 = \rho \sin \theta$ and

$$\vec{K} = K^x \hat{e}_x + K^\theta \hat{e}_\theta . \quad (4.6)$$

The assumptions adopted above, since no angular mode dependency is expected, also allow to split the problem in two parts or wave-modes: the mode where the electrical field is parallel to the plane defined by \hat{e}_x and \vec{k} (transverse magnetic mode or TM-mode) is related to the presence of K^x , while the mode where the magnetic field is parallel to this same plane (transverse electric mode or TE-mode), is related to K^θ . It's thus convenient to make use of the two vector potentials \vec{A}_s and \vec{F}_s for the scattered fields [69]. The TM-mode can be analyzed using the vector potential \vec{A}_s , in the Lorentz gauge¹, with $\vec{F}_s = 0$:

$$\vec{A}_s(\vec{r}) = \frac{\mu_0}{4\pi} \int d^3r' \vec{J}(\vec{r}') \frac{e^{-ikR}}{R} , \quad (4.7)$$

$$\vec{E}_s(\vec{r}) = -\frac{ic^2}{\omega} \vec{\nabla}(\vec{\nabla} \cdot \vec{A}_s(\vec{r})) - i\omega \vec{A}_s(\vec{r}) , \quad (4.8)$$

$$\vec{H}_s(\vec{r}) = \frac{1}{\mu_0} \vec{\nabla} \times \vec{A}_s(\vec{r}) , \quad (4.9)$$

where μ_0 is the permeability in vacuum, and $R^2 = (x-x')^2 + (y-y')^2 + (z-z')^2$. Since here we are only dealing with the longitudinal component of the surface current density, we only take into account the A^x component of the vector potential, while $A_s^\rho = A_s^\theta = 0$. When the wavelength of the incident wave is much larger than the wire radius (in our specific case this condition is well satisfied, since $\lambda \sim 0.5 \div 3.5 \text{ mm} \gg a = 6\mu\text{m}$), it can be shown that:

$$A_s^x(\vec{r}) = -\frac{i\pi\mu_0 a}{2} K^x H_0^{(2)}(k'\rho) e^{-i\varphi} , \quad (4.10)$$

where $k' = k\sqrt{1-\alpha^2}$, $\varphi = k(\alpha x + \beta y_0 + \gamma z_0)$ and $H_n^{(2)}$ is Hankel's function of the second kind of order n [72].

The TE-mode instead is best described by the vector potential F_s , in the suitable gauge where $A_s = 0$ [69]. This time it's convenient to consider the magnetization vector \vec{M} induced by the azimuthal component of the current density:

¹ $\partial^\mu A_\mu = 0$ in the 4-vector notation, that is $\vec{\nabla} \cdot \vec{A} + \frac{1}{c} \frac{\partial \phi}{\partial t} = 0$, where \vec{A} is a generic vector potential and ϕ a generic scalar potential.

$$\vec{J}(\vec{r}) = \vec{\nabla} \times \vec{M}(\vec{r}) , \quad (4.11)$$

$$\vec{F}_s(\vec{r}) = \frac{i\omega\mu_0\epsilon_0}{4\pi} \int d^3r' \vec{M}(\vec{r}') \frac{e^{-ikR}}{R} , \quad (4.12)$$

$$\vec{E}_s(\vec{r}) = -\frac{1}{\epsilon_0} \vec{\nabla} \times \vec{F}_s(\vec{r}) , \quad (4.13)$$

$$\vec{H}_s(\vec{r}) = -\frac{ic^2}{\omega} \vec{\nabla} (\vec{\nabla} \cdot \vec{F}_s(\vec{r})) - i\omega \vec{F}_s(\vec{r}) . \quad (4.14)$$

Since the azimuthal component of the surface current density is the only contribution to the vector fields, we need to consider only the M^x and F^x components of the magnetization and vector potential ($M^\rho = M^\theta = F_s^\rho = F^\theta = 0$). Again, when the wavelength of the incident wave is much larger than the wire radius, it can be shown that:

$$F_s^x(\vec{r}) = \frac{\pi\omega\mu_0\epsilon_0 a^2}{4} K^\theta H_0^{(2)}(k'\rho) e^{-i\varphi} , \quad (4.15)$$

It's easy to combine the expressions above to obtain the scattered fields, using eqs. 4.8, 4.9, 4.10 for the TM-mode and eqs. 4.13, 4.14, 4.15 for the TE-mode:

$$E_s^\rho(\vec{r}) = -i\alpha\sqrt{1-\alpha^2} F K^x H_1^{(2)}(k'\rho) e^{-i\varphi} , \quad (4.16)$$

$$E_s^\theta(\vec{r}) = -\sqrt{1-\alpha^2} \frac{ka}{2} F K^\theta H_1^{(2)}(k'\rho) e^{-i\varphi} , \quad (4.17)$$

$$E_s^x(\vec{r}) = -(1-\alpha^2) F K^x H_0^{(2)}(k'\rho) e^{-i\varphi} , \quad (4.18)$$

$$H_s^\rho(\vec{r}) = \frac{\alpha ka\sqrt{1-\alpha^2}}{2Z_0} F K^\theta H_1^{(2)}(k'\rho) e^{-i\varphi} , \quad (4.19)$$

$$H_s^\theta(\vec{r}) = -i \frac{\sqrt{1-\alpha^2}}{Z_0} F K^x H_1^{(2)}(k'\rho) e^{-i\varphi} , \quad (4.20)$$

$$H_s^x(\vec{r}) = -i \frac{\alpha ka(1-\alpha^2)}{2Z_0} F K^\theta H_0^{(2)}(k'\rho) e^{-i\varphi} , \quad (4.21)$$

with $F = (\pi\mu_0\omega a)/2$ and $Z_0 = \sqrt{\mu_0/\epsilon_0} = 376.7 \Omega$ is the impedance of vacuum. Eqs. 4.16-4.21 are expressed in terms of the two components of the total surface current density, which need to be determined yet. In order to do this, the incident plane wave must be expressed in the appropriate (cylindrical) coordinate system, again splitting the incident field in the two modes defined above and using the relation:

$$e^{-ik(\beta y + \gamma z)} = \sum_{n=-\infty}^{+\infty} (-i)^n J_n(k'\rho) e^{in\theta'} \quad \text{with} \quad \theta' = \theta - \arctan \frac{\gamma}{\beta} \quad [71][69], \quad (4.22)$$

where $J_n(x)$ is the Bessel function of order n . Now the fields can be matched by means of the usual boundary conditions for their tangential components at the surface of the wire. For the TM-mode we have:

$$E_s^x + E_s^x = Z_s(H_s^\theta + H_s^\theta), \quad (4.23)$$

where $Z_s = (i + 1)\sqrt{\mu_0\omega/2\sigma}$ is the surface impedance of the wire. Recalling the assumption $\lambda \gg a$ and considering a solution with no angular dependency, it can be shown that:

$$E_i^x \simeq \alpha' E_0 e^{-ik(\alpha x + \gamma z_0)}, \quad (4.24)$$

$$H_i^\theta \simeq i\alpha' \frac{E_0 ka}{Z_0 2} e^{-ik(\alpha x + \gamma z_0)}, \quad (4.25)$$

while for the TE-mode we get:

$$E_s^\theta + E_s^\theta = -Z_s(H_s^x + H_s^x), \quad (4.26)$$

$$E_i^\theta \simeq (\gamma'\beta - \beta'\gamma) E_0 \frac{ka}{2} e^{-ik(\alpha x + \gamma z_0)}, \quad (4.27)$$

$$H_i^x \simeq (\gamma'\beta - \beta'\gamma) \frac{E_0}{Z_0} e^{-ik(\alpha x + \gamma z_0)}. \quad (4.28)$$

These two sets of equations can be solved to obtain the two components of the total surface current density:

$$K^x = \frac{E_0}{F} \frac{\alpha' [1 - i(Z_s/Z_0)(ka/2)]}{(1 - \alpha^2)H_0^{(2)}(k'a) - i(Z_s/Z_0)\sqrt{1 - \alpha^2}H_1^{(2)}(k'a)}, \quad (4.29)$$

$$K^\theta = \frac{E_0}{F} \frac{-i(\gamma'\beta - \beta'\gamma) [1 + i(Z_s/Z_0)(2/ka)]}{\sqrt{1 - \alpha^2}H_1^{(2)}(k'a) + i(Z_s/Z_0)(1 - \alpha^2)H_0^{(2)}(k'\rho)}. \quad (4.30)$$

These two equations can be inserted in eqs. 4.16-4.21 to calculate the value of the fields at any point exterior to the wire. For a good conductor the internal fields are practically nonexistent, since $Z_s/Z_0 \ll 1$.

4.2.2 Wire-Grid

We can now think to the grid as an infinite number of wires of infinite length, separated by a distance d , under the simplifying assumption that every wire will be induced with the same surface current \vec{K} : the only difference will be a phase term in the current density $\vec{J}(\vec{r})$ of eq. 4.5, which depends on the position of the wire along the y -axis. The same thing can be said for the scattered fields from any given wire, thus we only have to replace $y_0 \rightarrow nd$ in eqs. 4.16-4.21, where n is an integer that determines the position of the wire. The scattered fields are now just the sum of all the different scattered fields from the individual wires, thus the operation of matching the boundary conditions has in principle to be done simultaneously at the surface of every wire. However, since we are dealing with an infinite number of infinitely long wires subjected to the same incident plane wave, it turns out that it is sufficient to do so for only one of the wires. It's convenient to work with the "central" wire, at $n = 0$, and to match the boundary conditions expressing the scattered fields of each wire in a cylindrical coordinate system centered on the position of this particular $n = 0$ wire. With these choices, we get the components of the induced total surface current density:

$$K^x = \frac{E_0}{F} \alpha' \frac{N_x}{\Delta_x}, \quad (4.31)$$

$$K^\theta = -i \frac{E_0}{F} (\gamma' \beta - \beta' \gamma) \frac{N_\theta}{\Delta_\theta}, \quad (4.32)$$

with

$$N_x = 1 - i \frac{Z_s}{Z_0} \frac{ka}{2}, \quad (4.33)$$

$$\Delta_x = (1 - \alpha^2) S_1 - i \frac{Z_s}{Z_0} \sqrt{1 - \alpha^2} H_1^{(2)}(k'a), \quad (4.34)$$

$$N_\theta = 1 + i \frac{Z_s}{Z_0} \frac{2}{ka}, \quad (4.35)$$

$$\Delta_\theta = \sqrt{1 - \alpha^2} H_1^{(2)}(k'a) + i \frac{Z_s}{Z_0} (1 - \alpha^2) S_1, \quad (4.36)$$

$$S_1 = H_0^{(2)}(k'a) + 2 \sum_{n=0}^{+\infty} H_0^{(2)}(k'nd) \cos(k\beta nd). \quad (4.37)$$

By means of the expansions for series of Hankel's functions, it's possible to write the expressions for the components of the total electric field far away from the grid:

$$E_T^x(\vec{r}) = \alpha' E_0 e^{-i\vec{k}\cdot\vec{r}} - \frac{1 - \alpha^2}{\gamma} \frac{\lambda F}{\pi d} K^x e^{-ik\gamma|z-z_0|} e^{-i\varphi}, \quad (4.38)$$

$$E_T^y(\vec{r}) = \beta' E_0 e^{-i\vec{k}\cdot\vec{r}} + \frac{\lambda F}{\pi d} \left[\frac{\alpha\beta}{\gamma} K^x + i \frac{ka}{2} K^\theta \frac{z - z_0}{|z - z_0|} \right] e^{-i(k\gamma|z-z_0|+\varphi)}, \quad (4.39)$$

$$E_T^z(\vec{r}) = \gamma' E_0 e^{-i\vec{k}\cdot\vec{r}} + \frac{\lambda F}{\pi d} \left[\alpha K^x \frac{z - z_0}{|z - z_0|} - i \frac{\beta ka}{\gamma 2} K^\theta \right] e^{-i(k\gamma|z-z_0|+\varphi)}. \quad (4.40)$$

From these expressions it's now straightforward to get the reflection and transmission coefficients in the far field, setting $z_0 = 0$ for simplicity:

$$R^x = -\frac{\lambda F}{\pi d E_0} \frac{1 - \alpha^2}{\gamma} K^x, \quad (4.41)$$

$$R^y = \frac{\lambda F}{\pi d E_0} \left[\frac{\alpha\beta}{\gamma} K^x - i \frac{ka}{2} K^\theta \right], \quad (4.42)$$

$$R^z = -\frac{\lambda F}{\pi d E_0} \left[\alpha K^x + i \frac{\beta ka}{\gamma 2} K^\theta \right], \quad (4.43)$$

$$T^x = \alpha' + R^x, \quad (4.44)$$

$$T^y = \beta' + \frac{\lambda F}{\pi d E_0} \left[\frac{\alpha\beta}{\gamma} K^x + i \frac{ka}{2} K^\theta \right], \quad (4.45)$$

$$T^z = \gamma' + \frac{\lambda F}{\pi d E_0} \left[\alpha K^x - i \frac{\beta ka}{\gamma 2} K^\theta \right]. \quad (4.46)$$

In order to handle these coefficients for predictions of laboratory measurements, it's better to transform them into the laboratory coordinate system: the coordinates for the incident/transmitted plane wave are (u, v, w) (see fig. 4.1), while for the reflected one we use (u', v', w') (see fig. 4.2). Recalling eqs. 4.4, we get:

$$R^{u'} = -\frac{\lambda F}{\pi d E_0} \frac{1}{\gamma \sqrt{1 - \gamma^2}} \left[\beta K^x - i \alpha \gamma \frac{ka}{2} K^\theta \right], \quad (4.47)$$

$$R^{v'} = -\frac{\lambda F}{\pi d E_0} \frac{1}{\gamma \sqrt{1 - \gamma^2}} \left[\alpha \gamma K^x + i \beta \frac{ka}{2} K^\theta \right], \quad (4.48)$$

$$R^{w'} = 0, \quad (4.49)$$

$$T^u = \alpha'' - \frac{\lambda F}{\pi d E_0} \frac{1}{\gamma \sqrt{1 - \gamma^2}} \left[\beta K^x + i \alpha \gamma \frac{ka}{2} K^\theta \right], \quad (4.50)$$

$$T^v = \beta'' - \frac{\lambda F}{\pi d E_0} \frac{1}{\gamma \sqrt{1 - \gamma^2}} \left[\alpha \gamma K^x - i \beta \frac{ka}{2} K^\theta \right], \quad (4.51)$$

$$T^w = 0, \quad (4.52)$$

with α'' and β'' related to the incident field by:

$$\vec{E}_i(\vec{r}) = E_0(\alpha''\hat{e}_u + \beta''\hat{e}_v) e^{-ikw} . \quad (4.53)$$

Such coefficients calculated in the laboratory frame clearly show the property that the reflected and transmitted fields have no component along their respective direction of propagation, as required for the propagation of plane waves in free space. It's now convenient to define the *principal axes* of the grid, mak-

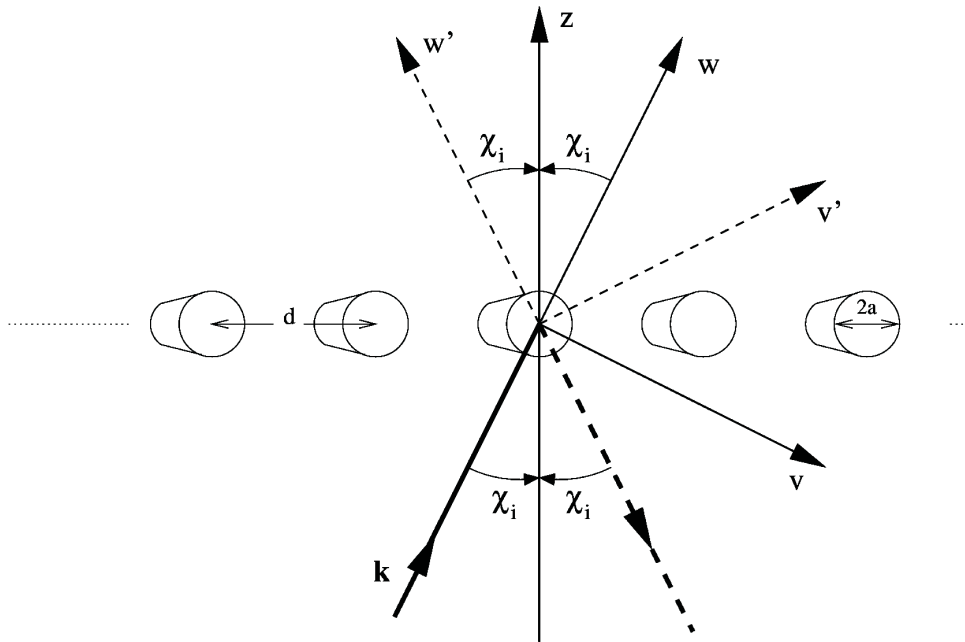


Figure 4.2: Definition of the system of coordinates (u', v', w') for the reflected wave in relation to the (u, v, w) system of the incident/transmitted waves introduced in fig. 4.1. The u' and u -axes are one and the same, pointing out of the page. The direction of propagation of the reflected wave is along the negative w' -axis.

ing a change of coordinates and using the following as eigenvectors instead of (\hat{e}_u, \hat{e}_v) :

$$\hat{p}_{\parallel} = \frac{\beta\hat{e}_u + \alpha\gamma\hat{e}_v}{\sqrt{\beta^2 + \alpha^2\gamma^2}}, \quad \hat{p}_{\perp} = \frac{-\alpha\gamma\hat{e}_u + \beta\hat{e}_v}{\sqrt{\beta^2 + \alpha^2\gamma^2}}, \quad (4.54)$$

that is \hat{p}_{\parallel} and \hat{p}_{\perp} are the versors, respectively, parallel and perpendicular to the projection of the direction of the wires in the plane of the incident field. In this particular reference frame the reflection and transmission coefficients read as:

$$R_{\parallel} = -\frac{\lambda}{\pi d} \frac{1 - \alpha^2}{\gamma} \frac{N_x}{\Delta_x}, \quad (4.55)$$

$$R_{\perp} = \frac{1 - \alpha^2}{\gamma} \frac{a}{d} \frac{N_{\theta}}{\Delta_{\theta}}, \quad (4.56)$$

$$T_{\parallel} = 1 + R_{\parallel}, \quad (4.57)$$

$$T_{\perp} = 1 - R_{\perp}. \quad (4.58)$$

This last representation has the advantage of simplifying calculations, since it allows us to decompose any incident field into two noninteracting components, one along each one of the principal axes: a field polarized along one of the principal axes scatters only in this same polarization state. A perfect grid would completely reflect the component of the incident field along \hat{p}_{\parallel} ($R_{\parallel} = -1$), while the component along \hat{p}_{\perp} would be completely transmitted ($T_{\perp} = 1$). Looking at eq. 4.55, we see that in order to achieve perfect reflection the following relations for the real and imaginary parts of Δ_x must simultaneously be satisfied:

$$\Re(\Delta_x) = \frac{\lambda}{\pi d} \frac{1 - \alpha^2}{\gamma}, \quad \Im(\Delta_x) = 0. \quad (4.59)$$

Moreover, in our case of tungsten wires we have $Z_s \ll Z_0$, then $\Delta_{\theta} \sim 0$ and $N_x \simeq N_{\theta} \simeq 1$. With these further approximations we can rewrite the reflection and transmission coefficients in the laboratory frame:

$$R^{u'} = -\frac{1}{\sqrt{1 - \gamma^2}} \frac{\beta \alpha'}{1 - \alpha^2}, \quad (4.60)$$

$$R^{v'} = -\frac{1}{\sqrt{1 - \gamma^2}} \frac{\alpha \gamma \alpha'}{1 - \alpha^2}, \quad (4.61)$$

$$T^u = a - \frac{1}{\sqrt{1 - \gamma^2}} \frac{\beta \alpha'}{1 - \alpha^2}, \quad (4.62)$$

$$T^v = b - \frac{1}{\sqrt{1 - \gamma^2}} \frac{\alpha \gamma \alpha'}{1 - \alpha^2}. \quad (4.63)$$

4.2.3 The Reflecting Polarizer

After we have found out the solution to the problem of the polarizing grid, we can step forward and consider the more complicated problem of the reflecting

polarizer, in which we are more interested for its possible application as a modulator (see par. 4.4). A reflecting polarizer consists of an assembly where a polarizing grid, like the one studied in the last section, is followed by a plane mirror paralleling it at some distance z_0 behind (i.e. effectively placing the mirror at $z = 0$). We can think of describing this configuration in such a way that images of both the incident and scattered fields are emanating from the other side of the mirror, i.e. the image world is made of a grid positioned at $z = -z_0 = h$, with an image incident field arriving on it. Assuming that the mirror is made of a material of good conductivity, one can write for the image incident field $\vec{E}'_i(\vec{r})$:

$$\vec{E}'_i(\vec{r}) = E_0(\alpha'_m \hat{e}_x + \beta'_m \hat{e}_y + \gamma'_m \hat{e}_z) e^{-ik(\alpha x + \beta y - \gamma z)} , \quad (4.64)$$

where

$$\alpha'_m = \frac{1}{1 - \gamma^2} [\alpha'(\alpha^2 R_{TM} + \beta^2 R_{TE}) + \alpha\beta\beta'(R_{TM} - R_{TE})] , \quad (4.65)$$

$$\beta'_m = \frac{1}{1 - \gamma^2} [\beta'(\alpha^2 R_{TE} + \beta^2 R_{TM}) + \alpha\beta\alpha'(R_{TM} - R_{TE})] , \quad (4.66)$$

$$\gamma'_m = \gamma' R_{TM} , \quad (4.67)$$

where R_{TE} and R_{TM} are the reflection coefficients of the mirror, respectively for transverse electric and transverse magnetic modes of incoming radiation, with a dependency on the angle of incidence. It is important to note that these transverse modes of radiation are not the same as those introduced in par. 4.2.1; they are defined here in relation to the plane containing the normal vector out of the surface of the mirror ($-\hat{e}_z$) and the wavevector \vec{k} . The components of the total the surface current density \vec{K}' of the image grid can be expressed in terms of the ones of the real grid:

$$K'^x = \frac{\alpha'_m}{\alpha'} K^x , \quad (4.68)$$

$$K'^\theta = \frac{\gamma'_m \beta - \beta'_m \gamma}{\gamma' \beta - \beta' \gamma} K^\theta . \quad (4.69)$$

Using eqs. 4.68 and 4.69, together with the boundary conditions at the grid, we get the expressions for the reflection coefficients in the grid frame:

$$K^x = \frac{E_0}{F} \frac{2i\alpha' \text{sn}(k\gamma h) N_x}{(1 - \alpha^2) \Delta S_1 - i(Z_s/Z_0) \sqrt{1 - \alpha^2} \Delta S_2} e^{-ik\gamma h}, \quad (4.70)$$

$$K^\theta = -\frac{E_0}{F} \frac{2i(\gamma'\beta - \beta'\gamma) \text{cs}(k\gamma h) N_\theta}{\sqrt{1 - \alpha^2} \Sigma S_2 + i(Z_s/Z_0)(1 - \alpha^2) \Sigma S_1} e^{-ik\gamma h}, \quad (4.71)$$

$$R^x = \alpha'_m - i \frac{F}{E_0} \frac{2\lambda}{\pi d} \frac{1 - \alpha^2}{\gamma} \text{sn}(k\gamma h) K^x e^{ik\gamma h}, \quad (4.72)$$

$$R^y = \beta'_m + i \frac{F}{E_0} \frac{2\lambda}{\pi d} \left[\frac{\alpha\beta}{\gamma} \text{sn}(k\gamma h) K^x - \frac{ka}{2} \text{cs}(k\gamma h) N_\theta \right] e^{ik\gamma h}, \quad (4.73)$$

$$R^z = -\gamma' - i \frac{F}{E_0} \frac{2\lambda}{\pi d} \left[\alpha \text{sn}(k\gamma h) K^x + \frac{\beta ka}{2} \text{cs}(k\gamma h) N_\theta \right] e^{ik\gamma h}, \quad (4.74)$$

where

$$\text{sn}(x) = -\frac{i}{2}(e^{ix} - r_x e^{-ix}), \quad (4.75)$$

$$\text{cs}(x) = \frac{i}{2}(e^{ix} - r_\theta e^{-ix}), \quad (4.76)$$

$$\begin{aligned} \Delta S_1 &= H_0^{(2)}(k'a) - r_x H_0^{(2)}(2k'h) + \\ &+ 2 \sum_{n=1}^{\infty} \left[H_0^{(2)}(k'nd) - r_x H_0^{(2)}(k'\sqrt{n^2 d^2 + 4h^2}) \right] \cos(k\beta nd), \end{aligned} \quad (4.77)$$

$$\Delta S_2 = H_1^{(2)}(k'a) - r_x H_1^{(2)}(2k'h), \quad (4.78)$$

$$\begin{aligned} \Sigma S_1 &= H_0^{(2)}(k'a) + r_\theta H_0^{(2)}(2k'h) + \\ &+ 2 \sum_{n=1}^{\infty} \left[H_0^{(2)}(k'nd) + r_\theta H_0^{(2)}(k'\sqrt{n^2 d^2 + 4h^2}) \right] \cos(k\beta nd), \end{aligned} \quad (4.79)$$

$$\Sigma S_2 = H_1^{(2)}(k'a) + r_\theta H_1^{(2)}(2k'h), \quad (4.80)$$

$$r_x = -\frac{\alpha'_m}{\alpha'}, \quad (4.81)$$

$$r_\theta = -\frac{\gamma'_m \beta - \beta'_m \gamma}{\gamma' \beta - \beta' \gamma}. \quad (4.82)$$

As done in the case of the polarizing grid, we can transform those coefficients into the laboratory frame of coordinates (u', v', w') , obtaining:

$$R^{u'} = \alpha_m'' - i \frac{F}{E_0} \frac{2\lambda}{\pi d} \frac{e^{ik\gamma h}}{\gamma \sqrt{1-\gamma^2}} \left[\beta \text{sn}(k\gamma h) K^x - \alpha \gamma \frac{ka}{2} \text{cs}(k\gamma h) N_\theta \right], \quad (4.83)$$

$$R^{v'} = \beta_m'' - i \frac{F}{E_0} \frac{2\lambda}{\pi d} \frac{e^{ik\gamma h}}{\gamma \sqrt{1-\gamma^2}} \left[\alpha \gamma \text{sn}(k\gamma h) K^x + \beta \frac{ka}{2} \text{cs}(k\gamma h) N_\theta \right], \quad (4.84)$$

$$R^{w'} = 0, \quad (4.85)$$

where α_m'' and β_m'' are given by:

$$\alpha_m'' = \frac{1}{1-\gamma^2} \left[\alpha'' (\alpha^2 R_{TM} + \beta^2 R_{TE}) + \alpha \beta \beta'' (R_{TM} - R_{TE}) \right], \quad (4.86)$$

$$\beta_m'' = \frac{1}{1-\gamma^2} \left[\beta'' (\alpha^2 R_{TM} + \beta^2 R_{TE}) + \alpha \beta \alpha'' (R_{TM} - R_{TE}) \right], \quad (4.87)$$

and α'' and β'' are those in eq. 4.53.

4.2.4 Grids and Beams of Radiation

Until now we have restricted our analysis to cases where the dimensions of the grid and the extent of the incident plane wave were assumed to be infinite. If, however, the incoming excitation can be properly represented as a beam of radiation which is of size a few times smaller than the actual dimensions of the grid, the results obtained with our analysis should still be valid. In fact the incident beam should induce currents only in the vicinity of the area where it impinges on the grid. There should therefore be little or even no difference in its response depending on whether it is infinite or not. Nevertheless the characteristics of the incoming radiation can be important in some cases. Let us begin noting that we can always mathematically express a beam of radiation $E_0(\vec{r})$ as a summation of plane waves with different amplitudes, phases and \vec{k} vectors: in the laboratory coordinate system (u, v, w) the electric field along the u -axis, $E_i^u(\vec{r}, t) = \alpha'' E_0(\vec{r}) e^{i\omega_0 t}$, can be expressed, using its Fourier transform and assuming the beam to be monochromatic at $\omega_0 = |\vec{k}|c$, by:

$$E_i^u(\vec{r}, t) = \frac{\alpha''}{(2\pi)^4} \int_{-\infty}^{+\infty} d\omega \, d^3k \, E_0(\vec{k}, \omega) e^{-i(\vec{k}\cdot\vec{r} - \omega t)}, \quad (4.88)$$

$$E_0(\vec{k}, \omega) = 2\pi \delta(\omega - \omega_0) \int_{-\infty}^{+\infty} d^3r' \, E_0(\vec{r}') e^{i\vec{k}\cdot\vec{r}'}. \quad (4.89)$$

The incident radiation can thus be modeled using a circular Gaussian beam

with a beam waist of radius w_0 and a Rayleigh range $z_R = \pi w_0^2/\lambda$ (see par. 3.3). As explained in par. 4.4.3, we also know that the resonance will occur for a grid-mirror separation of $h = 2n\pi/k_z$ where $n = 0, 1, 2, \dots$ and $k_z = 2\pi(\lambda \cos \chi_i)^{-1}$ is the projection of the wavevector along the z -axis perpendicular to the reflecting polarizer (in the coordinate system of the grid, see fig. 4.1). It's thus possible to express the width of the resonance Δh as a function of k_z and Δk_z the spectrum extent along the same axis:

$$\Delta h \simeq 2n\pi \frac{\Delta k_z}{k_z^2} , \quad (4.90)$$

Using the wave uncertainty relation, we can evaluate the spectrum extent in the laboratory system of axes as:

$$\Delta k_u \simeq \frac{1}{w_0} , \quad \Delta k_v \simeq \frac{1}{w_0} , \quad \Delta k_w \simeq \frac{1}{z_R} . \quad (4.91)$$

Transforming these quantities in the coordinate system of the grid and inserting the result in the expression for the width of the resonance, we find:

$$\Delta h \simeq \frac{2n\pi}{(k\gamma w_0)^2} \sqrt{w_0^2(1 - \gamma^2) + \left(\frac{2\gamma}{k}\right)^2} . \quad (4.92)$$

Although these expressions represent only a rough calculation of what could be expected, they nevertheless tell us that there will be a significant broadening of the resonant feature: as we'll understand in section 4.4, this fact turns out to be useful to our aim.

4.3 The New Polarizer

In chapters 1 and 2 we drew an Inflation-founded cosmological scenario: the presence of two peculiar patterns (rotational, B-modes and irrotational, E-modes) is expected in the polarization of the Cosmic Microwave Background, which is predicted to be purely linear. In particular the detection of one of these components (the curl component, rotational) will be an indirect proof of the presence of primordial gravitational waves, which is a generic prediction of all inflationary models. The popular way to depict experiments for B-modes detection is to measure the Stokes parameters Q,U (characterizing linear polarization, see Appendix A) with the highest possible angular resolution, and then analyze the measured data with mathematical methods. An array of detectors is needed to perform this measurement. In this section we present an innovative proposal for analyzing a curl polarization field using a new polarization modulator concept. Instead of an array detectors (polarization sensitive

or coupled to common linear polarizers), we introduce in the focal plane of big throughput telescope (see chapter 5) a polarizer shaped to match the curl polarization pattern (CAD realizations in figs. 4.4 and 4.5). The size of the polarizer on the focal plane defines the sky area under analysis (field of view, FOV), which can be around one degree or more, depending on the shape of the theoretical power spectrum expected for the B-modes (see par. 2.6). A single detector behind the polarizer measures the intensity coming from the whole collecting area of the polarizer. Recalling the geometrical characterization of such curl polarization field given in par. 2.5.4 (see in particular fig. 2.13), it turns out that a shear-like path of the metallic strips has the required property of optimally modulating the curl component of the polarization field. Alternating such polarizer and its mirror image, we modulate the curl component, while we do not modulate the gradient (irrotational) component of the polarization field in the sky region under analysis. This is just the experimental point of view of what we described in chapter 2 from a theoretical point of view: eqs. 2.51 tell us that the E and B components of the CMB polarization field have opposite behaviour under parity transformation, while they are both invariant under rotation. The two typical twin shear-like patterns are obtained the one from the other just by means of a 180° flip, while the typical E-mode radial-tangential patterns are not. Therefore this latter gradient component will not survive such flipping modulation, whereas rotational structures will emerge: what we expect from an observational point of view is that, for each pointing direction on the sky, the difference in signal (integrated on the whole collecting area of the polarizer) between the two 180° flipped configurations is very close to zero in the case of a pure irrotational field, while in the case of a pure rotational field its value is significantly higher. This approach has several advantages:

- it reduces the number of needed detectors, and does not require an array;
- it concentrates on a single detector all the radiation power coming from the full area considered for the B-modes analysis, thus increasing the signal;
- the noise is lower, since the required information is obtained from a single detector, while in the array approach the same information is obtained from N detectors, with an increase in noise of a factor \sqrt{N} ;
- it allows multiband operations, by means of polarization-optimized dichroics². As we'll see in the following, one of the main disadvantages of our approach is the possible presence of point sources (such as QSO's and Blazars) in the field of view, which would produce a strong signal. Multi-band channel separation will instead provide a powerful tool to recognize

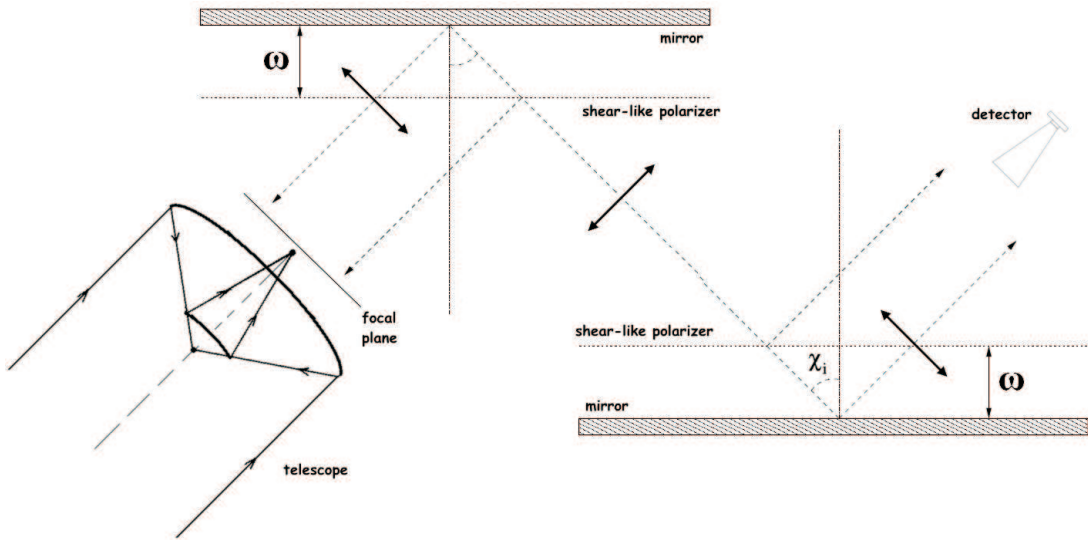
²Dichroic filters are very accurate color filters, used to selectively pass light in a small range of wavelengths, while reflecting the others.

and remove point sources from the field of view, since they present a characteristic strongly non thermal spectrum.

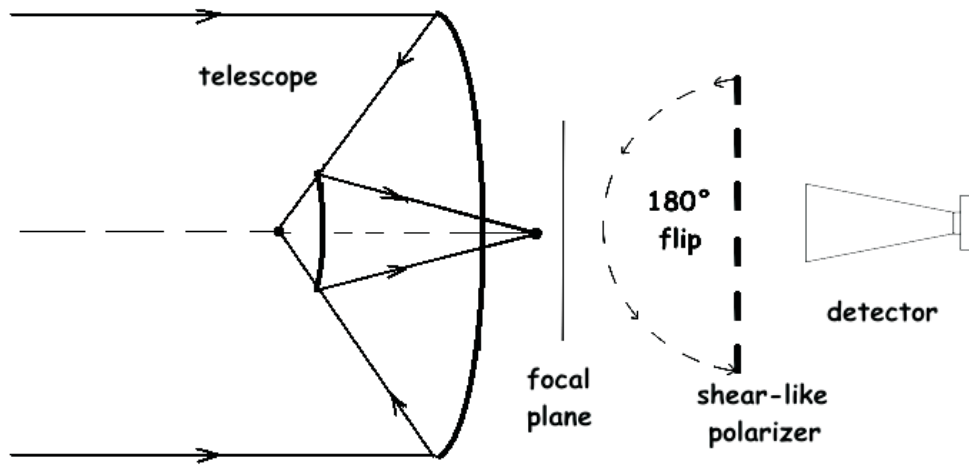
We propose here two different solutions for modulating rotational polarization fields by means of shear-like polarizers:

- the reflecting polarizer described in par. 4.4. We will show that a plane mirror can be shifted forth and back behind a parallel polarizer with mechanical frequency ω , between two particular fine tuned positions. Two polarizers are needed to perform such differential measurements, together with their coupled plane mirror, moving out of phase (see fig. 4.3a). The main advantage of this technique is possibility of continuous acquisitions. Second, the mechanical frequency of modulation is completely uncorrelated with the polarizer. Third, as we'll see, in this case double-sided lithography is not required for the polarizers. The main disadvantages are from a mechanical point of view: two shear-like polarizers and coupled mirrors are required, together with two linear actuators providing synchronous modulated shift of the mirrors behind the polarizers.
- 180° flip of the same shear-like polarizer (see fig. 4.3b). Modulation is achieved scanning the sky at constant rate, so that the polarization signals are detected at a frequency far from the 1/f knee of the noise and far from the effect of instrumental drifts. After one scan is complete, the polarizer is flipped and the scan is repeated. Such solution is quite simpler from a mechanical point of view: we only need to flip the polarizer, ensuring a perfect 180° rotation. Apart from the required double-sided lithography for the polarizer, the main disadvantages arise during the sky scans. Flipping of the polarizer cannot be so fast, at least some seconds, during which several problems must be taken into account: first, the detectors must be electronically blinded to avoid off-axis reflections during the flip; second, extremely accurate pointing and map reconstruction are required.

Of course we must point out here that such solution is thought for a balloon-borne experiment, that in principle can also be optimized to perform an accurate characterization of linear polarization patterns from galactic foregrounds, occurring in the same range of wavelengths of our interest (millimetric and sub-millimetric): this can be achieved by focusing on low frequency channels, particularly in the range 30-100 GHz (a few millimeters wavelengths). Polarized microwave foregrounds must be absolutely taken into account since their presence can strongly affect CMB polarization measurements: balloon-borne and ground-based missions are thus required as supporting cast to satellite missions (such as the forthcoming satellite BPOL from the European Space Agency), entirely dedicated to CMB polarization. We shall not give in this work the details of foregrounds polarized emission, which is mainly due to



(a) Two reflecting polarizers with mirrors moving at frequency ω , out of phase.



(b) 180° flip of the same polarizer, working in transmission.

Figure 4.3: The two techniques proposed for modulating a rotational field of polarization. See text for details.

thermal emission from grains of interstellar dust, aligned because of the galactic magnetic field. The following works are completely dedicated to polarized foregrounds modelling and characterization, and we refer to them for a detailed description: [63],[64],[65],[66],[67] and [68]. For the aim of this work it is sufficient to say that at frequencies below 60 GHz interstellar emission of spinning dust grains, free-free and synchrotron emission from the interstellar medium dominate over the cosmological background, while at higher frequencies, above 400 GHz, the clumpy foreground from “cirrus clouds” of interstellar dust dominates the sky brightness even at high Galactic latitudes. An experiment focusing on foregrounds should therefore work with at least two frequency channels below 100 GHz, one at ~ 217 GHz (peak frequency of the brightness fluctuation spectrum generated by the CMB polarization field, see par. 2.7), and two high frequency channels (for example at 410 and 540 GHz, as planned for the OLIMPO ballon-borne experiment, see chapter 5). Peculiar shear-like patterns from foregrounds should be detected at low frequency channels, as well as at high frequency channels. At ~ 217 GHz the CMB polarization field peaks in power and CMB rotational structures can reasonably be expected to emerge from the foregrounds, even if their amplitude in power is incredibly small (see 2.6). Such a ballon-borne instrument is thus required to possess a big throughput telescope, as highlighted in par. 2.7 and extremely sensitive cryogenic detectors again with very high throughput, in order to collect as much power as possible. In chapter 5 we therefore focus on OLIMPO, which is an high-resolution microwave balloon-borne 2.6 m on-axis Cassegrain telescope, the biggest one ever flown on a ballon. The coupling of such a microwave polarization experiment with a two-mirrors on-axis telescope (Cassegrain, primary parabolic mirror, secondary hyperbolic mirror) is optimal, because any off-axis optical element can produce unwanted spurious polarization. The Cassegrain configuration has several advantages, such as the compact structure providing all the same large focal length due to the two-mirrors folding of the light beam, and the correction of light aberrations thanks to the compensation by the secondary mirror. One important disadvantage to take into account (besides the increased amplitude of the sidelobes due to on-axis configuration) for balloon-borne experiments is the possible diffraction introduced by the steel standoffs suspending the secondary mirror in front of the primary [76]. In par. 5.3.5 we shall evaluate their importance together with the sidelobes profile in the particular case of the OLIMPO telescope. Anyway some solutions have been developed to avoid both of these effects, such as in COMPASS [77]: it uses a radio-transparent expanded polystyrene (EPS) conic secondary supporting system.

The shear-like polarizers of figs. 4.4 and 4.5 have been designed adopting the same wiring specifications and criteria of a common linear wire-grid (including of course high and uninterrupted electric conductivity of the strips), such as those used for the polarimetry measurements of par. 4.4. What is needed in

addition for such geometry are circular concentric rings as supports and starting point of the strips, which must form a $\pm 45^\circ$ angle with each of the straight tangent lines to the considered circular ring. The circular rings are needed to avoid spreading of the strips: in fact the strips are never parallel the one to the other, but instead tend to diverge the one from the other as the force lines of a dipole-generated magnetic field. The strips are $\sim 1\mu m$ thick and the minimum distance between two strips is $25\mu m$. The circular rings are optimized to achieve a small angular discontinuity between them (i.e. maximum distance between two strips very close to $25\mu m$): an incoming field sees in fact a shear-like pattern of strips that is continuous and homogeneous with precision of at least 1° . When approaching the center the concentric rings must have progressively smaller radius, because no rotational field can be generated from a point, that is we always need a ring to generate the characteristic shear-like pattern. It's clear the physical analogy with the absence of magnetic monopoles (i.e. isolated magnetic charges), which reveals itself here as a geometric property. In order to avoid border effects we must thus reduce the central hole as much as possible, as compared to the typical working wavelengths, by means of concentric rings of decreasing radius. Such polarizers can be realized with the lithographic technique on a mylar substrate. The main requirements are:

- High electric conductivity of the strips (e.g. gold, $\sigma = 4.52 \cdot 10^7 \Omega^{-1}m^{-1}$);
- Electric continuity of the strips;
- In the case of flipping modulation, a double-sided lithography is necessary, to avoid spurious polarized signal arising from emission of mylar, which would be modulated at the same flipping frequency.

4.3.1 Mueller Matrix Characterization

Now we can try to apply the Stokes formalism to such polarizers and characterize their polarizing action in terms of the usual Mueller matrices (see Appendix A). In order to do this, the best approach to the problem is rewriting the Stokes parameters in polar coordinates (r, θ) , instead of the common cartesian coordinates (x, y) . Moreover we have to rotate the polar coordinate system by, respectively, -45° for the polarizer in fig. 4.4, and $+45^\circ$ for the one in fig. 4.5. The Stokes parameters will carry exactly the same informations, but the linear system we need to solve in order to obtain the coefficients of the Mueller matrix is much simpler in this way.

Let us indicate with one prime the quantities in the -45° rotated polar system, with two primes the quantities in the $+45^\circ$ one, while the ones without primes are non-rotated quantities. Recalling that $\sin(\alpha \pm \beta) = \sin \alpha \cos \beta \pm \sin \beta \cos \alpha$, $\cos(\alpha \pm \beta) = \cos \alpha \cos \beta \mp \sin \alpha \sin \beta$, $\sin(2\alpha) = 2 \sin \alpha \cos \alpha$, $\cos(2\alpha) = \cos^2 \alpha - \sin^2 \alpha$, $\sin(\pi/4) = -\sin(-\pi/4) = \sqrt{2}/2$ and $\cos(\pi/4) = \cos(-\pi/4) =$

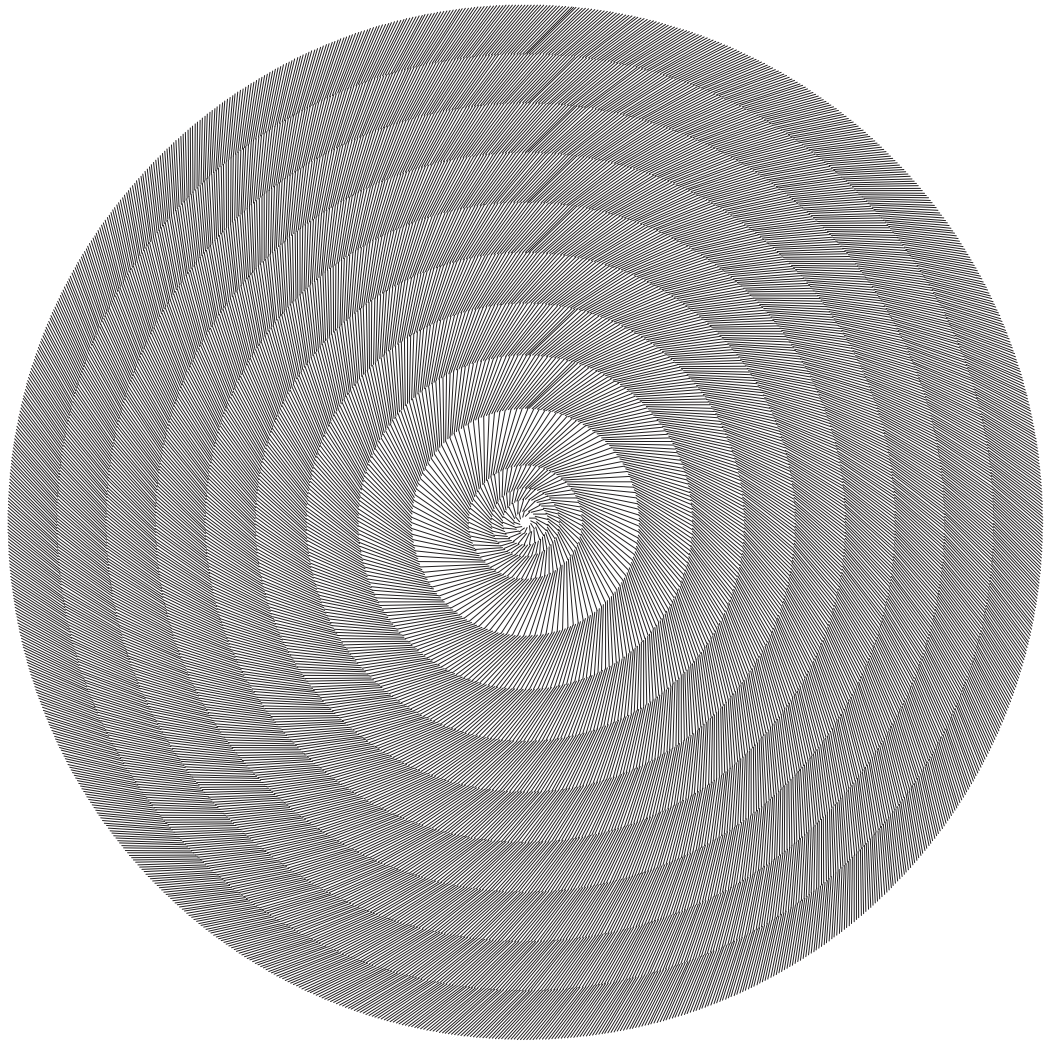


Figure 4.4: CAD project of the -45° shear-like polarizer.

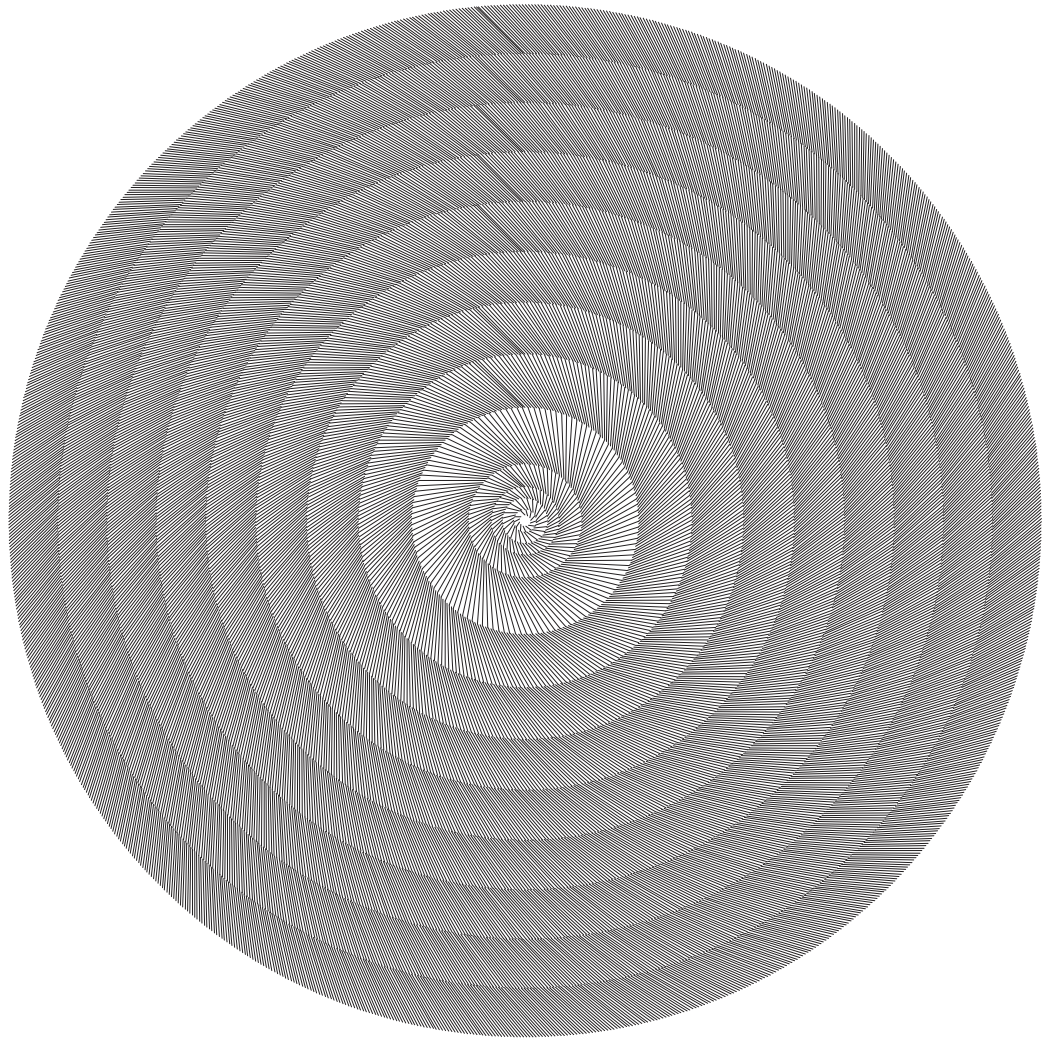


Figure 4.5: CAD project of the twin $+45^\circ$ shear-like polarizer.

$\sqrt{2}/2$, we have:

$$r = \sqrt{x^2 + y^2}, \quad \theta = \arctan\left(\frac{y}{x}\right), \quad (4.93)$$

$$x = r \cos \theta, \quad y = r \sin \theta, \quad (4.94)$$

$$x' = r \cos\left(\theta - \frac{\pi}{4}\right) = \frac{\sqrt{2}}{2} r (\cos \theta + \sin \theta), \quad (4.95)$$

$$y' = r \sin\left(\theta - \frac{\pi}{4}\right) = \frac{\sqrt{2}}{2} r (\sin \theta - \cos \theta), \quad (4.96)$$

$$x'' = r \cos\left(\theta + \frac{\pi}{4}\right) = \frac{\sqrt{2}}{2} r (\cos \theta - \sin \theta), \quad (4.97)$$

$$y'' = r \sin\left(\theta + \frac{\pi}{4}\right) = \frac{\sqrt{2}}{2} r (\cos \theta + \sin \theta), \quad (4.98)$$

$$E_x = E_r \cos \theta e^{i\varphi_x}, \quad E_y = E_r \sin \theta e^{i\varphi_y}, \quad E_r = \sqrt{|E_x|^2 + |E_y|^2}, \quad (4.99)$$

$$E'_x = \frac{\sqrt{2}}{2} E_r (\cos \theta + \sin \theta) e^{i\varphi_x}, \quad (4.100)$$

$$E'_y = \frac{\sqrt{2}}{2} E_r (\sin \theta - \cos \theta) e^{i\varphi_y}, \quad (4.101)$$

$$E''_x = \frac{\sqrt{2}}{2} E_r (\cos \theta - \sin \theta) e^{i\varphi_x}, \quad (4.102)$$

$$E''_y = \frac{\sqrt{2}}{2} E_r (\cos \theta + \sin \theta) e^{i\varphi_y}, \quad (4.103)$$

$$E_r^2 = |E_x|^2 + |E_y|^2 = |E'_x|^2 + |E'_y|^2 = |E''_x|^2 + |E''_y|^2. \quad (4.104)$$

Defining $\Delta\varphi = \varphi_y - \varphi_x$, the Stokes parameters (Appendix A) are now:

$$I = E_x E_x^* + E_y E_y^* = |E_x|^2 + |E_y|^2 = E_r^2, \quad (4.105)$$

$$Q = E_x E_x^* - E_y E_y^* = |E_x|^2 - |E_y|^2 = E_r^2 (\cos^2 \theta - \sin^2 \theta) = E_r^2 \cos(2\theta), \quad (4.106)$$

$$U = E_x E_y^* + E_y E_x^* = 2E_r^2 \sin \theta \cos \theta \cos \Delta\varphi = E_r^2 \sin(2\theta) \cos \Delta\varphi, \quad (4.107)$$

$$V = i(E_x E_y^* - E_y E_x^*) = 2E_r^2 \sin \theta \cos \theta \sin \Delta\varphi = iE_r^2 \sin(2\theta) \sin \Delta\varphi, \quad (4.108)$$

$$I' = E'_x (E'_x)^* + E'_y (E'_y)^* = |E'_x|^2 + |E'_y|^2 = E_r^2, \quad (4.109)$$

$$Q' = E'_x (E'_x)^* - E'_y (E'_y)^* = |E'_x|^2 - |E'_y|^2 = E_r^2 \sin(2\theta), \quad (4.110)$$

$$U' = E'_x (E'_y)^* + E'_y (E'_x)^* = -E_r^2 \cos(2\theta) \cos \Delta\varphi, \quad (4.111)$$

$$V' = iE'_x (E'_y)^* - iE'_y (E'_x)^* = -iE_r^2 \cos(2\theta) \sin \Delta\varphi, \quad (4.112)$$

$$I'' = E''_x (E''_x)^* + E''_y (E''_y)^* = |E''_x|^2 + |E''_y|^2 = E_r^2, \quad (4.113)$$

$$Q'' = E''_x (E''_x)^* - E''_y (E''_y)^* = |E''_x|^2 - |E''_y|^2 = -E_r^2 \sin(2\theta), \quad (4.114)$$

$$U'' = E''_x (E''_y)^* + E''_y (E''_x)^* = E_r^2 \cos(2\theta) \cos \Delta\varphi, \quad (4.115)$$

$$V'' = iE''_x (E''_y)^* - iE''_y (E''_x)^* = iE_r^2 \cos(2\theta) \sin \Delta\varphi. \quad (4.116)$$

We can thus write down our two linear systems in matrix form:

$$\vec{S}' = \mathcal{M}_{-45^\circ} \times \vec{S} \Rightarrow \begin{pmatrix} I' \\ Q' \\ U' \\ V' \end{pmatrix} = p^2 \begin{pmatrix} a'_{11} & a'_{12} & a'_{13} & a'_{14} \\ a'_{21} & a'_{22} & a'_{23} & a'_{24} \\ a'_{31} & a'_{32} & a'_{33} & a'_{34} \\ a'_{41} & a'_{42} & a'_{43} & a'_{44} \end{pmatrix} \times \begin{pmatrix} I \\ Q \\ U \\ V \end{pmatrix} \quad (4.117)$$

$$\vec{S}'' = \mathcal{M}_{+45^\circ} \times \vec{S} \Rightarrow \begin{pmatrix} I'' \\ Q'' \\ U'' \\ V'' \end{pmatrix} = p^2 \begin{pmatrix} a''_{11} & a''_{12} & a''_{13} & a''_{14} \\ a''_{21} & a''_{22} & a''_{23} & a''_{24} \\ a''_{31} & a''_{32} & a''_{33} & a''_{34} \\ a''_{41} & a''_{42} & a''_{43} & a''_{44} \end{pmatrix} \times \begin{pmatrix} I \\ Q \\ U \\ V \end{pmatrix} \quad (4.118)$$

where the factor p^2 parameterizes non-ideal absorption of the wires, assuming isotropic behaviour for simplicity. We obtain solutions only if $\Delta\varphi = 0, \pi$ (linear polarization):

$$\mathcal{M}_{-45^\circ} = \begin{pmatrix} p^2 & 0 & 0 & 0 \\ 0 & 0 & p^2 & 0 \\ 0 & -p^2 & 0 & 0 \\ 0 & 0 & 0 & 0 \end{pmatrix} \quad (4.119)$$

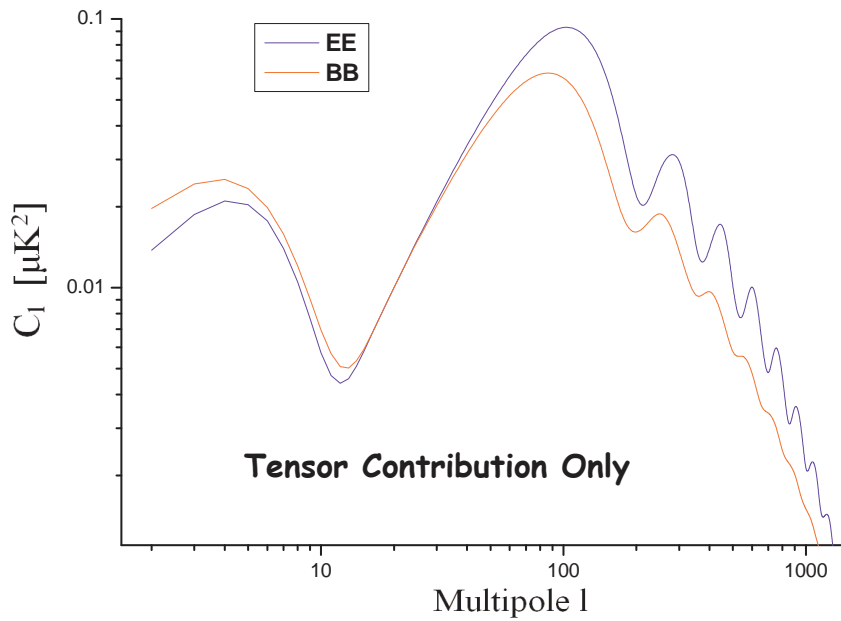
$$\mathcal{M}_{+45^\circ} = \begin{pmatrix} p^2 & 0 & 0 & 0 \\ 0 & 0 & -p^2 & 0 \\ 0 & p^2 & 0 & 0 \\ 0 & 0 & 0 & 0 \end{pmatrix} \quad (4.120)$$

From eqs. 4.119 and 4.120 we see that the action of such polarizers is exactly the one we could expect for symmetry and parity reasons (see par. 2.5 and Appendices A,B), that is as net effect $Q \rightarrow -U$, $U \rightarrow Q$ for \mathcal{M}_{-45° , while $Q \rightarrow U$, $U \rightarrow -Q$ for \mathcal{M}_{+45° .

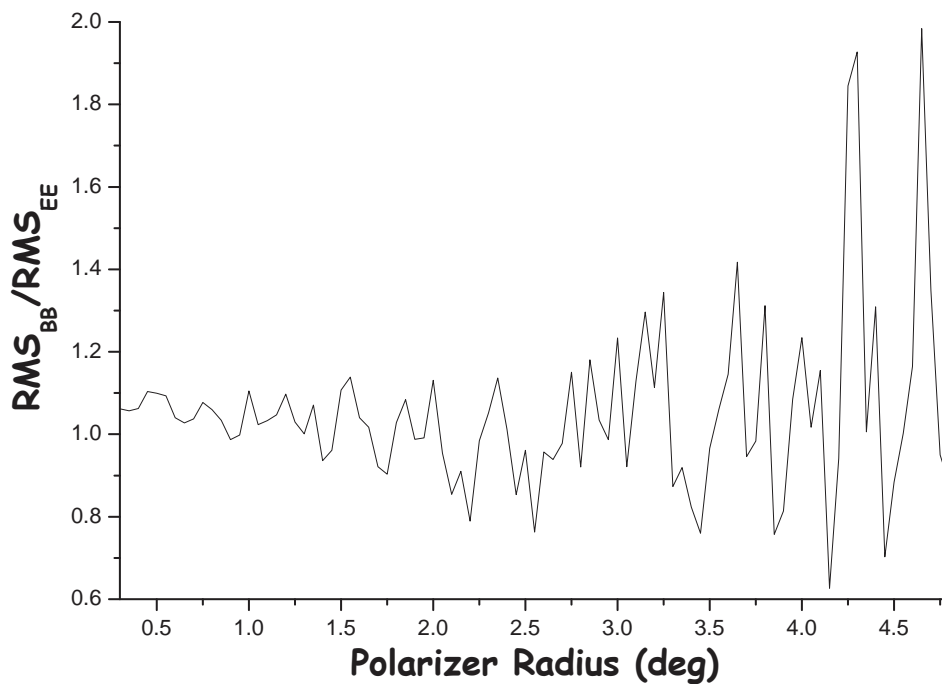
4.3.2 Signal Extraction From Simulated Maps of the Polarized CMB Sky

In order to understand the behaviour of such shear-like polarizers when applied on a rotational field of polarization, we need to perform intensive simulations on the polarized CMB sky. We do not give the details of the whole process, we limit ourselves to describe in a qualitative way the several steps needed, then we will present the first results. First of all, we generated simulated pixelized fullsky maps of the CMB field, which include also the information about polarization. This is achieved by means of the “HEALPIX” routines and facilities [47]. The basic concept is that the celestial sphere is divided into a precise, user-defined number of pixels ($N_{pix} = 12 \cdot n_{side}^2$), substantially equal in area. This number is directly related to the resolution required for such maps: in our case we chose $n_{side} = 1024 \Rightarrow N_{pix} = 12582912$, leading to an ~ 3.4 arcmins resolution of the maps. Each pixel contains the information about the temperature, together with the values of the Stokes parameters Q,U in that particular direction of the sky. The theoretical framework on which the “HEALPIX” routines and facilities are build upon is that depicted in par. 2.4.3: the fundamental numeric codes are CMBFAST [33][34] and CAMB [35], which are based on integration over the sources along the photon past light cone. The routine we used is called *Synfast*: it allows to generate fullsky simulated CMB maps (including polarization), provided certain input spectra of primordial fluctuations and the beam of the experiment. In our case this latter is fixed, FWHM= 4 arcmins, the reason being explained in par. 5.3.5. The input spectra must contain only the tensor contribution, as explained in detail in par. 2.5. The spectra are given in the form of C_l (units: μK^2): their shape is shown in fig. 4.6a. From these, it is possible to create separate maps of pure B-modes and pure E-modes, which of course has no physical meaning, since we saw that tensor fluctuations produce both the gradient and curl components of the polarization field (par. 2.5.4). However this turns out to be the best way to characterize the behaviour of our shear-like polarizer: we need to compare its action on a rotational field, as well as that on an irrotational field. Alternating the shear-like polarizer and its mirror image on the sky, we

can evaluate the difference in signal received by the detector between the two specular configurations, integrating all over the area of the polarizer (all over the pixels of the sky contained in the field of view of the experiment). In fact the polarizer, placed in the focal plane of the experiment, projects its area on the sky, thus defining the field of view: if all of the radiation is collected by a single detector, it turns out that the resulting signal comes from all of the photons in the field of view. In a pixelized map, this means that we need to perform an integration of the polarized signal all over the pixels subtended by the polarizer in the sky. What we expect is that, for a certain angular size (depending on the power spectrum of B-modes), rotational structures in the CMB polarization field will be highlighted, while irrotational patterns will not survive our modulation. The core of such simulations is thus the extraction of a differential integrated signal all over a certain patch of the sky, with a sampling of the pointing directions which depends on the size of the polarizer. In fact we chose to sample the sky at pointing directions separated in both the spherical angular coordinates by half of the angular size of the polarizer. The sky patch analyzed substantially coincides with the “shallow region” of the BOOMERanG experiment [11], i.e. RA= 80 ÷ 100, DEC= −50 ÷ −30. The extraction of the signal is achieved by means of three fundamental steps: we first calculate, given a certain pointing direction j , the direction β_i of the wires of the shear-like polarizers for each one of the i -th pixels contained in a circle centered in the pointing direction with radius R , with respect to a reference meridian in the sky. Then, for each pixel i in the same circle, we evaluate the polarization direction $\theta_i = \arctan(Q_i/U_i)/2$, with respect to the same reference meridian. The signal resulting from each single pixel is obtained as the polarization degree $Q_i^2 + U_i^2$ times the projection along the wires of the polarization direction, i.e. $\cos^2(\beta_i - \theta_i)$ (Malus’ Law). The signal resulting from each pointing direction is thus the integral all over the signals from the i pixels contained in a circle (polarizer) of radius R . During the last step, we calculate the difference in signal with the specular image of the polarizer, that is when the direction of the wires is rotated 90° away with respect to the its mirror polarizer. These operations are carried out over CMB polarization maps of pure B-modes, as well as of pure E-modes. The *rms* signal all over the pointing directions is evaluated for both pure E and B-modes, as a function of the angular dimensions R of the polarizer in the sky. We finally perform the ratio RMS_{BB}/RMS_{EE} . The results of the first set of simulations are shown in fig. 4.6b. The ratio RMS_{BB}/RMS_{EE} is plotted against R . From fig. 4.6b we see that this ratio is almost always greater than unity, with several peaks, indicating the best angular scales for such an analysis. Even if the rotational structures appear to emerge systematically, however this ratio was expected to be much higher, in order to achieve significative extraction of the curl component. A possible reason for such non optimal extraction is the E-B mixing predicted for small patches of sky [46]. It turns out that intensive simulations on fullsky maps



(a) The shape of the spectra (EE and BB) used for our simulations. Both of them arise only from tensor contribution to the polarization field.



(b) Results from the first set of simulations. The ratio of the *rms* signal of a pure rotational field to that of a pure irrotational field is plotted against the radius of the polarizer.

Figure 4.6: Simulations on the polarized CMB sky.

need to be performed to characterize in a satisfactory way such polarizers. Note that an adequate level of computational power is required to perform these simulations.

4.3.3 Effect of Point Sources on CMB Polarization Measurements

As previously anticipated, the presence in the field of view of point sources, such as QSO's and Blazars, can seriously contaminate polarization measurements of the Cosmic Microwave Background (see for example [75] for details). In this paragraph we shall evaluate their importance by means of a quantitative approach on the brightness fluctuations, both in temperature and polarization, due to the integrated flux coming from point sources in a given field of view. The observables we need for such treatment have been already defined in pars. 2.2 and 2.7.

From [75] we learn that the number of sources per steradian N (units: $srad^{-1}$) as a function of their specific flux F_ν (units: $WHz^{-1}m^{-2}$, or more popularly Janskies, $1 Jy = 10^{-26} WHz^{-1}m^{-2}$) can be evaluated from surveys at radio and X-rays frequencies, as a $\log N - \log F_\nu$ relation. The variance of the total flux F_{tot} produced by all of the sources from different directions is:

$$\langle(\Delta F_{tot})^2\rangle = \int_{F_{\nu,min}}^{F_{\nu,max}} F_\nu^2 \frac{dN}{dF_\nu} dF_\nu , \quad (4.121)$$

where the number of sources with flux greater than F_0 is:

$$N(F_\nu > F_0) = \int_{S_0}^{+\infty} \frac{dN}{dF_\nu} dF_\nu \quad \Rightarrow \quad \frac{dN}{dF_\nu} = \frac{d}{dF_\nu} N(F_\nu > F_0) . \quad (4.122)$$

For frequencies between 40 and 100 GHz we get $\langle(\Delta F_{tot})^2\rangle \sim 30 Jy^2 srad^{-1}$ [75]. Focusing first on temperature contamination, we shall evaluate which fluctuation in the CMB temperature is able to produce on the detector the same signal as $\langle(\Delta F_{tot})^2\rangle$ does. The fluctuation in power induced by ΔF_{tot} is:

$$\langle(\Delta W)^2\rangle = A^2 \Omega \langle(\Delta F_{tot})^2\rangle . \quad (4.123)$$

The same fluctuation is induced by a temperature anisotropy ΔT , which produces a brightness fluctuation $\Delta B(\nu, T) = \Delta B$ (see par. 2.7):

$$\langle(\Delta W)^2\rangle = A^2 \Omega^2 \langle(\Delta B)^2\rangle . \quad (4.124)$$

It turns out that:

$$\begin{aligned}
\langle (\Delta W)^2 \rangle &= \Omega \langle (\Delta B)^2 \rangle = \Omega \langle (\Delta T)^2 \rangle \left[\frac{\partial}{\partial T} B(\nu, T) \right]^2 \\
&= \Omega \langle (\Delta T)^2 \rangle \left[B(\nu, T) \frac{x e^x}{e^x - 1} \right]^2,
\end{aligned} \tag{4.125}$$

where $x = \frac{2\pi h\nu}{k_B T}$, as usual. Recalling the definition given in par. 2.4.2 for the power spectrum coefficients, we obtain from eq. 4.125:

$$C_{l, F_{tot}} = \Omega \langle (\Delta B)^2 \rangle = \Omega C_{l, T} \left[B(\nu, T) \frac{x e^x}{e^x - 1} \right]^2, \tag{4.126}$$

$$C_{l, T} = \frac{C_{l, F_{tot}}}{\Omega \left[B(\nu, T) \frac{x e^x}{e^x - 1} \right]^2}. \tag{4.127}$$

As explained in par. 2.4.3, we can evaluate $C_{l, F_{tot}}$ for a Gaussian window function:

$$\langle (\Delta F_{tot})^2 \rangle = \frac{1}{4\pi} \sum_{l=2}^{\infty} (2l+1) W_l C_{l, F_{tot}} = \frac{C_{l, F_{tot}}}{4\pi} \sum_{l=2}^{\infty} (2l+1) W_l, \tag{4.128}$$

$$\sum_{l=2}^{\infty} (2l+1) W_l = \sum_{l=2}^{\infty} (2l+1) e^{-l(l+1)\sigma_{beam}^2} \approx 2 \int_0^{+\infty} dx x e^{-x^2\sigma_{beam}^2} = \sigma_{beam}^{-2},$$

$$C_{l, F_{tot}} = 4\pi \sigma_{beam}^2 \langle (\Delta F_{tot})^2 \rangle, \tag{4.129}$$

In par. 5.3 and Appendix E we will show that the solid angle can be calculated as the integral over the sphere of the instrument *angular response* $AR(\theta, \phi)$, that in our simplified case coincides with a Gaussian of width σ_{beam} , function of only θ , since it is assumed to be symmetric in ϕ :

$$\begin{aligned}
\Omega &= \int_{4\pi} AR(\theta, \phi) d\Omega = \int_0^{2\pi} d\phi \int_0^{\pi} \sin\theta d\theta e^{-\frac{\theta^2}{2\sigma_{beam}^2}} \\
&\approx 2\pi \int_0^{\pi} \theta d\theta e^{-\frac{\theta^2}{2\sigma_{beam}^2}} = 2\pi \sigma_{beam}^2.
\end{aligned} \tag{4.130}$$

From eq. 4.127 we thus obtain:

$$C_{l, T} = \frac{4\pi \sigma_{beam}^2 \langle (\Delta F_{tot})^2 \rangle}{2\pi \sigma_{beam}^2 \left[B(\nu, T) \frac{x e^x}{e^x - 1} \right]^2} = \frac{2 \langle (\Delta F_{tot})^2 \rangle}{\left[B(\nu, T) \frac{x e^x}{e^x - 1} \right]^2}. \tag{4.131}$$

The resulting effect on CMB temperature measurements is shown in fig. 4.7a: using eq. 4.131, TT spectrum is compared to the strong non-thermal spectra characterizing point sources behaviour at different frequencies.

Let us now focus on contamination of polarization measurements. The Stokes parameters cannot be measured with an angular resolution that is greater than that of the experiment, of course. This means that the polarization information inside the beam will be averaged, in the sense that, for example, $Q_{tot} = F_x^{tot} - F_y^{tot}$. If the i -th source has flux F_ν^i , a polarization degree of p_i and polarization direction $\theta_i = 1/2 \arctan(U_i/Q_i)$, it will contribute to Q_{tot} with:

$$\Delta Q_i = F_\nu^i p_i (\cos^2 \theta_i - \sin^2 \theta_i) = F_\nu^i p_i \cos(2\theta_i) . \quad (4.132)$$

The polarization degree of such sources is typically of 5% or even less; we can assume for simplicity $p_i = p = \text{constant}$. Since the fluxes F_ν^i and the directions θ_i are uncorrelated, we can average all over the polarization directions, obtaining:

$$\langle (\Delta Q_{tot})^2 \rangle \approx \int_{F_{\nu,min}}^{F_{\nu,max}} p^2 F_\nu^2 \frac{dN}{dF_\nu} dF_\nu \cdot \left(\frac{1}{\pi} \int_0^\pi \cos^2(2\theta) d\theta \right) = \frac{p^2}{2} \langle (\Delta F_{tot})^2 \rangle . \quad (4.133)$$

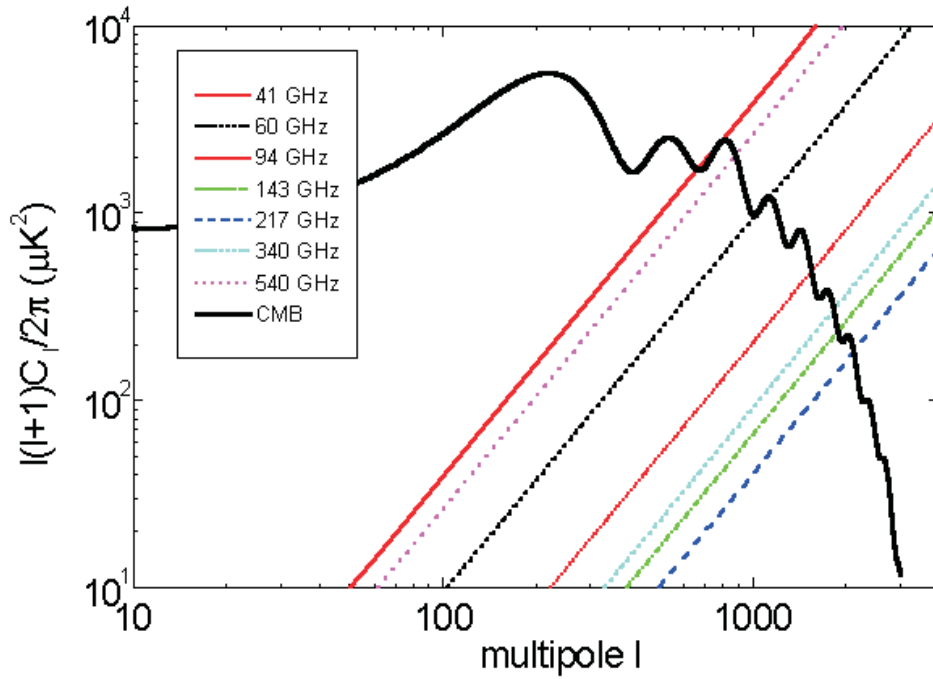
Substituting eq. 4.133 into eq. 4.131, with $C_{l,T} \rightarrow C_{l,Q}$ and $\langle (\Delta F_{tot})^2 \rangle \rightarrow \langle (\Delta Q_{tot})^2 \rangle$, we get:

$$C_{l,Q} \approx \frac{p^2 \langle (\Delta F_{tot})^2 \rangle}{[B(\nu, T) \frac{x e^x}{e^x - 1}]^2} = \frac{p^2}{2} C_{l,T} , \quad (4.134)$$

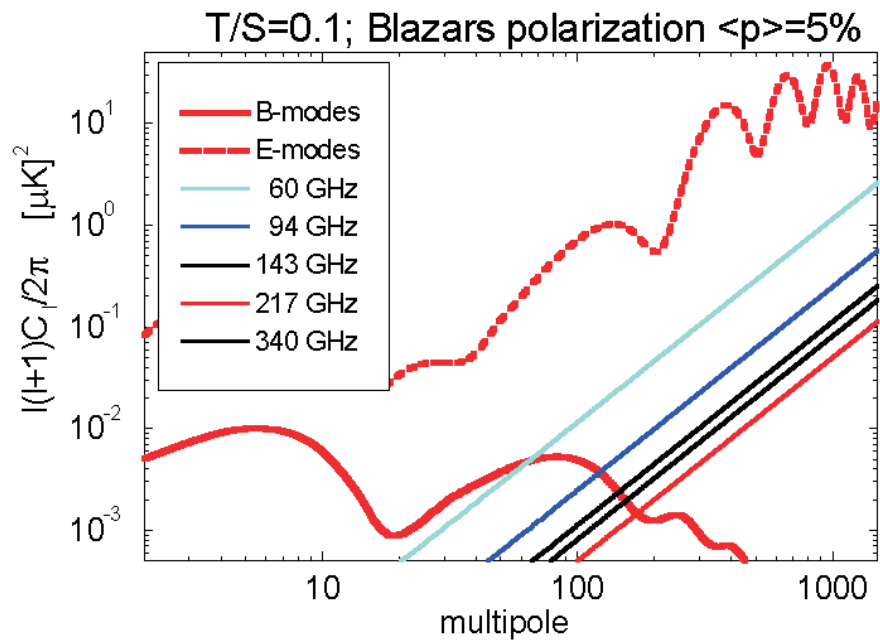
$$C_{l,Q} \simeq C_{l,U} \simeq C_{l,E} \simeq C_{l,B} \simeq \frac{p^2}{2} C_{l,T} . \quad (4.135)$$

4.4 A New Modulation Technique For Polarization: The Reflecting Polarizer

In this section we investigate a new technique of modulating the polarization by means of a reflecting polarizer. The idea has as starting point the exploitation of the Optical Path Difference (OPD) between the field component of the incoming beam which is reflected by the polarizer (that parallel to the wires) and that reflecting on the mirror, behind the polarizer (component perpendicular to the wires). This latter component will be transmitted twice by the polarizer:



(a) Temperature spectrum (TT).



(b) Polarization spectra (EE and BB). An average polarization degree of 5% is assumed.

Figure 4.7: Effect of point sources on CMB Measurements. TT, EE and BB power spectra (see pars. 2.4.3, 2.5.2 and 2.6) as compared to the strong non-thermal spectra, characterizing point sources behaviour at different frequencies.

first, when the incoming beam reaches the polarizer and second, after reflection on the mirror. In fact the mirror reflected component sees exactly the same orientation angle with respect to the wires as when it was first transmitted: so it is transmitted again through the wire-grid, introducing an optical path difference $\Delta\varphi = \frac{2\pi d}{\lambda \cos \chi_i}$, where d is the mirror-polarizer distance, χ_i is the angle of incidence (see fig. 4.9b) and assuming $n_{air} \simeq 1$. This physical effect has been recently investigated by [62]: they developed the so-called Rotating Half Wave Plate (RHWP, see Appendix A), by finely tuning the mirror-polarizer distance so that $\Delta\varphi = \pi \Rightarrow d = (\lambda \cos \chi_i)/2$. Modulation of the polarization is obtained by rotating the polarizer at mechanical frequency ω , so that the rotation angle is $\theta = \omega t$. Most of the spurious effects will have a frequency equal to the mechanical one, while the polarization signal will be modulated at 4ω (see eq. A.42), resulting in an improved extraction of the signal from foregrounds and systematic effects.

Taking this as starting point, here we present a new hardware technique for modulating the polarization, based again on the possibility of finely tuning the distance between the mirror and the polarizer, even if this time there are two peculiar values of the mirror-polarizer distance, which is thus varied continuously forth and back at mechanical frequency ω to achieve modulation, as we'll explain in the following. The idea is therefore to exploit the optical path difference (OPD) in such a way that at a certain distances from the mirror ($d = n\lambda \cos \chi_i$, with $n = 0, 1, 2, \dots$, see pars. 4.2.4, 4.4.3 and fig. 4.9b), the system mirror plus polarizer behaves as a simple mirror, in the sense that all of the incoming power is transmitted back to the detectors (OPD is finely tuned as to provide in-phase superposition of the two orthogonal components, respectively that reflected and that transmitted by the polarizer), while at a (larger) different distance the mirror is no longer efficient because of beam shifting: the output signal as a function of the polarizer rotation angle behaves exactly as if the incoming radiation would be reflected by the polarizer alone (i.e. only the component parallel to wires). A rough estimation of the distance required for excluding the mirror is $d = D_{mir}/\tan \chi_i$, where D_{mir} is the diameter of the mirror. This is true in the case that the polarizer has the same diameter as the mirror and its whole area is illuminated by the incoming parallel beam. Of course the illuminated area can be reduced to achieve smaller values of d : if D_{pol} is the diameter of the effective polarizer area under illumination, we get $d = (D_{mir} + D_{pol})/2 \tan \chi_i$. As anticipated before, modulation of the polarization is achieved moving the mirror forth and back at mechanical frequency ω between the two peculiar positions described above. Some care is needed in reproducing the two positions (an accuracy of 0.07 mm is required to reduce rotation angle dependance of the signal to 1%, as we'll see in par. 4.4.3), in the choice of the modulation frequency, which should be sufficiently high (at least some hertz) to avoid the 1/f noise knee, and finally in ensuring

that the back and forth sliding movement of the mirror is fully compatible with the cryogenic requirements. The main advantage is that this mechanical frequency is completely uncorrelated with the polarizer. In the following we present the first preliminary experimental tests of such a new hardware technique for modulating the polarization: the basic assumption in this method is in fact that there exists a precise position of the mirror with respect to the parallel polarizer where the system behaves as a simple mirror, that is the optical path difference is finely tuned as to provide in-phase superposition of the two orthogonal components, respectively that reflected and that transmitted by the polarizer. As we'll see in par. 4.4.3 this is exactly what happens at $d = n\lambda \cos \chi_i$ (with $n = 0, 1, 2, \dots$) from a theoretical point of view. Of course we need to test how good this theoretical prediction is: this test can be simply realized without a modulation mechanism. It only requires a static apparatus allowing rigid shifting of the mirror forth and back, possibly being controlled by a micrometer head for fine tuning of the position.

The experimental set-up for such polarimetry measurements basically requires a plane mirror parallel to a polarizer and of course a coherent modulated source of millimetric radiation, whose parallel beam hits the mirror-polarizer system with angle of incidence χ_i , and the reflected component propagates back to the detectors with reflection angle $\chi_r = \chi_i$. In the next section we describe the criteria adopted for building the plane mirror and its supporting system; the polarizer is the wire-grid described at the beginning of par. 4.2, while its rotating supporting system is described in par. 4.4.2.

4.4.1 Plane Mirror and Fine Tuned Supporting System

The plane mirror and its supporting system have been designed as in fig. 4.4 in order to satisfy at least the following two hardware requirements:

- as described in par. 4.2, the tungsten wires of the polarizer are tightened inside a steel circular ring (diameter: internal 12.75 cm, external 13.6 cm); such ring has a 2.6 mm step to the wires, which we chose to reduce to 2.5 mm for the coupled step of the mirror, thus guaranteeing a 0.1 mm hardware safety blockage when approaching the mirror to the wires. It turns out that 0.1 mm is the minimum possible mirror-polarizer distance.
- the system supporting the mirror has been designed to couple not only with the micrometer-head-pushed 25 mm diameter steel pivot (fig. 4.9b), used for our preliminary tests, but also for coupling directly to the oscillating arm of a linear actuator (Shaker LDS V404) for future modulation tests. LDS's permanent magnet shakers are designed for accelerometer calibration and small component testing. Low mass armature and a unique suspension system guarantee reliable performance over a wide frequency band.

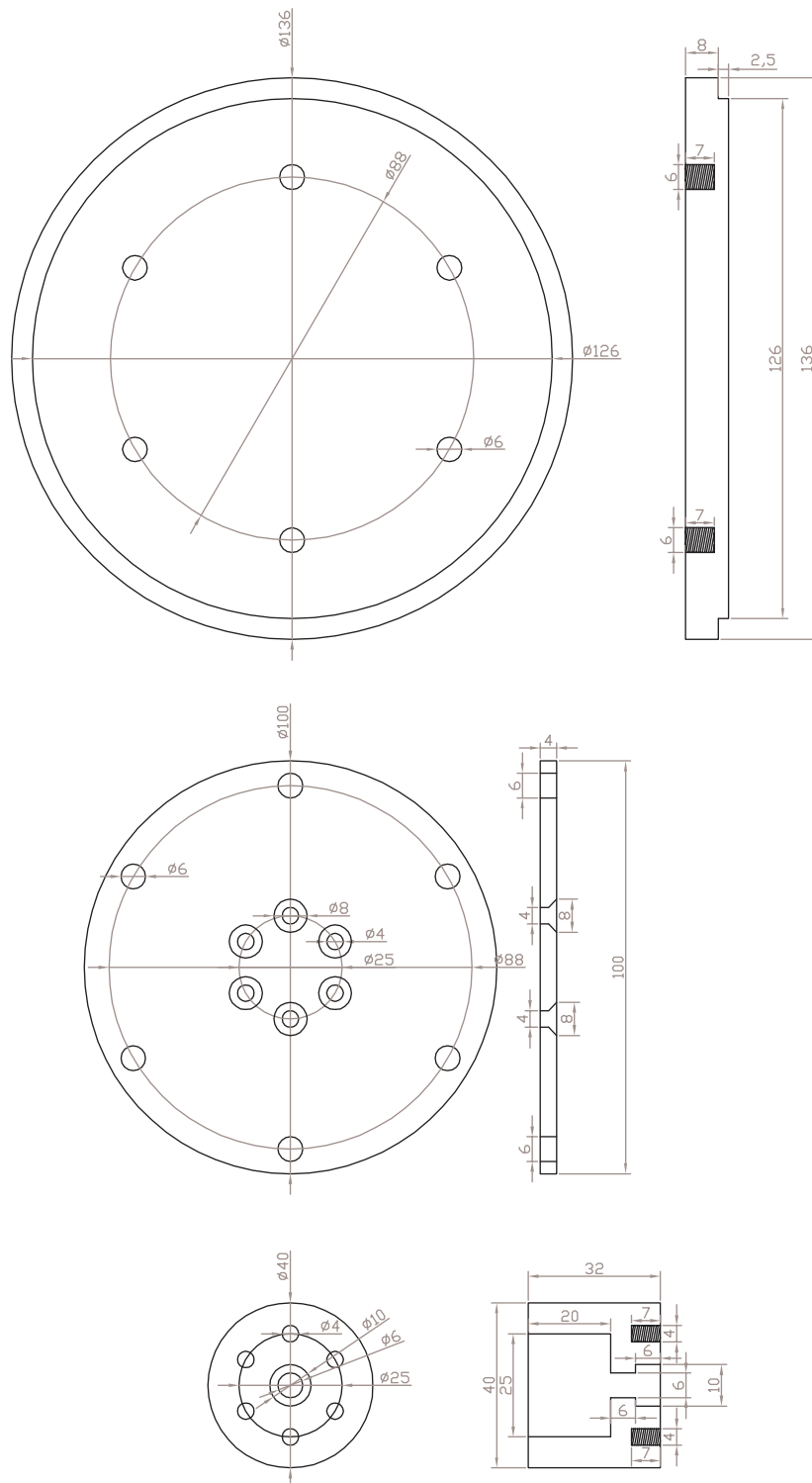
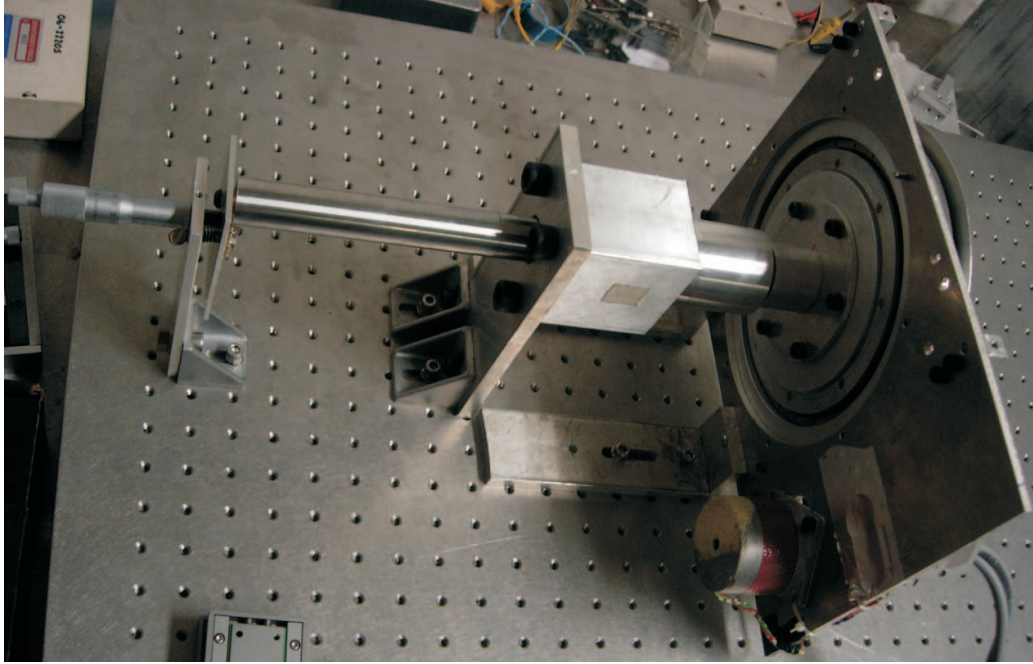
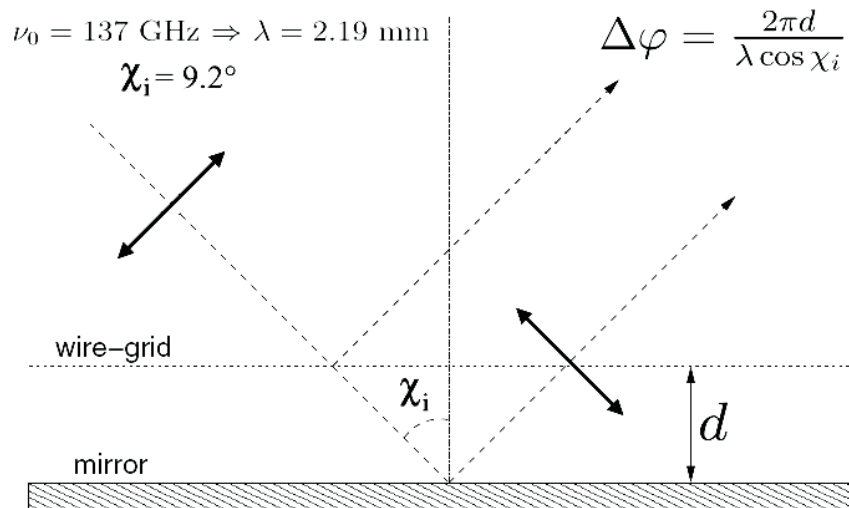


Figure 4.8: CAD drawings: plane mirror and part of its supporting system. Mechanical realization thanks to A. Iacoangeli (Physics Department workshop).



(a) Sketch of the assembled components: the plane mirror is located behind the polarizer (with its rotating support, see par. 4.4.2 and fig. 4.10a): the system supporting the mirror is anchored to the optical bench, while the mirror can rigidly slide back and forth on spherical bearings, thanks to a micrometer-head-pushed 25 mm diameter steel pivot.



(b) Drawing of the experimental set-up: view from the top. See text for details.

Figure 4.9: Experimental set-up for our polarimetry measurements with a reflecting polarizer: the mirror parallelizes the wire-grid at a distance d , which is finely tunable by means of a Mitutoyo 150-801 micrometer head.

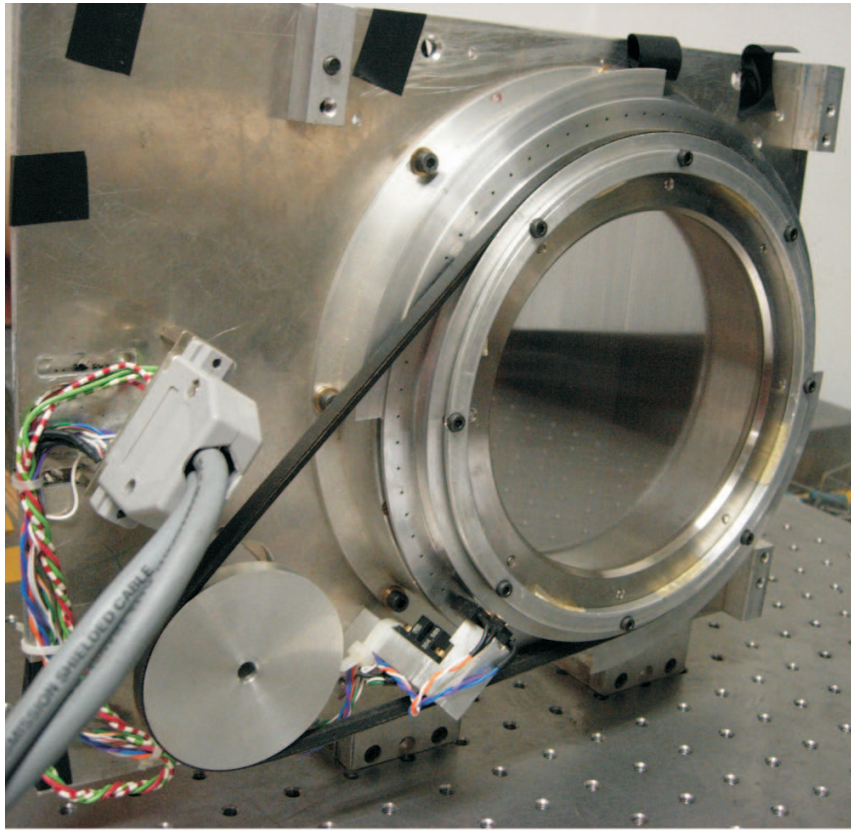
In fig. 4.9a we show a picture of the assembled components: the plane mirror is located behind the polarizer (with its rotating support, see par. 4.4.2 and fig. 4.10a): the system supporting the mirror is anchored to the optical bench, while the mirror can rigidly slide back and forth on spherical bearings, thanks to a micrometer-head-pushed 25 mm diameter steel pivot. The micrometer head is produced by Mitutoyo, model 150-801: this has spherical face, 0-25 mm range, 0.01 mm resolution and 0.002 mm accuracy.

4.4.2 The Rotating Support

The wire-grid, described in par. 4.2, is fixed on an ad-hoc rotating support, providing rotations of the grid about the axis perpendicular to the plane containing the grid. The rotation is performed by a step motor, which transmits the motion to a steel ring surrounding the grid by means of a transmission strap. The step motor is supplied in power by the “IM483 PLG” controller produced by Intelligent Motion System. The step motor is fixed on an aluminium board, together with the ring rotating on spherical bearings, on which the wire-grid is mounted (see fig. 4.10a). A photodiode fixed on the aluminium board is able to read the position of the rotating ring by means of little holes placed at equal angular distance the one from the other on the rotating ring. The system has $360^\circ/2^{12} \simeq 5.3'$ angular resolution. The power supplying the motor and the photodiode readout are interfaced to the electronics box of fig. 4.10b by means of a 25-pin connector. The electronics box has several options, for moving the step motor either continuously or with automatic stepping (driven by the period of an input square wave): we only needed to rotate the system step by step and manually, since we had to wait for the demodulated signal to be stable (because of the Lock-in time constant, see par. 3.8). Furthermore it's possible to select the angular amplitude of the steps by means of an electronic step divider: the amplitude of the step is encoded in digital units (DU) by a binary system counter, from the shortest $2^0 = 1$ to the widest $2^8 = 256$, where $360^\circ = 4096$ DU. We chose to work with step amplitude of $2^6 = 64$ DU $\Rightarrow 5.625^\circ$. A 25-pin connector out of the electronics box provides the parallel output carrying the information of the angular position. By means of an ad-hoc parallel cable, the incoming bytes were read by the parallel port of a laptop, controlled by a C program using the *parapin* library (see also par. 3.11).

4.4.3 Mueller Matrices Characterization: Expected Behaviour

In this section we shall outline the expected behaviour of a reflecting polarizer with variable mirror-polarizer distance. We shall adopt the formalism of Stokes vectors and Mueller matrices, widely treated in Appendix A. The trick is to consider such a complex optical system as a rotating tunable wave plate (phase-shifting element), where the phase shift is simply given by $\Delta\varphi = \frac{2\pi d}{\lambda \cos \chi_i}$,



(a) The wire-grid fixed to its rotating support.



(b) Electronics box controlling the wire-grid rotating support: external view.

Figure 4.10: The wire-grid rotating support and its electronics box.

depending on the mirror-polarizer distance d (see fig. 4.9a). In addition we have to take into account the fact that both the source and the detector used for these measurements are single mode TE₁₀ transmitting and receiving devices (see pars. 4.4.4, 3.2, 3.4 and 3.5). They are able, respectively, to produce and detect, only horizontally polarized beams. In this context this means that both the source and the detector behave exactly as they are coupled with an ideal horizontal polarizer. The incoming beam will thus be characterized by the Stokes vector:

$$\vec{S}_{in} = \begin{pmatrix} I \\ Q \\ U \\ V \end{pmatrix} = \frac{1}{2}I_0 \begin{pmatrix} 1 \\ 1 \\ 0 \\ 0 \end{pmatrix} \quad (4.136)$$

while such single mode TE₁₀ detector will have Stokes vector $\vec{D}_{hor} = \mathcal{M}_P^{hor} \times \vec{D} = (1/2, 1/2, 0, 0)$ where $\vec{D} = (1, 0, 0, 0)$ is the Stokes vector for a common intensity detector and \mathcal{M}_P^{hor} is the Mueller matrix of an ideal horizontal polarizer (see Appendix A). We can now focus on the rotating variable wave plate, also introducing a possible anisotropic behaviour along x and y components of the field. The problem is investigated from two different points of view: both derivations will furnish exactly the same theoretical prediction.

As a first approach, we introduce the anisotropic behaviour in the phase-shifting element, i.e. we find the Mueller matrix of a non-rotating Anisotropic Tunable Wave Plate (ATWP). The field components are:

$$E'_x = p_x E_x e^{i\Delta\varphi/2} \quad \text{and} \quad E'_y = p_y E_y e^{-i\Delta\varphi/2}, \quad (4.137)$$

where $0 \leq p_x, p_y \leq 1$ parameterize anisotropic behaviour along x and y field components. The resulting Stokes parameters are now:

$$I' = E'_x (E'_x)^* + E'_y (E'_y)^* = p_x^2 E_x E_x^* + p_y^2 E_y E_y^*, \quad (4.138)$$

$$Q' = E'_x (E'_x)^* - E'_y (E'_y)^* = p_x^2 E_x E_x^* - p_y^2 E_y E_y^*, \quad (4.139)$$

$$\begin{aligned} U' &= E'_x (E'_y)^* + E'_y (E'_x)^* = p_x p_y (E_x E_y^* e^{i\Delta\varphi} + E_y E_x^* e^{-i\Delta\varphi}) \\ &= p_x p_y [\cos \Delta\varphi (E_x E_y^* + E_y E_x^*) + i \sin \Delta\varphi (E_x E_y^* - E_y E_x^*)] , \end{aligned} \quad (4.140)$$

$$\begin{aligned} V' &= i E'_x (E'_y)^* - i E'_y (E'_x)^* = i p_x p_y (E_x E_y^* e^{i\Delta\varphi} - E_y E_x^* e^{-i\Delta\varphi}) \\ &= p_x p_y [\cos \Delta\varphi (E_x E_y^* - E_y E_x^*) + i \sin \Delta\varphi (E_x E_y^* + E_y E_x^*)] , \end{aligned} \quad (4.141)$$

Recalling eqs. A.14 and A.24 such linear system is easily solved to obtain the Mueller matrix of a non-rotating Anisotropic Tunable Wave Plate (ATWP):

$$\mathcal{M}_{ATWP} = \frac{1}{2} \begin{pmatrix} p_x^2 + p_y^2 & p_x^2 - p_y^2 & 0 & 0 \\ p_x^2 - p_y^2 & p_x^2 + p_y^2 & 0 & 0 \\ 0 & 0 & 2p_x p_y \cos \Delta\varphi & 2p_x p_y \sin \Delta\varphi \\ 0 & 0 & -2p_x p_y \sin \Delta\varphi & 2p_x p_y \cos \Delta\varphi \end{pmatrix} \quad (4.142)$$

In this first approach the output signal, S_{out} , is thus simply obtained sandwiching this matrix between the usual rotation matrices $\mathcal{M}_{rot}(-\theta)$, $\mathcal{M}_{rot}(\theta)$, and inserting the expressions for the incoming Stokes vector and the polarization sensitive intensity detector:

$$\begin{aligned} S_{out} &= \vec{D}_{hor} \times \mathcal{M}_{rot}(-\theta) \times \mathcal{M}_{ATWP} \times \mathcal{M}_{rot}(\theta) \times \vec{S}_{in} \\ &= \frac{1}{4} I_0 (2p_x^2 \cos^4 \theta + p_x p_y \cos \Delta\varphi \sin^2 (2\theta) + 2p_y^2 \sin^4 \theta) . \end{aligned} \quad (4.143)$$

The second approach is equivalent from a physical point of view, but mathematically different: therefore we expect the resulting expression for the output signal to coincide with the one in eq. 4.143. What changes now is that the anisotropic behaviour is introduced in the rotator, while the Mueller matrix for the tunable wave plate is that of eq. A.32. Let us now find the Mueller matrix of such anisotropic rotator. The field components are:

$$E'_x = p_x E_x \cos \theta + p_y E_y \sin \theta \quad \text{and} \quad E'_y = -p_x E_x \sin \theta + p_y E_y \cos \theta , \quad (4.144)$$

The resulting Stokes parameters are now:

$$\begin{aligned} I' &= p_x^2 E_x E_x^* \cos^2 \theta + p_y^2 E_y E_y^* \sin^2 \theta + p_x^2 E_x E_x^* \sin^2 \theta + p_y^2 E_y E_y^* \cos^2 \theta + \\ &+ 2p_x p_y E_x E_y^* \cos \theta \sin \theta - 2p_x p_y E_y E_x^* \cos \theta \sin \theta \\ &= p_x^2 E_x E_x^* + p_y^2 E_y E_y^* , \end{aligned} \quad (4.145)$$

$$\begin{aligned} Q' &= p_x^2 E_x E_x^* \cos^2 \theta + p_y^2 E_y E_y^* \sin^2 \theta + 2p_x p_y E_x E_y^* \cos \theta \sin \theta + \\ &- p_x^2 E_x E_x^* \sin^2 \theta - p_y^2 E_y E_y^* \cos^2 \theta + 2p_x p_y E_y E_x^* \cos \theta \sin \theta \\ &= \cos(2\theta) (p_x^2 E_x E_x^* - p_y^2 E_y E_y^*) + p_x p_y \sin(2\theta) (E_x E_y^* + E_y E_x^*) , \end{aligned} \quad (4.146)$$

$$\begin{aligned} U' &= p_x p_y (E_x E_y^* + E_y E_x^*) (\cos^2 \theta - \sin^2 \theta) + \\ &- 2 \sin \theta \cos \theta (p_x^2 E_x E_x^* + p_y^2 E_y E_y^*) \\ &= p_x p_y (E_x E_y^* + E_y E_x^*) \cos(2\theta) - \sin(2\theta) (p_x^2 E_x E_x^* + p_y^2 E_y E_y^*) , \end{aligned} \quad (4.147)$$

$$\begin{aligned} V' &= i p_x p_y (E_x E_y^* - E_y E_x^*) (\cos^2 \theta + \sin^2 \theta) \\ &= i p_x p_y (E_x E_y^* - E_y E_x^*) . \end{aligned} \quad (4.148)$$

The Mueller matrix of an anisotropic rotator is thus:

$$\mathcal{M}_{rot}^{ani}(\theta) = \frac{1}{2} \begin{pmatrix} p_x^2 + p_y^2 & p_x^2 - p_y^2 & 0 & 0 \\ (p_x^2 - p_y^2) \cos(2\theta) & (p_x^2 + p_y^2) \cos(2\theta) & 2p_x p_y \sin(2\theta) & 0 \\ -(p_x^2 - p_y^2) \sin(2\theta) & -(p_x^2 + p_y^2) \sin(2\theta) & 2p_x p_y \cos(2\theta) & 0 \\ 0 & 0 & 0 & p_x p_y \end{pmatrix} \quad (4.149)$$

This time the output signal is obtained sandwiching the Mueller matrix of the Tunable Wave Plate of eq. A.32 between the anisotropic rotation matrices $\mathcal{M}_{rot}^{ani}(-\theta)$, $\mathcal{M}_{rot}^{ani}(\theta)$, and inserting the expressions for the incoming Stokes vector and the polarization sensitive intensity detector:

$$\begin{aligned} S_{out} &= \vec{D}_{hor} \times \mathcal{M}_{rot}^{ani}(-\theta) \times \mathcal{M}_{TWP} \times \mathcal{M}_{rot}^{ani}(\theta) \times \vec{S}_{in} \\ &= \frac{1}{4} I_0 (2p_x^2 \cos^4 \theta + p_x p_y \cos \Delta\varphi \sin^2(2\theta) + 2p_y^2 \sin^4 \theta) , \end{aligned} \quad (4.150)$$

which coincides with 4.143, as expected. We see that the condition for S_{out} to be independent on θ is to achieve $\cos \Delta\varphi = 1$ so that we get (if $p_x \simeq p_y$):

$$2p_x^2 \cos^4 \theta + p_x p_y \sin^2(2\theta) + 2p_y^2 \sin^4 \theta = constant . \quad (4.151)$$

Of course such condition is satisfied for $\Delta\varphi = 2n\pi$, with $n = 0, 1, 2, \dots$, implying $d = n\lambda \cos \chi_i$. In fig. 4.11 we show the expected behaviour as a function of both θ and $\Delta\varphi$, in the case $p_x \simeq p_y$.

4.4.4 Measurement Strategy

The experimental apparatus used for such preliminary test is described in pars. 4.4.1 and 4.4.2. The modulated microwave coherent source is described in chapter 3, together with the detector, the coupled feed horns and the HDPE lenses used as focusing elements. Amplifiers were not used. Working frequency was set to be $\nu_0 = 137$ GHz $\Rightarrow \lambda = 2.19$ mm (120-147 GHz Gunn oscillator, see Appendix C), while the angle of incidence was $\chi_i = (9.2 \pm 0.2)^\circ$, as shown in fig. 4.9a. An horizontally polarized parallel beam came out of the oscillator-waveguide-horn-lens system, hitting with angle χ_i the polarizer-mirror system (with micrometer tunable reciprocal distance) and reflecting back to the lens-horn-waveguide-detector system. All of the non optically active surfaces were covered with eccosorb, in order to avoid reflections from the surroundings: also the rotating support and the optical bench surface were hidden with eccosorb. The scans were first performed varying the rotation angle of the wire-grid from 0° to 180° (vertical wires), while the mirror-polarizer distance d was kept fixed

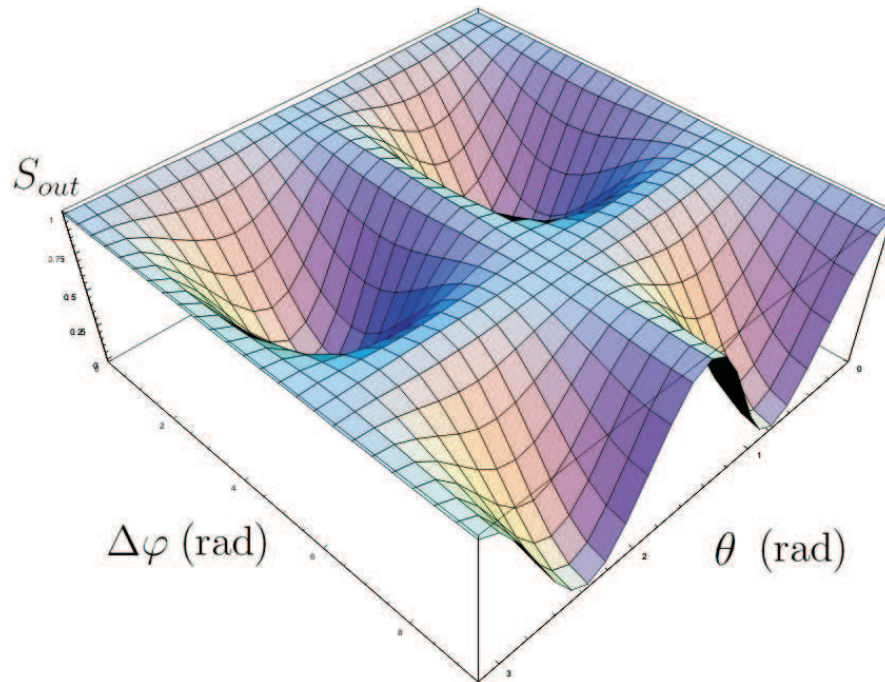


Figure 4.11: The expected normalized signal as a function of the phase shift $\Delta\varphi$ and the rotation angle θ . We take $I_0 = 2$, $p_x \simeq p_y$, $0 \leq \theta \leq \pi$ and $0 \leq \Delta\varphi \leq 3\pi$.

(see par. 4.4.2). Then we performed scans varying the mirror-polarizer distance from 0.1 to 23.6 mm, while the rotation angle was kept fixed. Data acquisition is described in par. 3.11. Each experimental point is the mean value upon at least 10 measures, with associated statistical uncertainty. We saw in par. 4.4.1 that it is impossible to place the mirror closer than 0.1 mm to the polarizer (hardware safety blockage). Since the dependance of S_{out} on d is strong, it turns out that we should not focus on the first resonance ($n = 0$), but rather on the second one ($n = 1 \Rightarrow d = \lambda \cos \chi_i \simeq 2.16$ mm). We also performed scans when the mirror is excluded, thanks to beam shifting, where the system is expected to behave simply as a polarizer.

4.4.5 Reflecting Polarizer: Results

In the following we present the results: the red solid line represents the least-squares fit to the data, which allows to evaluate the absorption parameters p_x, p_y . Also the mirror-polarizer distance d is derived from the fitting method, and compared to the one we measured with the micrometer head: we always found these two quantities to agree with satisfying grade. The angle of incidence χ_i is instead kept fixed in the fit, since the dependence of S_{out} on it is very weak, as compared to the one in d . Figs. 4.13, 4.14, 4.15 and 4.16 clearly show the optimal agreement with the expected behaviour (see par. 4.4.3): note

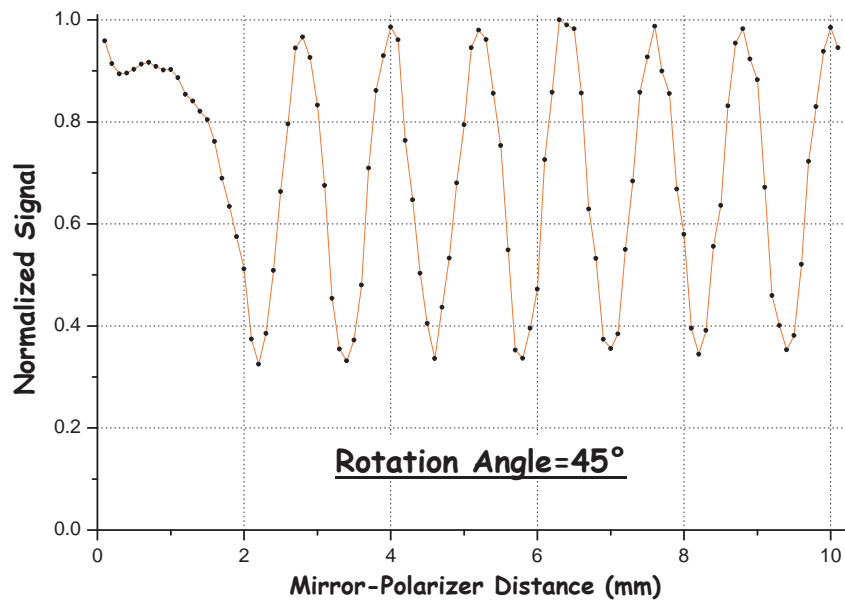


Figure 4.12: The scan is performed varying the mirror-polarizer distance from 0.1 to 23.6 mm, while the rotation angle is kept fixed at 45°. Each experimental point is the mean value upon at least 10 measures, displayed with the associated uncertainty.

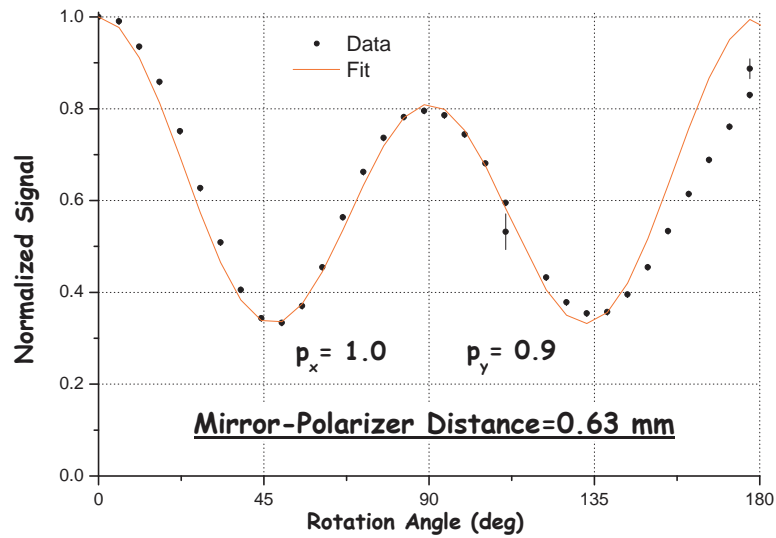


Figure 4.13: The scan is performed varying the rotation angle from 0° to 180° (vertical wires), while the mirror-polarizer distance is kept fixed at 0.63 mm. At 90° (horizontal wires) the incoming polarization state is parallel to the wires. Each experimental point is the mean value upon at least 10 measures, displayed with the associated uncertainty. The absorption parameters p_x, p_y are found by means of a least-squares fit (red solid line).

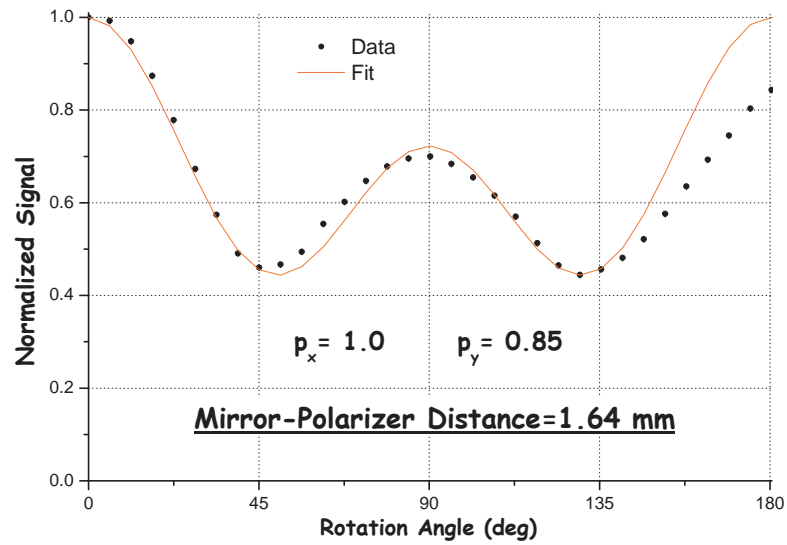


Figure 4.14: The scan is performed varying the rotation angle from 0° to 180° (vertical wires), while the mirror-polarizer distance is kept fixed at 1.64 mm. At 90° (horizontal wires) the incoming polarization state is parallel to the wires. Each experimental point is the mean value upon at least 10 measures, displayed with the associated uncertainty. The absorption parameters p_x, p_y are found by means of a least-squares fit (red solid line).

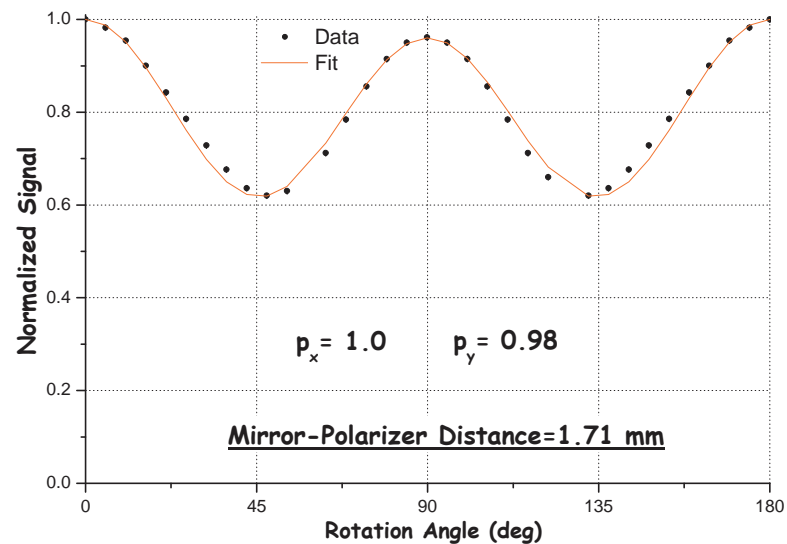


Figure 4.15: The scan is performed varying the rotation angle from 0° to 180° (vertical wires), while the mirror-polarizer distance is kept fixed at 1.71 mm. At 90° (horizontal wires) the incoming polarization state is parallel to the wires. Each experimental point is the mean value upon at least 10 measures, displayed with the associated uncertainty. The absorption parameters p_x, p_y are found by means of a least-squares fit (red solid line).

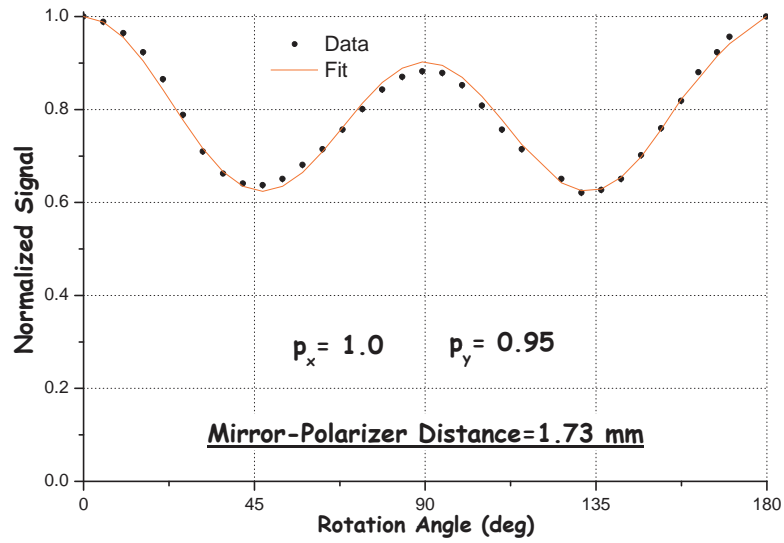


Figure 4.16: The scan is performed varying the rotation angle from 0° to 180° (vertical wires), while the mirror-polarizer distance is kept fixed at 1.73 mm. At 90° (horizontal wires) the incoming polarization state is parallel to the wires. Each experimental point is the mean value upon at least 10 measures, displayed with the associated uncertainty. The absorption parameters p_x, p_y are found by means of a least-squares fit (red solid line).

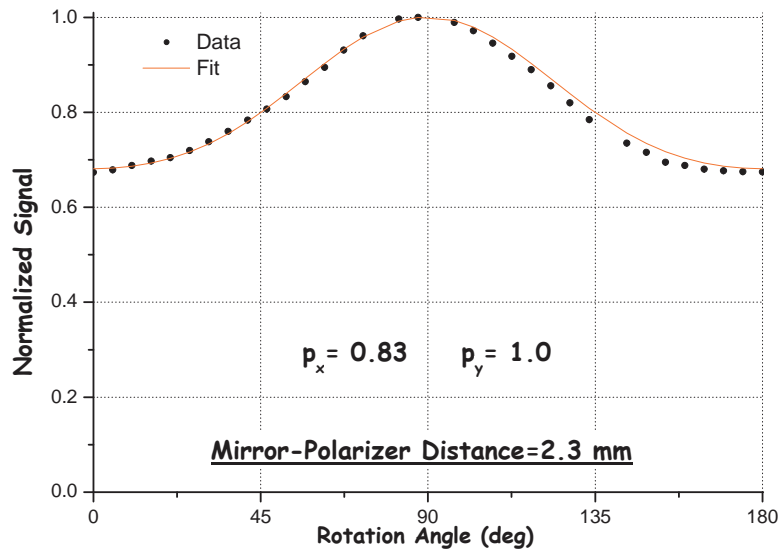


Figure 4.17: The scan is performed varying the rotation angle from 0° to 180° (vertical wires), while the mirror-polarizer distance is kept fixed at 2.30 mm. At 90° (horizontal wires) the incoming polarization state is parallel to the wires. Each experimental point is the mean value upon at least 10 measures, displayed with the associated uncertainty. The absorption parameters p_x, p_y are found by means of a least-squares fit (red solid line).

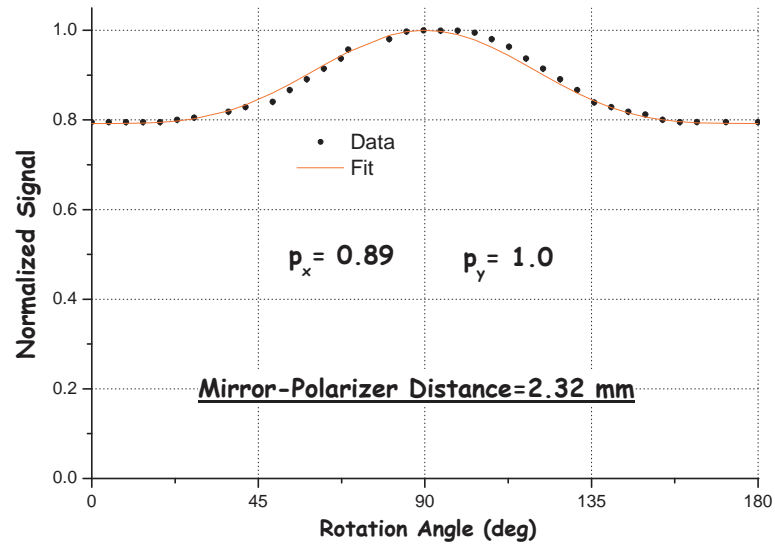


Figure 4.18: The scan is performed varying the rotation angle from 0° to 180° (vertical wires), while the mirror-polarizer distance is kept fixed at 2.32 mm. At 90° (horizontal wires) the incoming polarization state is parallel to the wires. Each experimental point is the mean value upon at least 10 measures, displayed with the associated uncertainty. The absorption parameters p_x, p_y are found by means of a least-squares fit (red solid line).

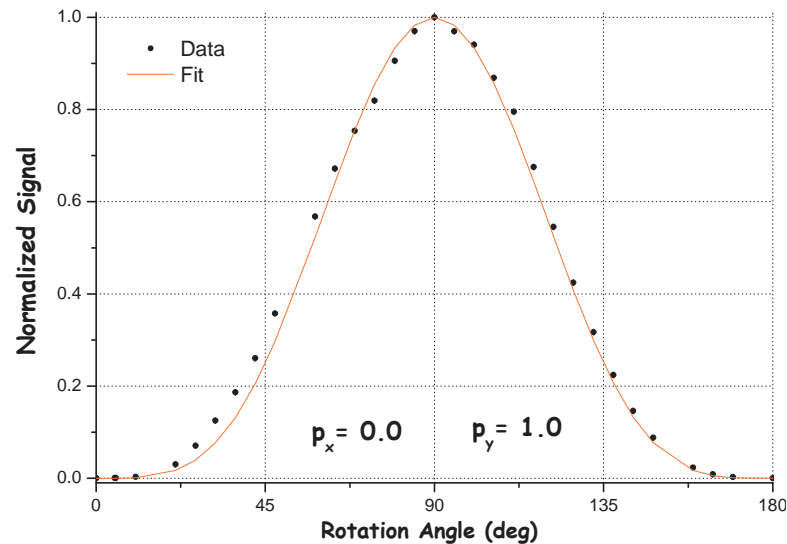


Figure 4.19: The mirror is excluded thanks to beam shifting: the system behaves as a simple polarizer. The scan is performed varying the rotation angle from 0° to 180° (vertical wires). At 90° (horizontal wires) the incoming polarization state is parallel to the wires. Each experimental point is the mean value upon at least 10 measures, displayed with the associated uncertainty. The absorption parameters p_x, p_y are found by means of a least-squares fit (red solid line).

that the value of p_y changes at each measurement, suggesting a non perfect optical alignment of the system and also an effect of beam shifting, probably due to non optimal vignetting of the beams. These aspects need to be improved. Looking at figs. 4.17 and 4.18, representing the preliminary measurements for testing the reflecting polarizer in the proximity of the first resonance, we clearly see a residual polarizing action. The resonance lies at about 2.32 mm (instead of the 2.16 mm predicted), but the system does not behave as a perfect mirror, there is still a polarizing effect. Finally, in fig. 4.19 we show the results obtained excluding the mirror, thanks to beam shifting: the system becomes a simple polarizer in reflection, with the characteristic $\sin^4\theta$ behaviour. We conclude that such a system appears to follow the expected behaviour, thus suggesting a possible future application for modulating a rotational field of polarization. Anyway, further work is needed to improve such measurements, starting with the two problems highlighted above, i.e. non perfect optical alignment of the system and non optimal vignetting of the beams.

Chapter 5

The Telescope

5.1 Introduction

The actual effectiveness of an experiment involving a telescope is mainly characterized by means of the throughput, a quantity defined as the effective area of the telescope times the solid angle subtended by the telescope itself on the sky (the angular resolution), i.e. $A\Omega$. Moreover it is well-known that the best configuration for a microwave polarization experiment is with a two-mirrors on-axis telescope (Cassegrain, primary parabolic mirror, secondary hyperbolic mirror), because any off-axis optical element can produce unwanted spurious polarization. The Cassegrain configuration has several advantages, such as the compact structure providing all the same large focal length due to the two-mirrors folding of the light beam, and the correction of light aberrations thanks to the compensation by the secondary mirror. These are the reasons why a polarization experiment should make use of large-area on-axis Cassegrain telescope, such as the one designed for the OLIMPO experiment, for which experiment we shall give a brief description in par. 5.2. It's a great opportunity to deal with the biggest telescope ever flown on a balloon, in order to study the beam properties and the sidelobes design of such a on-axis configuration for a future polarization experiment. One important disadvantage to take into account (besides the increased amplitude of the sidelobes due to on-axis configuration) for balloon-borne experiments is the possible diffraction (and spurious polarization) introduced by the steel standoffs suspending the secondary mirror in front of the primary [76]. In the following we shall evaluate their importance together with the sidelobes profile in the particular case of the OLIMPO telescope. Anyway some solutions have been developed to avoid both of these effects, such as in COMPASS [77]: it uses a radio-transparent expanded polystyrene (EPS) conic secondary supporting system. Finite Element Analysis (FEA) was used to design such foam support system to minimize the optical depth while providing sufficient stiffness to position and stabilize the secondary mirror with 1 mm resolution.

OLIMPO is a high-resolution microwave balloon-borne 2.6 m on-axis Cassegrain telescope, mainly developed between the physics department of “La Sapienza” in Rome and the CNR area of “Tor Vergata” University, also in Rome. It will measure the Sunyaev-Zel’dovich effect in clusters of galaxies during a long-duration flight (> 10 days). OLIMPO will carry out a survey of 40 clusters in four frequency bands centered at 140, 220, 410 and 540 GHz. We briefly describe in section 5.2 the OLIMPO instrument and its scientific goals, closely following [51]. Then we focus on the telescope (par. 5.2.4) and its angular response measurements (par. 5.2.4): we first describe the expected behaviour of such Cassegrain system (par. 5.3.1), i.e. a few arcmin angular resolution, depending on the frequency; the ground attitude control system of the telescope is described in par.5.3.2, while the whole experimental apparatus needed for such measurement is described in detail in chapter 3. After defining the experimental strategy (par. 5.3.3) and investigating the optical coupling between the telescope and the receivers (par. 5.3.4), we finally give the results in par. 5.3.5. In the last section (5.4) we concentrate on the optics box re-imaging system, for which alignment measurements have been carried out both in the optical (par. 5.4.1) and at microwave frequencies (par. 5.4.2).

5.2 Description of the OLIMPO Experiment

OLIMPO will carry out a survey in four frequency bands centered at 140, 220, 410 and 540 GHz. The high Galactic latitude sky at infrared and millimetric frequencies has three main sources of diffuse emission: the Cosmic Microwave Background (CMB) primary anisotropy, the Sunyaev-Zel’dovich effect in clusters of galaxies, and the Far Infrared Background (FIRB) from early galaxies. At low frequencies (below 60 GHz) interstellar emission of spinning dust grains, free-free and synchrotron emission from the interstellar medium dominate over the cosmological background, while at high frequencies (above 400 GHz) the clumpy foreground from “cirrus clouds” of interstellar dust dominates the sky brightness even at high Galactic latitudes. The OLIMPO bands are chosen in order to optimally separate these components and isolate the SZ effect. The possibility to carry out simultaneous observations at frequencies where the SZ spectrum is negative and at frequencies where it is positive, together with the large-area telescope, make the OLIMPO instrument unique (see [50] for a review of the SZ effect). We also emphasize the importance of an experiment with such high angular resolution to investigate the small scale anisotropies, in order to constrain the damping scale of the CMB temperature power spectrum (see the end of par. 2.4.3), which turns out to be an indirect probe of adiabatic primordial fluctuations, predicted by all generic inflationary models.

5.2.1 Small Scale Temperature Anisotropy of the CMB

Taking advantage of its high angular resolution (a few arcmin, depending on the frequency), and concentrating on a limited area of the sky, OLIMPO will be able to measure the angular power spectrum of the CMB up to multipoles $l \lesssim 3000$, significantly higher than BOOMERanG, WMAP and Planck. A realistic simulation of the measurement is shown in fig. 5.1:

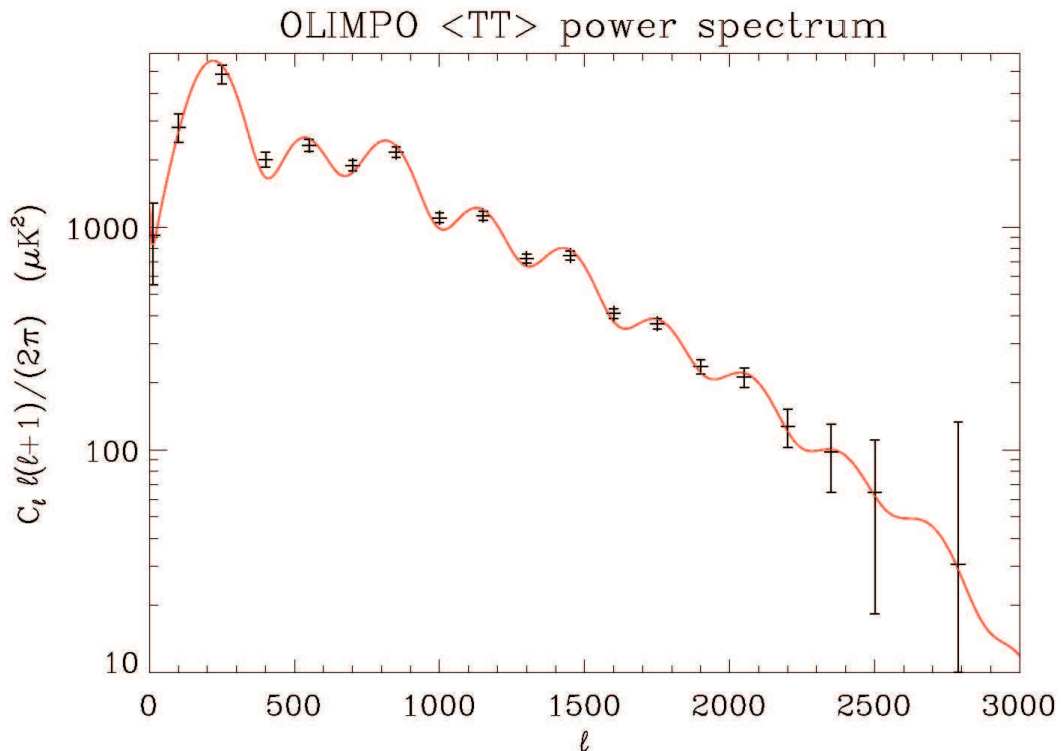


Figure 5.1: Angular power spectrum of CMB anisotropy expected from OLIMPO observations. The simulations assume 4 days of integration over $f_{sky} = 0.3\%$ of the sky; 37 detectors with $NET = 200 \mu K / \sqrt{Hz}$, and an angular resolution of $5'$ FWHM (see par. 3.7 for the definition of NET).

The high multipoles tail of the power spectrum of the sky includes contributions from populations of discrete sources, such as distant clusters, early galaxies and Active Galactic Nuclei (AGNs). Only multi-band observations can discriminate between these contributions. For example, the OLIMPO measurements will shed light on the problem of “excess” fine-scale anisotropy detected by CBI and BIMA at multipoles $\gtrsim 2000$ [52],[53] and also on the typical damping scale of the temperature power spectrum. I wish to stress here that constraining the damping scale of the CMB temperature power spectrum will provide an indirect probe of the adiabatic nature of primordial fluctuations, which is a

generic prediction of all inflationary models (see the end of par. 2.4.3). The bands of OLIMPO listed above have been selected for optimal component separation by means of extensive simulations of the mm/sub-mm sky [80].

5.2.2 S-Z Effect in Cluster of Galaxies

The OLIMPO bands are chosen to bracket the null of the thermal S-Z effect (see fig. 5.2).

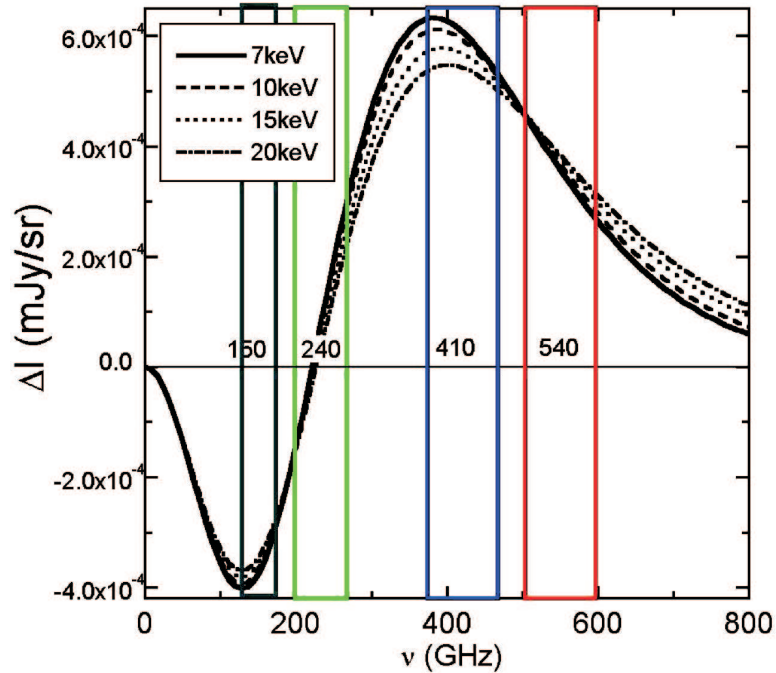


Figure 5.2: Spectrum of the Sunyaev-Zel'dovich effect in a rich cluster of galaxies, for different temperatures of intra-cluster electrons. The spectrum is compared with the OLIMPO bands at 150, 240, 410 and 540 GHz.

The peculiar shape of the effect allows an effective separation from CMB primary anisotropies and other foregrounds. OLIMPO is planned to map about 40 known clusters during each of the planned flights. Reasonable integration time for each target can thus easily be several hours, spread on a sky patch of about 1 square degree centered on the cluster. Assuming a detector noise similar to the one achieved with BOOMERanG (i.e. $150\mu K/\sqrt{Hz}$ for each detector at 140 GHz), and using the nominal configuration of the four arrays of bolometers (one for each frequency channel), simulations show that the typical cluster parameters, the CMB (ΔT) and dust ($\Delta\tau$) anisotropy can all be recovered with $\lesssim 10\%$ accuracy. These measurements will be combined with X-ray measurements to build a ‘‘Hubble’s diagram’’ for the determination of

H_o (see par. 1.2). It's also expected the detection of previously unknown clusters in the deep CMB anisotropy survey by OLIMPO. Such deep S-Z surveys will yield independent estimates of $\Omega_{\Lambda,0}$ and of $\Omega_{m,0}$ through the evaluation of clusters counts, and the shape of the S-Z power spectrum.

5.2.3 FIR Background

Many indications favor the bottom-up scenario for structure formation in the Universe, that is small structures formed first, and larger structures merged later. Star forming regions in early galaxies should have produced intense thermal radiation from heated dust particles, which is now visible in the sub-mm band as the Extragalactic Far Infrared Background (FIRB) detected by COBE-FIRAS [12]. Resolving the FIR Background and studying the unresolved component will allow to investigate the cosmic “middle ages” at $z = 1 - 10$, when light shone again in the Universe after the “dark ages” following recombination. Cosmic star formation history will thus be investigated in a way completely orthogonal to the visible and NIR deep surveys.

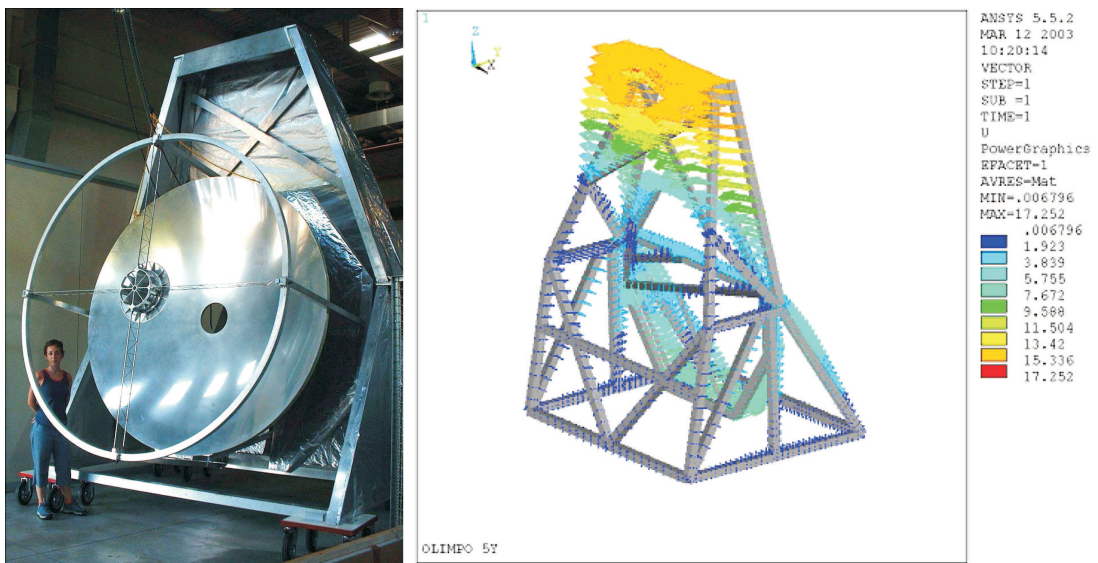


Figure 5.3: Left: The OLIMPO payload, all shields removed. Right: Structure deformations for a 5g horizontal load.

5.2.4 The Payload

OLIMPO implements a number of advanced technical solutions. The main frame (fig. 5.3) is made out of aluminum alloys, and has been optimized to withstand $10g$ shocks (vertical) and $5g$ shocks (horizontal, any azimuth) at parachute opening. The inner frame, with the attached telescope and the cryostat housing the detector system, can be tilted to set the observing elevation from 0° to 60° . The low elevations achievable allow accurate ground-based calibrations of the system and the observation of planets for calibration during polar flights. The telescope is an on-axis Cassegrain configuration with a 2.6 m aluminum parabolic primary mirror [54]. The 0.52 m diameter hyperbolic secondary mirror is suspended by means of thin stainless steel blades to minimize the background from local structures and to avoid beam vignetting (see fig. 5.4). Sky scans are performed by slowly scanning the primary mirror in the cross-elevation direction. It's worth to repeat that such a big mirror has never flown on a balloon borne experiment, that's why OLIMPO is going to be the first high-resolution sky survey at millimetric and sub-millimetric wavelengths. The modulator design is similar to the ones in [55], [56], but allows

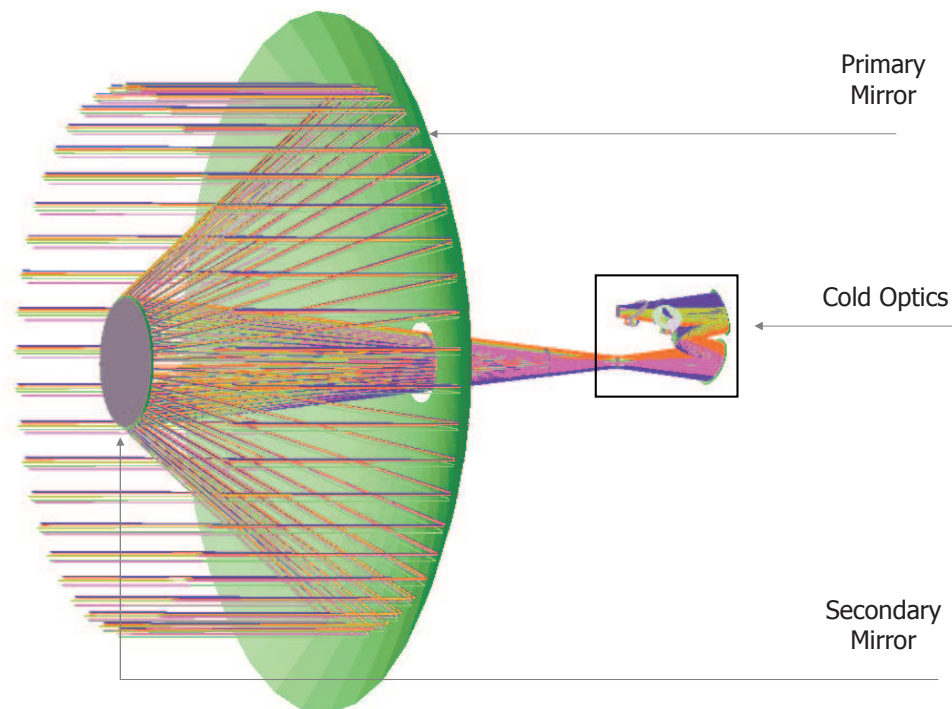
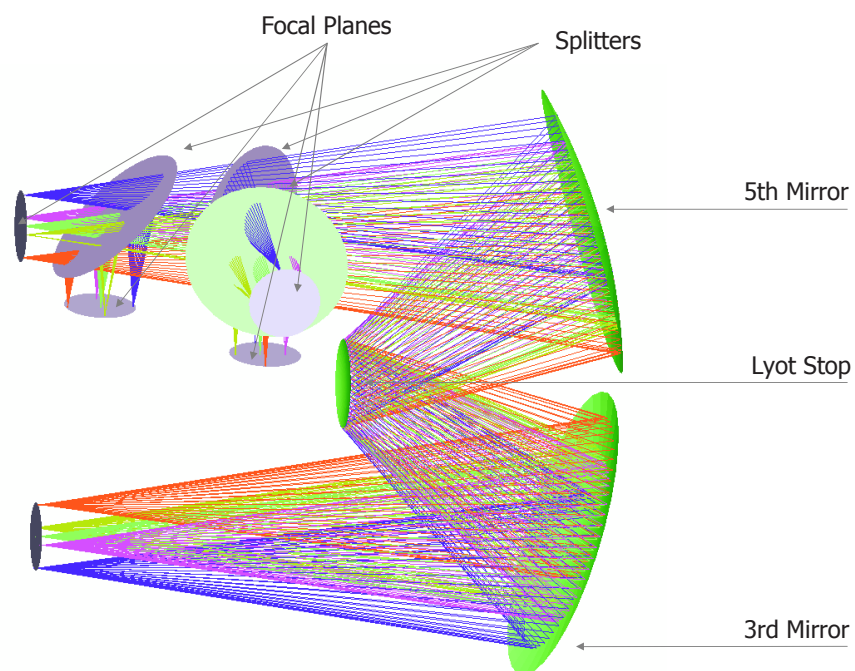


Figure 5.4: Ray Tracing of the OLIMPO Cassegrain configuration. The intensity distribution on the image plane is described in par. 5.3.1, taking into account the occlusion due to the secondary mirror.

a substantial reduction of the scan-synchronous offset by moving the primary mirror instead of the sub-reflector. Up to 3° wide, $1^\circ/s$ cross-elevation scans are possible with this system. The full payload can also perform azimuthal scans, to cover wider regions. The telescope has been already assembled: focusing and beam characterization at 90 and 137 GHz will be treated in section 5.3. The detector system is made of four bolometer arrays (one for each frequency channel), which are being developed in Cardiff together with the dichroics¹ that allow multiband operation. The detectors are an evolution of the highly successful devices used in BOOMERanG and Planck-HFI instruments [57]. In order to achieve low dispersion in the characteristics of the detectors, a fully photo-lithographic process producing TES (transition edge superconductor) sensors on silicon nitride islands on a *Si* wafer has been developed. In this way the entire bolometric arrays are being fabricated with a fully automated process. Filters and antennas can be integrated on the detectors wafer by means of micro-strip technology. The four arrays at 140, 220, 410 and 540 GHz will be composed of 19, 37, 37, 37 detectors, respectively. Each array will fill the optically correct area of the focal plane (about 0.25° in diameter projected on the sky). The cryogenic re-imaging optics is being developed in Rome (see fig. 5.5, [80]). It is mounted in the experiment section of the cryostat, at 2 K, while the bolometers are cooled at 0.3 K. Extensive baffling and a cold Lyot stop reduce significantly straylight and sidelobes. Optics have been optimized to allow diffraction-limited operation even with significant tilt of the primary mirror during sky scans. The bolometer arrays and the re-imaging optics will be arranged into a modified version of the long duration cryostat developed for BOOMERanG [58], [59]. The main difference in OLIMPO is the use of fiberglass cylinders to replace the kevlar cords suspending the LN and LHe tanks: these provide higher stiffness to the system, which is a primary requisite to keep the detector arrays centered on the optical axis within diffraction limits during operation at different elevations. Radiation is refocused into the cryogenic optics through a side of the cryostat, to allow operation of the system with the telescope axis horizontal or at low elevation, during ground based calibrations and in-flight calibrations on planets. The side window is made of anti-reflection coated polypropylene, ensuring minimum excess background on the detectors, while preserving excellent mechanical strength and vacuum tightness. The other payload systems (on-board data conversion and acquisition, Attitude Control System (ACS), Telemetry, Thermal Shields and Housekeeping) are similar to those of the BOOMERanG experiment [60]. ACS is derived from that of BOOMERanG and completed with day and night-time attitude sensors: laser gyroscopes, sun sensors, and star camera. The first flight will be a circumpolar flight launched from Svalbard and recovered in Greenland.

¹Dichroic filters are very accurate color filters, used to selectively pass light in a small range of wavelengths, while reflecting the others.



(a) Ray Tracing of the cryogenic section of the optics. From top to bottom are shown the vacuum window of the cryostat, the tertiary mirror, the Lyot Stop, the fifth mirror and the two dichroics splitting the beam on the four detector arrays [80].



(b) The optics box during the alignment measurements session (see par. 5.4). The drawings used for focal plane reconstruction are clearly visible.

Figure 5.5: The optics box: ray tracing drawing and picture.

5.3 Angular Response Measurements

As described in detail in Appendix E, a radiation receiving instrument, such as antennas or telescopes, is mainly described by a radiation pattern or beam, which is a three dimensional function of the usual spherical coordinates θ and ϕ . In the case of telescope it is commonly referred as the *angular response*, $AR(\theta, \phi)$: the power detected by a generic telescope of collecting area A is the integral of the source brightness over the solid angle, weighted with the angular response of the telescope:

$$P = A \int_{4\pi} B_\nu(\theta, \phi) AR(\theta, \phi) d\Omega . \quad (5.1)$$

An ideal receiving instrument has a three dimensional Dirac delta function as angular response, centered in the direction of the optical axis of the system (θ_0, ϕ_0) , where $P/P_{max} = 1$, while $P/P_{max} = 0$ elsewhere. Of course real instruments have broader angular response in the main lobe and also a certain fraction of the total power coming from the sidelobes or the backlobes (see Appendix E). In the case of CMB observations, the detected brightness is the sum of the brightness from the sky (dominant for the solid angles directed towards the sky, in the main lobe, Ω_{ml}) and the brightness from ground (dominant for the solid angles directed towards ground, in the sidelobes and backlobes, Ω_{sl+bl}):

$$P = A \left[\int_{\Omega_{ml}} B_\nu^{sky}(\theta, \phi) AR(\theta, \phi) d\Omega + \int_{\Omega_{sl+bl}} B_\nu^{ground}(\theta, \phi) AR(\theta, \phi) d\Omega \right] , \quad (5.2)$$

$$P = A \left[B_\nu^{sky}(\theta, \phi) \langle AR_{ml}(\theta, \phi) \rangle \Omega_{ml} + B_\nu^{ground}(\theta, \phi) \langle AR_{sl+bl}(\theta, \phi) \rangle \Omega_{sl+bl} \right] .$$

The CMB temperature signal is typically of the order of 1 K or even significantly lower in the case of polarization, against a ~ 300 K temperature signal from the ground, with $\Omega_{ml} \approx 10^{-6}$ sr (for a FWHM of a few arcmins), while $\Omega_{sl+bl} \approx 2\pi$ sr. It turns out that, in order to achieve a level of interesting signal that is much larger than the disturbance signal, we not only need $\langle AR_{ml} \rangle \simeq 1$, but also $\langle AR_{sl+bl} \rangle < 10^{-8}$ or even less. These low sidelobes levels are usually achieved during the satellite or balloon flights thanks to particularly effective ground and Sun shields, together with an appropriate sky scan strategy.

5.3.1 Point Spread Function for a Cassegrain System

In this section we briefly discuss the diffraction pattern that we should expect from the Cassegrain configuration of the OLIMPO telescope. When working

with telescopes, the source is normally infinitely distant as compared to a typical dimension of the telescope: this means that we are dealing with *Fraunhofer diffraction*. The intensity distribution in the case of circular apertures follows the *Airy pattern* (or *Airy profile*), which is a particular case of what is called in general *Point Spread Function* (PSF), i.e. the intensity distribution on the image plane. In fact the rays coming from an infinitely distant point source, passing through a generic optical element or system, undergo a spreading, because of unavoidable diffraction effects and optical aberrations: the intensity distribution in the image plane will thus not be infinitely narrow and concentrated in a point, it will instead have a peculiar shape, described precisely by the specific PSF. In the case of a Cassegrain configuration with aperture D (primary mirror diameter), an occlusion of diameter εD (secondary mirror diameter) and the source at infinite distance, we get the following Airy-modified unit normalized intensity distribution:

$$PSF = \frac{I(r, \phi)}{I_0} = \frac{1}{(1 - \varepsilon^2)^2} \left[\frac{2J_1(v)}{v} - 2\varepsilon^2 \frac{J_1(\varepsilon v)}{\varepsilon v} \right]^2, \quad (5.3)$$

where (r, ϕ) are the polar coordinates on the image plane and J_1 is the first order Bessel function; v is a dimensionless quantity, $v = \pi D \alpha / \lambda$, where λ is the wavelength and α is the pointing angle in the sky, with respect to the optical axis of the telescope, where $\alpha = 0$. Note that the PSF functions does not depend on the polar angle ϕ , i.e. it is assumed to be circularly symmetric. Moreover it does not depend explicitly on r , since for an infinitely distant source, in the far field of the telescope, the only meaningful quantity is α (see the end of par. 3.3.1).

5.3.2 Ground Attitude Control System

In order to reconstruct the beam profile of such a telescope, we needed to control its pointing with sub-arcmin accuracy. This accuracy level was achieved in both the scan directions of the telescope by means of two digital 16-bit rotation encoders. The whole gondola supporting the telescope was mounted on spherical bearings and was rotated by a linear actuator, thus providing azimuthal scans. Elevation angle was controlled also by a linear actuator, rotating the whole inner frame with respect to the gondola. The two encoders controlling azimuth and elevation have both $360^\circ / 2^{16} \simeq 0.3'$ angular resolution. An electronics box read the information coming from them, encoding it in a standard parallel output, which we could easily get through the parallel port of a laptop, controlled by a C program using the *parapin* library (see also par. 3.11). After the actuators were supplied in power, we could control their motion through another electronics box, which was able to carry out very little steps in both degrees of freedom: we could actually perform steps of single

digital unit (DU) amplitude, $1/65536$ DU, i.e. our effective angular resolution was always that of the rotating encoders.

5.3.3 Measurement Strategy

The angular response measurements of OLIMPO telescope needed a coherent microwave source to be located in the far field of the telescope. For such a 2.6 m diameter telescope, with working wavelengths of 2-3 mm, the far field is located at distances greater than about $2D^2/\lambda \sim 6.7$ km (see the end of par. 3.3.1). OLIMPO is currently hosted by the CNR research area in “Tor Vergata”: from this place it’s possible to point the telescope at an elevation up to about 20° and see the hills around Rome, where Villa Mondragone (now property of “Tor Vergata” University) is located, about 7 km far away from OLIMPO. The source was placed on a balcony of Villa Mondragone, with clear and direct sight of the experiment down in the CNR area. In order to avoid any disturbance effect from the environment surrounding the telescope down in the CNR area and also to prevent possible reflections from the ground, the whole gondola with the telescope, together with the electronics and all the measuring instruments, were raised about 4 meters from the ground by means of a wide platform, on which we could safely step up and easily work. We used as sources two microwave Gunn oscillators (described in detail in par. 3.2 and in Appendix C), working in the frequency ranges of 78-114 GHz and 120-147 GHz. We chose our measurements to be carried out at, respectively, $\nu_0 = 90$ GHz $\Rightarrow \lambda_0 = 3.3$ mm and $\nu_0 = 137$ GHz $\Rightarrow \lambda_0 = 2.2$ mm. The reason of these choices can be easily understood looking at the atmospheric absorption spectrum at millimetric wavelengths (see [84] for example): near 60 GHz we find the blended forest of fine structure transitions from O_2 , while a fine structure line of O_2 is centered at 118.75 GHz. On the other hand water completely dominates atmospheric absorption above 150 GHz. The water and oxygen lines thus delineate 4 atmospheric windows in the millimetric spectrum at 3, 2, 1.3 and 0.8 mm.

Here we resume the experimental set-up for both the telescope and the remote source, referring to the respective sections for the detailed descriptions:

- Telescope and payload
 - Primary and secondary mirrors were placed on the payload by means of the gondola (see fig. 5.3);
 - The inner frame of the gondola could be moved by a linear actuator, providing elevation scans with sub-arcmin accuracy (see par. 5.3.2);
 - The whole gondola was mounted on spherical bearings and was rotated by a linear actuator, providing azimuthal scans with sub-arcmin accuracy (see par. 5.3.2);

- Azimuth and elevation angles are acquired through two digital 16-bit encoders, read by the parallel port of a laptop (see par. 3.11);
 - The receiver was placed in the focal plane of the telescope (see par. 5.3.4). With receiver here we mean the whole system made up of the detector (par. 3.6) plus the feed horn (par. 3.5) plus the amplifier or pre-amplifier (par. 3.7);
 - The signal is acquired through the serial port of the laptop, after being synchronously demodulated by means of a Lock-in amplifier (see pars. 3.8, 3.9 and 3.11);
- Remote source
 - The 78-114 GHz and 120-147 GHz Gunn oscillators (together with their coupled feed horns, see par. 3.2 and Appendix C) had been placed subsequently in a stand-alone box on a balcony of Villa Mondragone;
 - An HDPE lens (par. 3.10) was used to convert the beam out of the source horn in a parallel beam of horizontally polarized light (see pars. 3.4, 3.5);
 - Two different electronics boxes provided modulation for the oscillators (par. 3.8);
 - The reference signal used to modulate the source was transmitted to the Lock-in amplifier down in the CNR area, by means of a pair of dual band radio transmitter/receivers (TX/RX, see par. 3.9)

5.3.4 Focal Plane and Beam Coupling to the Telescope

Before we present the results of such angular response measurements, let us recall now some basic optics concepts, in order to understand a very important matter about beam coupling between the telescope and the feed horns in the focal plane. We can think to the simplest astronomical telescope as a converging lens of focal length f : given a certain source at infinite distance (its brightness distribution, $B_\nu(\theta, \phi)$), the telescope will produce an image of the source in the *focal plane*, where the detectors lie. In general a detector is composed of an array of *pixels*, i.e. picture elements, (CCDs for example), or detectors themselves can be arranged to form an array, each one of them being a pixel: in any case each pixel receives radiation from a certain solid angle in the sky, given by $\Omega_p = A_p/f^2$, where A_p is the pixel area. If we suppose that the angular resolution is only limited by the geometric properties of the system, the power collected by each single pixel is:

$$P = A_t \Omega_p B_\nu(\theta, \phi) , \quad (5.4)$$

where A_t is the actual collecting area of the telescope. We see again that the most meaningful quantity is the throughput $A_t\Omega_p$. It turns out that we cannot ask simultaneously for high angular resolution (small Ω_p) and high sensitivity (large values of P on each pixel). Keeping Ω_p and $B_\nu(\theta, \phi)$ fixed, the collecting area A_t must be increased as much as possible to reach higher values of sensitivity. Let us introduce another fundamental quantity, the *f-number* $F\#$, which is defined as $F\# = f/D$, where D is the diameter of the telescope (OLIMPO telescope has $F\# = 3.5$). The power collected by each single pixel is now:

$$P = \frac{\pi}{4} D^2 \frac{A_p}{f^2} B_\nu(\theta, \phi) = \frac{\pi}{4} \frac{A_p}{F\#^2} B_\nu(\theta, \phi) . \quad (5.5)$$

We can now go back to our case and apply these concepts to understand which is the right beam coupling between the telescope and the radiation collector on the focal plane, i.e. the feed horn associated to each detector (see par. 3.6). Such angular response measurements do not require more than a single detector in the focal plane, but its horn should have the right beam coupling with the telescope. We can use the f-number $F\#$ to calculate the aperture angle into which radiation coming from the telescope is collimated towards the focal plane, that is the angle we need to fill out in the focal plane:

$$\theta_{fp} = 2 \arctan \left(\frac{1}{2F\#} \right) \simeq 16.26^\circ \quad \text{for the OLIMPO telescope.} \quad (5.6)$$

This number has to be compared to the FWHM of the Gaussian beam characterizing the feed horns and these two quantities should match up, as long as we require perfect beam coupling. Recall from par. 3.5 the FWHM angles we found for the horns (figs. 3.11, 3.12, 3.13 and 3.14, tabs. 3.4, 3.5, 3.6 and 3.7). It turns out that for the beam measurements at 90 GHz we chose the circular feed horn with $\text{FWHM}=(19.14 \pm 0.12)^\circ$ (fig. 3.13, tab. 3.6). The beam coupling here is optimal: the little excess in the feeding angle can only cause some straylight (radiation coming from outside the field of view of the telescope) to reach the detector. Nevertheless it should not be detected because modulation of the source ensures that only signals chopped at 1.3 kHz are demodulated and acquired (see pars. 3.8, 3.9). The situation is different at 137 GHz: none of the horns in our possess matches the optimal FWHM, they have both small apertures, $\text{FWHM}=(9.47 \pm 0.03)^\circ$ (fig. 3.12, tab. 3.4) and $\text{FWHM}=(10.48 \pm 0.03)^\circ$ (fig. 3.14, tab. 3.7). This means that we “underilluminated” the telescope, in the sense that our horn was not able to accept all of the rays coming from the telescope, but only a certain fraction FWHM/θ_{fp} , that is we are only investigating the $(\text{FWHM}/\theta_{fp})^2 \sim 40\%$ of the whole collecting area. The beam size should not be affected, since the rays coming from

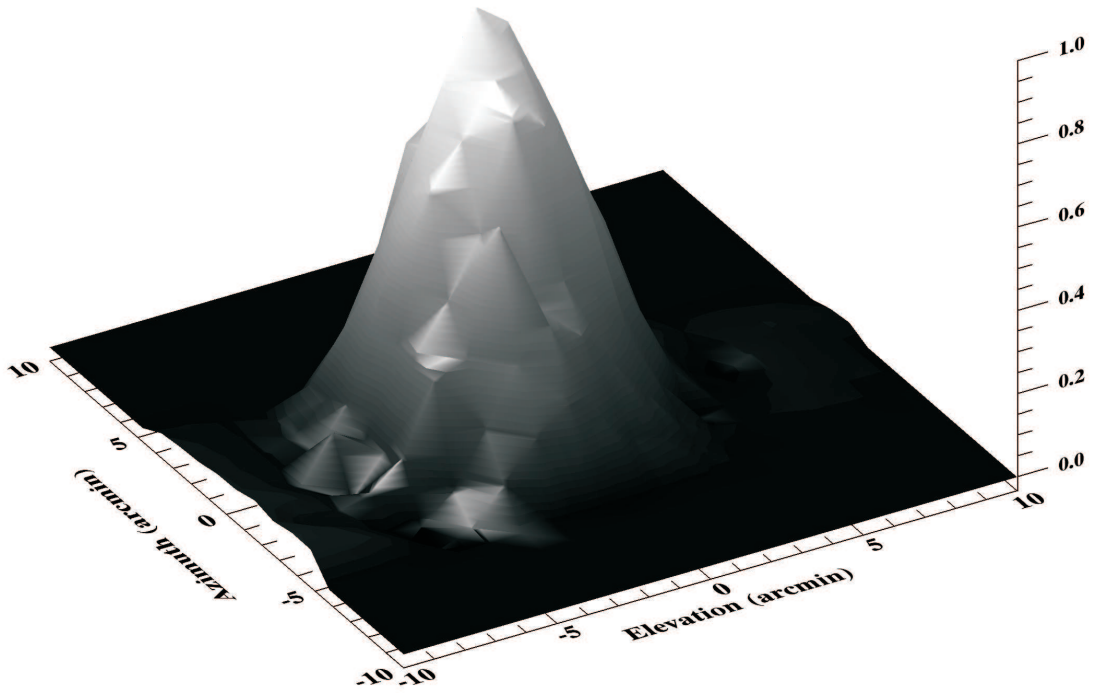
the outer parts of the mirrors have less and less weight in the angular response as we go towards the borders. What is instead critical it's the non optimal investigation of the physical collecting area (i.e. the surface of the mirrors). We can conclude that, even if this surface investigation will be complete at 90 GHz, of course another horn with larger FWHM is needed to test again the beam profile and the surface of the mirrors at 137 GHz.

5.3.5 Angular Response: Results

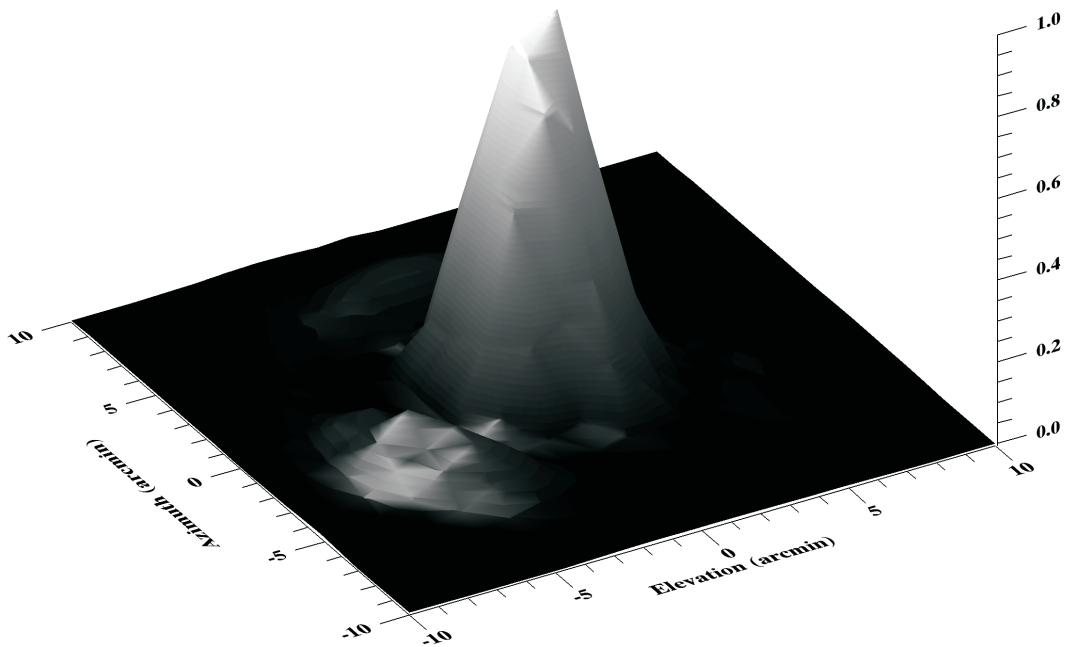
Before we present the results of our measurements, let us point out a couple of things. First, as indirectly anticipated in the previous section, there is no optics box here, the horn is in the focal plane and looks directly at the telescope. We will speak about the optics box in par. 5.4. Second, the scans were mainly performed varying the elevation angle, while azimuth was kept fixed. After one scan was completed, we stepped ahead in azimuth and repeated the scan in elevation. After such mapping was complete, we always provided at least two azimuthal scans at fixed elevation, in order to recover the beam profile as a convolution of all the previous elevation scans. In the following we present the three dimensional beam profiles and contour plots at 90 and 137 GHz; we also present several two dimensional plots, which represent the slices of the beam both in elevation and azimuth. Note that the 2-D slices we present are only those who lie very close to the absolute maximum of the signal, in order to furnish a meaningful estimation of the beam FWHM, which of course broadens as we move away from the central peak. The 2-D plots all show 2 curves superimposed to the data: the red one is always the appropriate Airy-modified Point Spread Function (PSF, defined in eq. 5.3), where the fitted parameters are the aperture D (primary mirror diameter), and the occlusion diameter εD (secondary mirror diameter). Since the only uncertainty estimations come from statistical errors in the repeated measurements, no systematics are introduced before the data analysis. The second superimposed curve (blue) is a Gaussian, from which we are able evaluate the FWHM by means of the least-squares fitting method. The results are summarized in tab. 5.1.

ν_0 (GHz)	Coordinate	Gaussian SD (')	FWHM (')	Diffraction Limit (')
90	azimuth	(2.28 ± 0.05)	(5.38 ± 0.13)	5.39
90	elevation	(2.31 ± 0.05)	(5.43 ± 0.13)	5.39
137	azimuth	(1.60 ± 0.05)	(3.77 ± 0.11)	3.54
137	elevation	(1.66 ± 0.03)	(3.91 ± 0.06)	3.54

Table 5.1: Resume of the measured beam sizes (in arcmins) at 90 and 137 GHz, both in elevation and azimuth. These final results are compared to the diffraction limit $\sim 1.22\lambda/D$, with $D = 2.6$ m.

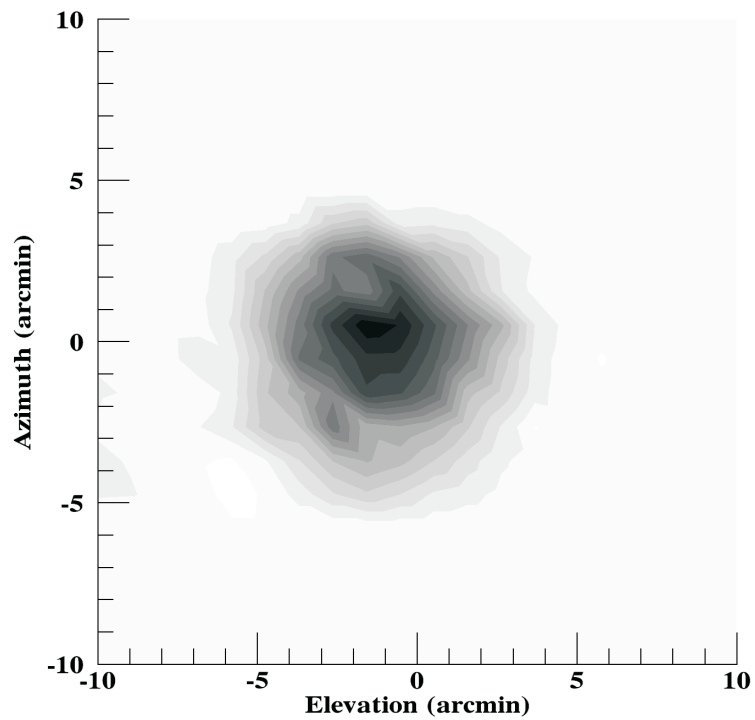


(a) At 90 GHz.

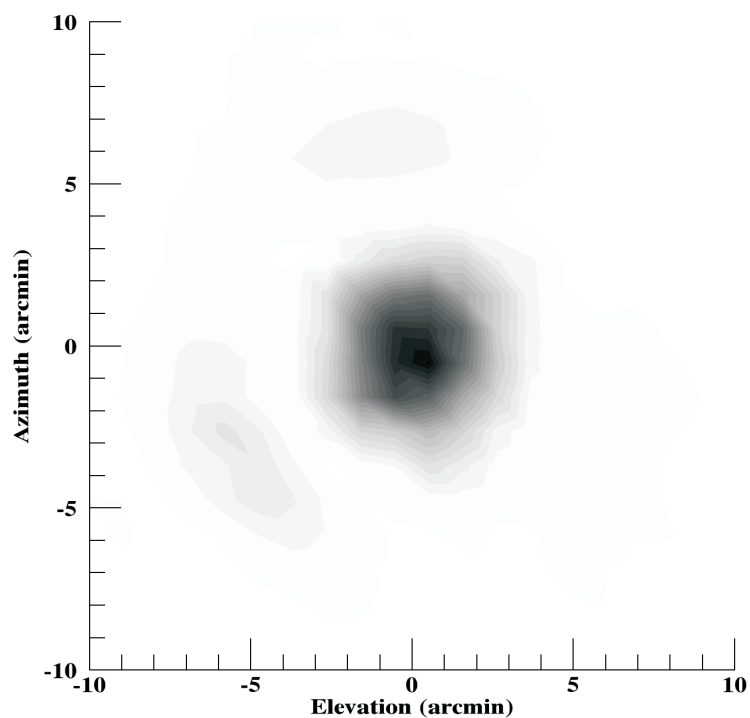


(b) At 137 GHz.

Figure 5.6: 3-D profile of OLIMPO telescope beam. Signal is normalized.

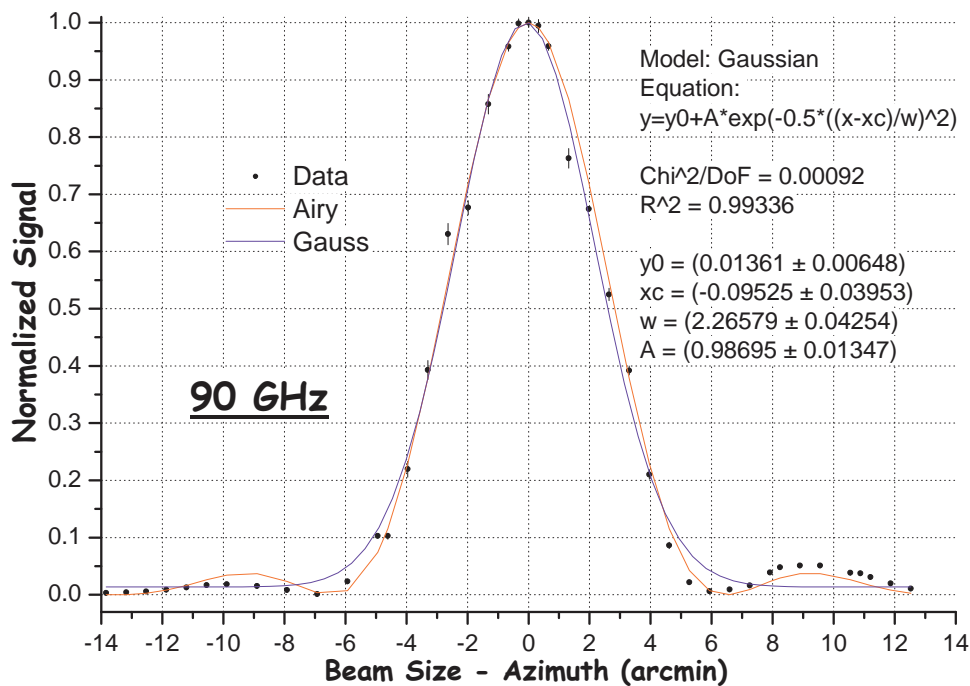


(a) At 90 GHz. $N=30$.

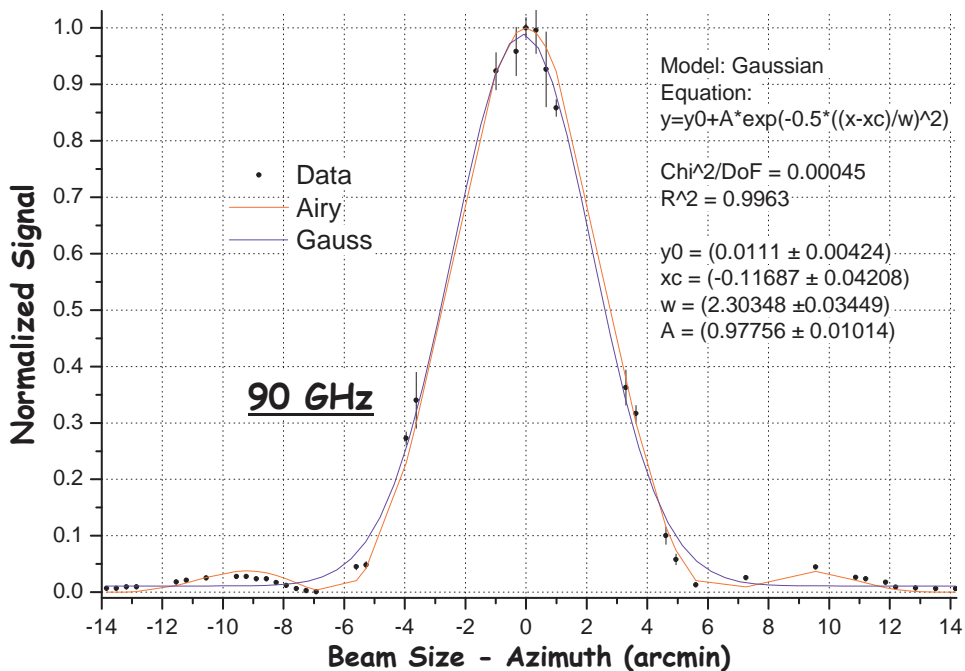


(b) At 137 GHz. $N=80$.

Figure 5.7: 2-D contour plot of OLIMPO telescope beam. Greyscale is divided into N levels, from pure white (null normalized signal), to pure black (unity normalized signal).

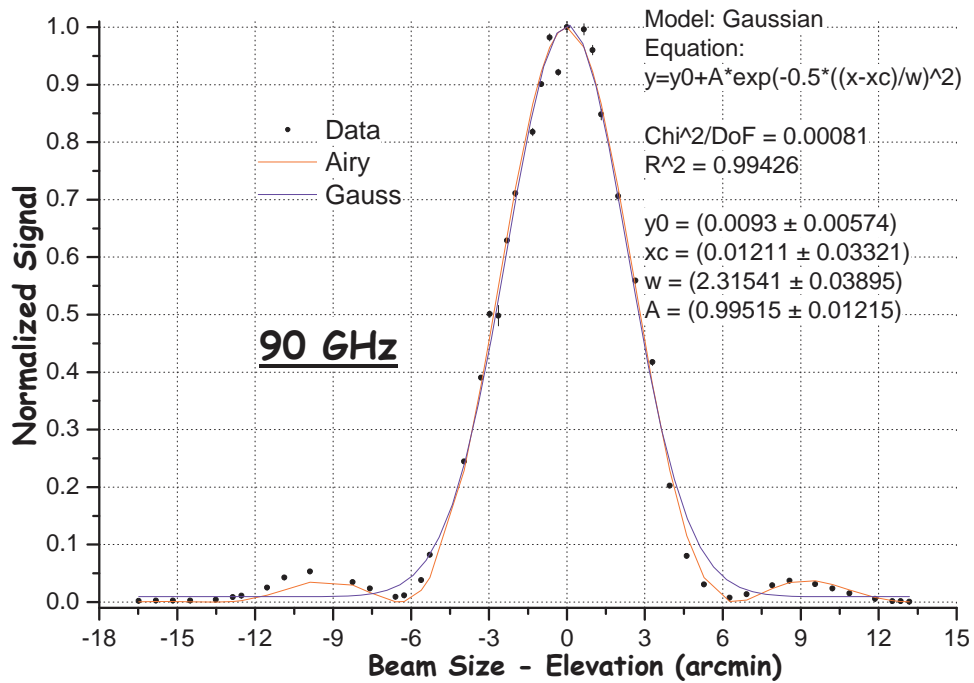


(a) First azimuthal slice, very close to the absolute maximum.

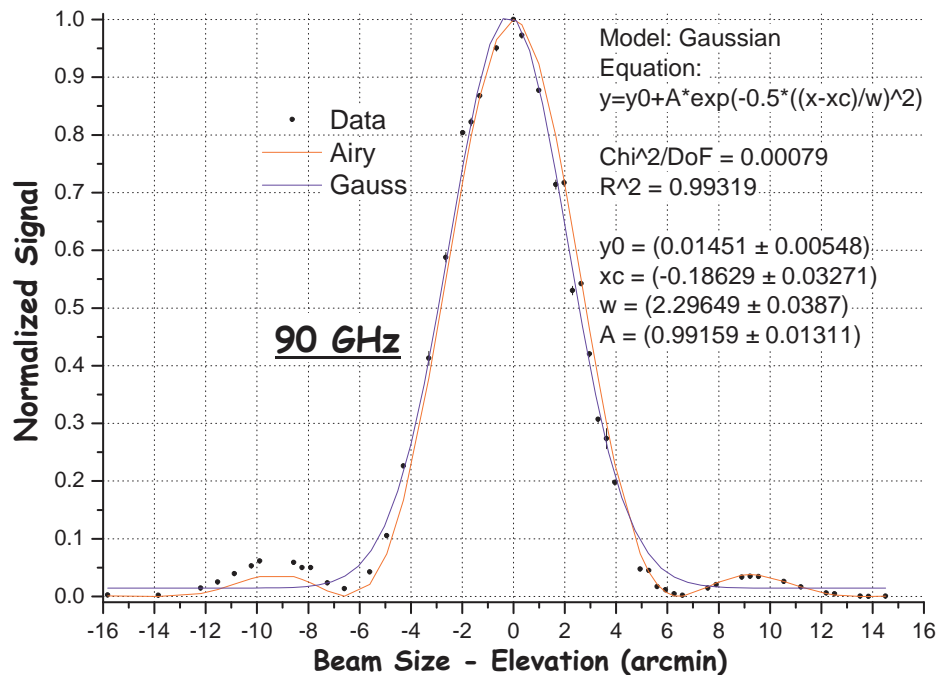


(b) Second azimuthal slice, very close to the absolute maximum.

Figure 5.8: 2-D slices of the OLIMPO telescope beam profile at 90 GHz. The scan is performed varying the azimuth, while elevation is kept fixed. Each experimental point is the mean value upon at least 10 measures, displayed with the associated uncertainty. The red line is the appropriate Airy-modified PSF function (eq. 5.3). The blue line is the Gaussian fit, whose parameters are shown.

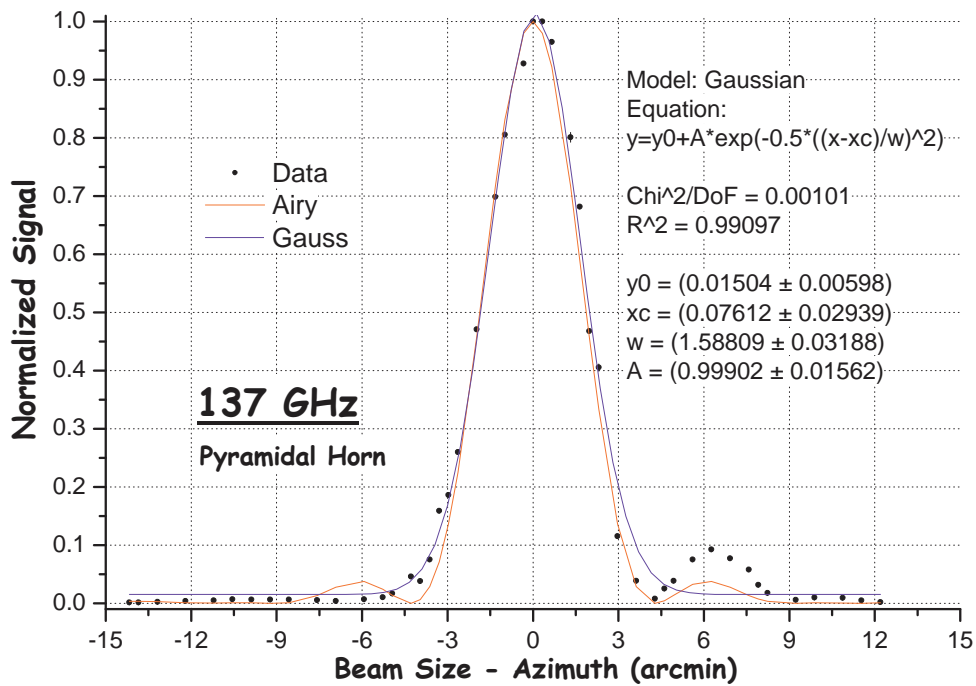


(a) First slice in elevation, very close to the absolute maximum.

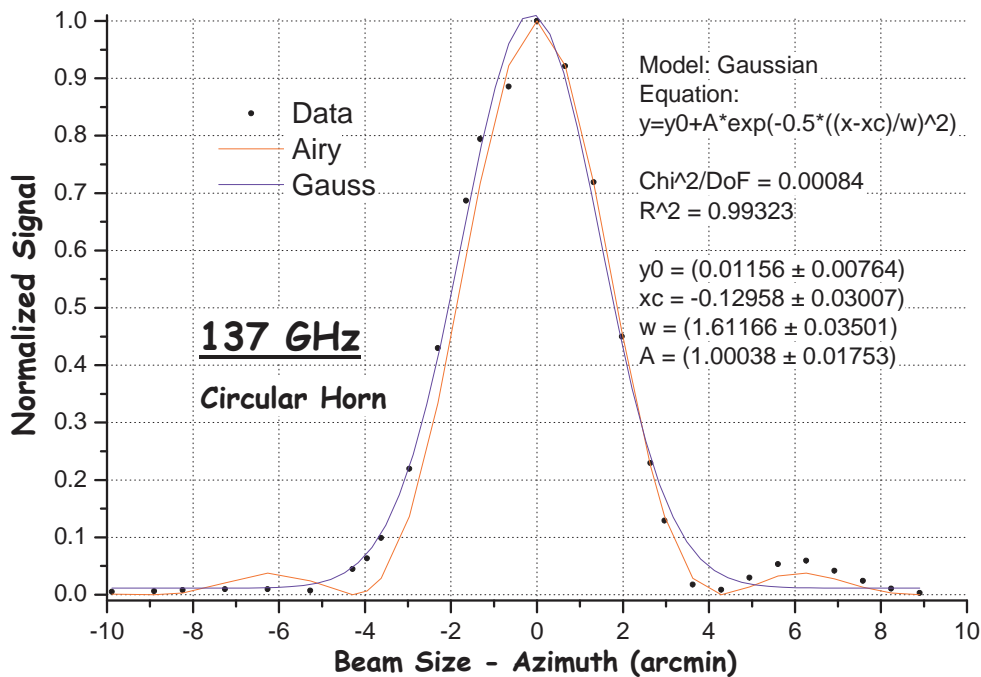


(b) Second slice in elevation, very close to the absolute maximum.

Figure 5.9: 2-D slices of the OLIMPO telescope beam profile at 90 GHz. The scan is performed varying the elevation, while azimuth is kept fixed. Each experimental point is the mean value upon at least 10 measures, displayed with the associated uncertainty. The red line is the appropriate Airy-modified PSF function (eq. 5.3). The blue line is the Gaussian fit, whose parameters are shown.

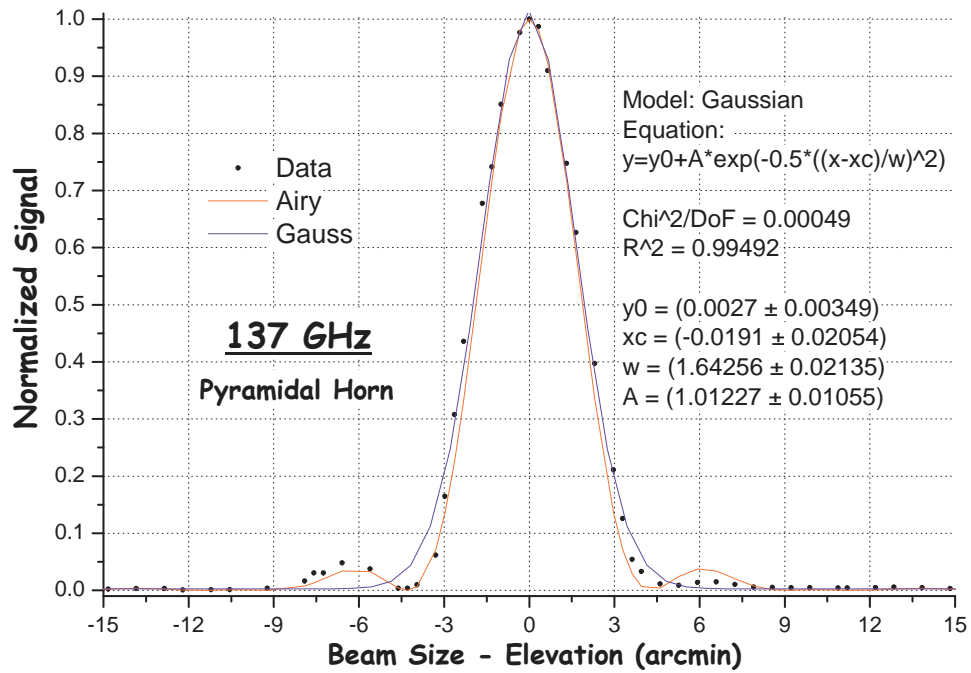


(a) Azimuthal slice with pyramidal horn, very close to the absolute maximum.

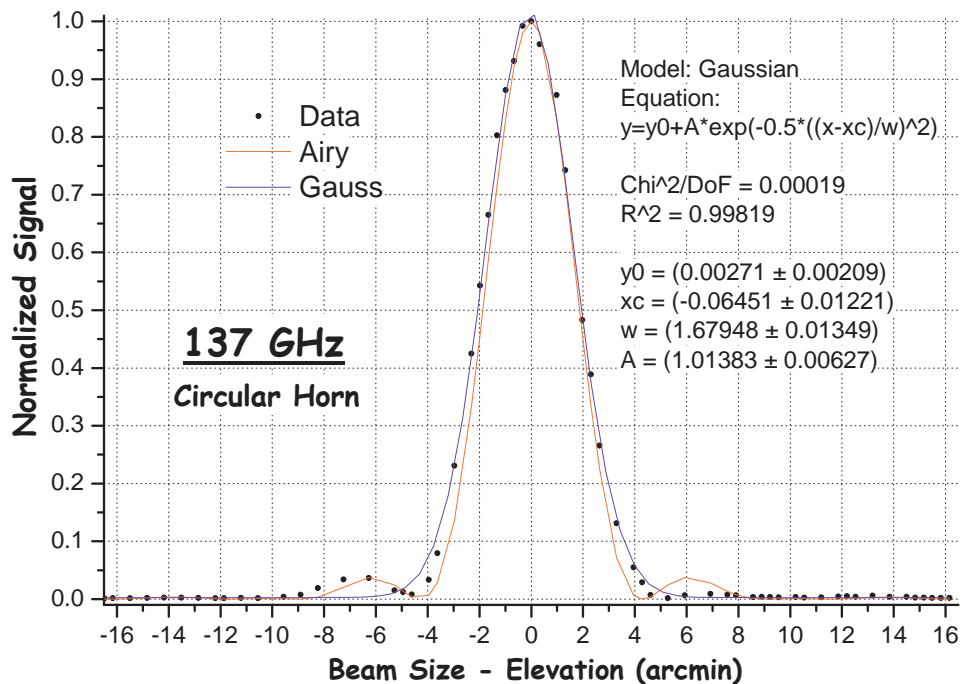


(b) Azimuthal slice with circular horn, very close to the absolute maximum.

Figure 5.10: 2-D slices of the OLIMPO telescope beam profile at 137 GHz. The scan is performed varying the azimuth, while elevation is kept fixed. Each experimental point is the mean value upon at least 10 measures, displayed with the associated uncertainty. The red line is the appropriate Airy-modified PSF function (eq. 5.3). The blue line is the Gaussian fit, whose parameters are shown.



(a) Slice in elevation with pyramidal horn, very close to the absolute maximum.



(b) Slice in elevation with circular horn, very close to the absolute maximum.

Figure 5.11: 2-D slices of the OLIMPO telescope beam profile at 137 GHz. The scan is performed varying the elevation, while azimuth is kept fixed. Each experimental point is the mean value upon at least 10 measures, displayed with the associated uncertainty. The red line is the appropriate Airy-modified PSF function (eq. 5.3). The blue line is the Gaussian fit, whose parameters are shown.

From figs. 5.6, 5.7, 5.8, 5.9, 5.10 and 5.11 we see that the agreement with the expected Airy modified curve is very good in the main lobe: the fitted values for the aperture and the occlusion substantially coincide with the nominal ones. The sidelobes present instead a systematic asymmetry, both at 90 GHz and 137 GHz, either in azimuth or elevation: this excludes the eventuality of possible effects due to reflections on the ground, which should not emerge during azimuthal scans. In order to explain such systematic asymmetry in the sidelobes, we performed some preliminary software tests with the “ZEMAX Optical Design Program”. With this software is possible to simulate exactly our optical configuration, i.e. on-axis Cassegrain telescope. Moreover it’s possible to introduce in the simulation slightly off-axis features: in particular we focused on possible translational decentering of the optical axes of the primary and secondary mirrors, or alternatively on rigid rotation (tilt) of the secondary with respect to the optical axis of the primary. We found that a ~ 2 mm decentering or, alternatively, a $\sim 0.15^\circ$ tilt of the secondary mirror optical axis with respect to the primary would cause an asymmetry comparable with ours. Of course further investigation on these aspects is needed. Finally, the most important results are shown in tab. 5.1: the measured FWHMs at 90 GHz and 137 GHz are substantially those of a diffraction-limited 2.6 m telescope.

5.4 Optics Box

The optics box is located inside the cryostat, cooled down to ~ 2 K, thanks to the thermal link with the ^4He bath,: it is a system of three mirrors (the tertiary, the so-called Lyot Stop and the quinary), whose fundamental function is to re-focus the image from the focal plane of the telescope into the four focal planes of the experiment, as shown in fig. 5.5a [80]. Receivers used at millimetric and sub-millimetric wavelengths are highly sensitive thermal detectors. In order to increase their sensitivity as much as possible, solid angle and frequency selection of the radiation of interest is required. The introduction of re-imaging optics has three main advantages:

- Solid angle selection consist in rejecting primary edge effects, sidelobes and straylight, i.e. the radiation arriving on the receivers without passing through the whole mirrors chain. This is achieved using a Lyot Stop, a cold mirror onto which the primary mirror image is focused, in order to select only a portion of primary mirror. Only light rays coming from the selected area reach the detectors, while light rays coming from the edges are focused on a cold absorber surrounding the Lyot Stop. More specifically, the Lyot stop provides the exact image of a 2 m diameter primary mirror (comprehensive of the central aperture), that is its main function is to cut out the sidelobes due to the primary mirror.

- The Lyot stop will introduce its own sidelobes. The advantage consists in the fact that it is cold, so the disturbance signal in eqs. 5.2 no longer comes from a ~ 300 K blackbody, but from one at ~ 2 K; moreover it is enclosed in a cold absorbing cavity with very low and constant emission (not modulated). Furthermore, the presence of the hole inside the Lyot Stop allows to disregard rays coming from the hole of the primary mirror, which is a significantly higher signal than that coming from the sky (again from eq. 5.2). Straylight radiation cannot reach directly the receivers and it will be thermalized to the optics box temperature.
- OLIMPO works at four different frequency bands (see par. 5.2.4): incoming radiation is split by three dichroics into four different focal planes (fig. 5.5a), while it is filtered entering the cryostat and again just before each focal plane. The presence of these dichroics between the fifth mirror and the focal planes implies an increase of the total focal distance, hence the final $F\#$ must be larger than the one of par. 5.3.4: due to space requirements, this can be only realized using three mirrors in the refocusing system. The first one (third mirror) is used to re-focus radiation onto the Lyot Stop (fourth mirror) and the third one (fifth mirror) recollects rays from the Lyot Stop to the detectors.

5.4.1 Optics Box Alignment: Laser Measurements

We also made room temperature alignment tests of the optics box and of the mirrors. The optics box is designed so that every part, including the mirrors, must fit in the proper way: there are no adjustable parts. The advantage is that there is no danger of losing the alignment during transportation or launching of the experiment; the drawback is that it would be very difficult to fix any misalignment. It is thus fundamental to verify the correct positioning of every element. This is achieved by means of two alignment tests: the first one is in the optical, using a laser, which is the usual way to perform an alignment test, since diffraction effects are strongly reduced at visible frequencies with respect to millimetric and sub-millimetric wavelengths, since the typical dimensions of the optical elements are orders of magnitude larger than typical laser wavelengths; the other test is a focal plane mapping at 140 GHz, described in the next section.

The test in the optical consisted in simulating a point-like beam coming from the telescope and verifying that it was correctly refocused on the four focal planes. Visible radiation was generated by a monochromatic He-Ne laser with working wavelength $\lambda = 633$ nm. We provided a suitable optical setup, made up of a beam expander coupled to the laser, properly illuminating a lens, in order to simulate OLIMPO telescope, which has $F\# = 3.5$; the incoming signal

was measured by means of a photodiode. The diverging bi-concave spherical lens we used has diameter $d_{lens} = 25.4$ mm and negative focal distance, $f_{lens} = -75$ mm. Assuming a parallel incident beam, i.e. as it would come from infinity, the lens was able to produce an $F\# = f_{lens}/d_{eff}$, where d_{eff} is the properly illuminated portion of the lens, i.e. the effective diameter: hence, $F\# \gtrsim 2.95$. The beam expander was able to enlarge the wavefront of the visible radiation generated by the laser, so that it illuminated the whole lens. However the beam expander should produce parallel rays, but we found that this is not exactly the case in practice. Our effective working focal distance of the lens, f_{eff} , thus differs from the nominal one: they are related by the equation:

$$\frac{1}{f_{eff}} = \frac{1}{f_{beam}} + \frac{1}{f_{lens}}, \quad (5.7)$$

where f_{beam} is the focal distance of the beam generated by the beam expander. We measured $f_{beam} = 1200$ mm, which gives $f_{eff} \simeq -80$ mm. We could exploit such an imperfection of the beam expander to our advantage: in fact the outgoing beam dimension is too small to fit the whole lens diameter; hence, by moving the lens away from the expander, we succeeded in illuminating its whole surface, obtaining the required $F\# = 3.5$. All of the distances are taken from the so-called “Reggetta In”, which is the radiation entrance hole in front of the tertiary mirror (see fig. 5.5b). A first measurement showed that the lens could not be placed exactly in the nominal position, i.e. 80 mm from the nominal focal plane position: in fact the dimensions of the spots on the image surface were larger than expected. Consequently, we decided to move the lens back and forth to find the optimal position, which was found to be 2 mm towards the “Reggetta In”. In order to verify the refocusing properties at the edges of the telescope focal plane for all the four image surfaces, we need to define different fields of view (see tab. 5.2). The results obtained for the signal at the edges of the focal plane, for all the four image surfaces, are shown in tab. 5.3. As a reference, the signal obtained observing directly the laser is 109.22 ± 0.14 mV: note that this is obtained without beam expander and lens, which scatter a lot of radiation. It turns out that the efficiency of the optical system is very high, even at optical wavelengths.

5.4.2 Optics Box Alignment: Focal Plane Mapping at 140 GHz

As anticipated, the second test we carried out on the optics box is a focal plane mapping at 140 GHz. This kind of measurement is usually never performed, because of the fact that tests in the optical already provide the needed informations about alignment. Nevertheless such a mapping is aimed to check how critical is the nominal focal plane position, given that in the optical a 2 mm

Field #	Sky Coordinates (')	Focal Plane (mm)
1	$x = 0, y = 0$	$x = 0, y = 0$
2	$x = 0, y = +10$	$x = 0, y = -20$
3	$x = 0, y = -10$	$x = 0, y = +20$
4	$x = +7.5, y = 0$	$x = -15, y = 0$
5	$x = -7.5, y = 0$	$x = +15, y = 0$

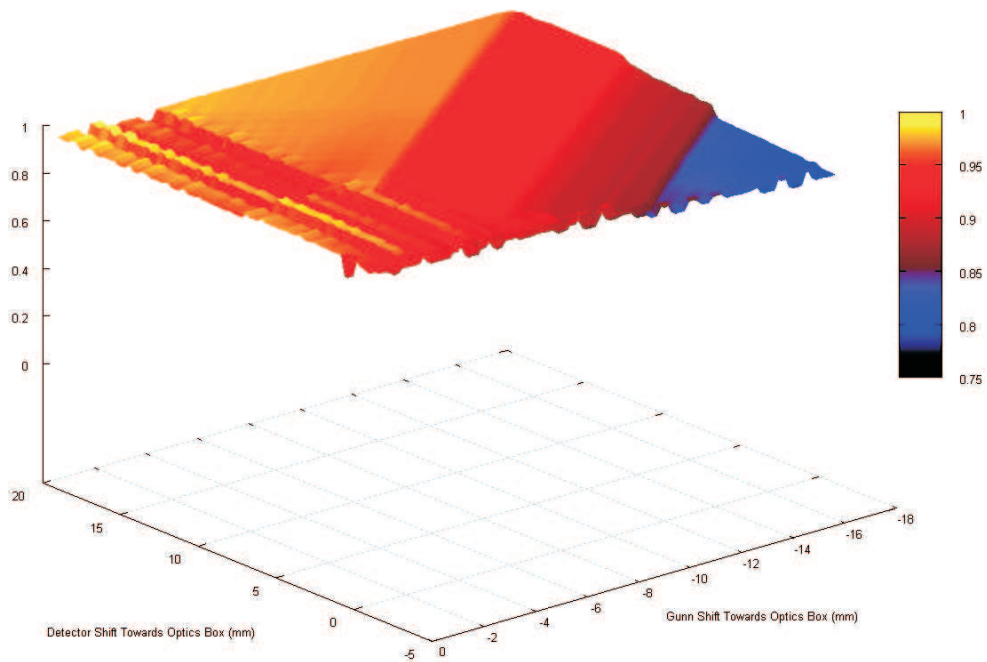
Table 5.2: Coordinates of the five fields of view used for the alignment test in the optical. The corresponding coordinates of the spots on the focal plane of the experiment are also shown. The fields are not the same in x and y because the dichroics partially limit the beam, since they are tilted at 45° with respect to the incident radiation: their projection on the beam is thus an ellipse.

	Signal (mV)	Signal (mV)	Signal (mV)	Signal (mV)
Field #	143 GHz	217 GHz	353 GHz	545 GHz
1	(59.92 ± 0.11)	(56.19 ± 0.19)	(54.14 ± 0.13)	(55.45 ± 0.18)
2	(60.91 ± 0.15)	(56.77 ± 0.16)	(50.69 ± 0.19)	(56.49 ± 0.14)
3	(67.24 ± 0.13)	(51.19 ± 0.13)	(49.54 ± 0.12)	(55.78 ± 0.19)
4	(60.58 ± 0.12)	(50.22 ± 0.11)	(56.54 ± 0.10)	(51.22 ± 0.13)
5	(56.28 ± 0.10)	(51.16 ± 0.14)	(50.11 ± 0.15)	(53.31 ± 0.11)

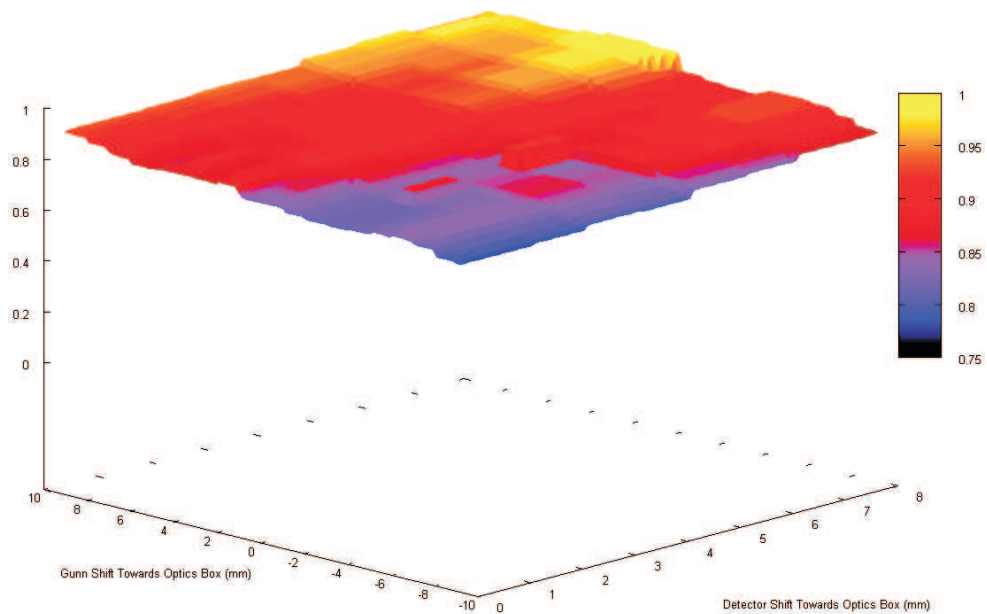
Table 5.3: Alignment and refocusing tests results. As a reference, the signal obtained observing directly the laser is 109.22 ± 0.14 mV: note that this is obtained without beam expander and lens, which scatter a lot of radiation. Hence, the efficiency of the optical system is very high, even at optical wavelengths. The coordinates of the five fields are described in tab. 5.2.

shift from the nominal value was found. Of course in the optical such shift cannot be disregarded, but it will have no relevant consequences at millimetric wavelengths, as we'll see. As experimental set-up for these measurements, we needed the coherent microwave source at 140 GHz (the 120-147 GHz Gunn oscillator, see 3.2 and Appendix C), together with the coupled feed horn (par. 3.5), and a receiving system, made up of the detector (par. 3.6) plus the feed horn plus the amplifier (par. 3.7). Working frequency was again set to be $\nu_0 = 137$ GHz $\Rightarrow \lambda_0 = 2.2$ mm, the reasons being explained in par. 5.3.3. We should expect some interference effect because of the monochromatic source. Our aim was thus to perform a bidimensional map of focal plane at 140 GHz, as a function of the distances from the two nominal positions of the focal planes of, respectively, the telescope and the optics box channel at 140 GHz. The source and the detector were therefore shifted back and forth from their respective nominal positions by means of micrometric sledges: we also took into account the beam waist offsets evaluated in par. 3.5 (see tab. 3.3). The left/right and

height degrees of freedom were preliminary adjusted, also by means of micro-metric sledges and elevators, in order to achieve the absolute maximum of the signal, while keeping fixed the two nominal focal planes positions. The results are shown in fig. 5.12. Disregarding the expected interference effects due to the monochromatic source, such mapping clearly reveals that the dependance of the signal on the nominal positions is very weak at millimetric wavelengths. However we should note in conclusion that the feed horn aperture angle in the receiving system is $(9.47 \pm 0.03)^\circ$ (see fig. 3.12 and tab. 3.4), which is half of the FWHM planned for the OLIMPO horns coupled to the 140 GHz detectors. This means that this test needs to be repeated with the right coupled horn.



(a) First measurements session.



(b) Second measurements session.

Figure 5.12: Focal plane mapping at 140 GHz. The source and the detector are shifted forth and back from the two nominal positions of the focal planes of, respectively, the telescope and the optics box channel at 140 GHz, by means of micrometric sledges. Signal is normalized to unity.

Conclusioni

Nei primi due capitoli abbiamo descritto uno scenario teorico fondato sull'Inflation, con l'unico chiaro intento di identificare delle osservabili che potessero porre dei vincoli sull'effettiva validità di un modello che prevede una brevissima espansione esponenziale dell'universo nelle sue epoche primordiali. Nel seguito ci siamo concentrati su un'osservabile in particolare, la componente rotazionale della polarizzazione della radiazione cosmica di fondo (modi B). La rivelazione di questa inequivocabile impronta nella radiazione fossile di fondo fornirebbe forti vincoli sperimentali sull'Inflation e, indirettamente, sull'esistenza delle onde gravitazionali primordiali. Nel capitolo 4 abbiamo descritto un approccio innovativo per compiere tale misura, che è da considerarsi estremamente difficile e rappresenta la nuova sfida nel campo della cosmologia sperimentale. L'idea di base è costruire due polarizzatori a griglia (wire-grid), i cui fili sono disposti in maniera da riprodurre esattamente il tracciato rotazionale tipico dei modi B. Ne abbiamo descritto i criteri per la realizzazione e la caratterizzazione dal punto di vista matematico, facendo uso del formalismo di Mueller. Abbiamo proposto due innovative tecniche per la modulazione della polarizzazione ad opera di tali polarizzatori. Uno di questi due metodi, il polarizzatore a riflessione, è stato studiato in laboratorio con misure preliminari, con risultati soddisfacenti. Siamo stati in grado di predire il comportamento, poi misurato, di questo sistema ottico di nuova concezione. Abbiamo inoltre effettuato delle simulazioni su mappe di polarizzazione di CMB, al fine di ottimizzare la dimensione angolare che tali polarizzatori dovranno proiettare in cielo, in funzione dello spettro di potenza teorico delle perturbazioni tensoriali primordiali. Nel capitolo 5 ci siamo concentrati sul telescopio OLIMPO, che è il più grande telescopio che abbia mai volato su pallone stratosferico. La sua caratteristica più importante per i nostri intenti è la grande rapidità ottica, ma in generale l'accoppiamento di un esperimento di polarizzazione nelle microonde con un telescopio in asse è ottimale. Durante questo lavoro abbiamo effettuato ripetute misure per caratterizzarne la risposta angolare da terra, giungendo ai fondamentali risultati del paragrafo 5.3.5. Infine abbiamo provveduto a test di allineamento dell'ottica di re-imaging dell'esperimento OLIMPO, sia nell'ottico che nelle microonde.

Conclusions

In the first two chapters we depicted an Inflation-founded theoretical scenario, with the only clear intent of identifying the observables that could constrain the effective suitability of a short period of exponential expansion occurred at very early times of the universe. In the following we focused on the fundamental observable of the curl component of the polarization of the Cosmic Microwave Background (B-modes). The detection of such a footprint in the relic cosmic radiation would provide observational constraints on both the Inflation and, indirectly, the existence of primordial gravitational waves. In chapter 4 we described an innovative approach to perform such an extremely difficult and challenging measurement. The basic idea is to build two polarizers shaped to match the curl polarization pattern of the B-modes. We gave the criteria for their realization and their mathematical characterization by means of the Mueller formalism. We proposed two different innovative techniques for modulating the polarizations by means of such polarizers. One of these two modulation methods, the reflecting polarizer, has been investigated with preliminary laboratory measurements, with satisfactory results. We were able to completely predict the measured behaviour of such an uninvestigated optical system. We also performed simulations on the polarized CMB sky, in order to optimize the angular scale that the polarizers should project on the sky, as a function of the theoretical power spectrum of primordial tensor fluctuations. In chapter 5 we focused on the OLIMPO telescope, which is the biggest telescope ever flown on a balloon. Its fundamental feature to our aim is the big throughput, and in general the coupling of a microwave polarization experiment with a two-mirrors on-axis telescope is optimal. We carried out intensive ground-based angular response measurements during this work, which led to the fundamental results of par. 5.3.5. We finally performed alignment tests for the re-imaging optics of the OLIMPO experiment, both at optical and microwave wavelengths.

Appendix A

Stokes Parameters and Mueller Matrices

The two components of the electric field of a generic electromagnetic wave propagating in the z direction are described by the plane waves of angular frequency $\omega = 2\pi\nu$:

$$\begin{aligned} E_x(t) &= E_{0,x}(t) \cos[\omega t + \varphi_x(t)] , \\ E_y(t) &= E_{0,y}(t) \cos[\omega t + \varphi_y(t)] . \end{aligned} \quad (\text{A.1})$$

The amplitudes $E_{0,x}(t)$, $E_{0,y}(t)$ and the phases $\varphi_x(t)$, $\varphi_y(t)$ fluctuate slowly with respect to the carrier $\cos(\omega t)$. Eliminating the term $\cos(\omega t)$ between the eqs. A.1 and defining $\Delta\varphi(t) \equiv \varphi_y(t) - \varphi_x(t)$, the generic expression for the *polarization ellipse* is obtained (see fig. A.1):

$$\frac{E_x^2(t)}{E_{0,x}^2(t)} + \frac{E_y^2(t)}{E_{0,y}^2(t)} + \frac{2E_x(t)E_y(t)}{E_{0,x}(t)E_{0,y}(t)} \cos \Delta\varphi = \sin^2 \Delta\varphi . \quad (\text{A.2})$$

For purely monochromatic waves amplitudes and phases must be constant with time, i.e. $E_{0,x}(t) = E_{0,x}$, $E_{0,y}(t) = E_{0,y}$, $\varphi_x(t) = \varphi_x$ and $\varphi_y(t) = \varphi_y$: therefore the polarization ellipse is also constant with time. In general a beam of light is elliptically polarized, but for particular values of the amplitudes and of the phases the ellipse degenerates to a line (linear polarization) or to a circumference (circular polarization). We have linear polarization for $\Delta\varphi = 0, \pi$, the direction of the vector $\vec{E} = \vec{E}_x + \vec{E}_y$ remains constant in the plane orthogonal to the direction of propagation z . Instead we have circular polarization for $\Delta\varphi = \pi/2, 3\pi/2$, the vector \vec{E} describes in time a circle in the plane orthogonal to the direction of propagation z with radius $E_0 = E_{0,x} = E_{0,y}$.

The polarization ellipse can be also expressed by the elliptical parameters

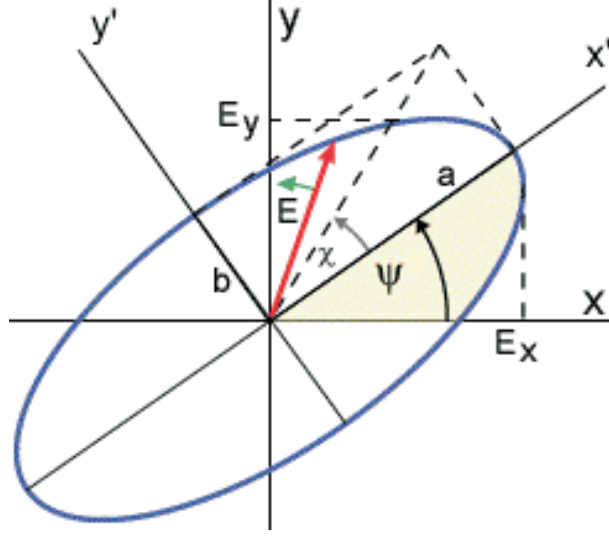


Figure A.1: Polarization ellipse with semi-major axis of length a and a semi-minor axis of length b .

and χ (see fig. A.1):

$$\tan(2\psi) = \frac{2E_{0,x}E_{0,y} \cos \Delta\varphi}{E_{0,x}^2 - E_{0,y}^2} \quad (\text{Orientation angle}), \quad (\text{A.3})$$

$$\tan \chi = \pm \frac{b}{a} \Rightarrow \sin(2\chi) = \frac{2E_{0,x}E_{0,y} \sin \Delta\varphi}{E_{0,x}^2 + E_{0,y}^2} \quad (\text{Ellipticity angle}). \quad (\text{A.4})$$

A typical microwave detector is not able to follow the time evolution of the electromagnetic field, what is actually measured is the time average of the field over periods much longer than $2\pi/\omega$. The time average of the polarization ellipse for purely monochromatic waves is:

$$\frac{\langle E_x^2(t) \rangle}{E_{0,x}^2(t)} + \frac{\langle E_y^2(t) \rangle}{E_{0,y}^2(t)} + \frac{\langle 2E_x(t)E_y(t) \rangle}{E_{0,x}^2(t)E_{0,y}^2(t)} \cos \Delta\varphi = \sin^2 \Delta\varphi. \quad (\text{A.5})$$

where the time averages $\langle \dots \rangle$ are taken over a single period of oscillation, because of the periodicity of the electromagnetic waves. Since $E_x(t)$, $E_y(t)$ are sine waves, their time averages are: $\langle E_x^2(t) \rangle = \langle E_y^2(t) \rangle = 1/2$. After some algebraic passage eq. A.5 becomes:

$$(E_{0,x}^2 + E_{0,y}^2)^2 - (E_{0,x}^2 - E_{0,y}^2)^2 - (2E_{0,x}E_{0,y} \cos \Delta\varphi)^2 = (2E_{0,x}E_{0,y} \sin \Delta\varphi)^2, \quad (\text{A.6})$$

which reduces to

$$S_0^2 = S_1^2 + S_2^2 + S_3^2 , \quad (\text{A.7})$$

with the definitions of the well-known Stokes parameters:

- $S_0 = E_{0,x}^2 + E_{0,y}^2$
- $S_1 = E_{0,x}^2 - E_{0,y}^2$
- $S_2 = 2E_{0,x}E_{0,y} \cos \Delta\varphi$
- $S_3 = 2E_{0,x}E_{0,y} \sin \Delta\varphi$

In general, if the waves are not purely monochromatic, their amplitudes and phases vary with time, leading to

$$S_0^2 \geq S_1^2 + S_2^2 + S_3^2 , \quad (\text{A.8})$$

where the equality is only valid for fully polarized light, while the inequality is valid for partially polarized or unpolarized light. The degree of polarization is usually defined as follows:

$$P = \frac{\sqrt{S_1^2 + S_2^2 + S_3^2}}{S_0} \quad \text{and} \quad 0 \leq P \leq 1 . \quad (\text{A.9})$$

The intensity I of an electromagnetic wave is related to S_0 , in fact:

$$I = \frac{cn\epsilon_0}{2}|E|^2 \propto (E_{0,x}^2 + E_{0,y}^2) = S_0 , \quad (\text{A.10})$$

where n is the refractive index of the medium and ϵ_0 is the electric permittivity in vacuum. The orientation of the polarization ellipse is related to S_1 and S_2 ,

$$\tan(2\psi) = \frac{2E_{0,x}E_{0,y} \cos \Delta\varphi}{E_{0,x}^2 - E_{0,y}^2} = \frac{S_2}{S_1} , \quad (\text{A.11})$$

while its ellipticity is related to S_3 (see fig. A.1):

$$\sin(2\chi) = \frac{2E_{0,x}E_{0,y} \sin \Delta\varphi}{E_{0,x}^2 + E_{0,y}^2} = \frac{S_3}{S_0} . \quad (\text{A.12})$$

For linear polarized light both the parameters S_1 and S_2 represent the difference in intensity carried by two orthogonal components: S_1 is the difference in

intensity between the components along the main axes x and y (see fig. A.2a), while S_2 is the difference in intensity between the components along the axes x' and y' rotated by $45\frac{1}{2}$ with respect to x and y (see fig. A.2b).

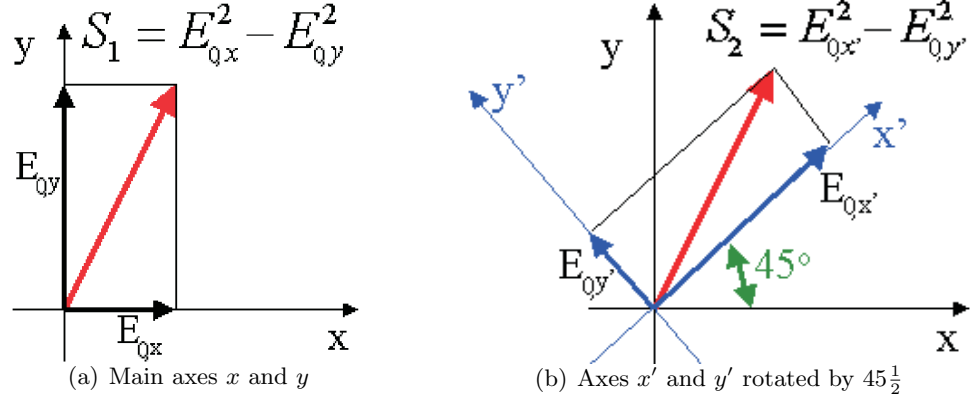


Figure A.2: The Stokes parameters S_1 and S_2 as difference in intensity carried by two orthogonal components rotated by $45\frac{1}{2}$.

At this point, we can introduce the more used Stokes vector \vec{S} , using the well-known complex formalism to represent the plane waves:

$$\begin{aligned} E_x(t) &= E_{0,x}(t) \cos[\omega t + \varphi_x(t)] = E_{0,x}(t) e^{i(\omega t + \varphi_x(t))} , \\ E_y(t) &= E_{0,y}(t) \cos[\omega t + \varphi_y(t)] = E_{0,y}(t) e^{i(\omega t + \varphi_y(t))} , \end{aligned} \quad (\text{A.13})$$

$$\vec{S} = \begin{pmatrix} S_0 \\ S_1 \\ S_2 \\ S_3 \end{pmatrix} = \begin{pmatrix} I \\ Q \\ U \\ V \end{pmatrix} = \begin{pmatrix} E_x E_x^* + E_y E_y^* \\ E_x E_x^* - E_y E_y^* \\ E_x E_y^* + E_y E_x^* \\ i(E_x E_y^* - E_y E_x^*) \end{pmatrix} = \begin{pmatrix} E_{0,x}^2 + E_{0,y}^2 \\ E_{0,x}^2 - E_{0,y}^2 \\ 2E_{0,x} E_{0,y} \cos \Delta\varphi \\ 2E_{0,x} E_{0,y} \sin \Delta\varphi \end{pmatrix} \quad (\text{A.14})$$

Using eqs. A.11 and A.12 we obtain:

$$\vec{S} = \begin{pmatrix} S_0 \\ S_1 \\ S_2 \\ S_3 \end{pmatrix} = \begin{pmatrix} I \\ Q \\ U \\ V \end{pmatrix} = S_0 \begin{pmatrix} 1 \\ \cos(2\chi) \cos(2\psi) \\ \cos(2\chi) \sin(2\psi) \\ \sin(2\chi) \end{pmatrix} \quad (\text{A.15})$$

It's now worth to make some examples with particular cases:

- Unpolarized light $\Rightarrow \Delta\varphi = \text{random}$ and $\langle E_{0,x}^2(t) \rangle = \langle E_{0,y}^2(t) \rangle = I_0$:

$$\begin{pmatrix} I \\ Q \\ U \\ V \end{pmatrix} = 2I_0 \begin{pmatrix} 1 \\ 0 \\ 0 \\ 0 \end{pmatrix} \quad (\text{A.16})$$

- Linearly polarized light $\Rightarrow \Delta\varphi = 0, \pi$:

- Horizontal $\Rightarrow E_{o,y} = 0$:

$$\begin{pmatrix} I \\ Q \\ U \\ V \end{pmatrix} = I_0 \begin{pmatrix} 1 \\ 1 \\ 0 \\ 0 \end{pmatrix} \quad (\text{A.17})$$

- Vertical $\Rightarrow E_{o,x} = 0$:

$$\begin{pmatrix} I \\ Q \\ U \\ V \end{pmatrix} = I_0 \begin{pmatrix} 1 \\ -1 \\ 0 \\ 0 \end{pmatrix} \quad (\text{A.18})$$

- Rotated by $45\frac{1}{2}$ with respect to the x axis counterclockwise $\Rightarrow E_{0,x} = E_{o,y} = E_0$:

$$\begin{pmatrix} I \\ Q \\ U \\ V \end{pmatrix} = I_0 \begin{pmatrix} 1 \\ 0 \\ \pm 1 \\ 0 \end{pmatrix} \quad (\text{A.19})$$

- Rotated by an angle θ with respect to the x axis ($\theta = 0\frac{1}{2}$) counterclockwise $\Rightarrow E_{0,x} = E_0 \cos \theta$, $E_{o,y} = E_0 \sin \theta$:

$$\begin{pmatrix} I \\ Q \\ U \\ V \end{pmatrix} = I_0 \begin{pmatrix} 1 \\ \pm \cos(2\theta) \\ \pm \sin(2\theta) \\ 0 \end{pmatrix} \quad (\text{A.20})$$

- Circular polarized light $\Rightarrow \Delta\varphi = \pi/2, 3\pi/2$ and $E_0 = E_{0,x} = E_{o,y}$:

- Left $\Rightarrow \Delta\varphi = 3\pi/2$:

$$\begin{pmatrix} I \\ Q \\ U \\ V \end{pmatrix} = I_0 \begin{pmatrix} 1 \\ 0 \\ 0 \\ -1 \end{pmatrix} \quad (\text{A.21})$$

– Right $\Rightarrow \Delta\varphi = \pi/2$:

$$\begin{pmatrix} I \\ Q \\ U \\ V \end{pmatrix} = I_0 \begin{pmatrix} 1 \\ 0 \\ 0 \\ 1 \end{pmatrix} \quad (\text{A.22})$$

- Partially polarized light: the Stokes vector of a combination of independent waves is the sum of the respective Stokes vectors of the separate waves; the combination of a fully polarized wave ($P = 1$) with an independent partially polarized one ($P < 1$) yields:

$$\begin{pmatrix} I \\ Q \\ U \\ V \end{pmatrix} = (1 - P) \begin{pmatrix} I' \\ Q' \\ U' \\ V' \end{pmatrix} + P \begin{pmatrix} I'' \\ Q'' \\ U'' \\ V'' \end{pmatrix} \quad (\text{A.23})$$

When a beam of light interacts with matter its polarization state is almost always changed. It is usually made the most of these effects creating polarization-active optical components, such as diattenuators (polarizers), retarders (waveplates) or rotators: they have the property of changing, respectively, the amplitudes, the phases and the directions of the orthogonal field components A.13. Their effect can be described mathematically by means of the so-called *Mueller matrices*, 4×4 matrices such that the resulting Stokes vector is:

$$\vec{S}' = \mathcal{M} \times \vec{S} \quad \Rightarrow \quad \begin{pmatrix} I' \\ Q' \\ U' \\ V' \end{pmatrix} = \begin{pmatrix} a_{11} & a_{12} & a_{13} & a_{14} \\ a_{21} & a_{22} & a_{23} & a_{24} \\ a_{31} & a_{32} & a_{33} & a_{34} \\ a_{41} & a_{42} & a_{43} & a_{44} \end{pmatrix} \times \begin{pmatrix} I \\ Q \\ U \\ V \end{pmatrix} \quad (\text{A.24})$$

In the following we shall characterize the main polarization-active optical components, i.e. polarizers, rotators and retarders (wave plates), together with common optical elements such as an intensity detector and a plane mirror. Every component described here has a precise application in this work (see chapter 4).

An intensity detector is simply represented by the Stokes vector $\vec{D} = (1, 0, 0, 0)$, in such a way that the power detected by the detector from a generic optical beam with Stokes vector \vec{S} is (eq. A.24) $S'_0 = I' = \vec{D} \times \vec{S}$.

A generic polarizer (or diattenuator) is a polarization active optical component which attenuates unequally the orthogonal components of an optical beam:

$$E'_x = p_x E_x \quad \text{and} \quad E'_y = p_y E_y, \quad (\text{A.25})$$

where $0 \leq p_{x,y} \leq 1$ are the polarization degrees of the two orthogonal components. From eqs. A.14 and A.24 we get:

$$\begin{pmatrix} I' \\ Q' \\ U' \\ V' \end{pmatrix} = \frac{1}{2} \begin{pmatrix} p_x^2 + p_y^2 & p_x^2 - p_y^2 & 0 & 0 \\ p_x^2 - p_y^2 & p_x^2 + p_y^2 & 0 & 0 \\ 0 & 0 & 2p_x p_y & 0 \\ 0 & 0 & 0 & 2p_x p_y \end{pmatrix} \times \begin{pmatrix} I \\ Q \\ U \\ V \end{pmatrix} \quad (\text{A.26})$$

Defining $p_x = p \cos \alpha$ and $p_y = p \sin \alpha$, the Mueller matrix of a generic polarizer becomes, from eq. A.26:

$$\mathcal{M}_P = \frac{p^2}{2} \begin{pmatrix} 1 & \cos(2\alpha) & 0 & 0 \\ \cos(2\alpha) & 1 & 0 & 0 \\ 0 & 0 & \sin(2\alpha) & 0 \\ 0 & 0 & 0 & \sin(2\alpha) \end{pmatrix} \quad (\text{A.27})$$

There are three special cases of particular interest:

- Attenuator $\Rightarrow p_x = p_y = p$:

$$\begin{pmatrix} I' \\ Q' \\ U' \\ V' \end{pmatrix} = \frac{p^2}{2} \begin{pmatrix} 1 & 0 & 0 & 0 \\ 0 & 1 & 0 & 0 \\ 0 & 0 & 1 & 0 \\ 0 & 0 & 0 & 1 \end{pmatrix} \times \begin{pmatrix} I \\ Q \\ U \\ V \end{pmatrix} \quad (\text{A.28})$$

- Ideal horizontal polarizer $\Rightarrow p_y = 0, p_x = 1$:

$$\begin{pmatrix} I' \\ Q' \\ U' \\ V' \end{pmatrix} = \frac{1}{2} \begin{pmatrix} 1 & 1 & 0 & 0 \\ 1 & 1 & 0 & 0 \\ 0 & 0 & 0 & 0 \\ 0 & 0 & 0 & 0 \end{pmatrix} \times \begin{pmatrix} I \\ Q \\ U \\ V \end{pmatrix} = \frac{1}{2} (I + Q) \times \begin{pmatrix} 1 \\ 1 \\ 0 \\ 0 \end{pmatrix} \quad (\text{A.29})$$

- Ideal vertical polarizer $\Rightarrow p_x = 0, p_y = 1$:

$$\begin{pmatrix} I' \\ Q' \\ U' \\ V' \end{pmatrix} = \frac{1}{2} \begin{pmatrix} 1 & -1 & 0 & 0 \\ -1 & 1 & 0 & 0 \\ 0 & 0 & 0 & 0 \\ 0 & 0 & 0 & 0 \end{pmatrix} \times \begin{pmatrix} I \\ Q \\ U \\ V \end{pmatrix} = \frac{1}{2} (I - Q) \times \begin{pmatrix} 1 \\ -1 \\ 0 \\ 0 \end{pmatrix} \quad (\text{A.30})$$

The net effect of an ideal linear polarizer is to convert any incoming (partially polarized or unpolarized) beam into a linearly polarized beam.

Let us now step forward and characterize a phase-shifting element, i.e. a retarder or wave plate: its effect is to advance the phase of the x component of the field by $+\Delta\varphi/2$, while retarding the y component by $-\Delta\varphi/2$. The field emerging from such optical element is thus:

$$E'_x = E_x e^{i\Delta\varphi/2} \quad \text{and} \quad E'_y = E_y e^{-i\Delta\varphi/2}. \quad (\text{A.31})$$

From eqs. A.14 and A.24 it's easy to see that:

$$\begin{pmatrix} I' \\ Q' \\ U' \\ V' \end{pmatrix} = \begin{pmatrix} 1 & 0 & 0 & 0 \\ 0 & 1 & 0 & 0 \\ 0 & 0 & \cos \Delta\varphi & \sin \Delta\varphi \\ 0 & 0 & -\sin \Delta\varphi & \cos \Delta\varphi \end{pmatrix} \times \begin{pmatrix} I \\ Q \\ U \\ V \end{pmatrix} \quad (\text{A.32})$$

When $\Delta\varphi = \pi$ the retarder is called *Half Wave Plate* (HWP); it reverses the ellipticity and orientation of the incoming polarization state (see eqs. A.3 and A.4):

$$\mathcal{M}_{HWP} = \begin{pmatrix} 1 & 0 & 0 & 0 \\ 0 & 1 & 0 & 0 \\ 0 & 0 & -1 & 0 \\ 0 & 0 & 0 & -1 \end{pmatrix} \quad (\text{A.33})$$

If instead $\Delta\varphi = \pi/2$ the retarder is called *Quarter Wave Plate* (QWP); it converts a $\pm 45^\circ$ linearly polarized beam into a left/right circularly polarized beam (see eqs. A.21 and A.22):

$$\mathcal{M}_{QWP} = \begin{pmatrix} 1 & 0 & 0 & 0 \\ 0 & 1 & 0 & 0 \\ 0 & 0 & 0 & 1 \\ 0 & 0 & -1 & 0 \end{pmatrix} \quad (\text{A.34})$$

So far we have worked under the assumption that the optical axis of the components were aligned to the coordinates system in which the electromagnetic waves propagate along the z axis and oscillate in the $x - y$ plane. In the real experiments a rotator is often introduced (e.g. for modulation) and we thus have to take this problem into account, working out the rotated coordinate system into the formalism of the Mueller matrices. The first step is to rotate the incident beam \vec{S}_{in} from the original coordinate system to the one aligned with the optical component, $\vec{S}' = \mathcal{M}_{rot}(\theta)\vec{S}_{in}$, where θ is counted with respect to the x axis ($\theta = 0^\circ$) counterclockwise; then we can apply the Mueller matrix of the component to \vec{S}' and get: $\vec{S}'' = \mathcal{M}_C \vec{S}'$. Finally the output beam has to

be rotated back to the original coordinate system: $\vec{S}_{out} = \mathcal{M}_{rot}(-\theta)\vec{S}''$. The final Stokes vector can be directly written as a multiple matrix product:

$$\vec{S}_{out} = \mathcal{M}_{rot}(-\theta) \times \mathcal{M}_C \times \mathcal{M}_{rot}(\theta) \times \vec{S}_{in}, \quad (\text{A.35})$$

where $\mathcal{M}_{rot}(\theta)$ is the usual rotation matrix

$$\mathcal{M}_{rot}(\theta) = \begin{pmatrix} 1 & 0 & 0 & 0 \\ 0 & \cos(2\theta) & \sin(2\theta) & 0 \\ 0 & -\sin(2\theta) & \cos(2\theta) & 0 \\ 0 & 0 & 0 & 1 \end{pmatrix} \quad (\text{A.36})$$

Recalling eqs. A.26 and A.27, and with the following definitions

$$\begin{cases} \Xi = \cos(2\theta) \\ \Lambda = \sin(2\theta), \\ \Sigma = p_x^2 + p_y^2 = p^2(\cos^2 \alpha + \sin^2 \alpha) = p^2, \\ \Delta = p_x^2 - p_y^2 = p^2(\cos^2 \alpha - \sin^2 \alpha), \\ \Upsilon = 2p_x p_y = 2p^2 \sin \alpha \cos \alpha, \end{cases} \quad (\text{A.37})$$

we obtain the Mueller matrix for a rotating generic polarizer, $\mathcal{M}_P(\theta) = \mathcal{M}_{rot}(-\theta) \times \mathcal{M}_P \times \mathcal{M}_{rot}(\theta)$:

$$\mathcal{M}_P(\theta) = \frac{1}{2} \begin{pmatrix} \Sigma & \Xi\Delta & \Lambda\Delta & 0 \\ \Xi\Delta & \Xi^2\Sigma + \Lambda^2\Upsilon & \Xi\Lambda(\Sigma - \Upsilon) & 0 \\ \Lambda\Delta & \Xi\Lambda(\Sigma - \Upsilon) & \Lambda^2\Sigma + \Xi^2\Upsilon & 0 \\ 0 & 0 & 0 & \Upsilon \end{pmatrix} \quad (\text{A.38})$$

In the case of an ideal horizontal polarizer ($p = 1$ and $\alpha = 0, \pi$ in eqs. A.27 and A.37 $\Rightarrow \Sigma = 1, \Delta = 1, \Upsilon = 0$), eq. A.38 becomes:

$$\mathcal{M}_P(\theta) = \frac{1}{2} \begin{pmatrix} 1 & \cos(2\theta) & \sin(2\theta) & 0 \\ \cos(2\theta) & \cos^2(2\theta) & \sin(2\theta)\cos(2\theta) & 0 \\ \sin(2\theta) & \sin(2\theta)\cos(2\theta) & \sin^2(2\theta) & 0 \\ 0 & 0 & 0 & 0 \end{pmatrix}, \quad (\text{A.39})$$

while in the case of an ideal vertical polarizer ($p = 1$ and $\alpha = \pi/2, 3\pi/2$) we get:

$$\mathcal{M}_P(\theta) = \frac{1}{2} \begin{pmatrix} 1 & -\cos(2\theta) & -\sin(2\theta) & 0 \\ -\cos(2\theta) & \cos^2(2\theta) & \sin(2\theta)\cos(2\theta) & 0 \\ -\sin(2\theta) & \sin(2\theta)\cos(2\theta) & \sin^2(2\theta) & 0 \\ 0 & 0 & 0 & 0 \end{pmatrix}. \quad (\text{A.40})$$

Analogously we obtain the Mueller matrix for a rotating generic wave plate (WP), $\mathcal{M}_{WP}(\theta) = \mathcal{M}_{rot}(-\theta) \times \mathcal{M}_{WP} \times \mathcal{M}_{rot}(\theta)$:

$$\mathcal{M}_{WP}(\theta) = \tag{A.41}$$

$$\begin{pmatrix} 1 & 0 & 0 & 0 \\ 0 & \cos^2(2\theta) + \sin^2(2\theta) \cos \Delta\varphi & \sin(4\theta) \sin^2\left(\frac{\Delta\varphi}{2}\right) & -\sin(2\theta) \sin \Delta\varphi \\ 0 & \sin(4\theta) \sin^2\left(\frac{\Delta\varphi}{2}\right) & \cos^2(2\theta) \cos \Delta\varphi + \sin^2(2\theta) & \cos(2\theta) \sin \Delta\varphi \\ 0 & \sin(2\theta) \sin \Delta\varphi & -\cos(2\theta) \sin \Delta\varphi & \cos \Delta\varphi \end{pmatrix}$$

Remembering that $\cos(2\theta) = \cos^2 \theta - \sin^2 \theta$, from eq. A.34 we get the Mueller matrix for a Rotating Half Wave Plate (RHWP):

$$\mathcal{M}_{HWP}(\theta) = \begin{pmatrix} 1 & 0 & 0 & 0 \\ 0 & \cos(4\theta) & \sin(4\theta) & 0 \\ 0 & \sin(4\theta) & -\cos(4\theta) & 0 \\ 0 & 0 & 0 & -1 \end{pmatrix} \tag{A.42}$$

The last optical element we describe is a plane metallic mirror, which simply reflects the incoming radiation. Also such a polarization non-active optical component can be described by means of a Mueller matrix. Defining the angles of incidence α_i and reflection α_r of the beam with respect to normal versor relative to surface of the mirror, and also defining $\alpha_{\pm} = \alpha_i \pm \alpha_r$, the reflection Mueller matrix results to be (see fore example [73], chapter 8):

$$\mathcal{M}_R = \frac{1}{2} \left(\frac{\tan \alpha_-}{\sin \alpha_+} \right)^2 \times \tag{A.43}$$

$$\begin{pmatrix} \cos^2 \alpha_- + \cos^2 \alpha_+ & \cos^2 \alpha_- - \cos^2 \alpha_+ & 0 & 0 \\ \cos^2 \alpha_- - \cos^2 \alpha_+ & \cos^2 \alpha_- + \cos^2 \alpha_+ & 0 & 0 \\ 0 & 0 & -2 \cos \alpha_+ \cos \alpha_- & 0 \\ 0 & 0 & 0 & -2 \cos \alpha_+ \cos \alpha_- \end{pmatrix}$$

Appendix B

Spin-weighted Functions

In this appendix we give an introduction to the theory of spin-weighted functions and their expansion in spin- s spherical harmonics, closely following the discussion by Goldberg et al. [48], which is based on the work by Newsman and Penrose [49].

For any given direction on the sphere specified by the usual spherical coordinates (θ, ϕ) , one can define three orthogonal unit vectors (versors), one radial and two tangential to the sphere. Let us denote the radial direction versor with \hat{n} and the tangential with (\hat{e}_1, \hat{e}_2) . The latter two are only defined up to a rotation around \hat{n} . A function ${}_s f(\theta, \phi)$ defined on the sphere is said to have spin- s if under a right-handed rotation of (\hat{e}_1, \hat{e}_2) by an angle α , it transforms as ${}_s f'(\theta, \phi) = e^{-is\alpha} f(\theta, \phi)$. For example, given an arbitrary vector \vec{a} on the sphere, the quantities $(\vec{a} \cdot \hat{e}_1 + i\vec{a} \cdot \hat{e}_2)$, $(\hat{n} \cdot \vec{a})$ and $(\vec{a} \cdot \hat{e}_1 - i\vec{a} \cdot \hat{e}_2)$, have spin 1, 0 and -1 respectively. A scalar field on the sphere can be expanded in spherical harmonics $Y_{lm}(\theta, \phi)$, which form a complete and orthonormal basis. These functions are not appropriate to expand spin-weighted functions (with $s \neq 0$). There exist an analogous sets of functions, the so-called spin- s spherical harmonics, ${}_s Y_{lm}(\theta, \phi)$, that satisfy the same completeness and orthogonality relations:

$$\int_0^{2\pi} d\phi \int_{-1}^1 d\cos\theta \, {}_s Y_{lm}(\theta, \phi) \, {}_s Y_{l'm'}^*(\theta, \phi) = \delta_{ll'} \delta_{mm'} , \quad (\text{B.1})$$

$$\sum_{l=0}^{\infty} \sum_{m=-l}^{m=l} {}_s Y_{lm}(\theta, \phi) \, {}_s Y_{lm}^*(\theta', \phi') = \delta(\phi - \phi') \delta(\cos\theta - \cos\theta') .$$

Let us define the spin raising and lowering operators, $\bar{\eth}$ and \eth , with the property of, respectively, raising and lowering the spin-weight of a function:

$$\begin{aligned}
\eth &= -\sin^s(\theta) \left[\frac{\partial}{\partial\theta} + i \csc(\theta) \frac{\partial}{\partial\phi} \right] \sin^{-s}(\theta) , \\
\ethbar &= -\sin^{-s}(\theta) \left[\frac{\partial}{\partial\theta} - i \csc(\theta) \frac{\partial}{\partial\phi} \right] \sin^s(\theta) .
\end{aligned} \tag{B.2}$$

Their action on a spin-weighted function ${}_s f(\theta, \phi)$ is:

$$\begin{aligned}
(\eth {}_s f(\theta, \phi))' &= e^{-i(s+1)} \eth {}_s f(\theta, \phi) , \\
(\ethbar {}_s f(\theta, \phi))' &= e^{-i(s-1)} \ethbar {}_s f(\theta, \phi) ,
\end{aligned} \tag{B.3}$$

where θ is again the rotation angle. As explained in par. 2.5.2, the polarization field is a quantity of spin ± 2 . The operators \eth and \ethbar acting twice on a function ${}_{\pm 2} f(\mu, \phi)$ ($\mu \equiv \cos\theta$) that satisfies $\partial_\phi {}_{\pm 2} f(\mu, \phi) = im {}_{\pm 2} f(\mu, \phi)$, can be expressed as:

$$\begin{aligned}
\eth^2 {}_2 f(\mu, \phi) &= \left(-\partial\mu + \frac{m}{1-\mu^2} \right)^2 (1-\mu^2) {}_2 f(\mu, \phi) , \\
\ethbar^2 {}_{-2} f(\mu, \phi) &= \left(-\partial\mu - \frac{m}{1-\mu^2} \right)^2 (1-\mu^2) {}_{-2} f(\mu, \phi) .
\end{aligned} \tag{B.4}$$

The most important consequence of the introduction of these spin raising and lowering operators is that the spin- s spherical harmonics can be expressed in terms of the usual zero-spin spherical harmonics Y_{lm} :

$$\begin{aligned}
{}_s Y_{lm} &= \sqrt{\frac{(l-s)!}{(l+s)!}} \eth^s Y_{lm} & (0 \leq s \leq l) , \\
{}_s Y_{lm} &= \sqrt{\frac{(l+s)!}{(l-s)!}} (-1)^s \ethbar^{-s} Y_{lm} & (-l \leq s \leq 0) .
\end{aligned} \tag{B.5}$$

We also list some useful properties of the spin-weighted spherical harmonics:

$$\begin{aligned}
{}_s Y_{lm}^* &= (-1)^s {}_{-s} Y_{l-m} , \\
\eth {}_s Y_{lm} &= \sqrt{(l-s)(l+s+1)} {}_{s+1} Y_{lm} , \\
\ethbar {}_s Y_{lm} &= -\sqrt{(l+s)(l-s+1)} {}_{s-1} Y_{lm} , \\
\eth\ethbar {}_s Y_{lm} &= -(l-s)(l+s+1) {}_s Y_{lm} .
\end{aligned} \tag{B.6}$$

Appendix C

Gunn Oscillators

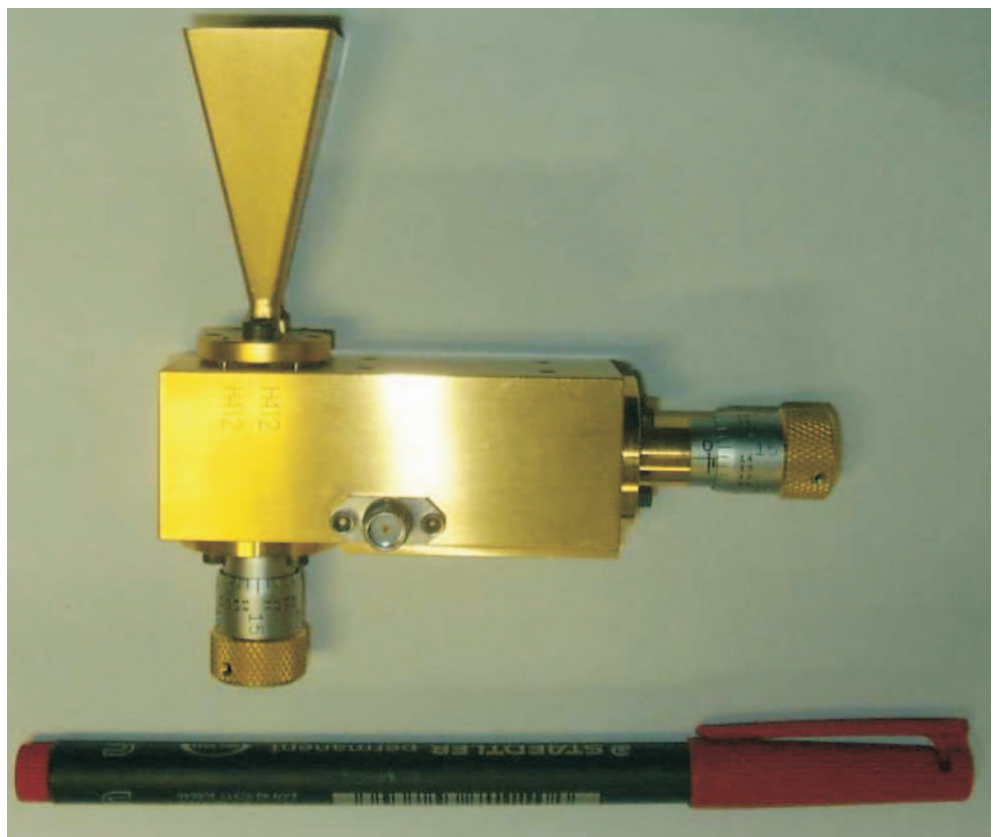
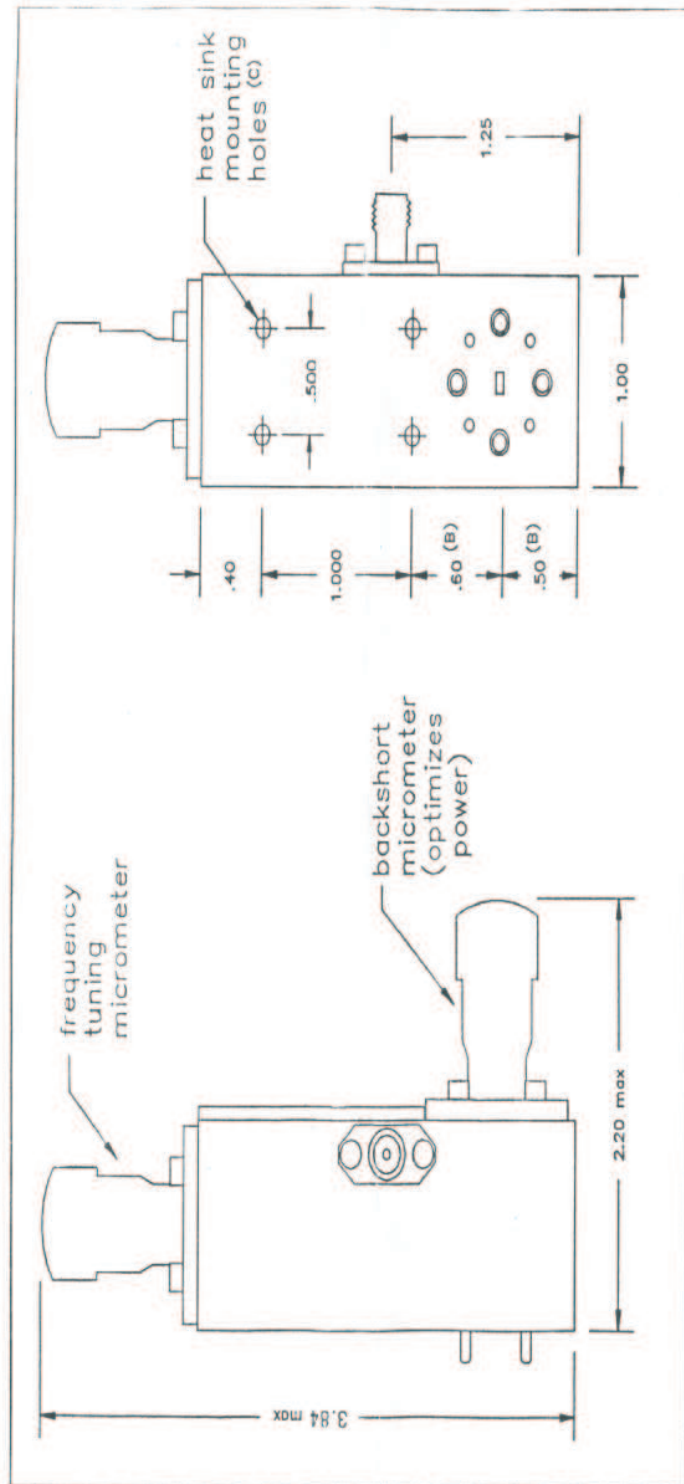


Figure C.1: Picture of the 78 – 114 GHz Gunn oscillator.

J. E. Carlstrom Co
Chicago, IL U.S.A.

WIDEBAND MECHANICALLY TUNED GUNN OSCILLATORS



NOTES: (A) all dimensions in inches
(B) these dimensions measured to bottom edge of waveguide
(C) 4 holes, 0.25 inches deep, threaded 4-40

Figure C.2: Gunn oscillators provided by J.E. Carlstrom Co., Chicago IL (U.S.A.).

Frequency (GHz)	Tuning Mic (mils)	Backshort (mils)	Output Power (mW)	Bias tuning dV/(100MHz)
78.0	75.6	57.0	38	0.30
79.0	70.9	56.0	49	0.25
80.0	66.3	53.5	53	0.25
81.0	61.5	50.0	51	0.25
82.0	57.0	47.0	49	0.20
83.0	52.6	42.0	52	0.20
84.0	48.6	37.5	51	0.25
85.0	45.1	33.5	52	0.25
86.0	41.9	29.5	53	0.30
87.0	38.8	26.0	53	0.30
88.0	36.0	24.0	53	0.20
89.0	33.4	16.5	54	0.25
90.0	30.8	11.5/97.0	52	0.25
91.0	28.6	87.0	56	0.20
92.0	26.5	75.0	57	0.20
93.0	24.6	60.0	54	0.25
94.0	22.9	59.0	48	0.20
95.0	21.3	50.0	46	0.20
96.0	19.9	46.5	45	0.20
97.0	18.4	41.0	41	0.25
98.0	17.0	36.5	38	0.25
99.0	15.8	35.0	40	0.20
100.0	14.7	31.0	41	0.20
101.0	16.5	28.0	38	0.20
102.0	12.4	26.0	35	0.15
103.0	11.3	23.0	35	0.20
104.0	10.4	20.5	38	0.20
105.0	9.5	18.0	41	0.15
106.0	8.7	15.5	38	0.20
107.0	7.8	12.5	35	0.25
108.0	7.0	10.0	30	0.20
109.0	6.1	8.0	29	0.20
110.0	5.3	5.0	27	0.20
111.0	4.6	2.0/66.0	24	0.20
112.0	3.8	60.5	18	0.15
113.0	3.0	53.5	13	0.20
114.0	2.0	26.5	11	0.25

Bias = 10.0 Volts; ~180 mA; **Do not operate above 10.5 Volts.**

INTERNAL PROTECTIVE CIRCUITRY - Internal protection is provided against overvoltage and reverse bias. Bias greater than 10.8 Volts will trip crowbar circuit. Turn oscillator off to reset.

Do not remove micrometer knobs or disassemble oscillators.

Backshort position that provides highest output power and best frequency tuning is near position that 'pulls' to highest output frequency.

Figure C.3: Datasheet of the 78 – 114 GHz Gunn oscillator.

Frequency (GHz)	Tuning Mic (mils)	Backshort (mils)	Output Power (mW)	Bias tuning dV/(100MHz)
120.0	46.6	144.0	29	0.15
121.0	45.0	141.0	27	0.85
122.0	43.4	128.5	27	0.25
123.0	42.0	127.5	28	0.45
124.0	40.6	126.5	30	0.40
125.0	39.1	125.5	27	0.85
126.0	37.8	117.5	32	0.25
127.0	36.3	114.0	27	0.25
128.0	35.0	109.5	26	0.40
129.0	33.9	93.5	22	0.25
130.0	32.6	92.5	24	0.35
131.0	31.4	86.5	21	0.20
132.0	30.4	85.5	28	0.15
133.0	29.3	81.5	27	0.10
134.0	28.3	76.5	19	0.35
135.0	27.3	75.5	20	0.30
136.0	26.3	73.5	20	0.25
137.0	25.4	70.5	20	0.20
138.0	24.5	68.0	17	0.20
139.0	23.6	66.5	17	0.25
140.0	22.9	64.5	18	0.20
141.0	22.0	62.0	15	0.40
142.0	21.2	61.0	17	0.20
143.0	20.5	60.0	19	0.15
144.0	19.9	58.5	21	0.20
145.0	19.1	48.0	19	0.20
146.0	18.4	47.0	18	0.20
147.0	17.8	46.0	18	0.20

Bias = 9.0 Volts; ~180 mA; Do not operate above 9.5 Volts.

INTERNAL PROTECTIVE CIRCUITRY - Internal protection is provided against overvoltage and reverse bias. Bias greater than 9.8 Volts will trip crowbar circuit. Turn oscillator off to reset.

Do not remove micrometer knobs or disassemble oscillators.

Backshort position that provides highest output power and best frequency tuning is near position that 'pulls' to highest output frequency.

For best power output use a tunable waveguide phaseshifter for impedance matching.

Optimum backshort position will depend on output match.

Please note: the crowbar protection circuit tripping without apparent cause could indicate

a problem internal to the oscillator, such as an intermittent short which could destroy the Gunn diode. To inspect for this problem, turn off oscillator and remove bias supply. Then check the bias port for a short condition with an ohm meter as the oscillator is mechanically tuned though its full range. The typical resistance is 5 - 10 ohms.

Do not operate the oscillator if any short circuits are found.

Figure C.4: Datasheet of the 120 – 147 GHz Gunn oscillator.

Appendix D

Waveguides and Flanges

RECTANGULAR TE ₁₀ WAVEGUIDE INFORMATION					
EIA	FREQUENCIES IN GHz.			WAVEGUIDE DIM.	
WR #	WAVEGUIDE BANDWIDTH	CUT OFF	LOSS dB/FT. LOW - HIGH	INSIDE "a" - "b"	OUTSIDE "A" - "B"
10	75.00 - 110.0	59.05	2.0 - 1.4	.100 - .050	.180 - .130
08	90.00 - 140.0	73.84	3.0 - 2.0	.080 - .040	.160 - .120
06	110.0 - 170.0	90.94	3.2 - 2.7	.0650 - .0325	.145 - .112

MOST COMMON MATING FLANGES TO MILLIMETER WAVEGUIDE						
FLANGE TYPES AND DESCRIPTIVE INTERFACE STANDARDS						
MIL. SPECS	DESCRIPTIVE FLANGE INFORMATION					AEROWAVE
MIL.-F-3922	SIZE - TYPE	FACE	JOINT	CONNECTIVE	ALIGNMENT	STANDARD
/67B - 010	.750 - RD.	CNT.	F/T.	THD. HOLES	FIXED A/PIN	→ 10-0120
/67B - M08	.750 - RD.	CNT.	F/T.	THD. HOLES	FIXED A/PIN	08-0120
/74 - 001	.375 - RD.	CNT.	F/T.	COUPLINGS	FIXED A/PIN	→ 08-0130
/67B - M06	.750 - RD.	CNT.	F/T.	THD. HOLES	FIXED A/PIN	06-0120
/74 - 002	.375 - RD.	CNT.	F/T.	COUPLINGS	FIXED A/PIN	→ 06-0130

Figure D.1: Specifications of Aerowave rectangular waveguides and flanges.

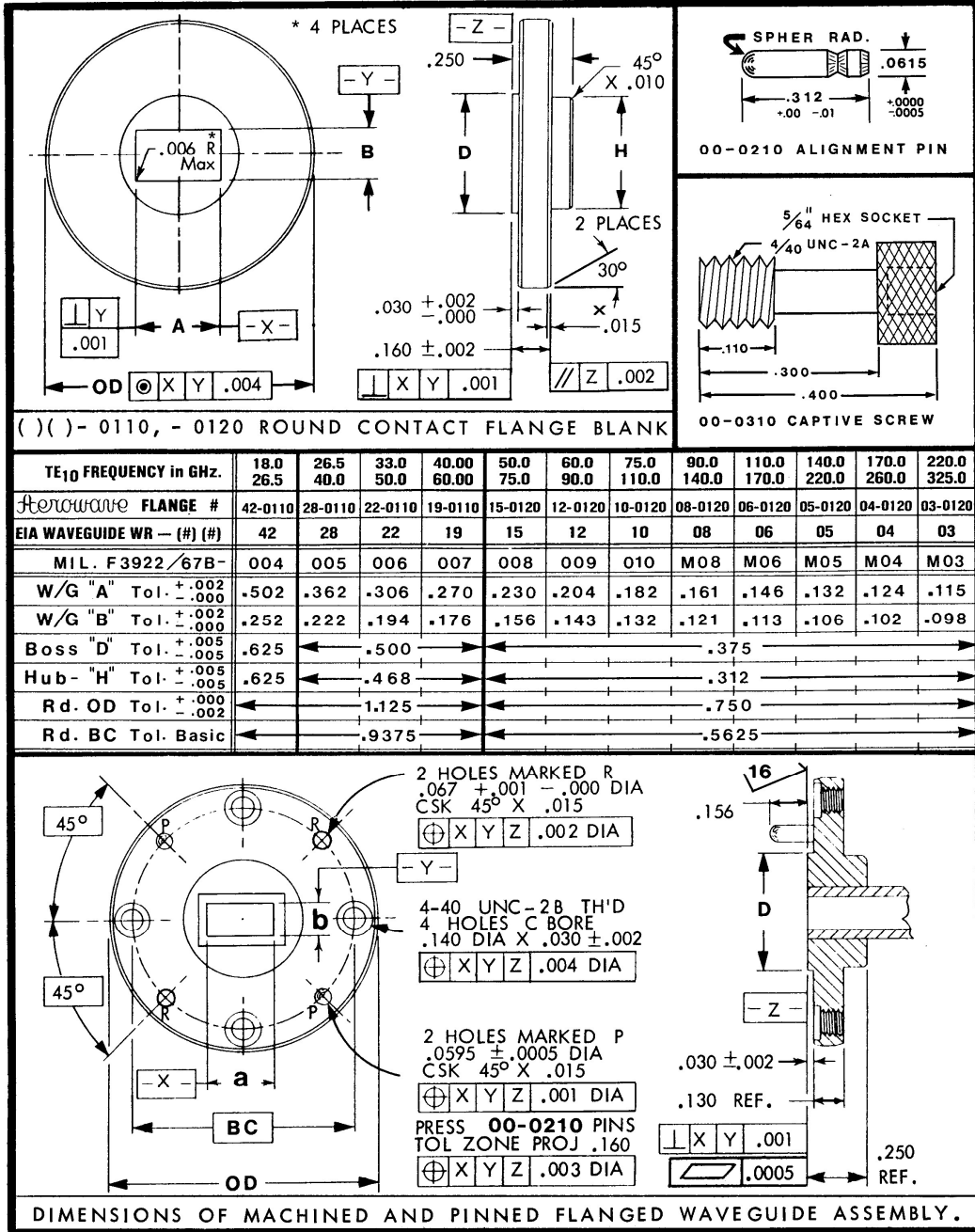


Figure D.2: Drawings with dimensions of Aerowave waveguides and flanges (1 of 3).

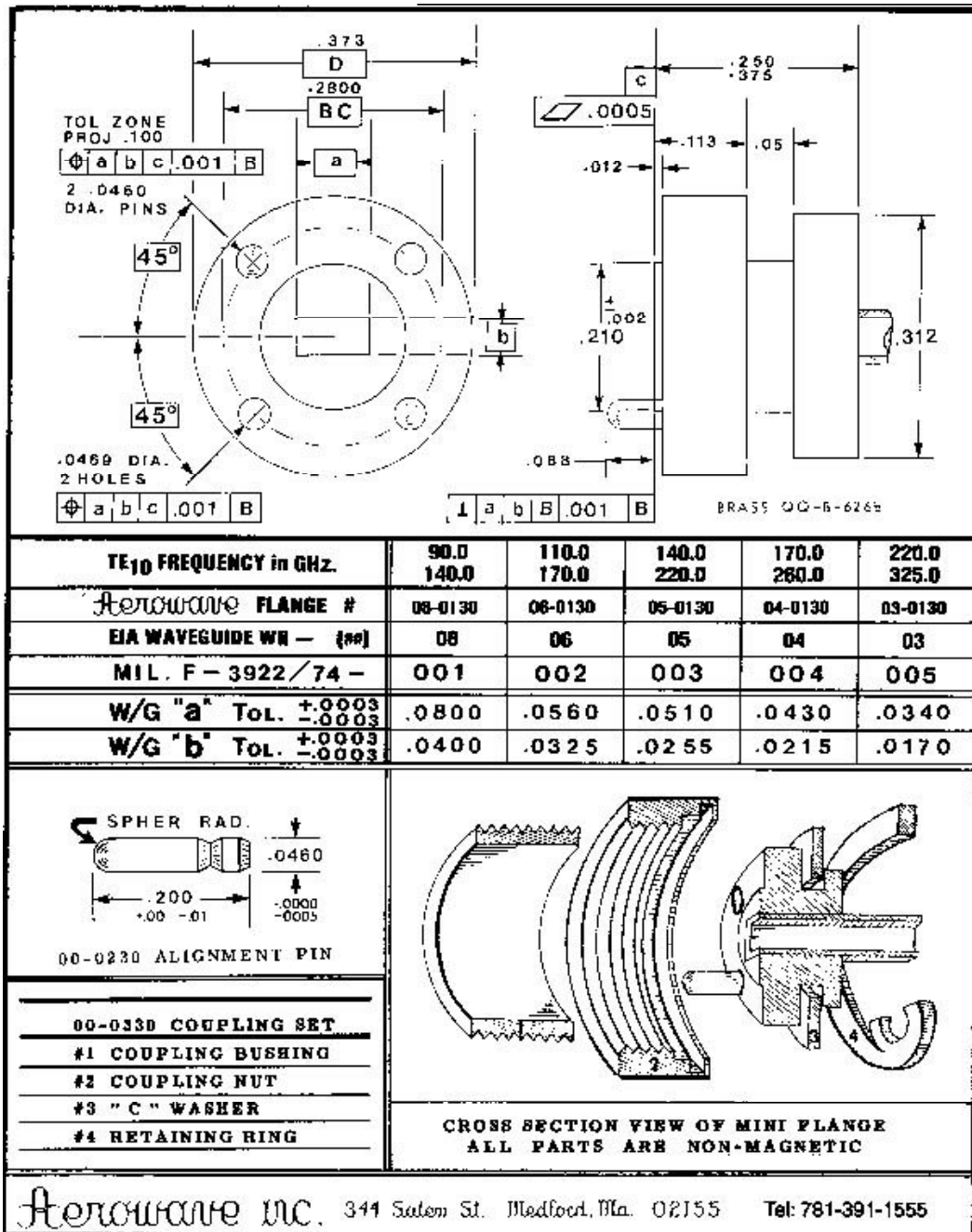


Figure D.3: Drawings with dimensions of Aerowave waveguides and flanges (2 of 3).

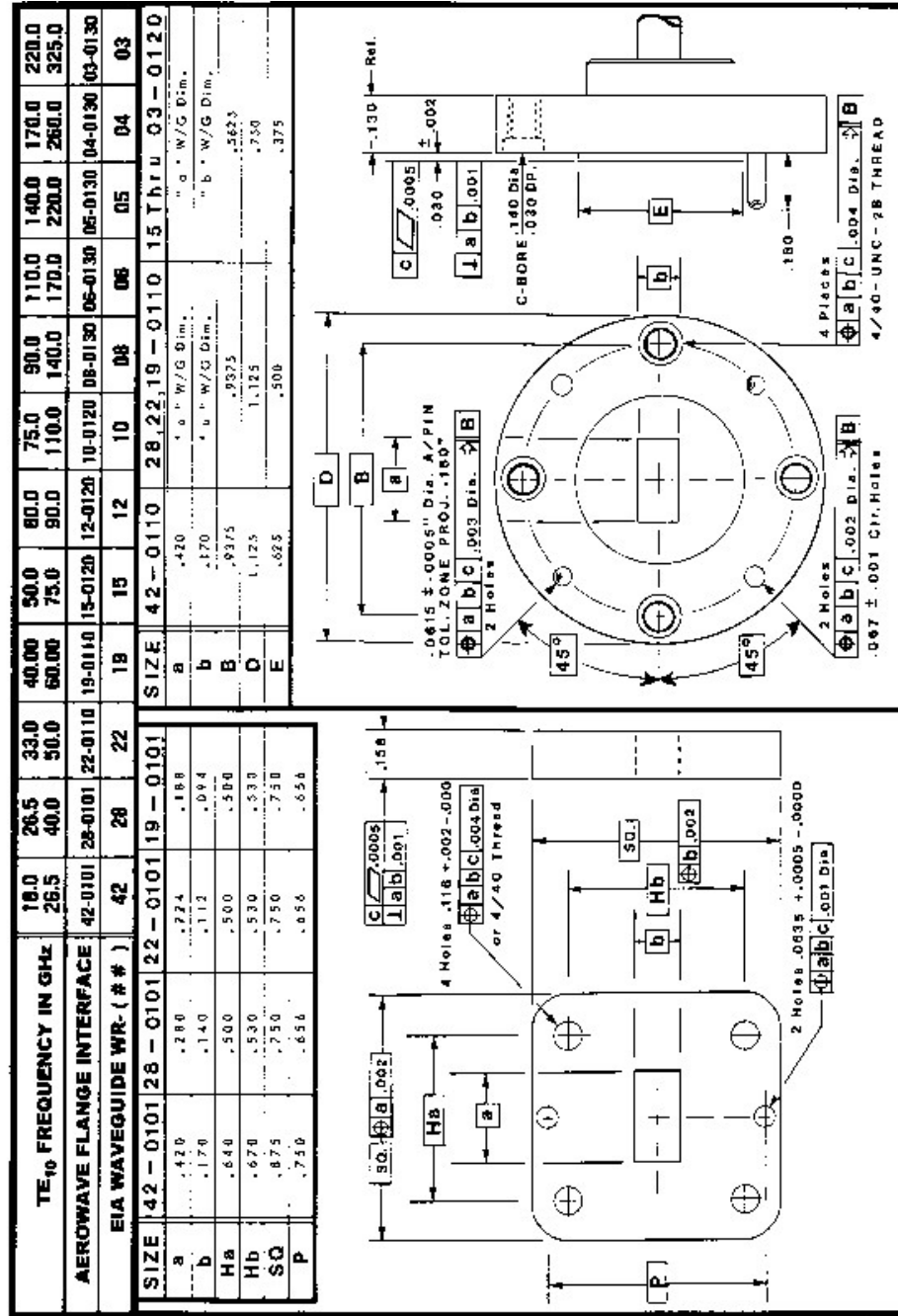


Figure D.4: Drawings with dimensions of Aerowave waveguides and flanges (3 of 3).

Appendix E

Antennas and Beams

In this Appendix we give some elements of antenna patterns and beams of radiation: a full treatment is given, for example, in [70]. The radiation patterns are three-dimensional quantities involving the variation of field or power as a function of the spherical coordinates θ and ϕ . Fig. E.1 shows a field pattern proportional to the field intensity in the direction θ and ϕ .

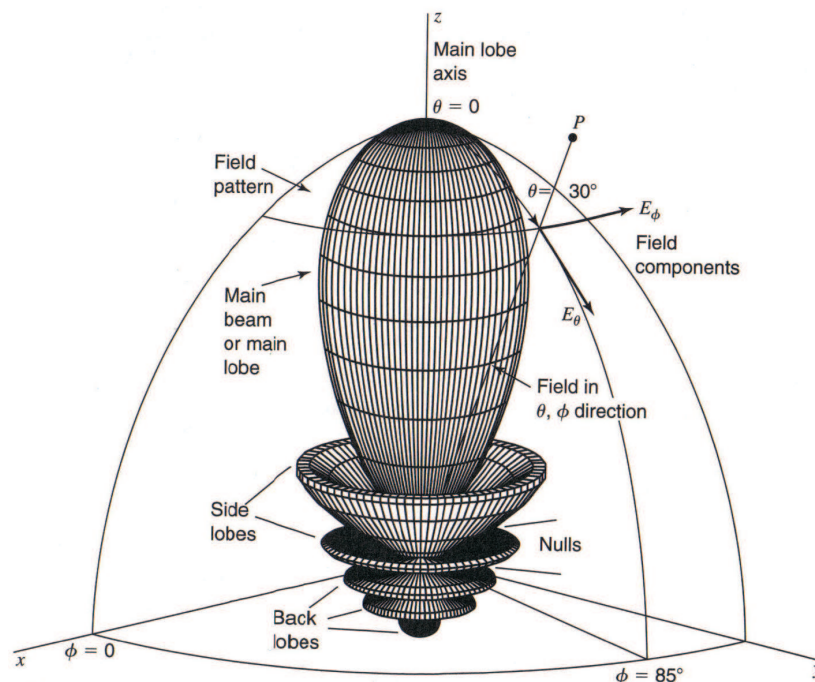


Figure E.1: 3D field pattern of a directional antenna with maximum of radiation at $\theta = 0$. Most of radiation is contained in the main lobe, but there are also minor lobes (side and back). This pattern is symmetric in ϕ and is a function of θ only.

The pattern has its *main lobe* in the z direction ($\theta = 0$) with *minor lobes* (*side*

and *back*) in other directions. In order to completely specify the radiation pattern with respect to field intensity and polarization we need the two components of the electric field along θ and ϕ , each as a function of both angles, $E_\theta(\theta, \phi)$ and $E_\phi(\theta, \phi)$, and finally the phases of these fields as a function of θ and ϕ .

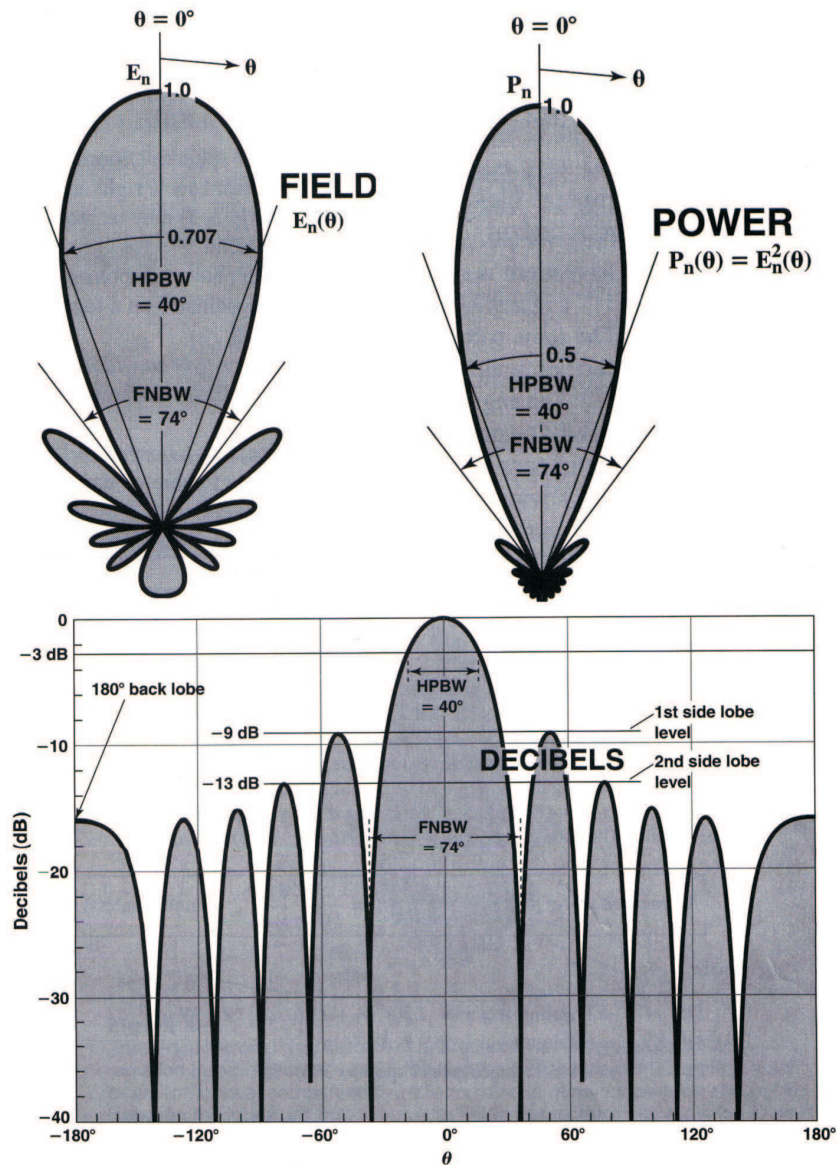


Figure E.2: 2D field, power and decibel plots of the 3D antenna pattern of fig. E.1.

In fig. E.2 we show the principal plane¹ field and power patterns in polar coordinates, together with the same field pattern in rectangular coordinates on a logarithmic (or decibel) scale. It's usual to define the angular beamwidth at half-power level or *half-power beamwidth* (HPBW) and the *beamwidth between first nulls* (FNBW). Dividing a field component by its maximum value, we obtain the dimensionless *normalized field pattern*:

$$E_{\theta,\phi}^n(\theta, \phi) = \frac{E_{\theta,\phi}(\theta, \phi)}{E_{\theta,\phi}^{max}(\theta, \phi)} . \quad (\text{E.1})$$

The half-power level occurs at those angles for which $E_{\theta}^n(\theta, \phi) = (2)^{-1/2} = 0.707$. At large distances compared to the size of the antenna (and to the wavelength), the shape of the field pattern is independent of distance (*far field* condition, see 3.3.1). Patterns may also be expressed in terms of the power per unit area by means of the Poynting vector² $S(\theta, \phi) = [E_{\theta}^2(\theta, \phi) + E_{\phi}^2(\theta, \phi)] / Z_0$, which in the far-field limit is always pointing radially outward. The dimensionless *normalized power pattern* is:

$$P_n(\theta, \phi) = \frac{S(\theta, \phi)}{S_{max}(\theta, \phi)} \frac{P(\theta, \phi)}{P_{max}(\theta, \phi)} . \quad (\text{E.2})$$

The decibel level is given by $dB = 10 \log_{10} P_n(\theta, \phi)$. We are now able to define the *beam solid angle* or *beam area* Ω_A of an antenna:

$$\Omega_A = \int_0^{2\pi} d\phi \int_0^{\pi} d\cos\theta P_n(\theta, \phi) . \quad (\text{E.3})$$

The beam area Ω_A of an antenna can often be described approximately in terms of the angles subtended by the half-power points of the main lobe in the two principal planes: $\Omega_A \simeq \theta_{HP} \cdot \phi_{HP}$. The (total) beam area Ω_A is the sum of the contribution from the main beam, Ω_M , plus the one from the minor-lobe area, Ω_m . The ratio of the main beam to the total beam area is called *beam efficiency*:

$$\varepsilon_M = \frac{\Omega_M}{\Omega_A} = \frac{\Omega_M}{\Omega_M + \Omega_m} , \quad (\text{E.4})$$

while the so-called *stray factor* is the ratio of the minor-lobe area to the total beam area:

$$\varepsilon_m = \frac{\Omega_m}{\Omega_A} = \frac{\Omega_m}{\Omega_M + \Omega_m} , \quad (\text{E.5})$$

¹Principal planes are the two orthogonal plane cuts ($x - z$ and $y - z$ planes) through the main lobe axis.

²The Poynting vector describes the energy flux of an electromagnetic field in Wm^{-2} . $Z_0 = \sqrt{\mu_0/\epsilon_0} = 376.7 \Omega$ is the impedance of vacuum.

Another very important parameter for an antenna is the *directivity* D , defined as the ratio of the maximum power density $P_{max}(\theta, \phi)$ (Wm^{-2}) to its average value over a sphere as observed in the far field of an antenna:

$$D = \frac{P_{max}(\theta, \phi)}{(4\pi)^{-1} \int_0^{2\pi} d\phi \int_0^\pi d\cos\theta P(\theta, \phi)} = \frac{4\pi}{\Omega_A}, \quad (\text{E.6})$$

Finally we introduce the concept of *aperture* of an antenna: let us consider a rectangular receiving horn immersed in the field of a uniform plane wave. The *physical aperture* of the horn is the area A_p , so if the horn is able to extract all the power from the wave over its entire physical aperture, then the total power absorbed from the wave is $P = A_p E_e / Z_0$. In real world the field response of the horn is not uniform across the aperture, because the electric field at the sidewalls must be null (see also par. 3.4 and 3.5). Thus the *effective aperture* A_e of the horn is less than A_p . The *aperture efficiency* gives the ratio between the effective and physical aperture, $\varepsilon_{ap} = A_e / A_p$. Consider now an antenna which radiates all of its power in a conical pattern of beam area Ω_A : assuming a uniform field E_a over the effective aperture, the power radiated is $P = E_a^2 A_e / Z_0$. Assuming a uniform field $E_r = E_a A_e / r \lambda$ in the far field at distance r , the power radiated is $P = E_r^2 \Omega_A r^2 / Z_0$. We thus get the *aperture-beam area relation*, $\lambda^2 = A_e \Omega_A$. The directivity is now $D = 4\pi A_e / \lambda^2$.

It's possible to regard the directivity from a purely geometrical point of view: suppose that an antenna concentrates all its energy uniformly within a cone of semi-angle α , while radiating none outside this cone. The cone cuts an ideal sphere of radius R in a curved surface of area A , thus the directivity D of this antenna is $4\pi R^2 / A$. For small values of α , the area of the plane disk at the mouth of the cone is very nearly equal to the area of the curved section of the sphere. Thus we can say that approximately $A \simeq \pi(R\alpha)^2 \Rightarrow D \simeq 4\alpha^{-2}$ and the semi-angle of the beam is given by $\alpha = 2D^{-1/2}$. The directivity of an antenna is often quoted in dB ³, $D_{dB} = 10 \log_{10} D = 20(\log_{10} 2 - \log_{10} \alpha)$.

³In this context it's worth to define the *gain*, that is proportional to the directivity by a factor of efficiency k , $G = kD$. The majority of antennas have often very high efficiency, $k \approx 1$. The gain is usually measured in dB, $G_{dB} = D_{dB} + 10 \log_{10} k$.

Appendix F

Feed Horns



Figure F.1: Picture of the circular corrugated feed horn tested at 137 GHz.

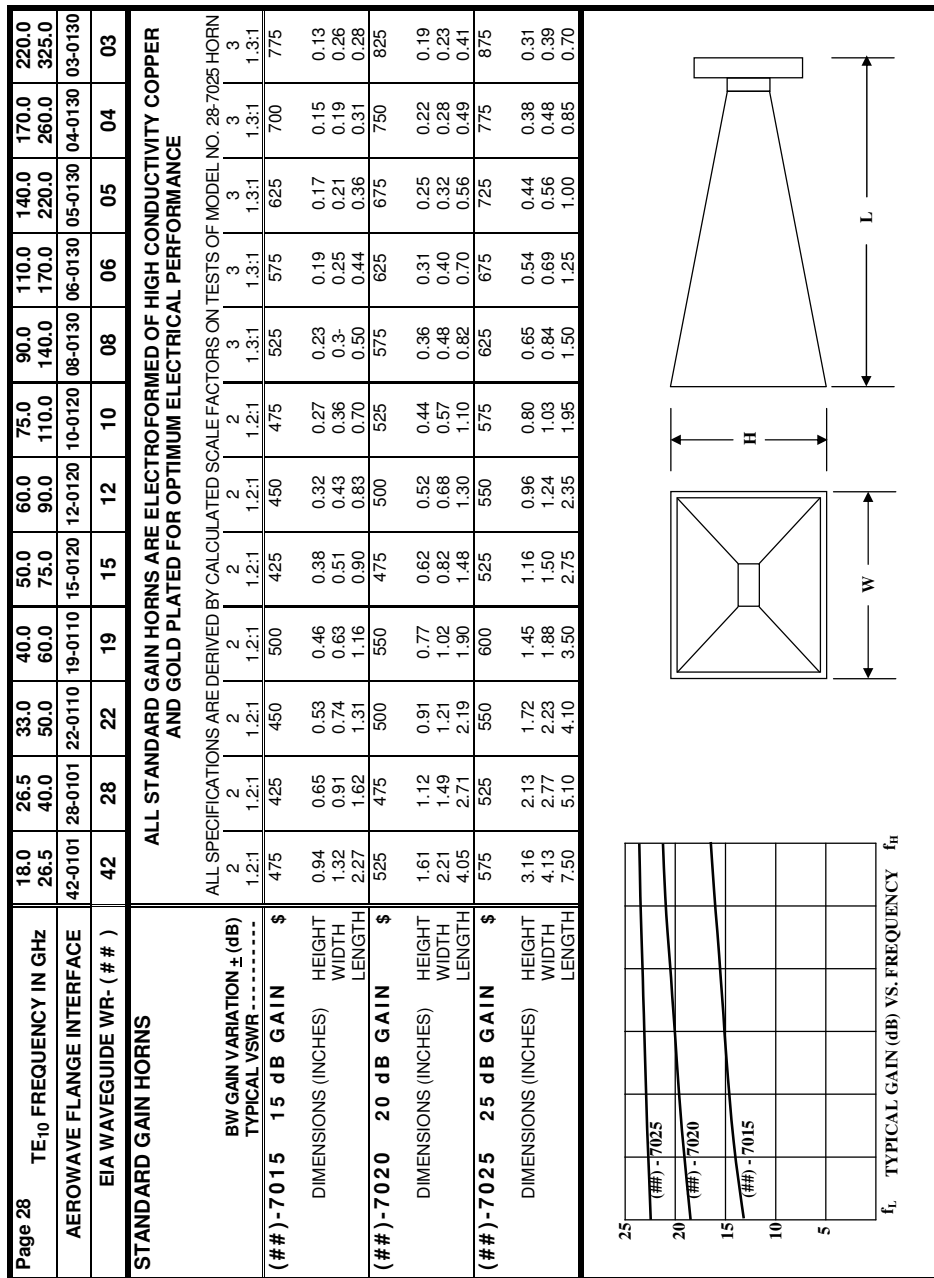


Figure F.2: Specifications of Aerowave Pyramidal Feed Horns.

List of Figures

1.1	Shape of a generic potential $U(\phi)$ giving rise to a period of exponential expansion for the universe.	27
2.1	Fullsky map provided by the COBE satellite [13] clearly showing the dipole anisotropy due to Earth's proper motion with respect to the Last Scattering Surface from which we see the incoming Doppler shifted CMB photons. The colors follows the usual convention: once T_0 (eq. 2.1) is subtracted, green regions are those with $\Delta T \approx 0$, red regions are the hottest ones, with $\Delta T \rightarrow +\Delta T_{max}$, while blue regions are the coldest ones, with $\Delta T \rightarrow -\Delta T_{max}$	42
2.2	The window function W_l is displayed against the multipole number l , for different values of $\text{FWHM} = 2\sqrt{2 \ln 2} \sigma_{beam}$. The effect of a finite beam width (angular resolution) of the instrument is clear: the smaller is σ_{beam} , the larger is the sensitivity to the highest multipoles, i.e. to the smallest angular scales.	50
2.3	Drawing of the qualitative expected behaviour of the Temperature Power Spectrum of the Cosmic Microwave Background. The three main physical effects acting on different angular scales are indicated.	51
2.4	Drawings of the dependence of the Temperature Power Spectrum on the cosmological parameters Ω_0 and Ω_b	52
2.5	The measured Temperature Power Spectrum of the Cosmic Microwave Background [32]. The data shown come from the WMAP (2006 [17]), Acbar (2004 [14]) Boomerang (2005 [11]), CBI (2003 [15]) and VSA (2004 [40]) instruments.	53
2.6	Thomson scattering of radiation with quadrupole anisotropy generates linear polarization. In the rest frame of the electron, blue lines represent hotter radiation, while red lines represent colder radiation. In par. 2.5.3 this color convention will be better understood in terms of redshift and blueshift with respect to the rest frame of the electron.	55

2.7	Scalar perturbations at recombination only generate E polarization modes. The color convention reflects redshift or blueshift with respect to the rest frame of the electron.	66
2.8	The scalar quadrupole moment ($l = 2, m = 0$). Flows from hot (blue) regions into cold (red) ones, produce the azimuth symmetric pattern Y_{20} shown ($\vec{v} \parallel \vec{k}$).	67
2.9	3-D sketch describing the transformation of $m = 0$ quadrupole anisotropies into linear E -mode polarization. (a) The orientation of the $m = 0$ quadrupole moment with respect to the scattering direction \hat{n} determines sense and magnitude of the linear E polarization, which is aligned with the cold long lobe in the plane identified by $(\hat{e}_\theta, \hat{e}_\phi)$. (b) $\hat{n} \cdot \hat{k} = \cos \theta$. The polarization points North-South (Q), with magnitude varying as $\sin^2 \theta$ (yellow lines).	68
2.10	Pure E -polarization pattern for $l = 2, m = 0$	69
2.11	Modulation of the local polarization pattern due to plane wave perturbations inside the Last Scattering Surface. Yellow points represent polarization out of the plane with magnitude proportional to their size. The plane wave modulation changes amplitude and sign of the polarization but does not mix Q and U . Modulation can however mix E and B U is also present (see par. 2.5.4).	69
2.12	Tensor quadrupole moment ($l = 2, m = 2$) due to gravity waves.	71
2.13	Shear-like polarization pattern of the B -modes as compared to the radial-tangential pattern of the E -modes. Only tensor perturbations (gravity waves) causing quadrupole anisotropy at recombination can produce such shear-like pattern of linear polarization.	72
2.14	Full polarization pattern for $l = 2, m = 2$, combination of both Q and U (eq. 2.76).	73
2.15	Temperature and polarization power spectra. For all curves $\Omega_{m,0} = 0.3, \Omega_{b,0} = 0.05, h = 0.7$ and $\tau = 0.17$ (see pars. 1.2 and 2.3). Blue (pink) curves refer to scalar spectral index $n_s = 0.99$ (0.95).	75
3.1	Characteristic I/V curve of a Gunn diode.	78
3.2	AC circuit analysis of a simple RLC resonant circuit and of one including also a negative resistance device.	80
3.3	Dynamic resistance behaviour of the load resistance plus a Gunn diode.	81
3.4	Average device resistance vs rms oscillation current.	81
3.5	Typical mm-wave coaxial cavity of a Gunn oscillator.	82

3.6	Schematic diagrams of Gaussian beam propagation along the z -axis.	86
3.7	Rectangular and circular microwave guides. The fields propagate in the z direction. The rectangular waveguide has the a side along the x -axis, while b is along y	91
3.8	Distribution of the electric and magnetic fields inside a rectangular waveguide in the TE ₁₀ and TM ₁₁ modes.	92
3.9	Pyramidal horn antennas.	95
3.10	Cross-section of a feed horn and the Gaussian beam it produces.	96
3.11	Beam measurements of the WR-6 horn along the H plane. The scan is performed varying the elevation, while the optimized azimuth is kept fixed. Each experimental point is the mean value upon 10 measures, displayed with the associated uncertainty. The red line is the Gaussian fit, whose parameters are shown.	98
3.12	Beam measurements of the WR-6 horn along the E plane. The scan is performed varying the azimuth, while the optimized elevation is kept fixed. Each experimental point is the mean value upon 10 measures, displayed with the associated uncertainty. The red line is the Gaussian fit, whose parameters are shown.	99
3.13	Beam measurements of the 90 GHz circular corrugated horn. The scan is performed varying the azimuth, while the optimized elevation is kept fixed. Each experimental point is the mean value upon 10 measures, displayed with the associated uncertainty. The red line is the Gaussian fit, whose parameters are shown.	100
3.14	Beam measurements of the 137 GHz circular corrugated horn. The scan is performed varying the azimuth, while the optimized elevation is kept fixed. Each experimental point is the mean value upon 10 measures, displayed with the associated uncertainty. The red line is the Gaussian fit, whose parameters are shown.	101
3.15	Circuit of the WDH detector composed by two diodes, an internal matched termination and a 3dB hybrid.	101
3.16	The detectors WDH (center) and DD (right) as compared in size to the standard WR-10 25dB feed horn (see Appendix F).	102
3.17	Low noise HEMT preamplifiers.	103
3.18	The circuit used to amplify signals out of the DD diode.	105
3.19	Expected behaviour of the signal-to-noise ratio (S/N) as a function of R_0 . The plot is obtained using the following typical values: $i_a^n = 0.4 \text{ pA}/Hz^{-1/2}$, $N_a^2 = 3 \text{ nV}/Hz^{-1/2}$, $N_d^2 = 10 \text{ nV}/Hz^{-1/2}$ (thin lines) and $N_d^2 = 40 \text{ nV}/Hz^{-1/2}$ (thick lines). The parameter is the internal impedance of the diode, Z_d	106

3.20	Measured behaviour of the signal-to-noise ratio (S/N) as a function of R_0 . Each point is the result of 10 measures. The number displayed close to the experimental points is the measured DC offset for each value of R_0	107
3.21	The circuit used to modulate the 78-114 GHz Gunn oscillator.	110
3.22	The circuit used to modulate the 120-147 GHz Gunn oscillator.	111
3.23	Cross-section of the meniscus lens [78].	113
4.1	Coordinate systems for the study of a polarizing grid or a single wire. The wavevector \vec{k} of the incident radiation is aligned with the w -axis, the u , x and y -axes are in the plane of the page, the w and z -axes are in the plane perpendicular to the u -axis, and the wires are parallel to the $x - y$ plane. (u, v, w) is the laboratory system, while (x, y, z) are the grid coordinates.	118
4.2	Definition of the system of coordinates (u', v', w') for the reflected wave in relation to the (u, v, w) system of the incident/transmitted waves introduced in fig. 4.1. The u' and u -axes are one and the same, pointing out of the page. The direction of propagation of the reflected wave is along the negative w' -axis.	124
4.3	The two techniques proposed for modulating a rotational field of polarization. See text for details.	132
4.4	CAD project of the -45° shear-like polarizer.	135
4.5	CAD project of the twin $+45^\circ$ shear-like polarizer.	136
4.6	Simulations on the polarized CMB sky.	141
4.7	Effect of point sources on CMB Measurements. TT, EE and BB power spectra (see pars. 2.4.3, 2.5.2 and 2.6) as compared to the strong non-thermal spectra, characterizing point sources behaviour at different frequencies.	145
4.8	CAD drawings: plane mirror and part of its supporting system. Mechanical realization thanks to A. Iacoangeli (Physics Department workshop).	148
4.9	Experimental set-up for our polarimetry measurements with a reflecting polarizer: the mirror parallelizes the wire-grid at a distance d , which is finely tunable by means of a Mitutoyo 150-801 micrometer head.	149
4.10	The wire-grid rotating support and its electronics box.	151
4.11	The expected normalized signal as a function of the phase shift $\Delta\varphi$ and the rotation angle θ . We take $I_0 = 2$, $p_x \simeq p_y$, $0 \leq \theta \leq \pi$ and $0 \leq \Delta\varphi \leq 3\pi$	155
4.12	The scan is performed varying the mirror-polarizer distance from 0.1 to 23.6 mm, while the rotation angle is kept fixed at 45° . Each experimental point is the mean value upon at least 10 measures, displayed with the associated uncertainty.	156

4.13	The scan is performed varying the rotation angle from 0° to 180° (vertical wires), while the mirror-polarizer distance is kept fixed at 0.63 mm. At 90° (horizontal wires) the incoming polarization state is parallel to the wires. Each experimental point is the mean value upon at least 10 measures, displayed with the associated uncertainty. The absorption parameters p_x, p_y are found by means of a least-squares fit (red solid line).	156
4.14	The scan is performed varying the rotation angle from 0° to 180° (vertical wires), while the mirror-polarizer distance is kept fixed at 1.64 mm. At 90° (horizontal wires) the incoming polarization state is parallel to the wires. Each experimental point is the mean value upon at least 10 measures, displayed with the associated uncertainty. The absorption parameters p_x, p_y are found by means of a least-squares fit (red solid line).	157
4.15	The scan is performed varying the rotation angle from 0° to 180° (vertical wires), while the mirror-polarizer distance is kept fixed at 1.71 mm. At 90° (horizontal wires) the incoming polarization state is parallel to the wires. Each experimental point is the mean value upon at least 10 measures, displayed with the associated uncertainty. The absorption parameters p_x, p_y are found by means of a least-squares fit (red solid line).	157
4.16	The scan is performed varying the rotation angle from 0° to 180° (vertical wires), while the mirror-polarizer distance is kept fixed at 1.73 mm. At 90° (horizontal wires) the incoming polarization state is parallel to the wires. Each experimental point is the mean value upon at least 10 measures, displayed with the associated uncertainty. The absorption parameters p_x, p_y are found by means of a least-squares fit (red solid line).	158
4.17	The scan is performed varying the rotation angle from 0° to 180° (vertical wires), while the mirror-polarizer distance is kept fixed at 2.30 mm. At 90° (horizontal wires) the incoming polarization state is parallel to the wires. Each experimental point is the mean value upon at least 10 measures, displayed with the associated uncertainty. The absorption parameters p_x, p_y are found by means of a least-squares fit (red solid line).	158
4.18	The scan is performed varying the rotation angle from 0° to 180° (vertical wires), while the mirror-polarizer distance is kept fixed at 2.32 mm. At 90° (horizontal wires) the incoming polarization state is parallel to the wires. Each experimental point is the mean value upon at least 10 measures, displayed with the associated uncertainty. The absorption parameters p_x, p_y are found by means of a least-squares fit (red solid line).	159

4.19	The mirror is excluded thanks to beam shifting: the system behaves as a simple polarizer. The scan is performed varying the rotation angle from 0° to 180° (vertical wires). At 90° (horizontal wires) the incoming polarization state is parallel to the wires. Each experimental point is the mean value upon at least 10 measures, displayed with the associated uncertainty. The absorption parameters p_x, p_y are found by means of a least-squares fit (red solid line).	159
5.1	Angular power spectrum of CMB anisotropy expected from OLIMPO observations. The simulations assume 4 days of integration over $f_{sky} = 0.3\%$ of the sky; 37 detectors with $NET = 200\mu K/\sqrt{Hz}$, and an angular resolution of $5'$ FWHM (see par. 3.7 for the definition of NET).	163
5.2	Spectrum of the Sunyaev-Zel'dovich effect in a rich cluster of galaxies, for different temperatures of intra-cluster electrons. The spectrum is compared with the OLIMPO bands at 150, 240, 410 and 540 GHz.	164
5.3	Left: The OLIMPO payload, all shields removed. Right: Structure deformations for a $5g$ horizontal load.	165
5.4	Ray Tracing of the OLIMPO Cassegrain configuration. The intensity distribution on the image plane is described in par. 5.3.1, taking into account the occlusion due to the secondary mirror.	166
5.5	The optics box: ray tracing drawing and picture.	168
5.6	3-D profile of OLIMPO telescope beam. Signal is normalized.	175
5.7	2-D contour plot of OLIMPO telescope beam. Greyscale is divided into N levels, from pure white (null normalized signal), to pure black (unity normalized signal).	176
5.8	2-D slices of the OLIMPO telescope beam profile at 90 GHz. The scan is performed varying the azimuth, while elevation is kept fixed. Each experimental point is the mean value upon at least 10 measures, displayed with the associated uncertainty. The red line is the appropriate Airy-modified PSF function (eq. 5.3). The blue line is the Gaussian fit, whose parameters are shown.	177
5.9	2-D slices of the OLIMPO telescope beam profile at 90 GHz. The scan is performed varying the elevation, while azimuth is kept fixed. Each experimental point is the mean value upon at least 10 measures, displayed with the associated uncertainty. The red line is the appropriate Airy-modified PSF function (eq. 5.3). The blue line is the Gaussian fit, whose parameters are shown.	178

5.10	2-D slices of the OLIMPO telescope beam profile at 137 GHz. The scan is performed varying the azimuth, while elevation is kept fixed. Each experimental point is the mean value upon at least 10 measures, displayed with the associated uncertainty. The red line is the appropriate Airy-modified PSF function (eq. 5.3). The blue line is the Gaussian fit, whose parameters are shown.	179
5.11	2-D slices of the OLIMPO telescope beam profile at 137 GHz. The scan is performed varying the elevation, while azimuth is kept fixed. Each experimental point is the mean value upon at least 10 measures, displayed with the associated uncertainty. The red line is the appropriate Airy-modified PSF function (eq. 5.3). The blue line is the Gaussian fit, whose parameters are shown.	180
5.12	Focal plane mapping at 140 GHz. The source and the detector are shifted forth and back from the two nominal positions of the focal planes of, respectively, the telescope and the optics box channel at 140 GHz, by means of micrometric sledges. Signal is normalized to unity.	186
A.1	Polarization ellipse with semi-major axis of length a and a semi-minor axis of length b	190
A.2	The Stokes parameters S_1 and S_2 as difference in intensity carried by two orthogonal components rotated by $45\frac{1}{2}$	192
C.1	Picture of the 78 – 114 GHz Gunn oscillator.	201
C.2	Gunn oscillators provided by J.E. Carlstrom Co., Chicago IL (U.S.A.).	202
C.3	Datasheet of the 78 – 114 GHz Gunn oscillator.	203
C.4	Datasheet of the 120 – 147 GHz Gunn oscillator.	204
D.1	Specifications of Aerowave rectangular waveguides and flanges.	205
D.2	Drawings with dimensions of Aerowave waveguides and flanges (1 of 3).	206
D.3	Drawings with dimensions of Aerowave waveguides and flanges (2 of 3).	207
D.4	Drawings with dimensions of Aerowave waveguides and flanges (3 of 3).	208
E.1	3D field pattern of a directional antenna with maximum of radiation at $\theta = 0$. Most of radiation is contained in the main lobe, but there are also minor lobes (side and back). This pattern is symmetric in ϕ and is a function of θ only.	209

E.2	2D field, power and decibel plots of the 3D antenna pattern of fig. E.1.	210
F.1	Picture of the circular corrugated feed horn tested at 137 GHz. .	213
F.2	Specifications of Aerowave Pyramidal Feed Horns.	214

List of Tables

1.1	Current values for the cosmological parameters introduced [18].	16
3.1	Relative cut-off wavelengths of TE_{mn} modes in a standard waveguide.	91
3.2	Standard waveguides frequency bands and interior dimensions. .	93
3.3	Main parameters for the four Aerowave pyramidal feed horns used in this work (two WR-10). We refer to Appendix F for the drawing and the specifications.	96
3.4	Measured beamwidth for the WR-6 pyramidal feed horn in both H and E planes (see figs. 3.11 and 3.12).	98
3.5	Measured beamwidth for the WR-10 pyramidal feed horn in both H and E planes [78].	99
3.6	Measured beamwidth for the 90 GHz circular corrugated feed horn.	99
3.7	Measured beamwidth for the 137 GHz circular corrugated feed horn (see Appendix F for a picture).	100
3.8	Specifications of the two broadband diodes produced by Millimeter Pacific Products. Maximum input power 100 mW. Responsivity (see next section for definition) is measured into 1 $M\Omega$ load.	102
5.1	Resume of the measured beam sizes (in arcmins) at 90 and 137 GHz, both in elevation and azimuth. These final results are compared to the diffraction limit $\sim 1.22\lambda/D$, with $D = 2.6$ m. .	174
5.2	Coordinates of the five fields of view used for the alignment test in the optical. The corresponding coordinates of the spots on the focal plane of the experiment are also shown. The fields are not the same in x and y because the dichroics partially limit the beam, since they are tilted at 45° with respect to the incident radiation: their projection on the beam is thus an ellipse.	184

5.3 Alignment and refocusing tests results. As a reference, the signal obtained observing directly the laser is 109.22 ± 0.14 mV: note that this is obtained without beam expander and lens, which scatter a lot of radiation. Hence, the efficiency of the optical system is very high, even at optical wavelengths. The coordinates of the five fields are described in tab. 5.2. 184

Bibliography

- [1] Guth A.H., The Inflationary Universe: A Possible Solution to the Horizon and Flatness Problems, *Physical Review D* 23, 347 (1981).
- [2] Linde A., A New Inflationary Universe Scenario: A Possible Solution Of The Horizon, Flatness, Homogeneity, Isotropy And Primordial Monopole Problems, *Physical Letters B* 108, 389 (1982).
- [3] AA. VV., Impact of Gravitational Lensing on Cosmology (IAU S225), Proceedings of the International Astronomical Union Symposia and Colloquia, edited by Mellier Y. and Meylan G. (2004).
- [4] Cole S. et al., The 2dF Galaxy Redshift Survey: Power-spectrum analysis of the final dataset and cosmological implications , *Mon.Not.Roy.Astron.Soc.* 362 (2005) 505-534 (2005), astro-ph/0501174.
- [5] Eisenstein D. J. et al., Detection of the Baryon Acoustic Peak in the Large-Scale Correlation Function of SDSS Luminous Red Galaxies, *Astrophysical Journal*, 633, 560-574 (2005), astro-ph/0501171.
- [6] Krauss L.M. and Chaboyer B., Age Estimates of Globular Clusters in the Milky Way: Constraints on Cosmology, *Science* Vol. 299, 5603, pp. 65 - 69 (2003).
- [7] Filippenko A.V., Type Ia Supernovae and Cosmology, *Astrophysics and Space Science Library*, Vol. 332 (2005).
- [8] Type Ia Supernovae: Theory and Cosmology, edited by Niemeyer J.C. and Truran J.W., Cambridge University Press (2000).
- [9] C.B. Netterfield et al., A measurement by BOOMERANG of multiple peaks in the angular power spectrum of the cosmic microwave background, Submitted to *Ap. J.*, April 2001, astro-ph/0104460.
- [10] MacTavish C.J. et al., Cosmological Parameters from the 2003 flight of BOOMERANG, *Astrophysical Journal*, 647, 799 (2006), astro-ph/0507503.

- [11] Masi et al., Instrument, Method, Brightness and Polarization Maps from the 2003 flight of BOOMERanG (2005), astro-ph/0507509.
- [12] Fixsen D.J. et al., The Cosmic Microwave Background Spectrum from the Full COBE/FIRAS Data Set, *Astrophysical Journal*, 473, 576 (1996).
- [13] Smoot G.F. et al., Description of COBE DMR, *Astrophysical Journal*, 360, 685 (1990).
- [14] Kuo C.L., High Resolution Observations of the CMB Power Spectrum with ACBAR, *Astrophys.J.* 600 (2004) 32-51, astro-ph/0212289.
- [15] Mason, B.S. et al., The anisotropy of the microwave background to $l=3500$: Deep field observations with the Cosmic Background Imager, *Astrophysical Journal*, 591, 540-555 (2003).
- [16] Hanany et al. , A Measurement of the Cosmic Microwave Background Anisotropy on angular scales of 10 arcminutes to 5 degrees, *Astrophysical Journal*, 545 (2000),astro-ph/0005123.
- [17] N. Jarosik et al., Beam Profiles, Data Processing, Radiometer Characterization and Systematic Error Limits, astro-ph/0603452, submitted to *ApJ*.
- [18] <http://lambda.gsfc.nasa.gov/product/map/current/parameters.cfm>
- [19] C. L. Bennett et al., First Year Wilkinson Microwave Anisotropy Probe (WMAP) Observations: Foreground Emission, *Astrophys.J.Suppl.* 148 (2003) 97, astro-ph/0302208.
- [20] Moncy V.J., Cosmographic Evaluation of the Deceleration Parameter Using Type Ia Supernova Data, *The Astrophysical Journal*, 614 (2004).
- [21] Liddle A.R. and Lyth D., *Physical Reports*, 231, 1 (1993).
- [22] Peacock J.A., *Cosmological Physics* (1999).
- [23] Dodelson S., *Modern Cosmology* (2003).
- [24] Dodelson S. et al., *Physical Review Letters*, 72, 3443 (1994).
- [25] Knox L. and Turner M., *Physical Review Letters*, 73, 3447 (1996).
- [26] Kofman L.A. and Linde A.D., *Generation Of Density Perturbations in Inflationary Cosmology* (1986).
- [27] Sachs R.K. and Wolfe A.M., *Astrophysical Journal*, 147, 73 (1967).
- [28] Coles P. and Lucchin F., *Cosmology - The Origin and Evolution of Cosmic Structures* (2002).

- [29] Silk J.I., *Astrophysical Journal*, 211, 638 (1977).
- [30] Kaiser N., *MNRAS*, 202, 1169 (1983).
- [31] Silk J. and Wilson M.L., *Physica Scripta*, 21, 708 (1980).
- [32] Hinshaw G. et al., Three-Year Wilkinson Microwave Anisotropy Probe (WMAP) Observations: Temperature Analysis, *Astrophysical Journal*, in press, January 5 (2007), astro-ph/0603451.
- [33] Seljak U. and Zaldarriaga M., *Astrophysical Journal*, 469, 437 (1996).
- [34] Seljak U., Zaldarriaga M., Bertschinger E., *Astrophysical Journal*, 494, 491 (1998).
- [35] Lewis, A., Challinor A., and Lasenby A., Efficient Computation of CMB anisotropies in closed FRW models, *Astrophysical Journal*, 538 (2000), astro-ph/9911177.
- [36] White M., Constraints From The Damping Tail, *Astrophysical Journal*, 555 (2001).
- [37] Hu W., White M., *Astrophysical Journal*, 471, 30 (1996).
- [38] Hu W., Turner M.S., Weinberg E.J., *Physical Review D*, 49, 3830 (1994).
- [39] Liddle A.R., *Physical Review D*, 51, 5347 (1995).
- [40] Clive Dickinson et al., High sensitivity measurements of the CMB power spectrum using the extended Very Small Array, submitted to *MNRAS* (2004).
- [41] Chandrasekhar S., *Radiative Transfer*, Dover, New York (1960).
- [42] Zaldarriaga M., Seljak U., All-sky analysis of polarization in the microwave background, *Physical Review D* 55, 1830 (1997).
- [43] Zaldarriaga M., *Fluctuations in the Cosmic Microwave Background*, PhD Thesis (1998).
- [44] Zaldarriaga M., Seljak U., Signature of Gravity Waves in Polarization of the Microwave Background, astro-ph/9609169 (1997).
- [45] Zaldarriaga M., Seljak U., *Astrophysical Journal*, 469, 437 (1996).
- [46] Bunn E.F., E/B Decomposition of finite pixelized CMB maps, astro-ph/0207338 (2002).
- [47] <http://healpix.jpl.nasa.gov>

- [48] Goldberg J.N. et al., *J. Math. Phys.* 8, 2155 (1967).
- [49] Newman E. and Penrose R., *J. Math. Phys.* 7, 863 (1966).
- [50] Birkinshaw M., The Sunyaev-Zel'dovic Effect, astro-ph/9808050 (1998), to appear in *Physics Reports*.
- [51] Nati F. et al., The OLIMPO experiment (2006), preprint submitted to Elsevier.
- [52] Mason B.S. et al., *Astrophysical Journal*, 591, 540 (2003).
- [53] Dawson K.S. et al., *Astrophysical Journal*, 581, 86 (2002).
- [54] De Petris M., Liberati F., Gervasi M., *Applied Optics*, 28, 1785D (1989).
- [55] de Bernardis P. et al., *Infrared Physics*, 29, 1005 (1989).
- [56] Mainella G. et al., *Applied Optics*, 35, 2246 (1996).
- [57] Mauskopf P. et al., *Applied Optics*, 36, 765 (1997).
- [58] Masi S. et al., *Cryogenics*, 39, 217 (1999).
- [59] Masi S. et al., *Cryogenics*, 38, 319 (1998).
- [60] Piacentini F. et al., *Astrophysical Journal Supplement*, 138, 315 (2002).
- [61] Houde M. et al., *Polarizing Grids, Their Assemblies and Beams of Radiation*, *Publications of the Astronomical Society of the Pacific*, 113, 622-638 (2001).
- [62] Siringo G. et al., A new polarimeter for (sub)millimeter bolometer arrays, *Astronomy and Astrophysics*, 422, 751–760 (2004).
- [63] Stivoli F. et al., Separating polarized cosmological and galactic emissions for CMB B-mode polarization experiments, astro-ph/0505381 (2006).
- [64] Lazarian A. and Finkbeiner D., Microwave Emission from Aligned Dust, astro-ph/0307012 (2003).
- [65] Martin P.G., On Predicting the Polarization of Low Frequency Emission by Diffuse Interstellar Dust, astro-ph/0606430 (2006).
- [66] Prunet S. and Lazarian A., Polarized Foreground from Thermal Dust Emission, astro-ph/9902314 (1999).
- [67] Lazarian A. and Prunet S., Polarized Microwave Emission from Dust, astro-ph/0111214 (2001).

- [68] Sethi S.K. et al., Galactic dust polarized emission at high latitudes and CMB polarization, astro-ph/9803158 (1998).
- [69] Balanis C.A., Advanced Engineering Electromagnetics, chapter 6 (1989).
- [70] Kraus J.D. and Marhefka R.J., Antennas for All Applications (2002).
- [71] Bowman F., Introduction to Bessel Functions (1958).
- [72] Arfken G., Hankel Functions, Mathematical Methods for Physicists (1985).
- [73] Collett E., Polarized Light - Fundamentals and Applications (1993).
- [74] Goldsmith P.F., Quasioptical Systems (1998).
- [75] Giommi P. and Colafrancesco S., Evidence for a Significant Blazar Contamination in CMB Anisotropy Maps, astro-ph/0306206 (2003).
- [76] Kildal, Per-Simon et al., Losses sidelobes, and cross polarization caused by feed-support struts in reflector antennas: design curves, IEEE Transactions on Antennas and Propagation, 36, 2 (1988).
- [77] Farese P.C., COMPASS: An upper limit on Cosmic Microwave Background polarization at angular scale of 20', The Astrophysical Journal, 610:625–634 (2004).
- [78] Marini Bettolo C., Polarimetria astrofisica e cosmologica con l'esperimento BOOMERanG, Degree Thesis in Physics (2005).
- [79] Nati F., OLIMPO: a balloon-borne arcminute-resolution survey of the sky at millimetric and sub-millimetric wavelengths, PhD Thesis in Astronomy (2005).
- [80] Conversi L., OLIMPO: a components separator of the microwave sky, PhD Thesis in Astronomy (2007).
- [81] Catalano A., Polarimetria nell'infrarosso, Degree Thesis in Physics (2003).
- [82] Mazzoldi P., Nigro M. and Voci C., Fisica Vol. II (1998).
- [83] Ediss G. A. and Koller D., 68.5 to 118 GHz Measurements of Possible Infrared Filter Materials: Black Polyethylene, Zitex, and Grooved and Un-Grooved Fluorogold and HDPE, ALMA MEMO 412 (2002).
- [84] Cernicharo, J., ATM: A Program to compute Theoretical Atmospheric Opacity for Frequencies below 1 THz, PhD Thesis Paris, and IRAM report 52 (1998).

Acknowledgements

Thanks to my uncles Antonella and Enrico, for the unique opportunity of studying in Rome they offered to me, nothing would be possible without their support. Thanks to Alceo's son, for being an example for me of how to be a man and a father, to my mother, my sister and my whole family for their neverending support. Thanks to Paolo de Bernardis, for just being an example of how to be a great scientist, to Federico Nati, Luca Pagano, Daniele Brienza, Luca Conversi, Andrea Conte, Mauro Maiello. Thanks to Daniele Pranzetti, Massimo Granata, Rocco Langone, Fabio Stefanini, Gianluca Ragnoni. Thanks to "The Gladiator" Amico Aprilia, for being my everyday antidote to Roma's unbelievable traffic. Thanks to all the metal bands I listen to, for the everyday energy and power they make flowing in me and for keeping me safe from useless speeches. Thanks to atheists, basketball, Spoken beer and Todis discount, strong wines from the South of Italy, coffee, NBA Live 2004, Acer mp3 reader, Skype, eMule and DivX format for keeping my mind unpolluted from any TV programs and spots.

Ringraziamenti

Grazie ai miei zii Antonella ed Enrico per l'opportunità unica di studiare a Roma che mi hanno offerto, niente sarebbe stato possibile senza il loro supporto. Grazie al figlio di Alceo, per essermi da esempio di uomo e padre, a mia madre, a mia sorella e a tutta la mia famiglia per il supporto costante. Grazie a Paolo de Bernardis, per essermi da esempio di grande scienziato, a Federico Nati, Luca Pagano, Daniele Brienza, Luca Conversi, Andrea Conte, Mauro Maiello. Grazie a Daniele Pranzetti, Massimo Granata, Rocco Langone, Fabio Stefanini, Gianluca Ragnoni. Grazie al gladiatorio Amico Aprilia, per essere stato il mio antidoto quotidiano all'incredibile traffico di Roma. Grazie a tutti i gruppi metal che ascolto, per l'energia e la forza che tutti i giorni fanno scorrere in me e per avermi salvato da discorsi e argomenti inutili. Grazie agli atei, alla pallacanestro, alla birra Spoken, al discount Todis, ai vini "tosti" del Sud Italia, al caffè, a NBA Live 2004, al lettore mp3 Acer, a Skype, a eMule e al formato DivX, per aver salvaguardato la mia mente dalla spazzatura della TV e della pubblicità.